The effects of realistic surface properties on low temperature space observatories

Thesis

UNRESTRICTED

The effects of realistic surface properties on low temperature space observatories

Robert Blake, B.Sc., M.Sc.

Submitted for the degree of Doctor of Philosophy

Department of Physics

The Open University

30 September 1997

Revised 24 February 1998

Date of submission: 30th September 1997
Date of award: 26th March 1998

Abstract

I investigate the effects of modelling radiative heat transfer correctly on equilibrium temperatures of passively cooled telescopes. I compare the traditional diffuse approximation with a surface exhibiting the directional properties of gold, both with an emissivity of 0.03. I also modeled surfaces with much lower, more realistic emissivities.

Directional surface properties are derived from values of optical constants at room temperature since there exists a dearth of reliable data at cryogenic temperatures. The effect of using optical constants at different wavelengths is also investigated.

My simulations show the diffuse assumption produces higher temperatures than the directional surface. Both surfaces produce higher temperatures than the low emissivity cases when conductivity is low, whilst the reverse is true for high conductivity. The directional surface always outperformed the diffuse surface.

For radiative exchange, the diffuse approximation simply produces pessimistic results. However, incorrect modelling of radiative exchange can have knock-on effects. The higher emissivity, diffuse approximation predicts much greater improvements due to tilted sunshields than would realistically occur. This may recommend unnecessary changes to telescope designs in the attempt to improve cooling performance.

The lack of reliable directional radiative data for candidate passive cooling materials will require a major measurement program before a mission is launched. In this thesis I describe apparatus to help in such measurements.

The bi-directional reflectometer quickly and accurately builds up a picture of directional surface properties, performing very well when combined with a reliable laser and measuring device, the few component parts being relatively cheap. Thus, the many directional measurements required for accurate modelling could be made cheaply and quickly.

The multiple reflection cell was designed to make high accuracy measurements at one angle only. This was not as effective as hoped due to laser problems, but should be able to make very good measurements. Further work is recommended.

Acknowledgments

I would like to thank my supervisor, Barrie Jones, for helping me at every stage of my research, from offering me the studentship over three other candidates to providing very useful feedback on the contents and layout of this thesis. The regular meetings over the course of my studies and the invaluable advice made my PhD proceed much more smoothly than it otherwise would have. Also, the evenings out during conferences, and parties at his own house added a great deal of fun to my time at the Open University.

I'd also like to thank the staff and research students of the Open University Physics Department for their help and advice over the years. In particular, the friendliness of everyone there really helped me settle in quickly and feel comfortable when I first arrived. Thanks to Roger and Martin for the work they did in the workshop, without which I'd have had considerably less experimental apparatus to play with. Thanks to Shirley and Ray for trusting me with root access. Thanks to Pete for helping me moan about how tough an experience writing up is. Thanks to Tim and Richard for helping to hone my skills at darts, pinball, and jive talking.

Special thanks must go to Chris Stoddart for taking the sysadmin pressures off my back at just about the right time. Also, more importantly, for giving me someone I could go and console and/or laugh with when the lusers seemed to be getting the upper hand, and for helping greatly in building my free PC on which most of this thesis was written.

I should also thank Alan Penny, Tim Hawarden, Harley Thronson, and John Davies for creating the EDISON design and proposing it for ESA's M3 mission. They should also be thanked for telling me and Barrie about all the exotic conferences we went to, and most especially for their encouragement and enthusiasm whenever we presented our results at these conferences, which really made me feel part of the wider I-R community. Special thanks to Alan for all the extra help and advice he gave out over the years, helping in the viva of my first year report, and supplying me with various publications.

Thanks to Ian Dobbie for a million things, including giving me a place to escape from Milton Keynes to, relaxing my mind with various alcoholic pursuits, lending me innumerable books, moving my stuff to Edinburgh, organising several asrlon meetings, and teaching me more about frog muscle than I ever wanted to know. Hope my speech was OK, and I look forward to hearing yours in May.

I should also thank my new friends at Harlequin for giving me a job to pay the bills, and for being so understanding by employing me part-time whilst I was writing up. In particular, thanks to everyone at the Edinburgh office for not having too many problems to distract me (or at least having enough of a clue to fix them yourselves in many cases).

Finally, and most importantly, I must thank Linda for everything. For letting me escape Milton Keynes (again) and keeping me happy and sane throughout my 3.5 years at the OU, and for spurring me on to finish this thesis on time. I doubt I'd have kept this up for so long without your encouragement and support, and I just hope I can do the same for you in a couple of years.

Contents

Chapter 1

Passive Cooling

1.1 Infra-Red astronomy

Infra-Red Astronomy began in about 1800 with William Herschel's discovery of infra-red emission from the Sun. This was followed by the pioneering work of Piazzi Smyth and Thomas Edison. However, it was not until the 1960's that solid state infra-red detectors began to make a significant contribution to astrophysical research. [1]

Today, infra-red astronomy is fast becoming one of the most interesting and exciting fields of astronomical research. With vibrational and rotational transitions of many molecules occurring in the infra-red, as well as the spectral features of interstellar and circumstellar dust particles, the infra-red spectrum can tell us much about the cosmic abundances of elements and interstellar chemistry. Infra-red astronomy is also invaluable in studying high redshift objects where optical spectra are shifted into the infra-red. Add to this the fact that the absorption of infra-red radiation by dust is much less than at optical wavelengths, and the attractions of infra-red astronomy are obvious.

This interest in infra-red astronomy can only improve in the next century with the current interest in finding Earth-like planets orbiting other stars. Such planets are very difficult to find by any method, and virtually impossible to image by anything other than an infra-red telescope of some description.

Infra-red astronomy's relatively recent growth is mainly due to the fact that it is very difficult from the ground and so the field has only really come into its own with the advent of space technology. The major problem infra-red astronomers have is the atmosphere. In optical work, the atmosphere is a problem due to turbulence causing 'seeing', although this can be countered by using new techniques (e.g. adaptive optics).

However, in infra-red work, the problem is altogether more insuperable. Infra-red light is actively

Wavelength range (μm)	Wavelength centre (μm)	Designated label	Transparency of atmosphere	Background from atmosphere
1.1-1.4	1.25	J	Good	Low
1.5-1.8	1.65	H	Good	Low
2.0-2.4	2.20	K	Good	Low
3.0-4.0	3.50	L	Fair	Moderate
4.6-5.0	4.80	M	Low	High
7.5-14.5	10.0	N	Fair	Very high
17-25	20.0	Q	Low	Very high
28-40	35.0	Z	Very low	Very high

Table 1.1 A list of atmospheric windows for infra-red astronomy

absorbed by molecular resonances in the constituents of the atmosphere (primarily H_2O and CO_2). There are a few 'windows' in the atmosphere, wavelengths at which infra-red light can penetrate. For historical reasons, these windows are labelled with the letters J, H, K, L, M, N, Q, and Z (see table 1.1).

However, even when we can detect the light, it is invariably swamped by the infra-red emissions of the very warm atmosphere which, being a warm 'body', emits infra-red light.

Despite these restrictions, it is a testament to the power of infra-red astronomy that in 1992 John Davies reported that 'the data produced by UKIRT* have been published in refereed journals at a rate of more than one paper per week over a period of years'[2].

Clearly, to make good infra-red observations, a prime advantage would be to get above the atmosphere. This first happened some 20 years ago with the AFGL† rocket missions. Since that time, there have not been a huge number of infra-red space observatories, due to the immense cost of such a mission. However, those that have been launched (IRAS‡, COBE§, and most recently ISO¶) have consistently produced impressive results that have sparked much interest and excitement in the astronomical community.

The advantages of going into space are so great that, despite the modest size of its 60cm aperture, ISO is considerably more sensitive than the largest ground based telescopes, even in one of the few good atmospheric windows.

As well as eliminating atmospheric interference, going into space carries another huge advantage.

*The UK Infra-Red Telescope
†The U.S. Air Force Geophysics Laboratory
‡The InfraRed Astronomical Satellite
§The NASA Cosmic Background Explorer
¶The ESA Infrared Space Observatory

Clearly, if a telescope is trying to detect very faint infra-red sources, it does not want emission from the telescope structure itself swamping the signals. Thus, the telescope must be kept as cold as possible. On the ground, it is impractical to cool the entire telescope structure. However, in the vacuum of space this becomes much easier.

However, just putting the telescope in space is not enough to cool it sufficiently to make sensitive observations in the infra-red. The Sun is still a major heat source, and if the telescope is in a low-earth orbit, parasitic heating from the Earth can also be a major factor. Thus, space based infra-red observatories also need to carry a supply of on-board cryogens to make sure they reach the optimal operating temperature.

At least, they did until now.

The main problem with cryogens is that they remove the excess heat by utilising the latent heat of vapourisation of the liquid Helium, with the gaseous Helium being vented into space. Thus, unless regular (and costly) trips are made to 'top up' the cryogens, the telescope will have a limited life-time. Also, the extra weight and bulk of the storage tanks for the cryogens put definite restrictions on the size of the telescope itself, since the standard launch rockets have strictly defined payload limits.

In 1993, a group of scientists from around the world proposed a radically new design for an infra-red space telescope in response to ESA's request for M3 mission proposals [3]. The telescope, christened EDISON (see figure 1.1), was a development of an original design (POIROT [4]) proposed some years earlier. It was intended to be the model for the next generation of telescopes to take infra-red astronomy into the 21st century.

Even more than 10 years before a possible launch, the success of this design can be gauged by the fact that it has already spawned many closely related missions (see below).

The key feature of the EDISON design is its so-called 'passive cooling'. Whereas all other infra-red space telescopes actively cool their systems by effectively 'dumping' liquid helium on them, EDISON is designed to cool to operating temperatures by radiating the heat away from the system.

All bodies radiate energy. If a telescope radiates energy away into space, it is lost from the system and the telescope cools. However, the telescope is in turn heated by the Sun, and possibly the Earth. Thus, the EDISON design plans to radiate that heat out of the system before it has a chance to reach the telescope tube itself.

This will be achieved by a number of steps. Firstly, place the telescope well away from the Earth, so both the Sun and Earth can be kept on the same side of the telescope. Then shield the telescope tube from these heat sources with a number of 'sun-shields'. The outermost shield will be

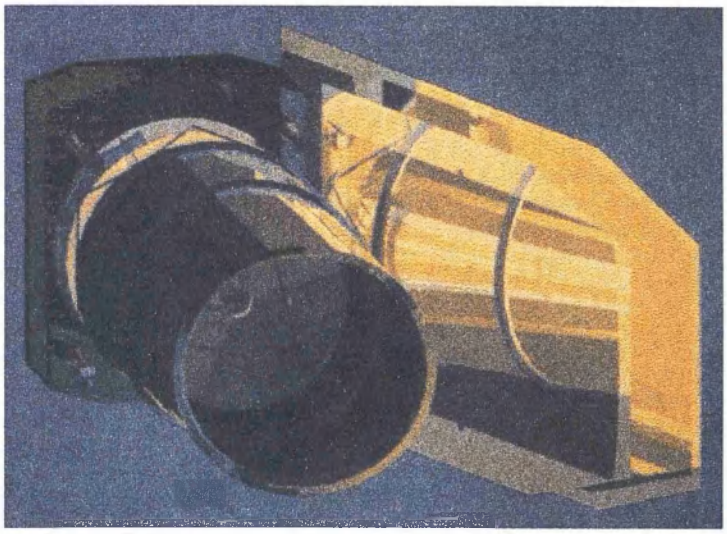

Figure 1.1 A proposed design for the EDISON observatory (reprinted from the EDISON M3 proposal document by kind permission of Alan Penny of RAL)

coated in a selective surface that reflects sunlight, whilst emitting strongly in the infra-red. The rest of the shields will then be coated in a very low-emissivity substance (e.g. gold).

In this way, it is hoped that all the energy from the Sun and Earth can be radiated into space by the sun-shields before it manages to get through to the telescope tube and warm it.

In order to predict whether or not this would be the case, computer simulations of the telescope were produced. However, as we shall see, these simulations left some important questions unanswered.

1.2 Infra-Red space telescopes

Radiative heat transfer theory is used in many branches of science, but perhaps the most demanding field is cryogenics, particularly the design of infra-red space telescopes.

As already explained above, infra-red astronomy is very difficult from the ground due to the interference of the atmosphere. With the atmosphere removed, the main problem with a space telescope is the infra-red emissions of the telescope itself. All bodies emit radiation roughly according to Planck's law (equation 2.1).

Figure 2.2 shows the radiation spectrum for a blackbody at 273K. This demonstrates the general form of the Planck curve with a definite peak in the emissive power. The position of this peak changes with the temperature of the body, moving towards longer wavelengths as the body gets colder (as

explained in section 2.4.1). For relatively cool surfaces (i.e. less than 300K), the peak emissive power occurs above 5μm.

Thus, with the walls of the telescope itself emitting significant radiation around 10μm, any signal in that wavelength region will be swamped by noise from the telescope and hence the near infra-red sensitivity of the telescope will be severely limited. One way to deal with this problem is to reduce the temperature of the telescope tube, since this will not only reduce the emissive power, thus improving the signal-to-noise ratio of the telescope, but will also push the peak emissive power further and further into the far infra-red, thus improving still further the performance of the telescope at near- to mid-infra-red.

In many current infra-red space telescopes, radiative cooling protects the telescope from the heating effects of the Sun, and tends to reduce the temperature to around 75K, although this is never explicitly designed. Usually it is assumed the cryogens will reduce the temperature to its working level. For the EDISON proposal, however, the telescope has been designed so that it needs no cryogens whatsoever. This is done by carefully selecting the materials, geometry, and orbit of the telescope to reduce the telescope tube temperature to around 20K. From there, closed cycle coolers will further reduce the temperature until it is comparable with the liquid helium missions already launched.

The big question with this design is whether or not these temperatures are actually achievable. The most convincing argument for this is the current states of previous infra-red space telescopes which have now exhausted their cryogens and are, therefore, now radiatively cooled. IRAS is currently in low-earth orbit, and radiative cooling is keeping it at around 100K [5]. More recently, the DIRBE instrument on COBE has stabilised at a focal plane temperature of approximately 60K [6].

The important thing to remember about these missions is that they were cryogenically cooled missions. This means that the radiative cooling was not planned in detail, but merely came about as a result of the telescope design. Thus, by planning the radiative cooling very carefully, much lower temperatures should be achievable.

The first main advantage of this design is the considerably extended life-time of the telescope. Since it is not losing any coolant, it can theoretically remain at the operating temperature as long as anyone wants to use it, or at least until the emitting surfaces degrade so much that they can no longer cool the telescope effectively. The standard estimation of life-time for the EDISON telescope is 10+ years, a considerable improvement on the 2-3 year lifetimes (at best) of the cryogenic missions.

Also, this life-time will not be affected if the telescope is accidentally pointed at a hot object like the Sun. Whereas, in a cryogenically cooled mission, such a temperature rise would mean the loss

of a considerable amount of coolant in order to reduce the temperature back to normal, and hence a shortening of life-span*, a passively-cooled telescope would just need time to cool down, before continuing operation as though nothing had happened.

This greatly extended lifespan also improves the cost-effectiveness of the telescope. In an age where funding is growing ever more scarce, it would make sense to invest such a large sum as is needed to build and launch a space telescope into a mission with a 10 year lifespan than one with a mere 2 year lifespan.

Passive cooling also allows the telescope to be launched warm, and then subsequently cool down in space. This would avoid the problems involved with trying to keep the entire structure at liquid helium temperatures during launch and, perhaps more importantly, whilst sitting in the launch vehicle waiting for launch with any delays that may occur. Launching warm also allows the telescope to avoid cryogenic vibration stress during launch, which is typically much more damaging than vibrational stress at room temperatures.

The other great advantage of EDISON would be its size. Since it doesn't have the extra bulk of large cryogen storage tanks, the aperture of the telescope can be considerably larger while still being able to be launched on the usual rocket payloads. Indeed, the EDISON design was deliberately chosen to be approximately the same overall size as ISO, but while ISO's aperture is a mere 60cm, EDISON would have an aperture of 1.7m.

One advantage of a larger aperture is the reduction of diffraction. All circular apertures cause diffraction in the signal passing through them. The resolving power (θ) of a telescope is defined by the Rayleigh criterion as:

$$\theta = \frac{1.22\lambda}{D}$$

where λ is the wavelength of light being studied and D is the diameter of the telescope. This can be a major problem, especially at longer wavelengths (e.g infra-red), but a larger aperture gives a corresponding improvement in the resolving power. Also, a larger aperture means more flux incident on the detectors, since the amount of flux collected is proportional to D^2. Greater flux on the detectors implies greater sensitivity which results in shorter integration times. Another improvement in sensitivity is caused by the diameter of the telescope 'beam' reducing as D^2 (due to the Rayleigh criterion) causing sensitivity for unresolved sources to increase as D^4.

Since the EDISON design has been proposed, passive cooling has been examined very carefully

*Witness the anxiety on 30 May 1996 when, by accident, the Earth marginally entered the field-of-view of ISO for just 2 minutes. Such a minor heating effect was estimated to have reduced ISO's operational lifetime by 1.5 days

in several respects to make sure the cooling predictions are accurate. As radiative cooling is the only method of heat loss in such a design, it is crucial that the predictions made before launch are correct. If this were another cryogenically cooled mission, a minor error would only mean a slight shortening of the mission life-time. However, since the closed cycle coolers operate optimally over a limited temperature range, if the cooling estimates are too optimistic, the whole project could be jeopardised.

Hawarden et al [7] show in figure 1 (a) the temperature of the instrument bay (cooled by closed cycle coolers) as it varies with the temperature of the telescope tube. As the telescope tube increases in temperature from 15K to around 23K, the instrument bay temperature is a constant 5K. However, once the telescope tube temperature rises above 23K, the instrument bay temperature doubles. As the authors note, 'quite a small increase [in the instrument bay temperature] will disable the instruments.'

Clearly, this kind of cooling behaviour is good if the passive cooling works as planned, since the increase in temperature caused by (say) the deterioration of the emissive surfaces over the lifetime of the mission will not affect the instrument bay temperature over quite a range. However, if the passive cooling does not perform as expected, and the telescope tube will not cool below 25K, then the instruments will be unusable.

Although these innovative radiative cooling designs have been proposed in conjunction with passively cooled missions, it is not merely beneficial to these projects. Even on a cryogenically cooled mission, the colder the telescope tube before the cryogens are brought into play, the longer the mission life-time. Thus, all subsequent infra-red space telescopes, whether they be cryogenically or radiatively cooled, stand to benefit from the findings of the research on passive cooling.

Clearly, passive cooling is not a panacea for infra-red space telescopes, and the disadvantages must also be highlighted. As mentioned above, the emissive surfaces of the telescope may well degrade over time, decreasing the effectiveness of the passive cooling. This is a particular problem when combined with the long life expectancy of such a mission, although (as also mentioned above) this will be compensated to some extent by the closed-cycle coolers.

The telescope temperature is also highly dependent on the outer surface temperature. This could well fluctuate as the attitude of the telescope is changed during the course of observations, affecting background noise levels from the telescope structure.

The idea of launching the telescope warm, while avoiding many problems currently associated with launching an infra-red space telescope, will involve a substantial cooling down time before the telescope is able to be used. This problem of cooling the telescope to operational temperature is one

of the biggest bones-of-contention about passive cooling designs with several astronomers believing it will take years for the cooling to finalise. Time and again, however, studies have shown that an operational temperature will be achievable on the order of a few months.

Even given these problems, however, the feeling that they are greatly outweighed by the prospective advantages of passive cooling is strong enough to inspire many missions to include passive cooling in their design.

ESA are currently considering a much bolder design called DARWIN [8] consisting of an interferometer made up of many EDISON-like telescopes. NASA is also working on two major projects for the next century. The Next Generation Space Telescope (NGST) [9] is essentially a scaled up version of the EDISON design. NASA are also designing an interferometer similar to DARWIN (the Terrestrial Planet Finder).

Although not strictly an infra-red telescope, ESA's Far Infra-Red and Submillimetre Space Telescope (FIRST) also plans to be passively cooled [10], although the final temperature estimates are much more conservative at around 150K.

The Japanese IRIS mission [11] will use passive cooling alongside closed-cycle coolers and the more traditional cryogenic cooling in order to reduce weight and increase the lifetime of the mission.

NASA's SIRTF mission [12] also plans to use passive cooling, but in this case primarily in the early mission stages before observations begin. The SIRTF plan is to launch the telescope warm and then to use passive cooling to reduce the telescope temperature to about 70K. From here, cryogens are also used to achieve normal operating temperatures.

1.3 Passive cooling design

The original design for POIROT [4] was based on the design for ISO and was proposed for ESA's second medium sized mission (M2). It consisted of a single sunshield protecting the telescope tube structure. The tube structure consisted of four concentric cylinders, each cooler than the one outside it. The central, and coldest, cylinder was the telescope tube itself.

Initially, based on the restrictions of the M2 proposal, POIROT was designed to have an eccentric orbit similar to ISO. When this proposal had been turned down by ESA the designers were free to consider other orbits. It was concluded that a high-Earth orbit would reduce the outer temperature of the telescope and also avoid the damaging environment of the Earth's radiation belts.

By the time the design had been re-christened EDISON [13], little had changed of the design still consisting of one sunshield and four concentric cylinders. An aperture shield was now added

to prevent Earthlight from shining into not only the aperture but also the annular radiators on the outer cylinders. The unusually large size of this shield was seen as a possible limiting factor of the size of the mission, and so an alternative orbit was considered.

The best candidate orbit was felt to be a 'halo' orbit about the Lagrangian point L2. Although this Lagrangian point is unstable, a satellite can orbit the point in a gravitaional 'lip' some distance out from the Lagrange point itself. This allowed the observatory to keep both Earth and Sun behind the sunshield, allowing the surfaces facing out into space to be painted black thus greatly improving the heat loss (something which would be impossible in Earth orbit).

In the official M3 proposal document [3] a second sunshield has been added to the design (see figure 1.1). Both sunshields are also tilted with respect to the tube-structure to encourage stray photons to escape into space. Some parts of the cylinders which avoid direct sunlight (i.e. those parts pointing into deep space) are not only painted black, but also cut away so that each cylinder has at least part of its surface directly exposed to space. The cooling effects of this are obvious.

At the 'Infrared and submillimeter space missions in the coming decade' conference in Saclay (1994), Léger et al presented a paper proposing the DARWIN interferometer design [14]. This interferometer consisted of several EDISON-type passively cooled telescopes working together for greater sensitivity. The mission was to launch either two 1.3m telescopes (the 'minimum' mission) or four 0.9m telescopes (the 'full' mission).

Another major difference between DARWIN and EDISON was its choice of orbit. It was already known that EDISON would be limited in sensitivity by scattered light and thermal emissions from the zodiacal dust within our solar system. However, this was not a serious problem since EDISON's mission plan included such a wide range of possible studies that it would be simple to choose those that weren't affected by the zodiacal emissions.

The DARWIN mission, by contrast, was designed specifically for the detection of extra solar terrestrial planets. For this study, the zodiacal light is totally prohibitive. One solution to this, put forward by Roger Angel [15], is to increase the size of the telescope apertures. This reduces the problem of the zodiacal flux which, being an extended object, is independent of aperture size, by increasing the flux from the distant planet being observed which, being a point source, increases as the square of the aperture size.

The DARWIN team, however, chose another solution to the zodiacal light problem. Simply put the telescopes far enough away from the Sun that the zodiacal emissions become weaker than emissions from the interstellar cirrus*. This means a circumsolar orbit at > 3.5AU. At first sight

*The cool, thin clouds of interstellar material discovered by IRAS. According to Léger et al[14] these

this seems likely to place a major burden on the mission but, with the aid of planetary gravitational assists, launching a satellite into such an orbit can take less energy than, say, launching it into a high-Earth orbit.

By the time of the 'Search for Extra-Solar Terrestrial Planets' conference in Boulder, Colorado (1995) the EDISON design team had combined with the DARWIN design team to produce a co-ordinated bid for one of ESA's Cornerstone missions. The DARWIN design [8] now had five EDISON-like telescopes (see figure 1.2), the asymmetric structure providing better discrimination against the zodiacal emissions of the remote solar system .

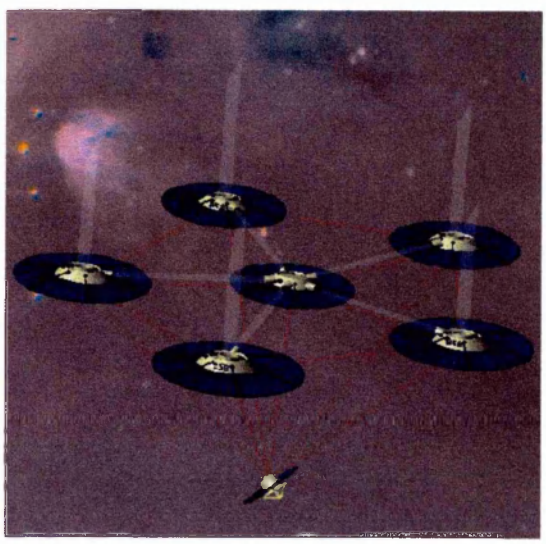

Figure 1.2 An artist's impression of the DARWIN infra-red interferometer (reproduced by kind permission of Alan Penny of RAL)

However, there are many problems still to be solved before DARWIN can be launched. How can the telescopes be reliably fixed at separations of 25m or more? Is it easier to have the individual telescopes 'free flying', with all the extra complications this introduces? Should the telescopes be shielded from direct sunlight individually, or should one large shield protect all five? How much of a problem will emissions between telescopes be? How best can communications with the interferometer be achieved when the distance to the Earth is constantly changing due to the difference in orbit periods? At the time of writing, these new problems are still under consideration.

clouds give a mean flux at 9.6μm of $N_{\rm cir} = 1.2 \times 10^4 (\frac{Res}{20})^{-1}$photons.hour^{-1} where Res is the spectrometer resolution

1.4 Where do I come in?

At this time, nobody has built and launched a passively cooled telescope. Although there have been studies of the thermal performance of helium cooled telescopes which have run out of helium, no-one has studied the real behaviour of a telescope specifically designed to be passively cooled. The only indication of the performance of these designs are the results of computer simulations. Many simulations of passively cooled telescopes have been produced using a wide variety of commercial simulation programs. Although the results produced by these packages are very impressive, they all seem to quite casually make the same assumption, that of diffuse emission.

It will be shown in figure 2.5 that the candidate materials for a passively cooled telescope certainly do not exhibit diffuse emission. What is not clear, however, is the size of the effect that this will have on the final temperature of the telescope. It was this question that my research set out to answer.

Clearly the highly directional emissive behaviour of gold should have *some* effect on the performance of the passive cooling designs. Consider for a moment the radiative exchanges between two parallel plates (like those in figure 1.3) in empty space, such that any emitted photons not hitting either plate are lost from the system.

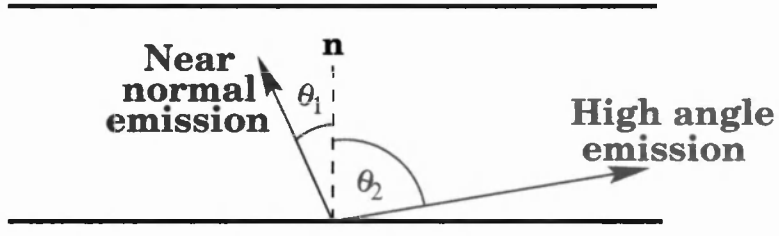

Figure 1.3 A comparison of high θ emission and low θ emission for parallel plates

If one surface emits a photon close to the normal to the surface (e.g. the green line at an small angle θ_1 to the normal) that photon must hit the other plate. If, however, the photon is emitted at high θ (e.g the red line at θ_2) the photon will miss the other plate. Of course, the exact angle of emission which defines whether the photon will hit or miss the other plate depends upon the size of the plates, the separation between the plates, the point on the surface from which the photon is emitted, and the direction of emission. As a general rule, though, we can say that photons emitted at low θ will tend to hit the other plate while those emitted at high θ will more likely miss and be lost to empty space.

If the plates are covered with gold, the emissivity of the surfaces will increase as θ increases

reaching a maximum as shown in figure 2.5. This means that more photons will be emitted at higher angles than for the diffuse case. This in turn means that more of these photons will miss the other plate, and therefore there will be less heat exchanged between the two plates than for the diffuse case.

This simple consideration seems to promise that modelling the directional radiative properties of the surfaces correctly would result in a lower temperature than modelling them diffusely. With my research, I have attempted to quantify this effect. If it is a minor effect, then current diffuse models would simply be a moderately pessimistic estimate, and probably safer in their prediction for that. If, however, it was a major effect, then these passive cooling designs could be over-engineered at the expense of lighter payloads or larger apertures.

Clearly the simple consideration above ignores many aspects of the radiative heat transfer which must be addressed. For a start, the sunshields and cylinder in the EDISON design are not parallel but tilted. Also, the outer cylinder surface which interacts with the inner sunshield is curved, not a flat plane.

Then there is the question of the $\sin\theta\cos\theta$ weighting function which is applied to the emissive power of a surface (described in section 2.5). This seems to work against the directional behaviour since the $\sin\theta\cos\theta$ function becomes smaller as the emissivity of gold becomes larger at high angles. Clearly, a realistic simulation is needed to investigate the effects of directional radiative properties.

After much searching the literature and personal communication with the other people involved with the EDISON project, it seemed that all commercially available CAD packages make the gross assumption of diffuse emission. This may seem a quite incredible oversight, but it must be remembered that modelling radiative heat transfer correctly is a very tricky business, and most commercial packages are used for systems where conduction and/or convection dominate, or where the geometry of the situation causes any directional behaviour to have little effect.

Lacking a commercial simulation package, I was forced to design my own computer simulation, described in chapter 3.

The major problem with modelling directional radiative behaviour was not the lack of a simulation package, however. There also exists a dearth of recorded data specifying this directional behaviour for many materials. The most common form of data is measurements of the optical constants of the materials. However, even these can vary dramatically from experimenter to experimenter and one is left wondering just who to believe. Eventually I concluded the only way to get reliable data would be to measure it myself.

It might be natural to conclude from the lack of data that there are simply not many people

interested in these properties. However, at the 'Infrared and submillimeter space missions in the coming decade' conference in Saclay (1994) I was surprised by how many participants enthused over my proposed research into measuring directly the radiative properties of candidate passive cooling surfaces (such as gold). People from many areas of telescope design, cryogenics, and instrument design told me of their need for accurate directional radiative data.

However, they also told me that they had no intention of making such measurements themselves. Everyone viewed such measurements as highly complicated requiring much expensive equipment and time. I set about the task of developing a quick, easy-to-use and cheap method for making these measurements which would still be sensitive enough to measure the low emissivities of samples such as gold.

1.5 Ground-based telescopes

Although, as mentioned above, space-based missions carry huge advantages for the sensitivity of the telescope, these advantages have to be increasingly weighed against the enormous cost of building, launching and operating such an observatory.

For this simple reason, ground-based observing will always be the most common form of astronomy, even for wavelengths such as the infra-red where it is so difficult.

Ground based telescopes have used passive cooling for years with slight increases in sensitivity during winter months when the temperature, and hence the noisy emissions, of the telescope structure drop. Unfortunately major cooling of ground based telescopes is strictly limited by thermal conduction to the Earth and by condensation of the atmosphere onto the structure.

The directional radiative properties discussed above play little rôle in cooling a ground based telescope. However, the one obvious requirement for any telescope is a high reflectivity mirror so that the signal is attenuated as little as possible by reflection. High reflectivity (as will be shown later) also implies low emissivity, which will prevent emissions from the mirror itself contributing towards the noise in the system. At many wavelengths, emissions from the mirrors are not a real problem. However, for an infra-red telescope with warm mirrors, the emissions from the mirrors will be a maximum in the mid-infra-red. For this reason it is especially important for infra-red telescope mirrors to be have very high reflectivities in the infra-red.

I became involved in the GEMINI program through my supervisor (Barrie Jones). I realised that the low emissivity surfaces they were producing for their mirrors would be excellent test cases for the equipment I planned to develop. I was lent 4 GEMINI mirror samples to test and hoped to

see if my equipment would be sensitive enough to distinguish between closely matched samples.

1.6 Thesis layout

Before we can fully discuss the solution to the problem of inadequate modelling of radiative properties, we must first explain the theory behind the subject. The following chapter, therefore, is a comprehensive tutorial on the relevant physics used in this field of study. A companion to this chapter is the fully worked example of radiative exchange for a simple geometry in appendix A.

To investigate what effect inadequate modelling had on the final temperature of the telescope, I constructed my own simulation model. This is described fully in chapter 3 along with the background theory behind the Monte Carlo techniques used in the model. The history of the model's development from scratch is interspersed with a description of test simulations at various stages of development to check the model was on the right track. The results from the studies using the model are presented at the end of chapter 3, with the entire code of the model presented in appendix B.

As well as computer simulations my research also involved the experimental measurement of radiative properties, as mentioned above. Chapter 4 describes the development of not only the equipment needed for these experiments, but also the experimental method used to obtain reliable data. Also included is a discussion of the relative advantages of different methods of making such measurements and an explanation of why I chose the method I did. The results of the experiments are summarised at the end of chapter 4 and the raw data is presented in graphical and tabular form in appendix C.

Finally, chapter 5 gives a discussion of the results and draws conclusions from the research. A brief discussion is included of where the research needs to go next as part of a continuing program of study aimed at improving our understanding of the radiative properties vital in planning a passively cooled infra-red space telescope.

Chapter 2

Theoretical Background

2.1 Introduction

The world of radiative heat transfer is one fraught with confusion. The main reason for this is the many different ways of describing essentially the same process. As an example, the reflectivity of a surface is, as one might expect, the fraction of some incident energy that is reflected by the surface. However, when you consider that even a simple concept such as reflectivity is divided up into bi-directional reflectivity, directional-hemispherical reflectivity, hemispherical-directional reflectivity, and hemispherical reflectivity, and that each of these terms can either be spectral or total, you can easily appreciate the confusion that might arise. Especially when, as happens all too often, figures are quoted as plain and simple 'reflectivity'*.

Although in the previous paragraph I have deliberately made this subject seem needlessly confusing, by presenting a brief overview of the basic physics behind all this jargon I hope to show that this nomenclature is not only very easy to understand but also quite necessary. The main problems arise when various authors do not use the nomenclature correctly.

2.2 Radiometric angles

The first definition that should be made before we go any further is that of 'radiometric angles'. The radiative properties of any surface will typically vary with the direction in which the radiation is

*In 1977, the National Bureau of Standards recommended that the '-ivity' ending should be reserved for describing an optically smooth substance with an uncontaminated surface, whereas any property which requires the surface conditions to be specified should have an '-ance' ending [16]. This means that we should only talk about the reflectivity of a brand new, optically perfect substance. Once it has weathered slightly, it no longer has a reflectivity, but rather a reflectance. Unsurprisingly, this can be another source of confusion.

exitant or incident. To fully describe any direction, two angles are used; θ and ϕ. These are known as the radiometric angles.

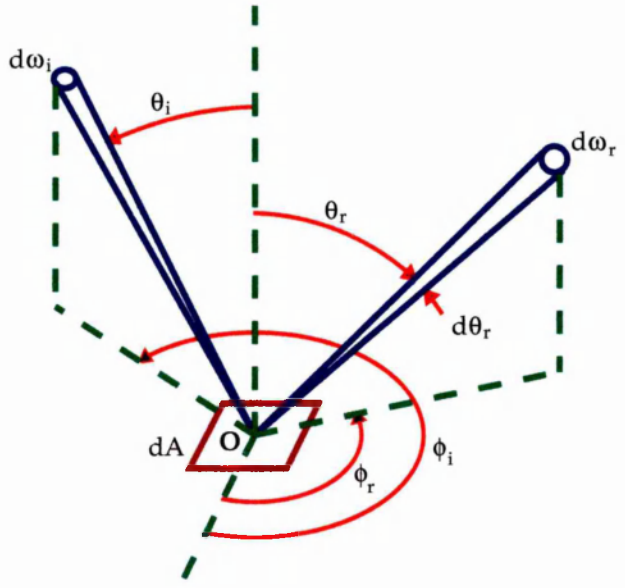

Figure 2.1 Radiometric angles

Figure 2.1 shows two examples of solid angles ($d\omega_i$ and $d\omega_r$) pointing in different directions. Both directions are defined by a corresponding pair of radiometric angles; (θ_i, ϕ_i) and (θ_r, ϕ_r).

The normal to the surface is used as a reference when specifying the radiometric angles. As is clear from figure 2.1, θ is defined as the angle between the direction of interest and the normal to the surface, and ϕ is defined as the angle between some reference line on the surface and the direction of interest, in the plane of the surface.

It is clear from the diagram that θ has a fixed reference direction in the normal, whereas ϕ is measured from some arbitrary line on the surface. This seems to imply that the experimenter must also specify the direction from which ϕ is referenced. However, this is not usually the case since most properties are independent of ϕ. Two obvious cases where this isn't true are (i) the bi-directional reflectivity (ρ''), which is dependent on ϕ_r, and (ii) where there is some asymmetric structure on the surface (e.g. linear grooves). In case (i), however, the important measurement is the difference between ϕ_i and ϕ_r, which is independent of where ϕ is measured from. In case (ii), ϕ can be measured with respect to the asymmetric structure (e.g. in the case of linear grooves, ϕ can be measured from a line parallel to the grooves).

2.3 Radiative properties

The three properties that describe how a surface will behave radiatively are its emissivity (ϵ), absorptivity (α), and reflectivity (ρ). For partially-transparent surfaces, another important property is the transmissivity, but this is not relevant for my work which deals solely with opaque surfaces.

The absorptivity and reflectivity quite simply describe what fraction of energy incident on the surface will be absorbed or reflected. The emissivity, however, is a little more subtle and compares the surface to a blackbody.

A blackbody is a fundamental concept in the study of radiation. It is simply defined as a surface which absorbs all energy incident on it regardless of the wavelength of the energy or which direction it is incident from. Thus, its absorptivity is 1 and its reflectivity is 0. For this reason, as will be explained in the next section, a blackbody is a very useful 'yardstick' in the field of radiative heat transfer.

2.4 Properties of a blackbody

The term used to describe the power emitted by any surface is the 'emissive power'. The most basic measure of emissive power is the directional-spectral emissive power, which is defined as the energy emitted by a surface, per unit surface area, per unit time, per unit wavelength interval centred around the wavelength λ (spectral) and per unit solid angle centred around the direction (θ, ϕ) (directional). For a blackbody, this term is given the symbol $e'_{\lambda b}(\lambda, \theta, \phi)$ where the subscripts denote, respectively, that a spectral quantity is being considered and that the properties are for a blackbody. The prime denotes that a directional quantity is being considered.

A blackbody is a very special type of surface in that its emissive power at each wavelength (its radiation spectrum) is defined theoretically by Planck's Law*. For the directional-spectral emissive power measured at the normal to the surface, this is given by:

$$e'_{\lambda b,n}(\lambda, T) = \frac{2C_1}{\lambda^5 \left(\exp(\frac{C_2}{\lambda T}) - 1\right)} \tag{2.1}$$

where $C_1 = hc^2 = 0.5955 \times 10^{-16}$ W.m^2/sr and $C_2 = \frac{hc}{k} = 0.01439$ m.K.

As mentioned above, a blackbody is a perfect absorber. It can also be shown by some fairly simple considerations [17, §2-4.1] that a blackbody is a perfect emitter. That is for a given temperature a

*The derivation of this formula, which cannot be derived from purely thermodynamic considerations, led Planck to a hypothesis that actually became the foundation of Quantum Theory.

blackbody emits the maximum possible energy at all wavelengths and in all directions. This provides us with a useful reference when comparing the emissive powers of other surfaces.

2.4.1 Emissive power variation

A blackbody's directional-spectral emissive power varies, as with all surfaces, with the direction and wavelength being considered. However, a blackbody is a special case in that these variations are precisely defined.

As explained above, the variation of a blackbody's emissive power with wavelength (its radiation spectrum) is defined theoretically by Planck's Law. Figure 2.2 shows a radiation spectrum for a blackbody at 273K.

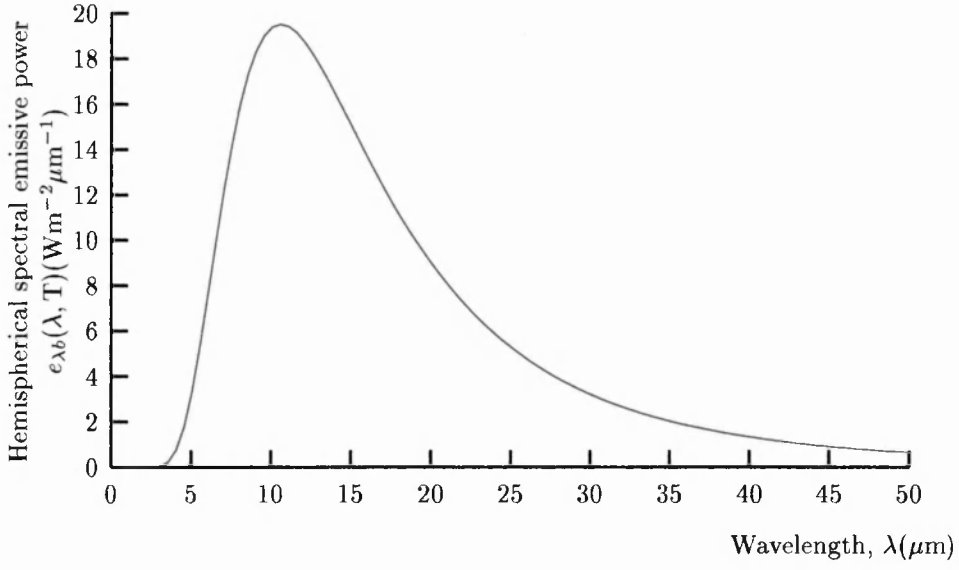

Figure 2.2 Spectral distribution of the hemispherical emissive power of a blackbody at 273K.

The distinctive shape of this radiation spectrum is typical of a blackbody. The wavelength at which the peak emissive power occurs is defined by Wien's displacement law. This is obtained by differentiating equation 2.1 by λ and setting the left hand side to zero. This gives:

$$\lambda_{\max} T = \frac{C_2}{5} \frac{1}{1 - exp(\frac{-C_2}{\lambda_{\max} T})}$$

Solving this equation for the $\lambda_{\max} T$ term results in the following:

$$\lambda_{\max} T = C_3$$

where $C_3 = 0.002897756$ m.K.

As the blackbody gets cooler, not only does the average emissive power reduce, but also, as is obvious from Wien's displacement law, the peak emissive power occurs at a longer wavelength. Thus, hot bodies such as the Sun emit most strongly in the visible, whereas colder bodies such as planets emit most of their radiation in the infra red.

Any surface that has a radiation spectrum which is the same *shape* as a blackbody's, but which is *not* a perfect absorber/emitter is referred to as a 'grey' surface (i.e. almost black). In this case the emissive power will be some fraction of a blackbody's emissive power:

$$\text{i.e. } e'_\lambda = \epsilon' e'_{\lambda b}$$

The coefficient ϵ' is known as the surface's emissivity (see below). A grey body is a special case in that this emissivity is the same at all wavelengths.

The emissive power of a blackbody also varies with direction. It falls off as $\cos\theta$, due to the effect of 'projected area'.

Imagine an eye looking at a surface at an angle θ to the normal. Since the eye is looking obliquely at the surface, the apparent area (or projected area) is smaller than the actual area. This is demonstrated in figure 2.3.

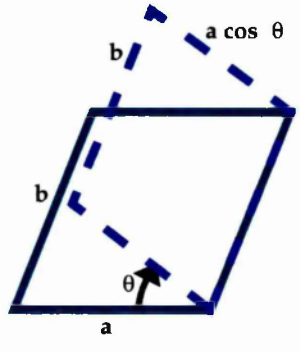

Figure 2.3 Demonstration of the 'projected area' effect.

This is clearly a special case since we have a regular shape (a rectangle) which is foreshortened on one side only, but the conclusion can be applied to all cases of projected area.

In figure 2.3 it is clear that two sides of the rectangle will appear foreshortened. These two sides (of length a) are parallel to the plane formed by the normal to the surface and the line of sight. From figure 2.3 we can see that these sides will appear to be of length $a\cos\theta$.

The other two sides of the rectangle are perpendicular to the plane formed by the normal to the surface and the line of sight, and will therefore appear unaffected. Thus, the area of the projected surface will be $ba\cos\theta$ as compared with an area of ba for the actual surface.

Clearly, the area of the projected surface is reduced by a factor of $\cos\theta$. Now, imagine a surface identical to the projected surface but placed some distance away from our original surface in the direction of the normal to the projected surface. If we make this distant surface black, it will radiate onto our original surface. Defining e as the emitted power of the original surface in the normal direction, it is easy to show that the distant surface will irradiate the original surface with a power e' where:

$$e' = Ce\cos\theta$$

where C is some constant describing the geometry of the situation. If the surfaces are in thermal equilibrium, the original surface must be irradiating the distant surface with exactly the same amount of energy. This leads to the conclusion that the emissive power of a blackbody falls off with angle as a function $\cos\theta$.

This effect is known as Lambert's cosine law, and surfaces having a directional emissive power that follows this relation, whether or not they are blackbodies, are known as 'diffuse' or 'Lambertian' surfaces.

It is worth noting that since the emissive power is reduced by the same fraction as the area of the surface, the surface will appear equally bright to the eye at any angle. In other words, the emitted radiation from the surface will have the same *intensity* at all angles.

The intensity of a surface is similar to the emissive power. The directional-spectral intensity (i'_λ) is defined as the energy emitted by a surface, per unit *projected* surface area, per unit time, per unit wavelength interval and per unit solid angle.

Thus, for a blackbody (or indeed any diffuse surface) we can say:

$$e'_{\lambda b}(\lambda,\theta,\phi) = i'_{\lambda b}(\lambda)\cos\theta \tag{2.2}$$

And, clearly, when $\theta = 0$ we have the normal emissive power:

$$e'_{\lambda b,n} = i'_{\lambda b} \tag{2.3}$$

2.5 Emissivity

The emissivity of a surface is defined as the ratio of the emissive power of the surface to the emissive power of a blackbody under the same conditions. As pointed out above, a blackbody is a perfect emitter. Thus, for any set of conditions, the emissivity of a surface will always be ≤ 1. In this way it is comparable to absorptivity and reflectivity.

As with the emissive power, and indeed all surface properties, the most basic measure of emissivity is the directional-spectral quantity, i.e the directional-spectral emissivity (ϵ'_λ) given by:

$$\epsilon'_\lambda(\lambda,\theta,\phi,T) = \frac{i'_\lambda(\lambda,\theta,\phi,T)}{i'_{\lambda b}(\lambda,T)} = \frac{e'_\lambda(\lambda,\theta,\phi,T)}{e'_{\lambda b}(\lambda,\theta,T)} \tag{2.4}$$

where

$$e'_{\lambda b}(\lambda,\theta,T) = f(\lambda,T)\cos\theta \tag{2.5}$$

The factor $f(\lambda,T)$ in equation 2.5 will be the same as equation 2.1. Equation 2.5 is written in such a way as to draw attention to Lambert's cosine law. Note that the blackbody emissive power is independent of ϕ.

Since it requires a huge amount of data to fully classify a surface at all angles and all wavelengths, the directional-spectral emissivity is often integrated over all angles, or all wavelengths, or both to give one of the properties listed below.

$$\text{Hemispherical-spectral emissivity } = \epsilon_\lambda = \int_\Omega \epsilon'_\lambda d\omega \tag{2.6}$$

$$\text{Directional-total emissivity } = \epsilon' = \int_0^\infty \epsilon'_\lambda d\lambda \tag{2.7}$$

$$\text{Hemispherical-total emissivity } = \epsilon = \int_\Omega\int_0^\infty \epsilon'_\lambda d\lambda\, d\omega \tag{2.8}$$

Remember, however, that the emissivity is defined in terms of the emissive power of the surface relative to a blackbody (equation 2.4). Thus we can rewrite equation 2.8 as:

$$\epsilon = \frac{e}{e_b} = \frac{\int_\Omega[\int_0^\infty e'_\lambda d\lambda]d\omega}{e_b} \tag{2.9}$$

The value of e_b is defined by the Stefan-Boltzmann law [17, §2-5.9] as σT^4. We can rewrite

equation 2.9 in terms of the directional-spectral emissivity by substituting from equation 2.4.

$$\epsilon = \frac{\int_{\Omega}[\int_0^{\infty} \epsilon'_{\lambda} e'_{\lambda b} d\lambda] d\omega}{\sigma T^4} \tag{2.10}$$

A blackbody is a diffuse surface, and so $e'_{\lambda b}$ can be defined simply in terms of the intensity as in equation 2.2. Substituting this into the above equation gives:

$$\epsilon = \frac{\int_{\Omega}[\int_0^{\infty} \epsilon'_{\lambda} i'_{\lambda b} d\lambda] \cos\theta d\omega}{\sigma T^4} \tag{2.11}$$

The $d\omega$ term in the above equations defines the infinitesimal solid angle (as in figure 2.1) being considered. This term is defined as $d\omega = \sin\theta d\theta d\phi$. Substituting this into the above equation gives:

$$\epsilon = \frac{\int_{\Omega}[\int_0^{\infty} \epsilon'_{\lambda} i'_{\lambda b} d\lambda] \cos\theta \sin\theta d\theta d\phi}{\sigma T^4} \tag{2.12}$$

An important result is obtained here. If the surface is diffuse in emission, then ϵ'_{λ} will be independent of θ and ϕ, as is $i'_{\lambda b}$ (mentioned above). Thus, in this case, the only variation of the directional emissive power (e') with angle will be the $\cos\theta \sin\theta$ term.

This will be very important when discussing my Monte-Carlo model. In order to get the correct distribution of emitted energy for a diffuse surface (i.e. equal intensity at all angles) the chosen angles must be weighted by a $\cos\theta \sin\theta$ factor.

Clearly the $\cos\theta$ term comes about as a direct result of Lambert's cosine law and describes the effect of projected area. The $\sin\theta$ term can also be demonstrated graphically. It is clear from figure 2.4 that an equal increment in θ will describe a much larger area when integrated over ϕ at large θ (e.g. the red line) than at small θ (the blue line).

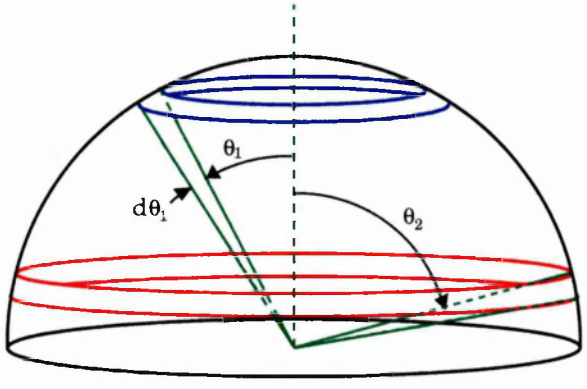

Figure 2.4 Integrating over a hemisphere.

The $\sin\theta$ term describes this effect. If little radiation is emitted at θ_1, and considerably more is emitted at θ_2, then this will average out to give equal flux through every part of the hemisphere.

2.5.1 Measuring emissivity

Obviously, the hemispherical-total emissivity (equation 2.8) is the least data intensive property to measure. To completely categorise the surface, only one measurement is required. However, in many ways it is also the most difficult to measure and may give rise to considerable errors.

Additionally, its use is rather limited, and is only important when considering first-approximations or those cases where the directional and spectral properties of the surface play little rôle in defining how the system behaves*.

The usual way to directly measure the hemispherical emissivity is to use an integrating sphere. This is essentially a detector mounted in a diffuse, white sphere which completely surrounds the surface to collect all radiation in all directions. Simple as this sounds, the integrating sphere is notoriously difficult to set up and get reliable data from, and it is very easy to produce large errors in the results unless the experimenter has considerable experience in using such equipment.

Measuring the emissivity over all wavelengths at once is also considerably harder than it sounds. This is mainly due to the fact that most commercially available detectors are tuned to a particular band of radiation. Very few detectors give good broad-band results, and due to the lack of work in this field some, like the Golay cell [18], are no longer manufactured.

These days, most emissivity measurements are made in a narrow band of radiation, and in a particular direction (usually normal to the surface). Unfortunately, many emissivity results are quoted without the vital information of the direction in which the emissivity was measured. As we shall see later, for highly directional surfaces (e.g. metals - see figure 2.5) the angle at which the emissivity is measured can make a huge difference to the result.

2.6 Absorptivity

As mentioned above, the absorptivity of a surface is defined as the proportion of the energy incident on a surface that is absorbed by that surface.

*This has been the case in most applications of radiative heat transfer theory until now, where the heat transfer is dominated by conduction or convection. Only with the advent of passively cooled space telescopes [4] are we experiencing systems where radiative heat transfer dominates in a situation where directionality is important.

Absorptivity has much the same properties as emissivity in that it can vary with wavelength and with the angle to the normal of the surface. Again the most basic measurement is the directional-spectral absorptivity. Of course in this case the direction specifies the *incoming* radiation. One of the great advantages of dealing with the incredibly data intensive directional-spectral properties is that, for any surface in thermal equilibrium with its surroundings, the directional-spectral emissivity and absorptivity are equal due to Kirchhoff's law of radiation.

Kirchhoff's law of radiation comes about due to some fairly simple considerations. Consider a surface placed inside a black enclosure. After a time, the surface will reach thermal equilibrium with its surroundings. Assume the surface is black. We shall denote the energy emitted by this black surface at one wavelength into one direction as $dQ'_{\lambda b}$. Clearly the black surface must be absorbing an equal amount of energy to remain in thermal equilibrium. Since $\alpha_b = 1$, the energy incident on the surface from the walls is also $dQ'_{\lambda b}$.

Now, replace the black surface with a surface of emissivity ϵ and absorptivity α. The emissivity is defined as the ratio of the energy emitted by the surface to that emitted by a blackbody. Thus, for a particular direction and wavelength:

$$\text{Energy emitted} = \epsilon'_\lambda dQ'_{\lambda b}$$

By definition, the amount of energy absorbed is simply the product of the incident energy and the absorptivity. But remember that the incident energy in this black enclosure is $dQ'_{\lambda b}$. Thus:

$$\text{Energy absorbed} = \alpha'_\lambda dQ'_{\lambda b}$$

According to the theory of the conservation of energy, when the surface is in equilibrium, the energy absorbed must equal the energy emitted. This allows us to say:

$$\alpha'_\lambda = \epsilon'_\lambda \tag{2.13}$$

Thus, by measuring one surface property, the other can also be obtained.

Kirchhoff's law of radiation does apply for the other integrated properties, but with each level of integration comes a set of restrictions for its application, as summarised in table 2.1. Only with the directional-spectral properties can Kirchhoff's law be applied without restriction.

Type of quantity	Equality	Restrictions
Directional Spectral	$\alpha'_\lambda(\lambda,\theta,\phi,T_A) = \epsilon'_\lambda(\lambda,\theta,\phi,T_A)$	None
Directional Total	$\alpha'(\theta,\phi,T_A) = \epsilon'(\theta,\phi,T_A)$	Incident radiation must have a spectral distribution proportional to that of a blackbody at T_A, or α'_λ and ϵ'_λ are independent of wavelength (directional-grey surface)
Hemispherical Spectral	$\alpha_\lambda(\lambda,T_A) = \epsilon_\lambda(\lambda,T_A)$	Incident radiation must be independent of angle, or α'_λ and ϵ'_λ do not depend on angle (diffuse-spectral surface)
Hemispherical Total	$\alpha(T_A) = \epsilon(T_A)$	Incident radiation must be independent of angle and have a spectral distribution proportional to that of a blackbody at T_A, or incident radiation is independent of angle and α'_λ and ϵ'_λ are independent of λ (directional-grey surface), or incident radiation from each direction has a spectral distribution proportional to that of a blackbody at T_A and α'_λ and ϵ'_λ are independent of angle (diffuse-spectral surface), or α'_λ and ϵ'_λ are independent of wavelength and angle (diffuse-grey surface)

Table 2.1 Table of restrictions of the use of Kirchhoff's law for varying levels of integration of radiative properties (reprinted from [17])

2.7 Reflectivity

As mentioned above, the reflectivity of a surface is defined as the proportion of energy incident on a surface which is reflected by that surface. As also indicated at the start of this chapter, reflectivity is considerably more complicated than emissivity or absorptivity. This is because the direction of both the incoming radiation and the reflected radiation have to be considered. The standard nomenclature is to have two terms describing the directional integration, the first describing the incoming radiation and the second describing the reflected radiation. For example, the directional-hemispherical reflectivity is the proportion of radiation incident from one particular solid angle which is reflected over the whole hemisphere. As before, this can either be spectral or total.

Just as emissivity can be diffuse, so can reflectivity. When a surface is diffuse in emission, it means that the surface emits energy with equal intensity in all directions (see page 20). Similarly, when a surface is diffuse in reflection, the radiation that is reflected from the surface is distributed evenly over all directions. A consequence of this is that the direction of reflection is completely

independent of the direction of incidence.

The other extreme case for reflection is for a surface to be 'specular'. In this case, the surface behaves like a perfect mirror. All the reflected radiation is concentrated into one direction which is totally dependent on the direction of incidence. The reflected direction is defined by the simple 'mirror law' where (referring to figure 2.1) $\theta_r = \theta_i$ and $\phi_r = \phi_i + 180°$.

It is clear that the directional-directional (or bi-directional) spectral reflectivity (ρ''_λ)* is the most data intensive surface property of all, since to completely categorise a surface, it is necessary to measure it at all incoming directions, at all reflected directions, and at all wavelengths. However, in many ways it is also the most useful surface property to know. If the bi-directional spectral reflectivity is integrated over all reflected directions, the directional-hemispherical spectral reflectivity is obtained (ρ'_λ). This gives all the radiation incident from one direction that is reflected.

Clearly, any radiation that is not reflected must be absorbed since, as already mentioned, my work only concerns opaque materials (i.e. those with a transmissivity of 0). Thus we get the relation

$$\alpha'_\lambda = 1 - \rho'_\lambda \tag{2.14}$$

The absorptivity is directional-spectral since the radiation is coming from one direction only, and is monochromatic. Also, from equation 2.13, we can obtain the directional-spectral emissivity.

Thus, by measuring the bi-directional spectral reflectivity, we can deduce all the other surface properties for an opaque surface.

At first sight, the idea of fully characterising a surface's bi-directional reflectivity seems a daunting task. However, there are ways to lighten the work-load. For instance, in my work I have been primarily interested in possible surface coatings for passively-cooled space telescopes (e.g. gold) and candidate mirror coatings. Both of these types of material are highly specular. When first measuring the bi-directional reflectivity, I quickly found out that the radiation reflected in non-specular directions was too small to be measured by the equipment I was using.

The detector's collecting area measured 15mm across and was placed 250mm from the sample. This defines the solid angle of the detector as 0.0113. The detector could measure signals down to 0.01mW, but was registering 0.00mW when in the non-specular direction. If we assume the pessimistic case that the signal was just below 0.01mW and was being rounded down, the error in signal by assuming there is no non-specular component would be $0.01 \times \frac{2\pi - 0.0113}{0.0113} = 5.55$mW.

For the 10.6μm laser, where signal strengths were typically around 3W, this represents a 0.185%

*Note the *double* prime denoting the fact that this is the *bi*-directional reflectivity

error. For the 5μm laser, signal strengths were typically only around 800mW. In this case, the assumption will produce a worst case error of 0.69%. Remember that this is the *worst* possible error introduced by assuming no non-specular reflections, and for this reason I felt safe in making this assumption.

Thus, in this case we can make the simplification that all the reflected light is being collected by the detector in the specular direction. This means that instead of measuring the bi-directional reflectivity, we are instead effectively measuring the directional-hemispherical reflectivity. As explained above, this is the most useful property in terms of calculating absorptivity and emissivity. It also means that, for each incident angle, only one measurement need be taken, in the specular direction. Also, since surface properties are generally independent of ϕ, only one reading need be taken for each value of θ.

2.8 Predicting directionality

Although optically rough surfaces tend to scatter the incident radiation and appear perfectly diffuse, both in reflection *and* emission, optically smooth surfaces have strongly directional properties. The general rule-of-thumb is that dielectrics have a maximum emissivity at low θ and drop off at higher angles, while metals have their minimum emissivity at low θ and peak sharply at higher angles.

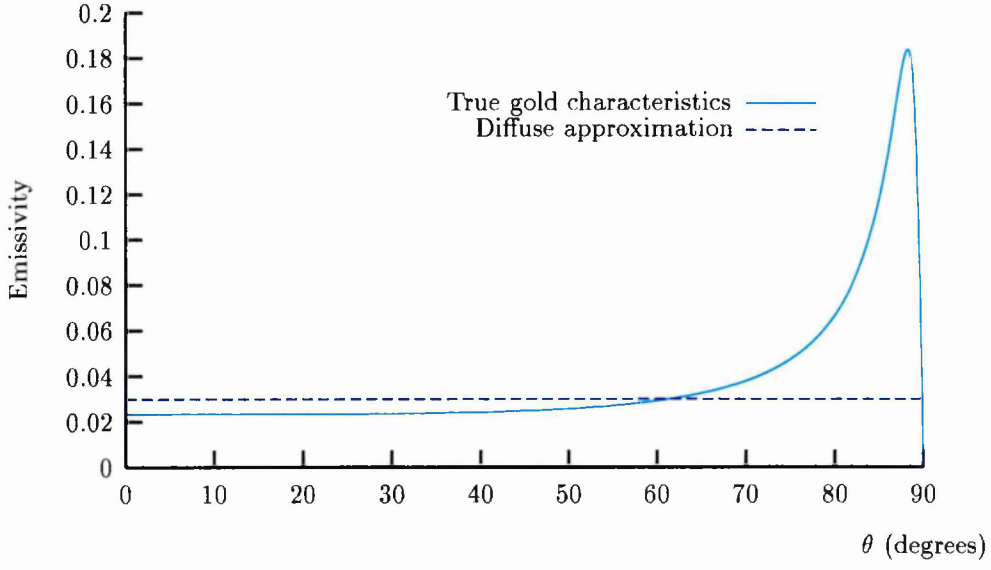

Figure 2.5 Comparison of realistic gold emissivity with diffuse approximation.

Figure 2.5 shows the directional emissivity of gold at 5μm compared with the directional emis-

sivity of a completely diffuse surface. Both cases have the same hemispherical-spectral emissive power which is consistent with a hemispherical-spectral emissivity of 0.03 (the commonly quoted emissivity of gold in the infra-red).

The high-angle peak of the gold is clearly visible. This means that a much larger proportion of energy is emitted at high angles than if the surface were diffuse. Also due to this large peak, the normal emissivity is noticeably lower than the diffuse case. This diagram elegantly shows the inherent errors introduced by modelling metal surfaces by using a single value of diffuse emissivity.

This highly-directional behaviour is a direct result of Maxwell's equations, and comes from the fact that the 'surface' is, in reality, an absorbing medium.

If the medium is a perfect dielectric, any electromagnetic wave passing through it will not be attenuated in any way. The refractive index (n) of this medium will then be simply the ratio of the wave speed in the medium (c_0) to the wave speed in a vacuum (c). That is:

$$n(\lambda, T) = \frac{c_0}{c}$$

However, if the medium is absorbing (such as a metal), the refractive index becomes complex and is usually expressed as $\tilde{n}(\lambda, T) = n(\lambda, T) - i\kappa(\lambda, T)$ where:

$$\tilde{n}(\lambda, T) = \text{complex index of refraction}$$

$$n(\lambda, T) = \frac{c_0}{c}(\text{as usual})$$

$$\kappa(\lambda, T) = \text{coefficient of extinction}$$

The coefficients $n(\lambda, T)$ and $\kappa(\lambda, T)$ are known as the 'optical constants' of the medium. Notice that they vary with both the wavelength of the light being considered and the temperature of the sample. For the sake of clarity, I will drop the (λ, T) suffix from here on, but this is a very important point that bears remembering.

In my research I have typically used the optical constants at the wavelength of peak emission to calculate the behaviour of a surface at some temperature. There are two ways of explaining this reasoning. Either it can be thought of as assuming that the Planck curve (figure 2.2) falls off so quickly with wavelength that only one wavelength need be considered, or it can be seen as assuming that the surface properties do not vary with wavelength (i.e. the surface is 'grey'). Both are simplifications, but modelling every surface at every wavelength would be an impossible task, even if enough data were available to make such refinements.

The optical constants can be used to deduce the variation of the radiative properties of a surface with the angle to the normal of the surface, θ thus:

$$\rho'_{\parallel}(\theta) = \frac{(n\cos\theta - 1)^2 + (\kappa\cos\theta)^2}{(n\cos\theta + 1)^2 + (\kappa\cos\theta)^2} \tag{2.15}$$

$$\rho'_{\perp}(\theta) = \frac{(n - \cos\theta)^2 + \kappa^2}{(n + \cos\theta)^2 + \kappa^2} \tag{2.16}$$

These equations essentially stem from Fresnel's equation, re-written with a complex index of refraction, and assume that $(n^2 + \kappa^2) \gg \sin^2\theta$ (which is invariably true for noble metals). The corresponding emissivity values are found from $\epsilon'(\theta) = 1 - \rho'(\theta)$, and simplify to:

$$\epsilon'_{\parallel}(\theta) = \frac{4n\cos\theta}{(n^2 + \kappa^2)\cos\theta + 2n\cos\theta + 1} \tag{2.17}$$

$$\epsilon'_{\perp}(\theta) = \frac{4n\cos\theta}{\cos^2\theta + 2n\cos\theta + n^2 + \kappa^2} \tag{2.18}$$

In equations 2.15 to 2.18 plane polarised light is being considered. The subscripts denote whether this light is polarised parallel ($\parallel$) or perpendicular ($\perp$) to the 'plane of incidence'. The plane of incidence is the plane formed by the path of the incoming or outgoing light (depending on the property being considered) and the normal to the surface*.

For the emission as a whole:

$$\epsilon'(\theta) = \frac{\epsilon'_{\parallel}(\theta) + \epsilon'_{\perp}(\theta)}{2} \tag{2.19}$$

Although equation 2.19 looks almost *too* simplistic, it is simply stating that emitted radiation is made up of equal quantities of each polarisation, the definition of unpolarised light. This is demonstrated in figure 2.6 which shows emissivity curves for each polarisation as well as the averaged curve reproduced from figure 2.5.

The values of the optical constants used in figures 2.5 and 2.6 are $n = 1.81$ and $\kappa = 32.8$. These are values quoted in [19] for gold at 5μm measured at room temperature. Equations 2.17 and 2.18 were used, although a scaling factor has been applied to produce a curve consistent with a hemispherical-spectral emissivity of 0.03.

For a fuller description of the derivation of equations 2.15 to 2.19 see [17] and [20].

Unfortunately, this is another area of radiative transfer theory that is fraught with confusion.

*When radiation is emitted normal to the surface, there is no 'plane of incidence' and the polarisations cease to have any meaning. Thus, for normal emissions, $\epsilon'_{\perp,n} = \epsilon'_{\parallel,n}$.

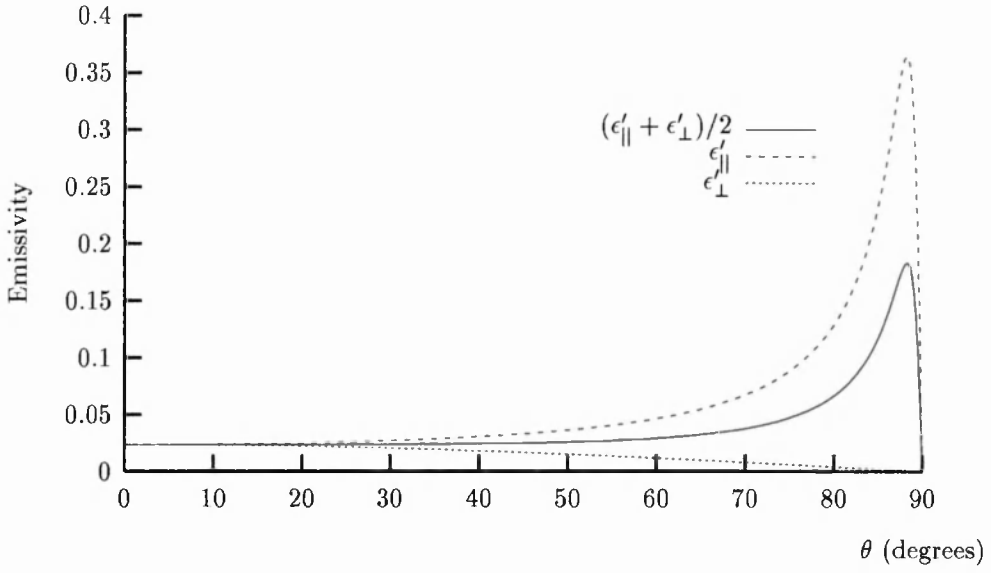

Figure 2.6 The directional emissivity of gold for each polarisation compared with the average of the two

The minus sign in the expression of the complex index of refraction is simply a convention chosen to simplify the mathematics in which this value appears. However, some researchers use a different convention, and it is possible to find the complex index of refraction expressed as $\tilde{n} = n + i\kappa$. Also, κ is not always the coefficient of extinction. Compare [17], where the coefficient of extinction is given as κ, and [21], where the coefficient of extinction is given as $\frac{\kappa}{n}$. Curiously enough, though, both give the same expression of the absorption coefficient as $\alpha = \frac{4\pi\kappa}{\lambda}$.

The statement above that dielectrics generally have their maximum emissivity at low θ and metals have their maximum emissivity at high θ is in fact another way of saying that dielectrics tend to have low coefficients of extinction while metals have much larger coefficients of extinction. For as the coefficient of extinction becomes larger, it dominates the equations of emission for the surface and causes the peak emissivity to occur at high θ.

Owing to the simplifications made in their derivation, these equations become invalid when the frequency of light approaches the order of the molecular vibrational frequencies of the medium. At such wavelengths, the photoelectric effect also begins to play a rôle in defining the behaviour of the surface. This restricts the equations to wavelengths longer than the visible spectrum. Also, the theory assumes the surfaces are perfectly clean and optically smooth, although in reality this is often far from the case.

Clearly, it is impossible to completely characterise the properties of a surface at every angle, so

a model is needed to predict the behaviour between the measurements. If the optical constants are known (measured by some reflectometry technique at one angle, say) it is possible to fully characterise the surface at all angles, at least according to the model. However, as already mentioned, the optical constants vary with the wavelength of the light and the temperature of the sample. Thus, the surface will be characterised only at the temperature and wavelength at which the optical constants were measured (unless some other theory allows extrapolation of the optical constants).

Such a model also provides a check for the measurements. Values of the optical constants measured at a particular angle of incidence can be used to predict what reflectivities should be at other angles. Also, if the optical constants can be measured independently* the predicted optical behaviour can be compared to the measurements, provided the theory is reliable of course.

2.9 Theories of optical constants

As well as varying with the angle to the normal of the surface (as discussed above), radiative properties also vary with the temperature of the surface and the wavelength of the radiation being considered. These are two more data spaces where it is impossible to completely characterise a surface, and so models are needed to predict the surface's behaviour.

For extrapolating readings of surface properties to other wavelengths, a very good model already exists. The Drude free electron model (see below) is shown by Ordal et al [22] and Bennett and Bennett [23] to give excellent agreement with experimental data over a large range of wavelengths. The Drude model does not work at short wavelengths (i.e. visible), but for infra-red work, and especially with noble metals such as gold, the Drude model performs very well.

It would also be advantageous to have an accurate model to predict the behaviour of surfaces at cryogenic temperatures, since measurements at such temperatures are very difficult. Cryogenics is now a wide and well-established technology, and thermal heat transfer is often a dominant effect in such circumstances. Thus, such a model would be very useful to a wide community.

Quite apart from the difficulties involved with cooling a sample down to cryogenic temperatures without degrading it (e.g. developing layers of frozen gases during the cooling down period), there is also the problem that the emissivities of surfaces typically reduce as a function of temperature. Thus, signal-to-noise ratios become much worse at lower temperatures, making the measurements very difficult.

*According to the Drude free electron theory (see section 2.9.1) n and κ are related to the electrical conductivity and dc relaxation time of a metal [22], both of which can be measured independently of light reflections

Unfortunately, the models for extrapolating to lower temperatures are much less reliable than for extrapolating to longer wavelengths. Currently there are three main models for predicting the behaviour of surfaces at cryogenic temperatures. These are covered very well by Toscano and Cravalho [24] and I shall summarise that paper here.

2.9.1 Drude free electron theory of metals

The Drude free electron theory [25] is a semi-empirical theory dating back to 1922. It models metal atoms as consisting of two components; the nucleus with the inner shell electrons tightly bound to it, and the electrons of the outer shells more weakly bound to the nucleus. This second component consists of the 'free' electrons that give the theory its name. These electrons are assumed to move freely about the lattice structure of the metal in response to some incident electric field.

The Drude free electron theory solves the Newtonian equation of motion for the free electrons in the presence of an applied electric field. This gives the position vector of a free electron as a function of time. From this, it is possible to obtain the dc relaxation time, τ, and to express n and κ in terms of τ and ω (the angular frequency of the electromagnetic wave). This relationship is defined as:

$$n^2 - \kappa^2 = 1 - \frac{4\pi N e^2}{m} \frac{\tau^2}{1 + \omega^2 \tau^2} \tag{2.20}$$

$$\frac{\omega n \kappa}{2\pi} = \frac{N e^2}{m} \frac{\tau}{1 + \omega^2 \tau^2} \tag{2.21}$$

Where N = number density of free electrons, e = electric charge of an electron, and m = rest mass of an electron.

The value of τ is given as:

$$\tau = \frac{m \sigma_0}{N e^2}$$

Where σ_0 is the dc conductivity of the metal.

Clearly we have an expression to derive the optical constants from measurements of the dc conductivity of the metal. All other coefficients are constant with the exception of the angular frequency of the electromagnetic wave.

Equations 2.20 and 2.21 show that, given the optical constants measured at some wavelength, we can predict how they will vary as a function of the angular frequency of the incident radiation.

Measured values of the dc electrical conductivity have been compared with those predicted by the Drude free electron theory, and the experimental values have been found to be slightly larger than predicted [26]. This can be compensated for by using the electron effective mass $m*$ and

the effective number density N_{eff} instead of the conventional values of m and N. This allows the theory to include the loss of energy by collision of the free electrons with the lattice, formed by the stationary nuclei and inner electrons, as well as with each other.

At non-cryogenic temperatures, and at long wavelengths, this form of the Drude free electron theory shows very good correlation with measured data [22], allowing accurate extrapolation of measurements to other wavelengths. However, at shorter wavelengths ($< 1\mu m$) the Drude model is invalidated due to the presence of the photoelectric effect.

Since σ_0 varies with the temperature of the sample it should, in theory, be possible to use the Drude free electron theory to extrapolate the optical constants to lower temperatures. Unfortunately, at temperatures less than 100K, the Drude model's predictions begin to significantly disagree with measured results due to quantum mechanical effects becoming significant at such temperatures.

The Drude model does not include any quantum mechanical effects and therefore does not accurately predict behaviour at low temperatures. Most significantly, the Drude model wrongly predicts an emissivity of zero as the temperature approaches 0K.

2.9.2 Anomalous skin effect theory

As an attempted improvement on the Drude free electron theory, Reuter and Sondheimer [27] and Dingle [28] developed the anomalous skin effect theory.

At low temperatures, the mean free path of an electron can become large compared to the spatial variation of the electric field. For sufficiently low and sufficiently high frequencies, the penetration of the electric field (the 'skin depth') is much larger than the mean free path of the electrons. The key region where the skin depth is not sufficiently large and the electron will encounter a variation of the electric field as it moves through the metal occurs when $v\tau \geq \frac{c}{\omega_p}$ where v is the electron velocity, τ is as defined above for the Drude free electron theory, and ω_p is the plasma frequency, defined as:

$$\omega_p = \left(\frac{4\pi N e^2}{m^*}\right)^{\frac{1}{2}}$$

For most metals this equality is satisfied in the visible and infra-red region. The anomalous skin effect theory takes into account the fact that the electric field is now space dependent as well as time dependent.

The combination of the applied electromagnetic field and the collisions of the electrons with the lattice causes a steady state to occur. The distribution function of the electrons in this steady state is determined by the Boltzmann equation. This allowed Reuter and Sondheimer to obtain an

expression for the current density involving values of the electric field at all points in the metal.

Combining this with Maxwell's equations led to an integro-differential equation for the electric field, the solutions to which took the form of definite integrals which were generally solved numerically. These results indicated that the wave propagation within the metal was no longer exponential. For this reason, Reuter and Sondheimer chose not to work with the dielectric constant and instead expressed the results in terms of the complex surface impedance.

Dingle extended and improved Reuter and Sondheimer's solutions and also eliminated the necessity of numerical integration by obtaining series expansions for the surface impedance.

A major influence on the results of this theory are the effects of reflection of the electrons from the surface of the metal. The common notation includes a variable 'p' which defines the fraction of electrons specularly reflected at the surface of the metal. Most studies so far published consider two extreme cases; completely specular reflection ($p = 1$) and completely diffuse reflection ($p = 0$).

In general, diffuse reflection of the electrons ($p = 0$) predicts lower reflectivities than the specular case ($p = 1$). Most experimenters have reported that their results agree more closely with the diffuse case, but this could conceivably be due to the samples being slightly tarnished or the surface irregularities being larger than the order of the wavelength of the conduction electrons (about 0.5nm in noble metals). Bennett and Bennett [23] describe a painstaking sample preparation technique, preparing samples under extremely high vacuum (10^{-9} Torr) conditions, and measuring reflectivities immediately after sample preparation, with the samples kept in a nitrogen atmosphere. Under these exacting conditions, the experimenters report results that fit more closely with the specular reflection case.

The anomalous skin effect theory predicts values for the normal absorptivity in terms of ω and τ. For the case of specular electron reflections ($p = 1$):

$$\alpha_{\lambda,n} = \left(\frac{2\pi Ne^2}{m\omega^2}\frac{v^3}{c^3}\right) + \left[\left(\frac{m}{\pi Ne^2}\right)^{\frac{1}{2}}\frac{1}{\tau} - \frac{1}{8}\frac{1}{\tau^3\omega^2}\left(\frac{m}{\pi Ne^2}\right)^{\frac{1}{2}}\right] + \text{correction and higher order terms}$$

and for the case of diffuse reflections ($p = 0$):

$$\alpha_{\lambda,n} = \left(\frac{3}{4}\frac{v}{c}\right) + \left[\left(\frac{m}{\pi Ne^2}\right)^{\frac{1}{2}}\frac{1}{\tau} - \frac{1}{8}\frac{1}{\tau^3\omega^2}\left(\frac{m}{\pi Ne^2}\right)^{\frac{1}{2}}\right] + \text{correction and higher order terms}$$

Notice the term in the square brackets is the same in both cases, and is identical to the normal-spectral absorptivity predicted by the Drude free electron theory.

At room temperatures, the anomalous skin effect theory agrees closely with the Drude free

electron theory. It is at low temperatures that the differences between the two become marked as the Drude theory predictions tend towards zero. The anomalous skin effect theory correctly predicts a residual emissivity even at very low temperatures. However, despite this improvement, it still disagrees with measured results by orders of magnitude at temperatures around 10-20K [29] for both values of p.

2.9.3 Holstein quantum mechanical model

Holstein [30] has produced a third model which takes into account quantum mechanical effects which, as mentioned above, play a much larger rôle at low temperatures.

Like the Drude free electron theory and the anomalous skin effect theory, the Holstein model is based on the motion of the 'free' electrons in the metal. In this approach, the motion of the electrons is described by the time dependent Schroedinger equation, solved using second order perturbation theory. This produces a quantum mechanically derived value for the dc relaxation time, τ, in terms of the Debye temperature $(\Theta)^*$ and the classical dc relaxation time (τ_{cl}) measured at a reference temperature (T_{ref}) much higher than the Debye temperature.

For low temperatures, the normal-spectral absorptivity is then given by replacing the value of the relaxation time in the Drude free electron theory with this new quantum mechanical value and adding an expression for the absorptivity occurring at the surface of the metal due to specular or diffuse reflection of the electrons. This yields:

$$\alpha_{\lambda,n} = p\frac{2\pi Ne^2}{m\omega^2}\frac{v^3}{c^3} + (1-p)\frac{3}{4}\frac{v}{c} + \frac{2}{5}\left(\frac{m^*}{\pi Ne^2}\right)^{\frac{1}{2}}\frac{\Theta}{T_{ref}\tau_{cl}}$$

Although this sounds the most sophisticated of the three models, its predictions disagree with experimental results even more than those of the anomalous skin effect. This model also predicts a residual emissivity at low temperatures, but a much higher one than the anomalous skin effect.

2.9.4 Experimental measurements

Of course, the true test of any model is how well it relates to experimentally measured results. Unfortunately, there exists such a lack of reliable data for the optical properties of metals, and such a variation in the data we do have, particularly at cryogenic temperatures, that it is difficult to draw

*According to Quantum Theory, the vibrations of a solid will achieve a maximum frequency, ν_m. The Debye temperature is given in relation to this frequency as $\Theta = \frac{h\nu_m}{k}$. It is also related to the heat capacity of a solid as $C_v \propto \frac{\Theta}{T}$

any concrete conclusions about these three models.

From published data of measurements of emissivity [31, 32, 33] it is clear that the Drude free electron theory behaves very poorly at low temperatures, giving a much lower result than that observed experimentally. As mentioned above, the Holstein quantum mechanical model correctly predicts a residual emissivity. However, the experimental results show a much lower residual emissivity than that predicted by the Holstein model.

Of the three models, the anomalous skin effect theory seems to most accurately follow the experimentally measured results, although even this differs markedly from experiment at temperatures less than 100K. The two extreme cases ($p = 0$ and $p = 1$) for the anomalous skin effect theory and the Holstein quantum mechanical model seem to lie either side of the data for at least one case [24]. However, the experimental data doesn't seem accurate enough to allow a decisive definition of the value of p.

Clearly, as yet there does not exist a model to allow us to confidently extrapolate room temperature measurements of radiative properties of metals to cryogenic temperatures. Whether any of the models are correct or not cannot be decided until there are considerably more data available to compare with theoretical predictions.

As of this time, the only way to accurately find the radiative properties of metals at cryogenic temperatures is to directly measure them.

Chapter 3

Monte-Carlo modelling

3.1 Background discussion

Previous published studies of passive cooling have predicted impressive results. However, as already discussed, none of them have modeled the directional nature of infra-red emissions from metals correctly. To find out how much difference this would make to the final results, I initially looked for a commercial modelling package which would allow me to specify such directionality.

Unfortunately, I soon realised that no package had yet been produced which had this level of finesse. Having looked into TRASYS and NEVADA [34] (including it's sub-programmes RENO and VEGAS), and I-DEAS VI [35] (with its TMG package), among others, I realised that the only way to investigate this effect would be to write my own simulation software.

Clearly, I could not hope to produce a generalised package capable of dealing with any geometry, but I could produce a simplified simulation of a specifically EDISON-like geometry to investigate just how much difference the diffuse assumption makes to the equilibrium temperature of the telescope.

The very first decision was which method to choose to model the heat transfer. There are several common ways of going about this. One way is to reduce the system under consideration to a 'heat circuit'. In this case, all the different emissivities, configuration factors (see below), etc., are reduced to a series of thermal resistances. Thus, the system is reduced to something resembling an electric circuit [36] with the voltages analogous to the temperatures of the surfaces. Although the solution of this circuit is fairly simple, the initial construction of such a circuit can be fraught with difficulty.

One of the most difficult aspects of this construction is the calculation of configuration factors. The configuration factor (or view factor, or form factor) for a system of two surfaces is defined as the proportion of radiation emitted by one surface that is incident on the other [37]. This includes any radiation reflected from other surfaces present but does not include multiple reflections between

the two surfaces*. Thus, to construct a definitive circuit representing a system of surfaces, one first needs to know the configuration factor from every surface to every other surface under consideration.

Equation A.24 gives the configuration factor for the simple case of two diffuse parallel planes. Just by looking at this equation, it is easy to see what problems can arise with even the simplest geometries when configuration factors need to be considered. For this reason, I decided against this approach.

Another commonly used technique is ray-tracing [38]. The general idea behind this method is to consider every possible angle of emission in turn. A 'ray' is sent out in the direction being considered, and followed as it is reflected, scattered, and finally completely absorbed. This is done for every surface, and the net energy flow is calculated. This approach has much to recommend it, and is not greatly different from the method I decided upon.

Taking the advice of John Howell (in a private communication), and following my own preference having had some experience with this method before, I decided on using a Monte-Carlo approach. Monte-Carlo is a very broad term, and is used in many fields. Fundamentally, it refers to the use of random numbers in a simulation and is named after the birth-place of roulette, that most lucrative exploitation of random numbers.

Instead of rays, my Monte-Carlo model deals with 'bundles' of photons. Clearly, in the real world, the infra-red radiation will be emitted from a surface as a number of discrete photons. To model this process would take an enormous amount of computing time and power. Instead, my model uses quanta of light with considerably more energy than one photon. Obviously, if the energy of a photon was increased, the wavelength would alter appropriately. Thus, since the quanta used in my model are of the same 'wavelength', but simply carrying more energy, the suggested way to picture this is as a bundle of photons.

The important thing to remember about this 'photon bundle' is that it is simply a finite amount of energy used by the model to simulate radiative transfer. A key property of the photon bundle is that it behaves as a single photon in that it is either completely absorbed or reflected and cannot be split into smaller energy packets. Here, though, the similarity with a photon ends.

The photon bundle has no wavelength as such. Any spectral behaviour comes as a result of how the model treats the bundle. In my model, the spectral behaviour of gold was chosen according to the wavelength at which the Planck curve (equation 2.1) was a maximum for the temperature of the surface emitting the radiation. Thus, as the temperature changed, the values of absorptivity and reflectivity experienced by the photon bundle changed as a result of the model using different values

*The surface the radiation is incident upon is, in this way, considered to be effectively black

of the surface properties appropriate to that temperature.

In my model, random numbers are used to follow such photon bundles as they are emitted (random θ and ϕ) from a random point on the surface, reflected (random θ_r and ϕ_r in the case of a diffuse surface), and finally absorbed. Since the random numbers generated were univariate (i.e. uniformly distributed between 0 and 1), generating a random point on the surface was very easy. For a plane of length l and width b, the random point was simply defined as having co-ordinates $(R1 \times l, R2 \times b)$ where $R1$ and $R2$ are random numbers. To generate a random point on the curved cylindrical surface, a random angle and a random height were generated in a similar way, these being the two co-ordinates required to specify any point on a cylinder.

Clearly, though, many of the processes (e.g. emission, reflection) are not uniformly random. Although individual bundles can be emitted in any direction, to obey the laws of physics the overall profile of emission must match the directional characteristics of the surface being modeled. Remember, though, that the random numbers are distributed *uniformly*. Thus we immediately see our first requirement for a Monte-Carlo model. That is the ability to weight the probabilities for some processes. The second requirement for a Monte-Carlo model is an extremely good random number generator.

The random number generator is obviously the core of a Monte-Carlo model, and there have been several cases of people using machine supplied random number generators without thinking, only to find that the random numbers it produced weren't quite as random as they thought. The key property of any random number generator is its period.

Software based random number generators are based on some iterative formula which produce 'pseudo random' numbers. The numbers are not random at all, since knowing the initial seed and the formula for the generator, one can work out the exact sequence of numbers. However, the numbers appear unrelated and random. All pseudo random number generators are cyclic, and the number of 'random' numbers that can be produced before the cycle repeats itself is referred to as the period of the random number generator. One sign of a good random number generator is a large period. In my model, I use L'Ecuyer's generator [39] which is quoted to have a period of $> 2 \times 10^{18}$ numbers.

There are several ways to weight univariate random numbers. One way is to plot the function with which you wish to weight the numbers (for instance, figure 3.1 shows the $\sin\theta\cos\theta$ function used to model a diffuse surface) and then generate the random numbers in pairs. These pairs of numbers are then plotted as co-ordinates on the same graph and only those which fall below the line of the function are used. Clearly, however, this is a very wasteful way of doing things, since you generate more than twice as many numbers as you need.

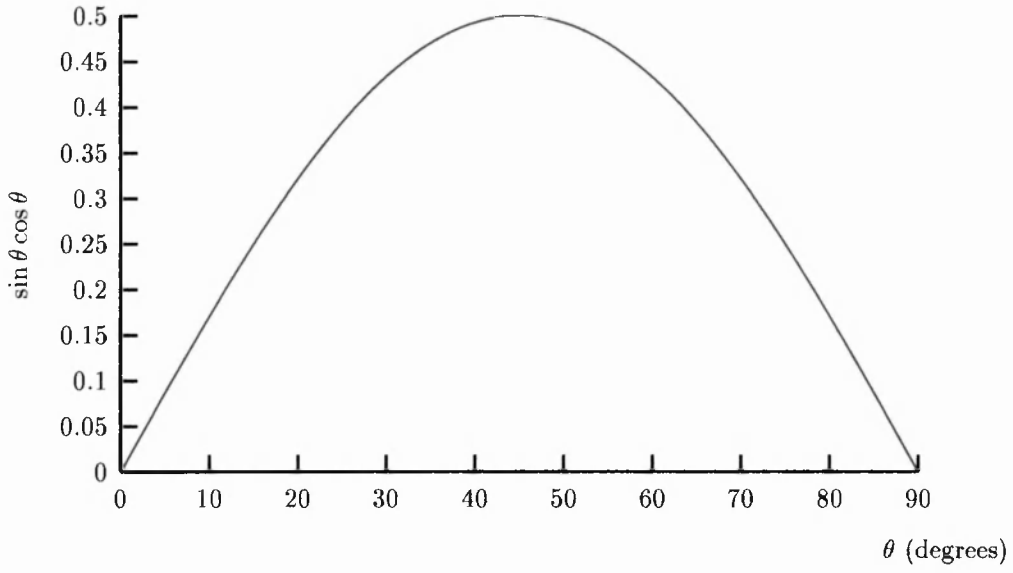

Figure 3.1 A plot of $\sin\theta\cos\theta$ from 0° to 90°

A much more efficient way of doing things is to use a Cumulative Distribution Function (CDF) as I did. A CDF is a plot of the integral of a function from $-\infty$ to θ against θ. I have deliberately used θ as the variable since this is how my model weights the numbers used to choose the θ direction, but a CDF can be used to model any non-uniform process.

Clearly, when we're talking about the angle to the normal of a surface, negative values are meaningless, so the CDF for this process is actually the integral from 0 to θ against θ. The plot is normalised by dividing by the entire area under the graph (the integral from $-\infty$ to $+\infty$, or in this case from 0° to 90°).

Figure 3.2 shows a CDF for the function $\sin\theta\cos\theta$. The random numbers are weighted by generating univariate numbers along the y-axis, and then reading off the appropriate value of θ on the x-axis. Clearly, this CDF will bias the numbers towards 45°, as one would expect from this function. It can be proven (see [17]) that this bias will actually give the appropriate probability distribution.

CDF's are relatively simple to construct, as long as the distribution of the function is known. Figure 3.3 shows a CDF designed to model the emissive properties of gold at $5\mu m$ where $\sin\theta\cos\theta$ is multiplied by ϵ'_λ. Once again the y-axis shows the integral of the quantity being plotted from 0 to θ normalised by dividing by the total integral over all possible angles (i.e. from $\theta = 0$ to $\theta = 90$). The bias towards high angles is clearly visible.

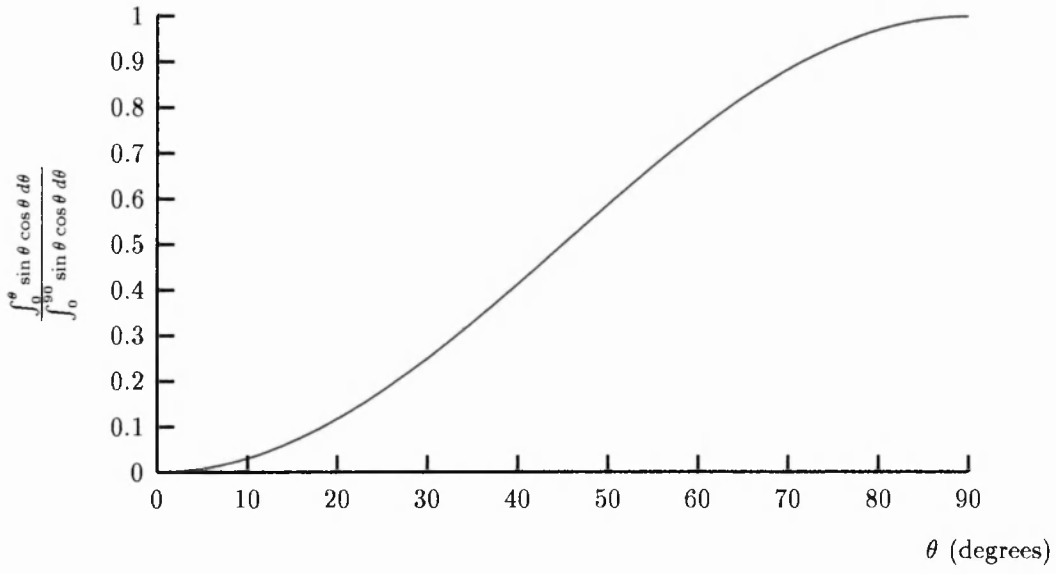

Figure 3.2 A cumulative distribution function for the function $\sin\theta\cos\theta$

In my model, the CDF consists of an array of 100 elements. Each element of the array corresponds to an interval of 0.01 on the y-axis of figure 3.2 and contains the corresponding x-axis value. Thus, to weight the univariate random numbers, I merely generated a random number, multiplied it by 100, and then used the value contained in that element of the CDF array.

Additionally, in order to gain greater accuracy, I used linear interpolation between the values stored in the array. Since the univariate random numbers generated had more than two significant figures, the decimal fraction left after multiplying by 100 was used to determine how far to interpolate between the chosen array element and the value stored in the next element. A typical example is demonstrated here.

$$\text{Generated random number} = \text{R} = 0.583743922 \text{ (say)}$$

$$\text{R} \times 100 = 58.3743922$$

$$\text{CDF value stored in element } 58 = 0.719185573$$

$$\text{CDF value stored in element } 59 = 0.734735781$$

$$\text{Thus, CDF value corresponding to } 58.3743922 = \text{element } 58 + ((\text{element } 59 - \text{element } 58) \times 0.3743922)$$

$$= 0.719185573 + (0.015550208 \times 0.3743922)$$

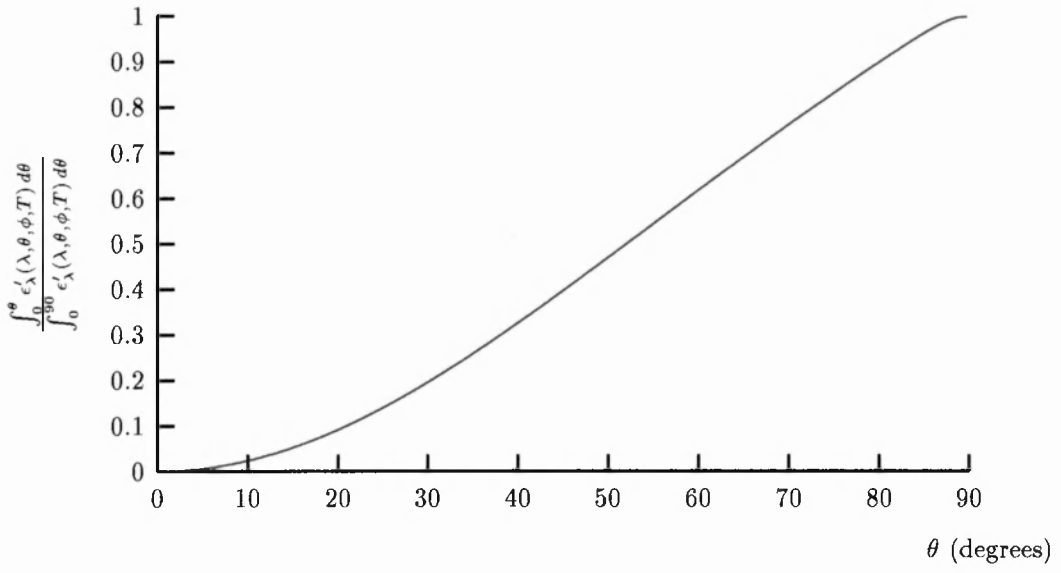

Figure 3.3 A cumulative distribution function for the emissive properties of gold

$$= 0.725007450$$

To model surfaces as they cooled down, it was necessary to proceed in small 'time steps'. The time step was simply a small period of time over which it was assumed that the temperatures of the surfaces being considered did not change significantly. Thus, at the beginning of each time step, the amount of power emitted by each surface was calculated. Then each surface was considered in turn as the emitted power was divided up into a large number of photon bundles and randomly bounced around the system.

A large number of bundles was used in order to obtain a good statistical distribution of emittance angles. Initially, the energy of the photon bundle was fixed, so the number of bundles was dependent on the amount of energy being emitted by the surface (which varied with the surface temperature). However, with parts of the model reaching cryogenic temperatures, the number of bundles per time step occasionally became uncomfortably low. Thus, one of the first improvements to the model was to make the number of bundles per time step a fixed parameter input at the start of the simulation (usually $\simeq 600$). The surface temperature then defined the energy of the photon bundles.

At the end of each time step, when all the emitted power from every surface had been accounted for, the total energy balance for each surface would be counted. The energy balance for all surfaces belonging to the same structure were summed, and the new temperature of the structure (and, hence, its surfaces) calculated using the heat capacity of the structure, input at the beginning of the

program. This new temperature would be the temperature of the surfaces belonging to the structure throughout the next time step.

The energy balance for each surface was a very simple sum. At the beginning of a time step, the energy balance was zero for each surface. The energy emitted (for each surface) was calculated according to the Stefan-Boltzmann law. This was then subtracted from the energy balance. Then, throughout the course of the time step, each time a photon bundle was absorbed by a surface, the energy of the bundle was added to the energy balance. Thus, reabsorptions were simply photon bundles being added back into the energy balance of the surface that originally emitted them.

In actual fact, in my model there were only, at most, three energy balances: one for each structural component of the model*. Since these components had at least two surfaces each, the energy balances for the relevant surfaces were summed for the individual components. In this way, and due to the fact that one temperature was used for the whole component, infinite thermal conductivity was assumed for each component of the model.

This method of modelling the cooling of surfaces has a great advantage in that it is simplicity itself to find, not only the final temperatures, but also how each surface evolves over time. This is often a matter of great interest, and with this method it simply involves measuring the temperature at each time step. Clearly, there is no way of knowing how the surface behaves over the course of one time step, but since the length of each time step is deliberately made very small, this is not a significant problem.

3.2 Initial model

Once the basic modelling method was decided upon, the model grew slowly, with careful checks at each stage in its development.

The first step was to produce a model of two parallel planes of identical size, with the Sun as the only heat source. This was a simple situation to test theoretically since the configuration factor for such a geometry (assuming diffuse emission) was readily available, and with only one heat source, it was not too difficult to calculate what the equilibrium temperatures should be.

Since the surfaces were parallel, it was a simple matter, given the angle of emission and the point on the surface from which the radiation was emitted, to determine whether or not a photon bundle emitted by one surface would hit the other.

*One or two sunshields and the telescope tube itself

Figure 3.4 is a diagram to explain how this was achieved. It shows the two planes facing each other, and the x, y and z axes as used by the model.

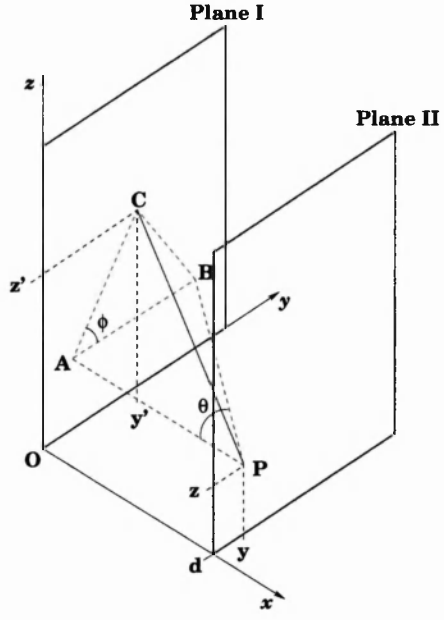

Figure 3.4 A diagram of the two-plane geometry.

Also shown in figure 3.4, as the solid blue line, is the path of a photon bundle which is emitted from a point P on Plane II with radiometric angles θ and ϕ.

To find where this photon will hit Plane I, we begin by taking the normal to Plane II at P which is the line $\overrightarrow{PA}$ in the diagram. We then rotate this line through an angle θ to form the line $\overrightarrow{PB}$. We then rotate this line through an angle ϕ about the normal to the surface to form $\overrightarrow{PC}$, the path of the photon bundle.

It is evident from the diagram that the co-ordinates of point C where the path of the photon bundle crosses Plane I are given by:

$$y' = y + |\overrightarrow{AC}| \cos\phi \tag{3.1}$$

$$z' = z + |\overrightarrow{AC}| \sin\phi \tag{3.2}$$

Given that the separation between the two planes is $\overrightarrow{AP}$ which is defined as length d, clearly $|\overrightarrow{AB}| = d\tan\theta$. Also, given that we have effectively rotated the triangle APB about the line $\overrightarrow{PA}$,

then $|\overrightarrow{AC}| = |\overrightarrow{AB}|$. Substituting this into equations 3.1 and 3.2 we obtain:

$$y' = y + d\tan\theta\cos\phi \tag{3.3}$$

$$z' = z + d\tan\theta\sin\phi \tag{3.4}$$

So, if $0 < y' <$ width of Plane I *and* $0 < z' <$ height of Plane I, the photon bundle will hit Plane I. Otherwise the photon bundle will be lost to empty space and the next bundle will be considered.

An important consideration is the angle of *incidence* of the path of the photon bundle on the plane. Since the emissivity varies as a function of the angle of emittance, then by Kirchhoff's law the absorptivity must vary as the same function of the angle of incidence. Thankfully, in this case, the angle of incidence on Plane I is the same as the angle of emittance from Plane II because of the geometry of the model.

To decide whether the photon bundle was absorbed, a look-up table of absorptivity values is consulted. This look-up table is in fact an array of 100 elements, each containing a value of the absorptivity at a particular angle of incidence. In general, the value stored in the n^{th} element of the array is the absorptivity for an angle of incidence of $\frac{n\pi}{200}$.

Thus, given the value of the angle of incidence, the absorptivity can be looked up in exactly the same way that the appropriate value of the CDF was found. Given this absorptivity, a univariate random number is then generated. If it is less than or equal to the absorptivity, the photon bundle is absorbed, otherwise it is reflected.

Clearly, since the geometry is completely symmetric, the above reasoning can also be applied to photon bundles emitted by Plane I.

If the photon bundle hit Plane I and was not absorbed, the photon bundle is then either followed along effectively the same path (in the case of specular reflection*) or new values of θ and ϕ were generated (for diffuse reflection).

3.3 Testing the model

This simulation was tested in two ways. Firstly, the planes were made diffuse and black, and a record was kept of the proportion of radiation leaving one plane that was incident on the other. This is simply the configuration factor which, as already mentioned, is well documented for such a case. Since both planes were black, reflections did not need to be considered.

*The photon bundle travels along the same path until it encounters the image of Plane II in Plane I.

The second check was to theoretically calculate the expected final temperatures of the planes when they were not black, thus ensuring that the part of the program that dealt with reflections was working properly. For the two outer surfaces (i.e. the one facing the Sun and the one facing empty space, assumed to be at 0K), this was merely a case of absorbing a certain amount of sunlight on one, and losing the hemispherical-total emissive power from each. The two surfaces facing each other then defined the equilibrium temperatures. This could then be solved quite easily, using enclosure theory, to reveal the expected final temperatures (see appendix A).

The first thing this model demonstrated was that, even for the case of a completely diffuse surface, the emissivity must be carefully calculated. Initially, I simply had both θ and ϕ chosen using univariate random numbers (e.g. $\theta = \frac{\pi}{2} \times R1$, $\phi = 2\pi \times R2$). However, this proved to be quite wrong due to some simple geometrical considerations.

As described in section 2.5, a $\sin\theta\cos\theta$ weighting function needs to be included in the CDF. This is shown in the results obtained from the simulation. For a 1:1:1 geometry, the simulation with no weighting function gave a result for the configuration factor of 0.2638, whereas the simulation with the $\sin\theta\cos\theta$ weighting function gave a value of 0.2001.

The value calculated from equation A.24 is 0.1998 which agrees well with the $\sin\theta\cos\theta$ weighted simulation. Clearly, the simulation with no weighting function gave the wrong answer.

Having satisfied myself that the model worked when the surfaces were black, the emissivity, absorptivity and reflectivity of the surfaces was then changed, as was the aspect ratio. Table A.1 gives a complete summary of all the values used, as well as the comparison between the calculated values and the results from the model. As explained in §A.2, the two values showed excellent agreement except in those regions where the enclosure theory caused the analytical results to be invalid.

Having achieved reliable results with the model, I tested how stable these results were. In particular, I altered the heat capacity of the plates and the length of the time step. I found that, as would be expected, the length of time step had no effect on the final result, or the 'real' time elapsed before equilibrium was reached. A smaller time step did, however, reduce the amount of variation in the tube temperature once thermal equilibrium had been achieved at the cost of much longer run times.

Reducing the heat capacity caused the plates to reach equilibrium faster, but had no effect on the final temperature. However, if the heat capacity was made very small, or the time step very long, the model exhibited a chaotic fluctuation which never settled down. It was noticeable that these fluctuations seemed to be centred around the previously measured equilibrium values.

Another important test was to check for any dependence of the final temperature of either plate on the initial temperatures. The model was examined with a wide variety of initial temperatures, including starting the sunward facing plate at nearly 0K and the other plate at 300K. In every simulation, the final temperatures of the two plates were the same.

Many more simulations were performed with ever changing parameters, including the number of photon bundles per time step (which had little effect provided the number was reasonably large) and the random number generator seed (which had no effect at all on the equilibrium temperatures). Through this study I gained an insight into the most important parts of the model and under which conditions they performed best.

3.4 A simple EDISON model

Having exhausted the possibilities of the two-plate geometry, and satisfied myself that it was working well, I proceeded to move on to the more relevant geometry of a cylinder and a plane.

This was a more challenging task as I was now modelling a curved surface. I decided the best way to follow photon bundles around the system was to employ vector algebra. In other words, the emittance angles θ and ϕ were converted into $\underline{i}$, $\underline{j}$ and $\underline{k}$ component vectors. These were then used to decide whether a photon bundle hits the other surface or not.

The red lines in figure 3.5 show a 2 dimensional projection of the model onto cartesian axes. Placing the origin of the axes at the centre of the cylinder greatly simplified matters, since the line from the origin to any point on the cylinder surface makes an angle with the x axis which is equal to the angle from the normal of the cylinder surface at that point to the normal of the plane *. Also, the plane is simply a line at a fixed value of x.

3.4.1 Emissions from the plane

Finding the component cartesian vectors for emissions from the plane is a fairly simple task owing to the fact that the normal to the surface always lies along the x axis. If we define the vector describing the path of emission as $a\,\underline{i} + b\underline{j} + c\underline{k}$, then the challenge is to find the values of a, b, and c given values for θ and ϕ.

For an emission from the plane it is clear, from figure 3.4, that the sizes of a, b, and c would be

*Since the normal to the plane is parallel to the x axis

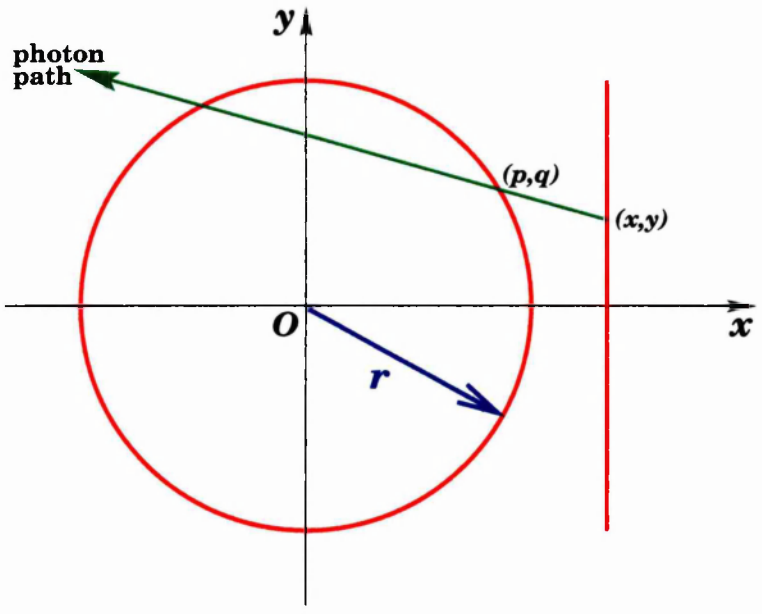

Figure 3.5 Two-dimensional projection onto cartesian axes of the model.

given by the change in the x, y and z co-ordinates between point P and point C. In other words:

$$a = -d$$

$$b = |\overrightarrow{AC}| \cos\phi = d \tan\theta \cos\phi \quad \text{(from equation 3.3)}$$

$$c = |\overrightarrow{AC}| \sin\phi = d \tan\theta \sin\phi \quad \text{(from equation 3.4)}$$

The sign of a indicates it is pointing in the negative x direction (i.e. in figure 3.4 from Plane II to Plane I). This is consistent with a line from the plane to the cylinder in figure 3.5.

A common factor of these three equations is d, which has no relevance in this case and can therefore be eliminated. Also, to make the vector in the direction of emission a unit vector, we multiply each term by $\cos\theta$. This gives:

$$a = -\cos\theta \tag{3.5}$$

$$b = \sin\theta \cos\phi \tag{3.6}$$

$$c = \sin\theta \sin\phi \tag{3.7}$$

Given these component vectors, we must now decide if a photon bundle emitted from the plane

will hit the cylinder. Shown on figure 3.5 in green is the path of a photon bundle projecting from a point on the plane. The point of emission of the bundle has the co-ordinates (x, y), and the point on the cylinder surface where the bundle hits has the co-ordinates (p, q).

The vector $(a\,\underline{i} + b\,\underline{j} + c\,\underline{k})$ is of unit length. Thus, we must scale this vector by some factor such that it describes the line between the plane and the cylinder.

It should be stressed at this point that figure 3.5 is a two dimensional projection of the model. Thus, we are not initially concerned with either $\underline{k}$ or the z co-ordinates of the point of emission or the point at which the photon bundle hits the cylinder. First of all we must find whether the photon bundle will actually be incident upon the cylinder. Once we know it is, and we know the scaling factor to apply to the component vectors, we then simply check to see if the z co-ordinate of the point at which the photon path crosses the 2-D projection of the cylinder is within the limits of the height of the cylinder.

For this first step we are effectively considering an infinitely long cylinder and seeing if the path of the photon bundle will intersect it. Using component vectors clearly makes this kind of projection much easier.

Denoting the appropriate scaling factor n, we can say:

$$p = x + na$$

$$q = y + nb$$

Note that p is clearly less than x since, as noted above, a is negative.

Now, since the point (p, q) is on the surface of a circle of radius r centred at O, we can additionally say:

$$p^2 + q^2 = r^2$$

$$\Rightarrow \quad (x + na)^2 + (y + nb)^2 = r^2$$

If we expand out the parentheses and gather together equal powers of n, we get:

$$n^2(a^2 + b^2) + n(2ax + 2by) + (x^2 + y^2 - r^2) = 0$$

This is clearly a basic polynomial of the form:

$$An^2 + Bn + C = 0$$

And so can be solved for n by using the formula:

$$n = \frac{-B \pm \sqrt{B^2 - 4AC}}{2A}$$

Substituting in our values of:

$$A = a^2 + b^2$$

$$B = 2ax + 2by$$

$$C = x^2 + y^2 - r^2$$

After some basic expansion and simplification, we end up with:

$$n = \frac{-(ax + by) \pm \sqrt{r^2(a^2 + b^2) - (ay - bx)^2}}{a^2 + b^2} \tag{3.8}$$

Firstly we must ensure that the square-root has a real solution. In other words:

$$r^2(a^2 + b^2) - (ay - bx)^2 \geq 0$$

If the solution to the square-root is imaginary, this corresponds to the situation where the path of the photon bundle does not intersect the infinitely long cylinder at any point. If this is the case, the photon bundle is lost to empty space, and the next bundle is considered.

If the photon bundle does hit the cylinder, we still need to choose between the two possible values for n. From figure 3.5, it is clear that any line from the plane that is not a tangent to the circle will cross the circle at two points corresponding to the $\pm$ sign in equation 3.8.

Obviously, of the two, the point of interest is the one nearest to the plane. Clearly, this corresponds to the smaller value of n. Thus, the model needs to calculate the two solutions, to whit:

$$\frac{-(ax + by) + \sqrt{r^2(a^2 + b^2) - (ay - bx)^2}}{a^2 + b^2} \quad \text{and} \quad \frac{-(ax + by) - \sqrt{r^2(a^2 + b^2) - (ay - bx)^2}}{a^2 + b^2}$$

then compare the two, and select the smaller for subsequent use. However, this is unnecessarily wasteful of computing time since the code would have to perform a whole series of arithmetic functions which are then discarded.

A more efficient way, used by my model, is to only calculate the $-(ax + by)$ term and test the sign of it. If it is negative, the smaller result will come from adding the result of the square-root (since square-roots are always positive). Alternatively, if it is positive, the square-root term should

be subtracted.

The fact that n has a real solution is not in itself enough to guarantee that the photon bundle will hit the cylinder. As mentioned earlier, we must now calculate the z co-ordinate of the point at which the photon bundle hits the cylinder. If we fully define the point of emission on the plane as (x, y, z) and the point of incidence on the cylinder as (p, q, s), it is clear that:

$$s = z + nc$$

If s is within the limits of the height of the cylinder then the photon bundle will hit the cylinder, else it will be lost to empty space.

3.4.2 Emissions from the cylinder

To choose a direction for a photon bundle to be emitted from the cylinder, first a random point on the cylinder surface was chosen. This was done by selecting a random angle α (between 0° and 360°, where a value of 0° corresponds to the positive y direction) and a random height (as mentioned earlier). Once the point was chosen, the two radiometric angles, θ and ϕ, were chosen appropriately to ensure the correct weighting of ϵ'_λ. These angles are always with reference to the normal of the surface. Thus, given α, θ and ϕ, we need to calculate the three component cartesian vectors.

To do this, I used the simple idea of rotating the frame of reference of the vectors. Figure 3.6 shows two cartesian axes. One set (x, y) are the conventional axes, whilst the other (x', y') have been rotated about the origin by an angle α.

Now consider the two unit vectors $\underline{i}$ and $\underline{j}$ in the unrotated frame of reference. Clearly these vectors can be expressed in terms of the unit vectors $\underline{i}'$ and $\underline{j}'$ in the rotated frame thus:

$$\underline{i} = \underline{i}' \cos\alpha + \underline{j}' \sin\alpha \tag{3.9}$$

$$\underline{j} = \underline{j}' \cos\alpha - \underline{i}' \sin\alpha \tag{3.10}$$

Similarly, the unit vectors in the rotated frame can be expressed in terms of the un-rotated unit vectors thus:

$$\underline{i}' = \underline{i} \cos\alpha - \underline{j} \sin\alpha \tag{3.11}$$

$$\underline{j}' = \underline{i} \sin\alpha + \underline{j} \cos\alpha \tag{3.12}$$

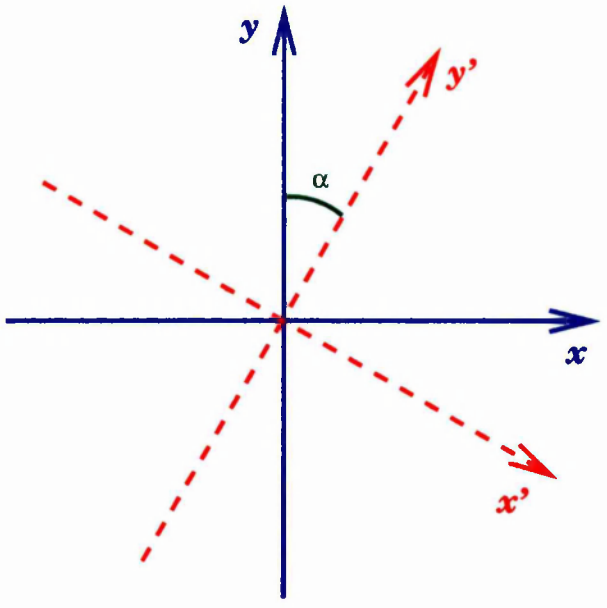

Figure 3.6 Two cartesian axes, one rotated through an angle α

So, given equations 3.9 to 3.12, we can easily rotate any given component vectors about any angle. Thus, to calculate the direction of emission from any point on the cylinder, we initially treat it as a plane perpendicular to the normal of the cylinder at that point.

It has already been shown how to express the component vectors given θ and ϕ for a plane perpendicular to the x axis, so we merely have to consider such a plane rotated around the z axis such that it is now perpendicular to the normal of the cylinder. We initially work out the component vectors in the rotated frame of reference, and then express them in terms of the conventional component vectors.

Figure 3.7 gives an example of a random point on the cylinder surface with a plane perpendicular to the normal of the cylinder at that point. Since the centre of the cylinder is defined as being at the origin of the axes, we can rotate the axes (as shown by the dashed lines) such that y' becomes the normal to the plane.

We now calculate the component vectors in exactly the same way as we did in equations 3.5 to 3.7 except this time we shall define the vector of emission in the rotated frame of reference as $a'\,\underline{i}' + b'\,\underline{j}' + c'\,\underline{k}'$. Notice, however, that in this case it is the y' axis that is normal to the plane. Thus we effectively transpose the a and b terms in the above equations to give:

$$a' = \sin\theta\cos\phi$$

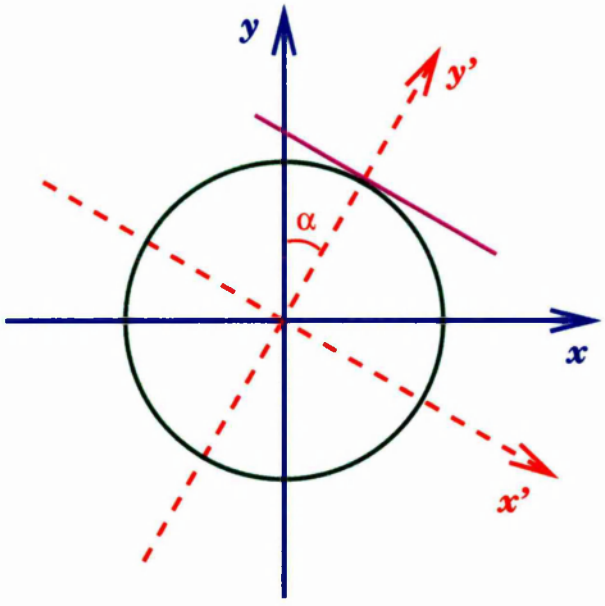

Figure 3.7 Top view of a cylinder with the tangential plane shown and the rotated frame of reference indicated by the dashed lines.

$$b' = \cos\theta$$

$$c' = \sin\theta \sin\phi$$

Notice also that b' is positive since the direction of emission is always in the positive y' direction.

Now we have our component vectors, we need to express them in terms of the unrotated unit vectors. If we define the vector of emission as $a\,\underline{i} + b\,\underline{j} + c\,\underline{k}$ (as before), we can find values for a, b and c using equations 3.9 and 3.10:

$$a = a' \cos\alpha + b' \sin\alpha = \sin\theta \cos\phi \cos\alpha + \cos\theta \sin\alpha$$

$$b = b' \cos\alpha - a' \sin\alpha = \cos\theta \cos\alpha - \sin\theta \cos\phi \sin\alpha$$

$$c = c' = \sin\theta \sin\phi$$

Notice that the coefficient of $\underline{k}$ (c) is unaffected, since we are rotating around the z axis. The angles θ and ϕ we know and, as mentioned at the start of this section, the angle α was generated when selecting the random point of emission.

To discover whether a photon bundle emitted in this direction will hit the plane, we simply find the distance to the plane from x (the x co-ordinate of the point of emission), calculate what multiple

of a this is, scale b and c appropriately and add this value to the original y and z co-ordinates to find the co-ordinates of the point at which the path of the photon crosses the plane. If both y and z are within the limits of the size of the plane, then the photon has hit the plane, else it has missed and is lost into empty space.

In other words:

$$\text{Distance to plane from point of emission } = d = x_{plane} - x$$

$$\text{Multiple of } a = m = \frac{d}{a}$$

Then the co-ordinates of the point where the photon's path crosses the plane are x_{plane}, y_{plane} and z_{plane}, where:

$$x_{plane} = x + (m \times a) \quad \text{(by definition)}$$

$$y_{plane} = y + (m \times b)$$

$$z_{plane} = z + (m \times c)$$

Define the width of the plane as W and the height as H. Then, if and only if $-\frac{W}{2} < y_{plane} < \frac{W}{2}$ *and* $0 < z_{plane} < H$, the photon will hit the plane. Otherwise it will be lost to empty space.

A useful time saving device was employed here. Clearly, if $a \leq 0$ then the photon bundle is traveling in the wrong direction and will never hit the plane. In these cases, the comparison of y_{plane} and z_{plane} with the dimensions of the plane need not be performed.

3.4.3 Reflections and absorptions

To find the angle of incidence of the photon bundle, I simply found the dot product of the vector describing the photon bundle with the normal to the surface at the point of incidence.

For the case of a photon bundle incident on the cylinder, we find the point on the cylinder surface, (p, q, s), where the photon bundle is incident. Since the centre of the cylinder is at the origin of the axes, the normal to the surface is described by the same vector as the line from the point $(0, 0, s)$ to the point (p, q, s); in other words $p\,\underline{i} + q\,\underline{j}$. The vector describing the path of the photon bundle is given as $a\,\underline{i} + b\,\underline{j} + c\,\underline{k}$. Thus, we have:

$$(p\,\underline{i} + q\,\underline{j}).(a\,\underline{i} + b\,\underline{j} + c\,\underline{k}) = |p\,\underline{i} + q\,\underline{j}||a\,\underline{i} + b\,\underline{j} + c\,\underline{k}| \cos\theta_{cylinder} \tag{3.13}$$

Where $\theta_{cylinder}$ is the angle of incidence on the cylinder. Clearly:

$$|p\,\underline{i} + q\,\underline{j}| = \sqrt{p^2 + q^2} = r$$

Where r is the radius of the cylinder, since (p, q) is a point on the surface of the cylinder (see figure 3.5). Also note the fact that a, b and c were specially chosen such that the photon-direction vector is of unit length:

$$\text{i.e.} \quad |a\,\underline{i} + b\,\underline{j} + c\,\underline{k}| = 1$$

Thus, equation 3.13 becomes:

$$(p\,\underline{i} + q\,\underline{j}).(a\,\underline{i} + b\,\underline{j} + c\,\underline{k}) = r\cos\theta_{cylinder}$$

$$pa + qb = r\cos\theta_{cylinder}$$

$$\cos\theta_{cylinder} = \frac{pa + qb}{r}$$

Thus, the angle of incidence is given by:

$$\theta_{cylinder} = \cos^{-1}\left(\frac{pa + qb}{r}\right) \tag{3.14}$$

In the case of a photon bundle incident on the plane, it was even easier since in this case the normal to the surface was a unit vector in the negative x direction (i.e. $-\underline{i}$). Once again, the length of the vector describing the direction of the photon bundle was 1. Following the same procedure, we get:

$$\theta_{plane} = \cos^{-1}(-a) \tag{3.15}$$

Knowing the angle of incidence of the photon bundle, the simulation then looks up the relevant value of the absorptivity to decide whether the photon bundle is absorbed (as described at the end of section 3.2).

If the photon bundle is reflected, a new set of problems arise. At least, in the case of specular reflection this is true. For diffuse reflection, the new set of component vectors are calculated as if the photon bundle is being emitted from the surface, since the reflected direction is independent of the angle of incidence (as explained in section 2.7).

For specular reflection, the new component vectors must be calculated based on the original

component vectors and the normal to the surface at the point of incidence. In the case of the plane, this is trivial. Since the normal to the surface lies along the x axis, reflecting a vector in the plane just involves reversing the sign of the $\underline{i}$ vector. The $\underline{j}$ and $\underline{k}$ vectors are unaffected.

Specular reflection from the cylinder is a little more tricky. However, it is made considerably easier by once again making use of rotated frames of reference.

As explained above, reflecting a vector in a plane the normal of which lies along one of the major axes is trivial. Thus, to reflect a vector from the curved surface of a cylinder, one needs only to rotate the frame of reference such that one of the axes is perpendicular to the cylinder at the point of incidence and reverse the direction of the component vector in that direction.

Once again using the convention of defining the vector describing the path of the photon bundle as $a\,\underline{i} + b\,\underline{j} + c\,\underline{k}$ we shall proceed as before. Figure 3.7 shows the projection of the cylinder, with the plane perpendicular to the normal at the point of incidence shown in magenta.

To reflect a vector in this plane, one must first express the vector in terms of the unit vectors of the rotated frame of reference. Again, we shall denote this expression as $a'\,\underline{i}' + b'\,\underline{j}' + c'\,\underline{k}'$. But we already know the values of a', b' and c' from equations 3.11 and 3.12:

$$a' = a\cos\alpha - b\sin\alpha$$

$$b' = a\sin\alpha + b\cos\alpha$$

and, of course:

$$c' = c$$

In figure 3.7 the perpendicular to the plane is the y' axis. Thus, to reflect the vector, we simply need to reverse the sign of the coefficient of $\underline{j}$:

$$b' = -a\sin\alpha - b\cos\alpha$$

We now have the values for the coefficients of the unit vectors of the reflected path in the rotated frame of reference. All we need do now is to express this vector in terms of the unrotated unit vectors in accordance with equations 3.9 and 3.10:

$$\begin{aligned} a^r &= a'\cos\alpha + b'\sin\alpha \\ &= \cos\alpha(a\cos\alpha - b\sin\alpha) + \sin\alpha(-a\sin\alpha - b\cos\alpha) \\ &= a(\cos^2\alpha - \sin^2\alpha) - 2b\sin\alpha\cos\alpha \end{aligned}$$

$$a^r = a\cos 2\alpha - b\sin 2\alpha$$

$$\begin{aligned} b^r &= b'\cos\alpha - a'\sin\alpha \\ &= \cos\alpha(-a\sin\alpha - b\cos\alpha) - \sin\alpha(a\cos\alpha - b\sin\alpha) \\ &= b(\sin^2\alpha - \cos^2\alpha) - 2a\sin\alpha\cos\alpha \\ b^r &= -b\cos 2\alpha - a\sin 2\alpha \end{aligned}$$

$$c^r = c' = c$$

When calculating the emission vector, the angle α was selected by the random number generator. In the case of reflection, however, we do not have such a luxury. Fortunately α is easily calculated since we have already deduced the co-ordinates of the point on the cylinder surface to be (p, q, s). It is fairly obvious from figure 3.7 that:

$$\alpha = \tan^{-1}\left(\frac{p}{q}\right)$$

.

3.5 Testing the EDISON-like model

Studies have been done [13] of a simple model of a radiatively cooled telescope consisting of the telescope tube and a sunshield. The sunshield is used to protect the telescope tube from direct sunlight. It does this in two ways. Firstly, the sunward side of the shield is coated in some selective surface (commonly Teflon coated silver) which has a very low absorptivity in the visible region, where the maximum emissive power of the Sun occurs, and a very high emissivity in the infra-red, where the maximum emissive power of the shield itself occurs. Also, on the side facing the telescope tube, the sunshield is coated with a substance of very low emissivity (particularly in the infra-red) to minimise the radiative transfer of heat to the telescope tube. The outside of the telescope tube is likewise coated with the same low emissivity material to reduce absorption of energy from the sunshield.

Studies already performed by Hawarden et al [13] consist of a sunshield with a surface of Teflon

coated silver facing the Sun, and vacuum deposited gold facing the telescope tube. The tube is also coated with vacuum deposited gold. The Teflon coated silver is quoted as having an absorptivity in the visible region of 0.08 and an emissivity in the infra-red of 0.787.

Hawarden et al point out that the ideal design of a passively cooled telescope is 'short and fat.' This minimises the outer area of the cylinder (through which radiation from the sunshields is absorbed) and maximises the area of the aperture. Since the inside surface of the telescope aperture is black, it makes for a very good emitter and is the main cooling mechanism for the tube. Clearly, the aperture is not completely black since it has the primary mirror at the bottom. However, using Gouffé's method of calculating the emissivity of a cavity, it can be shown that, for averaged wall emissivities between 0.5 and 0.8, the effective emissivity of the aperture is between 0.8 and 0.94 [1]. Taking the former as a conservative estimate, in accord with the previous studies, we now have a set of conditions for our simulation.

My model was based on the designs put forward by Hawarden et al and consisted of a cylinder, with a diameter equal to its height, sheltered from the Sun by a sunshield. The length of side of the sunshield was equal to the height and diameter of the cylinder. These dimensions are fairly arbitrary but since I was investigating the sensitivity of the final temperatures to the correct modelling of the radiative heat transfer, I considered the exact dimensions of the telescope of secondary importance.

By comparing this model to the previously published studies, we already have confirmation that it is performing correctly. However, we are still faced with the problem of simulating the directional properties of gold when there is no reliable published data (see chapter 2). In my model so far, I have used a theoretical model which approximates the directional emissivity of an optically smooth metal as given by equation 2.19.

One reported problem with this model is that, although the general shape of the graph versus θ is accurate, the magnitude is significantly less than experimental observations. Certainly the results from using the optical constants of gold gave emissivities much lower than the oft-quoted value of 0.03. Thus, it is necessary to scale the graph somehow to compare the results with previous studies. This was done by adjusting the value of the emissivity entered at the start of the simulation.

The emissivity entered at the start of a simulation was the hemispherically averaged emissivity. This was due to the way the model treated emissivity. As each surface in the model is considered in turn, the power emitted by that surface is calculated to define the energy associated with one photon bundle. This power is calculated using the Stefan-Boltzmann law for a blackbody scaled by the emissivity of the surface. Since this value is the total energy emitted by that surface for that time step, the hemispherical emissivity was needed. To find the correct value of the hemispherical

emissivity, however, some numerical integrations were necessary.

Siegel and Howell ([17]: equations 2-23,2-26) show the derivation for the following expression of the directional-total intensity of a blackbody:

$$i'_{\mathrm{b}} = \int_0^\infty i'_{\lambda \mathrm{b}}(\lambda) d\lambda = \frac{\sigma \mathrm{T}^4}{\pi} \tag{3.16}$$

Also given (in equation 3-6a) is the expression for the hemispherical-total emissive power:

$$\mathrm{e}(\mathrm{T_A}) = \int_\Omega \left[\int_0^\infty \epsilon'_\lambda(\lambda, \theta, \phi, \mathrm{T_A}) i'_{\lambda \mathrm{b}}(\lambda, \mathrm{T_A}) d\lambda \right] \cos\theta d\omega \tag{3.17}$$

If we assume that ϵ' doesn't vary with λ (i.e. the surface is 'grey'), equation 3.17 becomes much simpler:

$$\begin{aligned}
\mathrm{e}(\mathrm{T_A}) &= \int_\Omega \epsilon'(\theta, \phi, \mathrm{T_A}) \left[\int_0^\infty i'_{\lambda \mathrm{b}}(\lambda, \mathrm{T_A}) d\lambda \right] \cos\theta d\omega \\
&= \int_\Omega \epsilon' \frac{\sigma \mathrm{T}^4}{\pi} \cos\theta d\omega \\
&= \frac{\sigma \mathrm{T}^4}{\pi} \int_0^{2\pi} \int_0^{\frac{\pi}{2}} \epsilon' \cos\theta \sin\theta d\theta d\phi \\
&= 2\pi \times \frac{\sigma \mathrm{T}^4}{\pi} \int_0^{\frac{\pi}{2}} \epsilon' \cos\theta \sin\theta d\theta \\
&= (\sigma \mathrm{T}^4) \times 2 \int_0^{\frac{\pi}{2}} \epsilon' \cos\theta \sin\theta d\theta
\end{aligned} \tag{3.18}$$

Equation 3.18 is written to draw attention to the ratio between the hemispherical-total emissive power of a blackbody ($\sigma \mathrm{T}^4$) and the hemispherical-total emissive power of an imperfectly absorbing surface. This ratio is the hemispherical-total emissivity (at least for the purposes of calculating the power emitted from the surface) and it is this value I entered into my simulation.

Values for the directional emissivity were calculated from equation 2.19. These were then numerically integrated over all values of θ by a simple computer program, weighted with a $\sin\theta\cos\theta$ function, and multiplied by 2 to give the appropriate hemispherical emissivity.

3.6 Results of simulations using idealised material properties

Once the model had been developed and I was satisfied that it was working well, I studied the sensitivity of the final temperature of the telescope to two conditions [40]. One, as already mentioned, is the effect of real surface properties. I also studied the effect of varying the geometry of the telescope

very slightly. In this case, I simply varied the sunshield-telescope separation in order to emphasise the highly directional behaviour of gold.

All the simulations started at 100K * with a square sunshield of side equal to the height and diameter of the tube (see figure 3.8). The sunshield was assumed to have a heat capacity of 10^5 J/K, and the telescope tube a heat capacity of 5×10^5 J/K, these being guesstimates based on the quoted mass of the proposed telescope. Since my experiments are more interested in the final temperatures than the time it took to reach these temperatures, the heat capacities were not considered too important, provided they were large enough to prevent the kind of chaotic behaviour described in section 3.3.

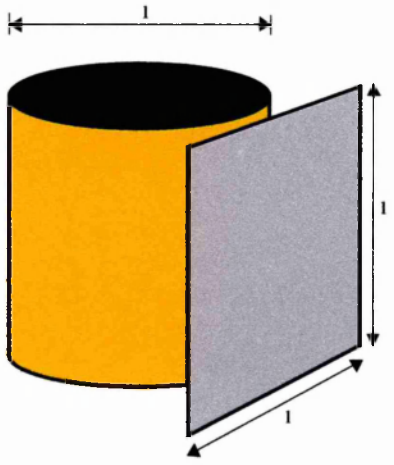

Figure 3.8 Simplified model of the EDISON telescope.

In all cases, the sunshield reached much the same equilibrium temperature (about 220K). This is not surprising when you consider how dominant the Sun would be as a heat source, especially compared with the telescope tube as the only other source of heat.

Figure 3.9 is a plot of how the telescope tube cools down over time. The time axis is marked in seconds. It is quite clear that all the simulations reached an equilibrium value after approximately 50000 seconds. This first set of simulations had the sunshield placed one-tenth of its height away from the tube. This defined the 'aspect ratio', given as the fraction $\frac{\text{height of sunshield}}{\text{minimum separation between sunshield and tube}}$, to be 10.

These four curves relate to four different sets of material properties. In all four cases, the

*There was no special reason for choosing this temperature. Earlier (and subsequent) testing of the model (see section 3.3) had assured me of the invariance of the final temperatures no matter what the initial temperatures, so 100K seemed as good a temperature as any.

Surface	Emission characteristics	Reflection characteristics
Double-diffuse	perfectly diffuse	perfectly diffuse
Specular-gold	directional (gold at 5μm)	perfectly specular
Diffuse-gold	directional (gold at 5μm)	perfectly diffuse
Bizarre	bizarre	bizarre

Table 3.1 Emissive and reflective properties of the surfaces referred to in figure 3.9

sunward side of the sunshield was covered with Teflon coated silver, with the properties described in section 3.5. The materials referred to are the ones coating the back of the plate and the outside of the telescope tube, and have the characteristics described in table 3.1. In all four cases, the emissivity was scaled such that the hemispherically averaged emissive power was consistent with a diffuse surface with a hemispherical-total emissivity of 0.03.

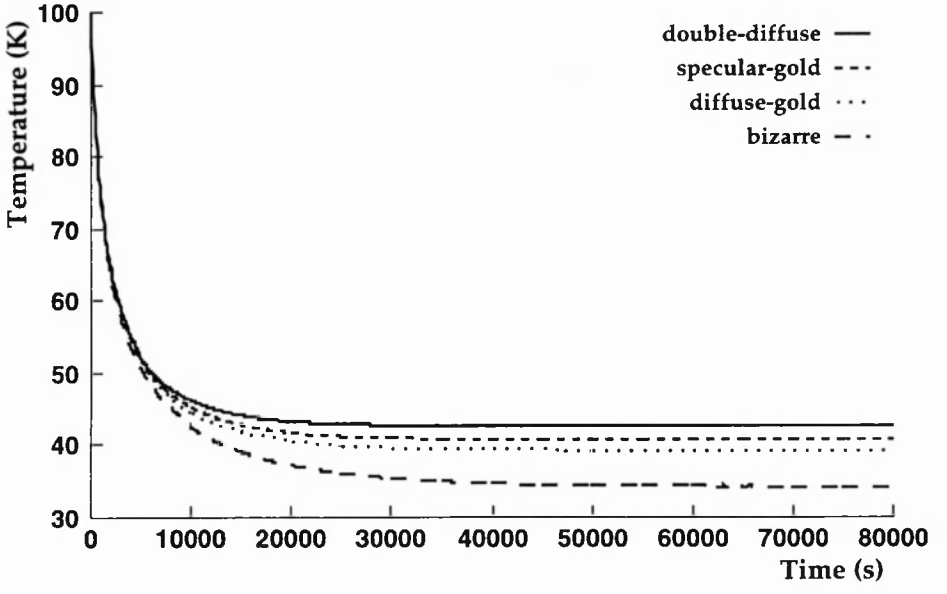

Figure 3.9 Results of simulations of the cooling of the telescope tube with varying materials properties. All surfaces have hemispherical-total emissivity (ϵ) of 0.03. (Aspect ratio = 10)

The hottest curve is the traditional diffuse in emission and reflection approximation. It reaches an equilibrium temperature of 42.6K, which agrees very well with previous studies of this simple geometry ([13] gives an example of such a geometry and reports a tube temperature of 42.5K). Next coolest is a pure gold surface. It is perfectly specular in reflection, and has the emissive properties described in figure 2.5. This stabilises some 2 degrees lower.

The next coolest is a surface which has the emissive properties of gold, but is perfectly diffuse

in reflection. I ran this simulation simply because the code for making the surface directional in emission, and the code for making it specular, were completely separate, so I decided to investigate what difference would be made just by making the surface specular. It is immediately obvious that the specular surface is some 1.5 degrees hotter that the diffuse one. This might suggest that a specular material like gold is not necessarily the right choice, and that better results could be obtained by using materials that are diffuse in reflection. Unfortunately it seems that the lowest-emissivity surfaces available are all metals and highly specular. Metals lose their specular properties when the surface becomes rough on the scale of the wavelength of interest, but unfortunately this tends to increase the emissivity as well.

The coldest curve is the result of using an, as yet, hypothetical material with extremely bizarre directional properties. I ran this simulation to see what could be achieved by using highly directional materials. Such materials can be manufactured in two ways. One way is to texture the surfaces, for instance having grooves with black bases and reflective sides [41]. A more subtle way is to coat the surfaces with thin films. This causes different properties at high angles due to the apparent thickness of the film to radiation at glancing incidence causing it to dominate the surface properties at high angles.

This bizarre material is a kind of idealised gold. It has the same normal emissivity as the gold case (0.0234) and, like gold, its directional emissivity at high angles rises to 10 times its normal value. Except, with this material, the transition occurs as a step function at 80 degrees.

Figure 3.10 shows the graph of the emissive powers of the three cases. Here we have the emitted power of each surface per unit angle θ, integrated around all ϕ *. I have already shown the difference in the final temperature of the telescope tube made by the directional properties of gold. Figure 3.10 demonstrates the slight but noticeable difference in terms of the emitted power. The bizarre material, though, has a much more pronounced directionality. Indeed it is easy to see exactly where the step function in the emissivity occurs as the emitted power actually goes off the scale of the graph.

As you can see from the cooling curve, this directionality makes a big difference in the final temperature, being some 8.5K lower than the diffuse case. It is easy to imagine what a difference this kind of temperature reduction would make to the performance of the telescope.

Figure 3.11 shows the same cooling curves, except this time the aspect ratio is 5 (i.e. the sunshield is twice as far away from the cylinder). As you can see, this is much like the first graph, except that all the final temperatures are lower. I was hoping that this geometry would enhance the performance of the directional materials, but it seems to have enhanced the performance of the

*The $\cos\theta \sin\theta$ weighting function of the diffuse case, mentioned in section 2.5, is clearly visible.

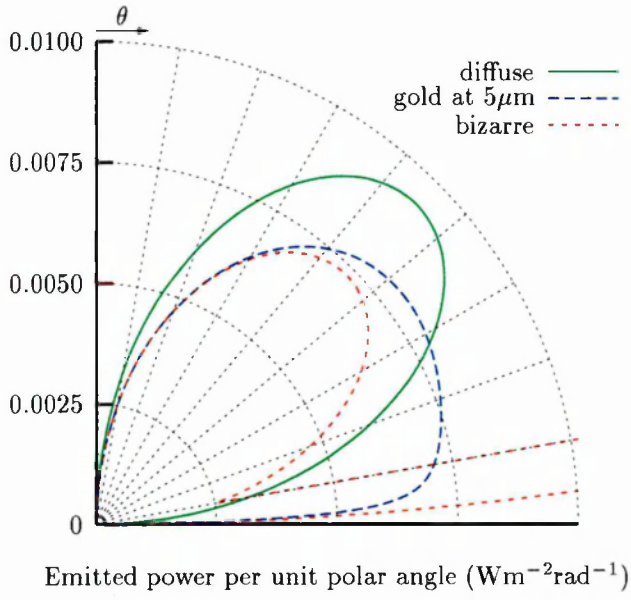

Figure 3.10 Emissive power per unit θ for three different surfaces at 42K. All three surfaces have the same hemispherical emissive power.

diffuse material just as much.

3.7 A two-shield EDISON model

In an attempt to make my model slightly more like the proposed design for EDISON, I decided to add a second sunshield. This was a very simple task since it was constructed such that the outer sunshield was always hidden from the telescope tube by the inner sunshield. This meant that the only energy incident on the cylinder came from the inner sunshield, and so the radiative exchange could effectively be split up into a parallel plates problem and a cylinder-plane problem.

Since I had already produced two pieces of code to solve these two problems, I merely combined the two into one program. The sunshields were still parallel to the axis of the cylinder and of the same height as the cylinder. The shields were the same size and had a width equal to the diameter of the cylinder (see figure 3.12).

This model was subjected to all kinds of variations and tests. The code was refined so that the directional absorptivities of the gold surfaces relied on the temperature of the *emitting* surface rather than the absorbing surface. This makes the implicit assumption that all the surfaces are the same material, but allows the change of radiative properties with wavelength to be simulated.

Effectively, this change was taking the peak wavelength of emission at the temperature of the

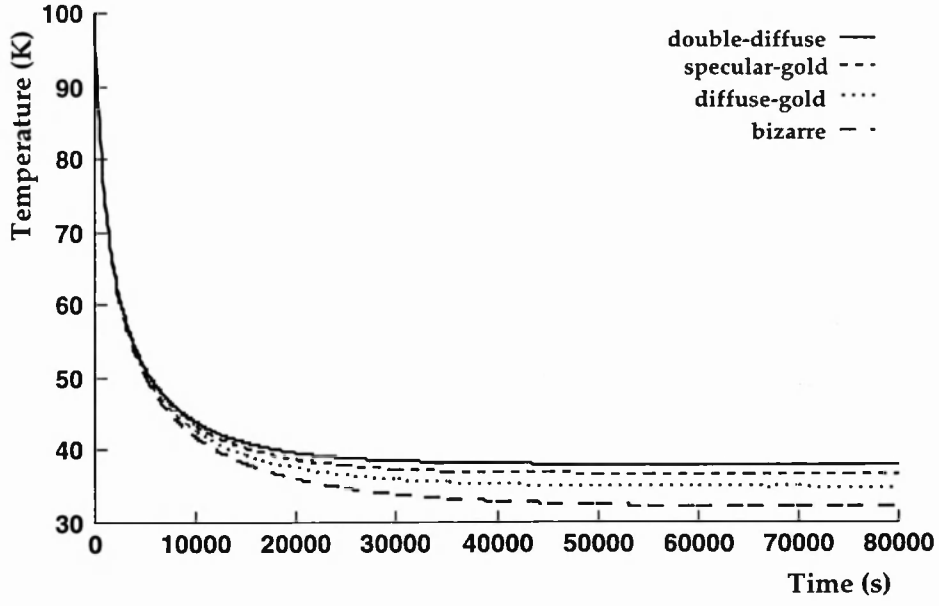

Figure 3.11 Results of simulations of the cooling of the telescope tube with varying materials properties. All surfaces have hemispherical-total emissivity (ϵ) of 0.03. (Aspect ratio = 5)

emitting surface as the characteristic wavelength for that emission. The radiative properties for each surface were, in fact, the radiative properties of gold at the temperature that the surface settled down to (this was already roughly known from previous simulations). Thus, by using the radiative properties of the emitting surface, the model was accurately modelling the radiative properties of gold at the temperature, and hence the wavelength, of the emitted radiation. As mentioned above, this assumes that all surfaces were coated with the same material and would not be applicable to a telescope with a mixture of surface coatings.

Simulations were done with the radiative properties calculated directly from equation 2.19 as well as those scaled to have an emissivity of 0.03. A variety of values of n and κ were used to calculate different emissivity values.

As mentioned above, the reported problem with equation 2.19 was the unusually low values for the emissivity. However, Siegel and Howell [17] suggest that the discrepancy between the measured values and those calculated from equation 2.19 could well be due to experimental errors caused by, among other things, imperfect samples being measured. Indeed, in my own experiments (see chapter 4) the emissivity of gold was noticeably less than the commonly quoted value of 0.03, as was the case in several other published sources [23, 31, 32, 42].

A simulation was also done with the optical constants of the material at different wavelengths

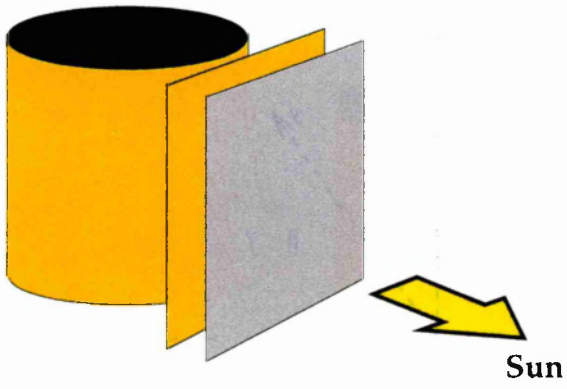

Figure 3.12 An EDISON-like model with two sunshields.

extrapolated to the low temperatures associated with those wavelengths. However, no firm conclusions were drawn since the method of extrapolation was based on the Drude model which, as mentioned in section 2.9.1, is notoriously unreliable at low temperatures

Another development of the code was to include the effects of different radiative properties at different polarisations. Polarisation effects were included in the model and seemed to produce a small but noticeable effect. However, the model suffered from being unable to properly model the change of polarisation as the photon bundles encountered the curved surface of the cylinder.

A more detailed study of the results is given at the end of this chapter.

3.8 Tilted sunshields

The final adjustment of the code was to tilt the sunshields with respect to the axis of the cylinder, as in the EDISON design proposal. This was a slight modification of the existing model and again used the idea of rotating the frame of reference.

Figure 3.13 shows a representation of the most sophisticated simulation model along with the axes used in calculating the component vectors used in the simulation. The origin of the axes is at the base of the cylinder in the centre of the curved surface. Thus, the z-axis is also the axis of the cylinder.

The x-axis is perpendicular to the bottom edge of both sunshields, and the y-axis forms a left-handed set with the other two. The minimum separation between the shields (and between the inner shield and the cylinder) is denoted as 'd'.

The angles the sunshields make with the vertical are labeled β and γ in the diagram, and are

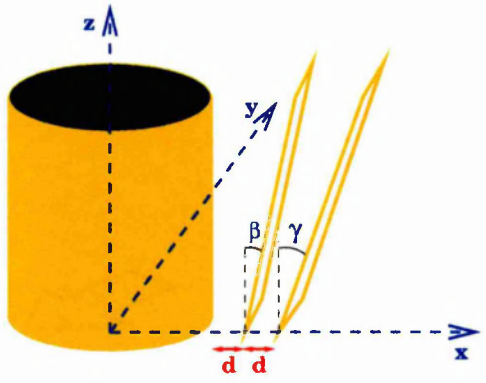

Figure 3.13 An EDISON-like model with two tilted sunshields.

denoted 'angleone' and 'angletwo' respectively in the simulation code (appendix B).

The component vectors for the direction of emission and reflection were calculated exactly as previously described for the cylinder (section 3.4.2 and following). In this case, however, the angle of rotation of the axes, α, was either β or γ depending on which sunshield was under consideration. Also, all the rotations were done in the xz plane rather than the xy plane. Nevertheless, the same equations could be applied.

Also, the angle between the incident photon bundle and the normal to the surface was again deduced from the dot product of the photon bundle vector with the normal. In the case of the sunshield, the normal was $\hat{\underline{n}} = -\underline{i}'$ where $\underline{i}'$ was the unit vector along the x-axis of a frame of reference rotated through an angle α such that the x-axis was normal to the sunshield. So, for the inner sunshield, $\alpha = \beta$, and for the outer sunshield $\alpha = \gamma$.

From equations 3.11 and 3.12 we can say:

$$\hat{\underline{n}} = -\underline{i}' = \underline{k}\sin\alpha - \underline{i}\cos\alpha$$

Notice we are using $\underline{i}$ and $\underline{k}$ since the sunshields are tilted in the xz plane. Using exactly the same logic that led to equation 3.14 we obtain the following:

$$\theta = \cos^{-1}(c\sin\alpha - a\cos\alpha)$$

Working out the scaling factor to apply to the component vectors was slightly different and deserves some explanation.

If the two sunshields were depicted by a 2-D projection in the xz plane, they would appear as

two diagonal lines. These lines would be described by the following equations (c.f. figure 3.13):

$$\text{For the inner shield} \ : \ x = r + d + z\tan\gamma \tag{3.19}$$

$$\text{For the outer shield} \ : \ x = r + 2d + z\tan\beta \tag{3.20}$$

where r is the radius of the cylinder.

Now, consider the case of a photon bundle traveling from the inner shield to the outer shield. The photon is emitted from a point (x, y, z) traveling in a direction $(a\,\underline{i}, b\,\underline{j}, c\,\underline{k})$. Once again, we shall scale this unit vector of direction by a factor n such that it describes the path between the two planes. The point of incidence on the outer sunshield will be at a point (x', y', z'). Thus:

$$x' = x + na \tag{3.21}$$

$$y' = y + nb \tag{3.22}$$

$$z' = z + nc \tag{3.23}$$

But, from equation 3.20 we know that:

$$x' = r + 2d + z'\tan\beta \tag{3.24}$$

Substituting in equations 3.21 to 3.23 gives:

$$\begin{aligned} x + n_{i\to o}a &= r + 2d + (z + n_{i\to o}c)\tan\beta \\ \Rightarrow n_{i\to o}a - n_{i\to o}c\tan\beta &= r + 2d + z\tan\beta - x \\ \Rightarrow n_{i\to o} &= \frac{r + 2d - x + z\tan\beta}{a - c\tan\beta} \end{aligned}$$

The subscript on the n indicates this scaling factor is concerned with photons traveling from the inner shield to the outer shield. If we substitute x from equation 3.19 into the above equation, we get:

$$n_{i\to o} = \frac{r + 2d - (r + d + z\tan\gamma) + z\tan\beta}{a - c\tan\beta}$$

$$\Rightarrow n_{i\to o} = \frac{d - z(\tan\gamma - \tan\beta)}{a - c\tan\beta} \tag{3.25}$$

Similarly, if we consider the case of a photon bundle traveling from the outer shield to the inner shield, equations 3.21 to 3.23 still apply, except here the point (x, y, z) is on the outer shield. Substituting these equations into equation 3.19 gives:

$$\begin{aligned} x + n_{o\to i}a &= r + d + (z + n_{o\to i}c)\tan\gamma \\ \Rightarrow n_{o\to i}a - n_{o\to i}c\tan\gamma &= r + d + z\tan\gamma - x \\ \Rightarrow n_{o\to i} &= \frac{r + d - x + z\tan\gamma}{a - c\tan\gamma} \end{aligned}$$

The subscript on the n indicates photons traveling from the outer shield to the inner shield. If we substitute x from equation 3.20 into the above equation, we get:

$$\begin{aligned} n_{o\to i} &= \frac{r + d - (r + 2d + z\tan\beta) + z\tan\gamma}{a - c\tan\gamma} \\ \Rightarrow n_{o\to i} &= \frac{z(\tan\gamma - \tan\beta) - d}{a - c\tan\gamma} \\ \Rightarrow n_{o\to i} &= (-1) \times \frac{d - z(\tan\gamma - \tan\beta)}{a - c\tan\gamma} \end{aligned} \tag{3.26}$$

Considering the similarity of equations 3.25 and 3.26, we can see a useful way of reducing the amount of calculation done by the simulation code. It is clear that, for the general case, we can say:

$$n = A \times \frac{d - z(\tan\gamma - \tan\beta)}{a - c\tan B} \tag{3.27}$$

Where, when going from the inner to the outer shield:

$$A_{i\to o} = 1$$

$$B_{i\to o} = \beta$$

And, when going from the outer to the inner shield:

$$A_{o\to i} = -1$$

$$B_{o \to i} = \gamma$$

So, the equation is essentially the same with just two variables changing depending on the incident surface. In my simulation code, these variables alternate between their two possible values as the photon bundle bounces back and forth between the shields. To further cut down on arithmetic calculations, the value of $\tan\gamma - \tan\beta$ (which is constant throughout the simulation) is calculated at the beginning of the simulation and assigned to a variable.

3.9 Bouncing code

My model follows photon bundles as they bounce between surfaces in two ways. For the plane-plane interactions, the photon bundles are handled by the 'bounce()' function (see appendix B). The first argument passed to this function is a number corresponding to the surface emitting the photon bundle. All the surfaces in the model which interact with another surface are numbered. Starting from 0 for the inner surface of the outer sunshield, and counting up to 3 for the curved surface of the cylinder.

Since the two planes are the same geometries, the same equations can be used for each to calculate such things as the angle of reflection (for specular reflections) and the distance from one surface to the next. An infinite loop allows the model to follow the photon bundle for however many reflections it takes for it to be absorbed or lost to space. This loop is broken when one of these two conditions is met. The loop consists of the necessary equations which are applied to each surface in turn.

As the photon bundle oscillates between the planes, the variable 'alpha', which stores the identifier of the surface the photon bundle is currently incident upon, alternates between 0 and 1. To do this, I make use of the behaviour of the C programming language in assigning a value of zero to mean 'false' and a value of not-zero to mean 'true'. At the end of each iteration of the loop, the code checks whether alpha is 'true' or 'false' (i.e. equal to zero or not) and toggles its value accordingly. The variable alpha is then used to look-up values for the surface properties for the next encounter of the photon bundle.

For the plane-cylinder interactions, the two surfaces are not the same geometry and quite different equations are needed. To achieve this, my code has two functions; 'ptc()', or Plane-To-Cylinder, and 'ctp()', or Cylinder-To-Plane. The final command of each of these two functions is a call to the other function. In this way the functions call each other recursively as the photon bundle bounces back-and-forth.

If the photon bundle is absorbed or lost to space, whichever function is currently considering the photon bundle aborts before it reaches the final command. This causes all the recursive calls to finish and return an answer describing the fate of the photon bundle.

The variables containing the co-ordinates on the surface from which the photon bundle was emitted or reflected (x, y, and z) are pointers which are passed from one function to the next. They are also used to signify whether the photon bundle was lost to space or absorbed by a surface. If the photon bundle was lost to space, all three variables are set to -1 (being a value they could never normally be ascribed) and returned to the main function. If the photon bundle was absorbed by the plane variable z is set to -3, if it is absorbed by the cylinder, variable z is set to -2.

Thus, if emissions from the plane were being considered and the functions ptc() and ctp() return a value of $z = -2$, the photon bundle has been absorbed by the cylinder. If, however, $z = -3$, the photon bundle was reabsorbed by the plane. The energy balances are amended appropriately.

Clearly, when ptc() and ctp() have finished considering the photon bundle, the variables x and y *must* be -1 and z can be -1, -2 or -3. If none of the above fit the values of x, y, and z, an error is produced by the main function. If as much as one error is produced over the course of a simulation, it is an indication that the code is not functioning correctly.

3.10 Results of Monte-Carlo Simulations

As mentioned earlier in this chapter, the Monte Carlo simulation model was run many times with a number of varying parameters. The basic parameters which were always kept constant were:

- Solar constant = 1353 Wm^{-2}
- Sunfacing surface had $\alpha_{visible} = 0.08$ and $\epsilon_{infrared} = 0.787$
- All other surfaces were coated with the same material as each other
- The open end of the telescope tube had $\epsilon = 0.8$

Note that the solar constant is actually that quoted at a distance of 1AU. Obviously, the further out in the solar system one travels, the smaller the solar constant will be, dropping off as R^2. However, at this time it has still not been decided whether the DARWIN interferometer will be placed just beyond the zodiacal dust (at $\simeq$ 3.5AU) or at the orbit of Jupiter ($\simeq$ 5AU). Also, other passively cooled missions will no doubt follow which may be placed nearer to Earth (such as the previously mentioned halo orbit around the Lagrangian point L2). Thus I chose the solar constant at 1AU as a pessimistic estimate of the amount of energy falling on the outer sunshield of the telescope.

Early results (summarised in [43]) concentrated on varying the directional properties of the gold surfaces. Some investigation of the effects of varying the dimensions of the telescope were performed as well as simple treatments of polarisation and conduction.

Although in this chapter and in [40] I gave graphs of the tube temperature as the telescope cooled down, I realised the most important results were the final temperatures and not the performance of these temperatures with time.

A big problem with the two-shield model was getting the tube to reach an equilibrium temperature without running the simulation for a very long time. This was solved by reducing the heat capacities of the inner sunshield and the telescope tube. Since these values for the heat capacities were only guesstimates, and since previous studies (see section 3.3) had assured me that the heat capacities had no effect on the value of the final equilibrium temperatures (just the time it took to reach them), I felt that reducing the heat capacities to achieve a result in a reasonable time was perfectly justified.

The temperature of each part of the model was still printed out at the end of each time step so that after a simulation run they could be plotted graphically to ensure that the model had indeed settled down to a steady state. Figure 3.14 shows a typical plot of the output of the last 500 time steps of a simulation lasting 10,000 time steps. Note that only the telescope tube temperature is plotted here since it typically takes the longest time to settle down.

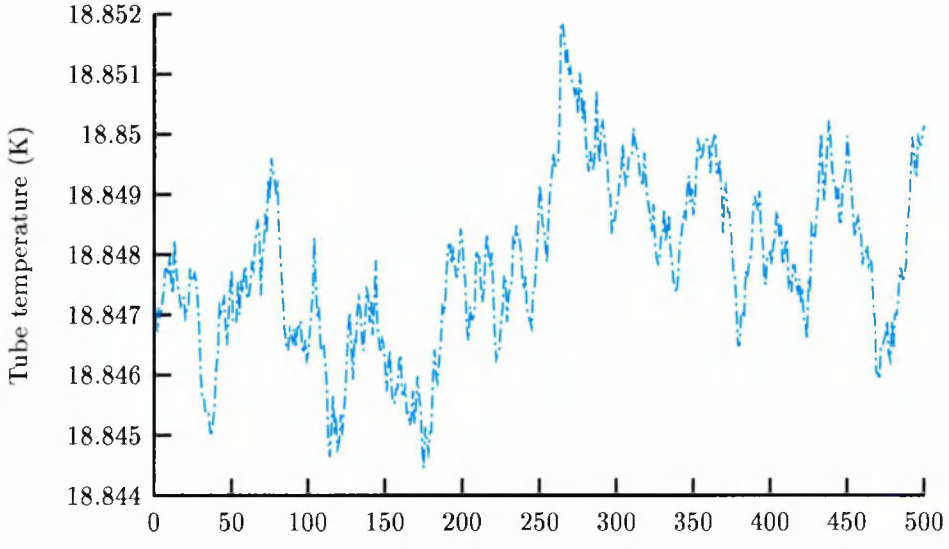

Figure 3.14 A plot of the telescope tube temperature over the last 500 time steps of a simulation lasting 10,000 time steps

Once the model has settled down, it exhibits small chaotic fluctuations typical of such a numerical method, but the fluctuations are very small, 0.008K in this case, and show no continuing downward trend. Having satisfied myself in this way that the final temperatures were indeed indicative of the equilibrium temperatures of the model, I recorded the temperatures of each component of the model. Only the final temperatures were reported in the Journal of Geophysical Research (JGR) [43] and will be reported below.

The model used for the results reported in the JGR paper was slightly different from that described in this chapter. The most significant difference was that the model used in the JGR paper did not check correctly for the $\pm$ coefficient in equation 3.8 (see page 50). It assumed that the $(ax + by)$ term was always positive, but I later realised that, over a small part of the parameter range, it was negative.

To check how much difference this would make to the results, I reproduced the simulations reported in the JGR paper. A comparison of the two sets of results is presented later in this chapter. One difference, however, was the lack of polarisation.

In the JGR paper I had tried to model the polarisation by considering the radiation as consisting of two distinct polarisations. The proportion of each polarisation was calculated using the values of emissivity for each polarisation. Thus, each photon bundle was effectively plane polarised, and the reflectivities encountered by this bundle depended on the polarisation of the bundle.

After some consideration and further advice, I realised that this method of modelling polarisation is too crude to be useful. Firstly, the model did not correctly model the change of polarisation as the radiation is reflected off of the cylinder. Due to the curved surface of the cylinder, the plane of incidence will not necessarily be the same as the plane of emittance from the sunshield, and hence the relative polarisation of the photon bundle will have changed. The model made no attempt to work out the new plane of polarisation.

Another problem is that emitted light is unpolarised. It consists of equal proportions of light polarised in all directions. The polarisation of an individual photon will define the values of the reflectivity experienced by it, but when these reflectivity values are averaged over all polarisations, the effective reflectivity will simply be the average of the reflectivity at each polarisation.

So, for all recent simulations, polarisation has not been modeled. Unfortunately this means that the effect of modelling polarisation properly could not be investigated. While I would have liked to make my model as realistic as possible, the complexities involved with modelling polarisation meant that I did not have sufficient time to adapt my Monte-Carlo code.

The results are shown in table 3.2, while table 3.3 shows the earlier results with polarisation modeled. In both tables, N is the aspect ratio, defined previously as:

$$N = \frac{\text{height of sunshields}}{\text{separation between sunshields}}$$

In all cases, the separation between the sunshields is the same as the minimum separation between the inner sunshield and the tube. Thus, the value of $N = 10$ refers to the situation where the length of sides of the sunshields are 10 times larger than the separation between them.

The coefficient of conduction, H, is given in units of WK^{-1}. This was modeled simply as a transfer of energy from a hotter component of the model to the next coolest component at the end of each time step. The conduction coefficient was multiplied by the difference in temperature of the two components to find the amount of energy to be transferred. In table 3.3 the conduction results are slightly exaggerated due to a bug in the code causing the conduction coefficient to be multiplied by the temperature of the hotter component (rather than the temperature *difference*). Clearly the temperature of the hotter component will always be greater than the temperature difference, thus causing a greater amount of energy to be conducted.

It should be noted at this point that the introduction of conduction imposes a definite size on the model. The emissive power is always proportional to the area of the emitting surface, and so is unaffected by the size of the telescope provided the *relative* dimensions of the components are the same. Since the conduction is not proportional to the surface area, it implies a size. In this case, the shields would be 10m×10m.

These results will still apply to a smaller telescope, but with a lower coefficient of conduction. Since the conduction is at the top end of the likely range, it will not result in unrealistically low values for the factor of 2 or 3 reduction needed to match the EDISON design*

The 'cases' in the fifth column refer to the directional properties of the emissivity and reflectivity. The letters refer to the curves in figures 3.15 and 3.16.

In cases A and B the hemispherical-total emissivity (ϵ_h) is 0.03, the commonly quoted value for 'gold in the infra-red'. Case A shows directional behaviour derived from the optical constants of gold at 5μm (data from [19]) while case B is diffuse. Case C is also derived from the optical constants of gold at 5μm, but in this case the emissivity is not scaled up to equal 0.03 as in case A and so $\epsilon_h = 0.00856$.

*The M3 proposal[3] estimated overall spacecraft dimensions of 5.3m×2.4m.

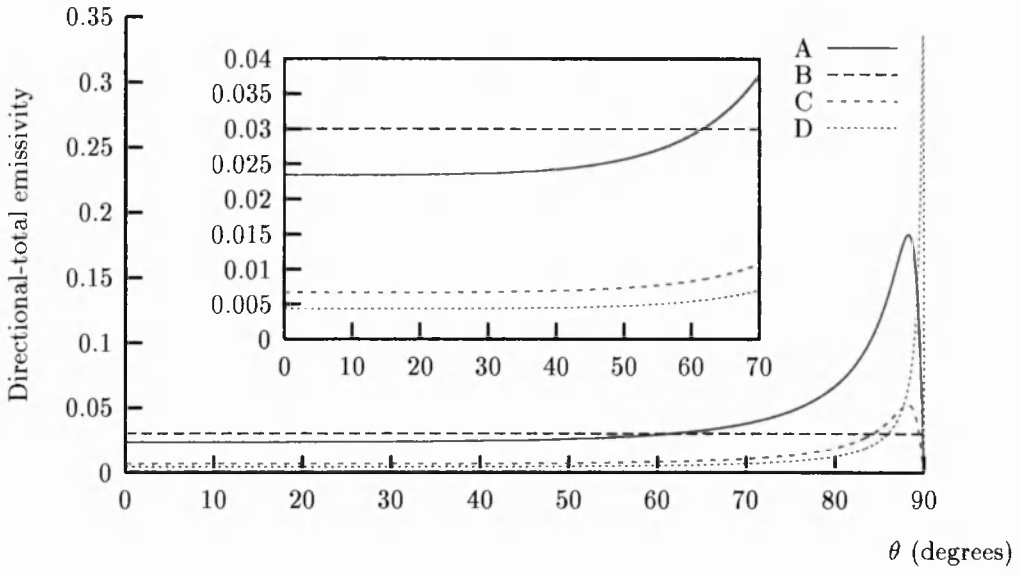

Figure 3.15 The directional-total emissivity of gold versus θ for several cases modeled in the Monte Carlo simulation (inset shows an expanded view at low θ)

Case D is derived from the optical constants of gold at 100μm (data from [44]) and $\epsilon_h = 0.00572$. Case E is derived from the optical constants at 10μm (data from [23]) and $\epsilon_h = 0.00766$. Case F is derived from the optical constants at 30μm (data from [23]) and $\epsilon_h = 0.00741$. All optical constants were measured at room temperature.

It is clear from figures 3.15 and 3.16 that the normal emissivities (ϵ'_n) are all around 0.005-0.006 when not scaled up. This is much lower than the oft-quoted 0.03, but these lower values are in fact slightly higher than the values quoted by Bennett and Ashley [42], Bennett and Bennett [23], Padalka and Shklyarevskii [32], and Toscano and Cravalho [31]. The lower values are also much closer to my own measurements of the emissivity of gold at 10.6μm which are significantly less than 0.03 (see table C.31).

Of the temperatures, T_1 refers to the outer sunshield, T_2 to the inner sunshield, and T_3 to the cylinder. The term 'opt. con.' refers to directional properties that have been directly derived from the optical constants with no scaling (i.e. cases C, D, E, and F). All optical constants were measured at room temperature (300K).

Compare the results from table 3.2 with table 3.3, a reproduction of the table in the JGR paper [43].

As usual, once the model had settled down to an equilibrium, the temperatures still showed some variation about the equilibrium value. Typical variations were $\simeq 3$ kelvin for T_1 and < 0.1

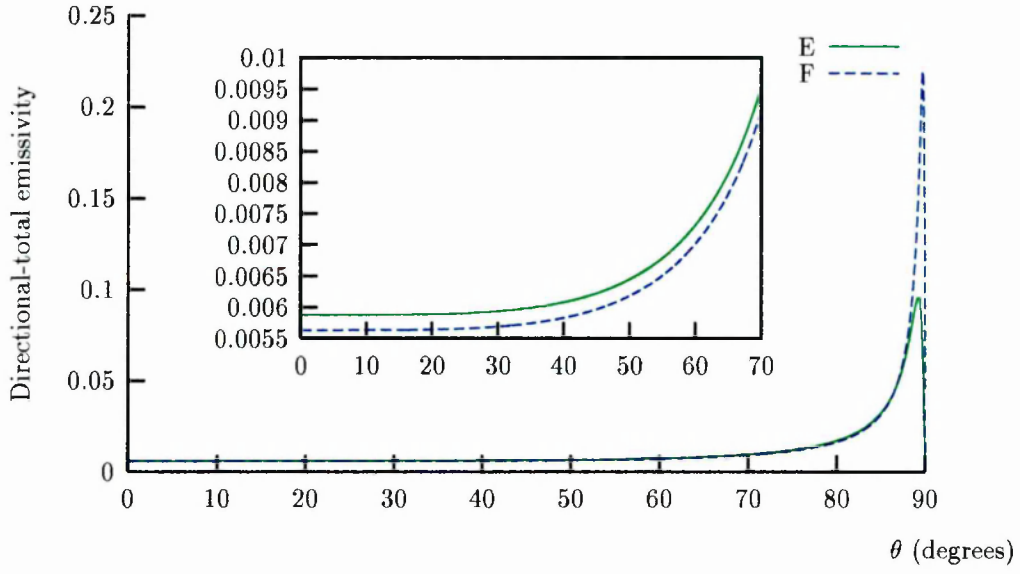

Figure 3.16 The directional-total emissivity of gold versus θ for two more cases modeled in the Monte Carlo simulation (inset shows an expanded view at low θ)

kelvin for T_2 and T_3.

All the values of T_1 in both tables agree within the typical 3K variation, regardless of the temperature of the rest of the telescope. This simply shows, unsurprisingly, what a major source of heat the Sun is for the outer sunshield, clearly swamping the effects of radiative transfer with the inner sunshield.

The line numbers in table 3.2 have been kept the same as those in table 3.3 for easier comparison. Note that lines 6 and 7 have not been reproduced. In the case of line 7, this is due to the problems

	N	H WK^{-1}	Radiative properties of gold	Case	T_1, K	T_2, K	T_3, K
1	10	0	high emissivity, directional	A	211.9	89.8	15.7
2	10	0	high emissivity, diffuse	B	212.2	98.8	17.6
3	10	0	opt. con. at 5μm, 300K	C	214.0	68.3	6.8
4	10	0	opt. con. at 100μm, 300K	D	214.2	61.5	5.8
5	10	0	opt. con. at 10, 30, 100μm, 300K	E,F,D	213.4	66.6	6.5
8	5	0	as line 5		212.7	56.3	5.7
9	2	0	as line 5		213.7	45.0	5.4
10	1	0	as line 5		214.3	39.0	5.3
11	10	0.1	as line 5		213.7	96.4	35.7
12	10	0.01	as line 5		213.8	73.9	19.6

Table 3.2 Results from the Monte Carlo simulation

	N	H WK^{-1}	Radiative properties of gold	Case	T_1, K	T_2, K	T_3, K
1	10	0	high emissivity	A	211.1	90.0	15.7
2	10	0	high emissivity, diffuse	B	211.2	97.0	17.7
3	10	0	opt. con. at 5μm, 300K	C	213.5	68.3	6.6
4	10	0	opt. con. at 100μm, 300K	D	214.1	61.5	4.9
5	10	0	opt. con. at $10, 30, 100\mu$m, 300K	E,F,D	212.6	66.7	6.0
6	10	0	temperature adjustment of cases F and D	E,G,H	214.0	67.0	4.3
7	10	0	same as line 5, with polarisation modeled		213.8	68.6	6.4
8	5	0	same as line 5, with polarisation modeled		213.8	57.6	4.8
9	2	0	same as line 5, with polarisation modeled		213.4	44.7	3.3
10	1	0	same as line 5, with polarisation modeled		213.2	37.3	2.9
11	10	0.1	same as line 5, with polarisation modeled		213.7	109.8	41.5
12	10	0.01	same as line 5,with polarisation modeled		213.8	78.6	21.5

Table 3.3 A reproduction of the table from Blake and Jones 1996

of modelling polarisation described above. Also note that because of this, lines 8-12 in table 3.2 do not have polarisation modeled.

Line 6 has not been repeated since it consisted of a theoretical extrapolation of the optical constants down to cryogenic temperatures that was based on the Drude theory. As explained in section 2.9.1, the Drude model is notoriously unreliable at low temperatures. For this reason, no conclusions could be drawn about this extrapolation and so it was decided not to repeat the simulation.

The most important lines to note are lines 1, 2, and 5. Line 2 is the traditional diffuse approximation used in previous studies by other researchers and has a hemispherical-total emissivity $\epsilon_h = 0.03$. Line 2 is identical to line 1 apart from the realistic directional properties and the specular reflections.

Line 5 is perhaps the most realistic of all the models. The directional properties of each component of the model are the directional properties of gold at the wavelength appropriate for the approximate equilibrium temperature of that component. Thus, the outer sunshield exhibits the properties of gold at 10μm, the inner sunshields exhibits the properties of gold at 30μm, and the telescope tube exhibits the properties of gold at 100μm. Unfortunately these properties are derived from values of the optical constants measured at room temperature owing to the lack of reliable cryogenic data, but it is still the most sophisticated treatment of radiative transfer of which I am aware.

On the whole there is very little difference between the two tables on lines 1-5. The new simulations appear slightly warmer, particularly lines 4 and 5. Lines 8-10 are noticeably different, however. Both tables show the expected behaviour of lower tube temperatures as the sunshields are

moved further apart from each other and the tube, but the incorrect modelling of the polarisation* seems to have enhanced this effect. In line 10 there is a 2.4K difference in the final tube temperature between the two tables, representing a 45% decrease from table 3.2.

The new simulations seem to indicate that moving the sunshields further apart would not benefit the tube temperature as much as expected. There is a difference of 0.8K between $N = 10$ and $N = 5$. This may not seem much, but at 6.5K it is a 12% effect. From here, the law of diminishing returns seems to come into play very quickly. From $N = 5$ to $N = 1$ there is only a 0.4K temperature drop. For such a large increase in the separation of the sunshields this seems a poor reward, and is probably caused by the directional nature of the gold surfaces. With more radiation emitted at high angles, the cooling is not enhanced by exposing more of the lower angles to space. For this reason, all subsequent simulations were performed with a value of $N = 10$.

In a way this may be good news for the design. Moving the sunshields further apart brings up the thorny problem of 'deployment'. Many satellite engineers are unhappy about designing deployable systems since they so often fail. If such deployment is unnecessary for reducing the telescope temperature, it would remove at least one problem from the telescope design.

Lines 3-5 show the effect of the optical constants of the metal surface. As would be expected, the longer wavelength properties result in lower temperatures owing, no doubt, to the lower normal emissivities and the peak emissivity moving out to higher values of θ. Although line 4 results in an impressive equilibrium temperature for the telescope tube, it is unrealistic to expect at least the outer sunshield to have a temperature of 214K and to be emitting radiation primarily at 100μm.

Line 5, being the most realistic as explained above, shows a slight but significant improvement over line 3 demonstrating the importance of modelling the radiative properties at the correct wavelengths.

3.10.1 Conduction

The most obvious effect on both tables is how the benefits of passive cooling are hampered by even small amounts of conduction in the system. The value of 0.1WK^{-1} was based on information given to me by Roger Emery of RAL about high conductivity materials currently in use by satellite designers. The value of 0.01WK^{-1} was used as a guesstimate of the values of low conductivity materials before I really had any reliable figures to include in my model.

*The small differences between the two tables on lines 1-5 indicate that the error over equation 3.8 plays a small effect. Thus I have concluded that the large differences between the tables in lines 8-10 are probably due to the incorrect modelling of polarisation.

Since that time, more simulations have been performed. For a low conductivity material, I based my studies on those published in the EDISON M3 proposal. Based on the figures given for the various contributions of the heat flow in the model [3, Appendix B–figure 2] there seemed to be a varying contribution of the conduction. I pessimistically chose the largest value of the coefficient of conduction (between shield 2 and shield 1) which gave a heat flow of 59.9 mW over a temperature difference of 14.2K. This gives a value of $H = 4.2 \times 10^{-3}\mathrm{WK}^{-1}$.

To see what effect conduction had on the other simulations lines 1-5 were repeated, each with $H = 0.1\mathrm{WK}^{-1}$, $H = 0.01\mathrm{WK}^{-1}$, and $H = 0.0042\mathrm{WK}^{-1}$. The results are shown in table 3.4.

	H WK^{-1}	Radiative properties of gold	T_1, K	T_2, K	T_3, K
13	0.1	high emissivity, directional	211.8	95.1	34.9
14	0.1	high emissivity, diffuse	211.2	102.1	35.9
15	0.1	opt. con. at 5μm	213.9	95.2	35.5
16	0.1	opt. con. at 100μm	214.1	98.6	36.0
17	0.1	opt. con. at $10, 30, 100\mu$m	213.7	96.4	35.7
18	0.01	high emissivity, directional	211.9	90.3	21.7
19	0.01	high emissivity, diffuse	212.2	99.1	22.9
20	0.01	opt. con. at 5μm	214.0	74.3	19.6
21	0.01	opt. con. at 100μm	214.2	72.6	19.5
22	0.01	opt. con. at $10, 30, 100\mu$m	213.8	73.9	19.6
23	0.0042	high emissivity, directional	211.9	90.0	19.0
24	0.0042	high emissivity, diffuse	212.2	98.9	20.4
25	0.0042	opt. con. at 5μm	214.0	71.1	15.9
26	0.0042	opt. con. at 100μm	214.2	67.2	15.6
27	0.0042	opt. con. at $10, 30, 100\mu$m	213.8	70.1	15.8

Table 3.4 Results from the Monte Carlo simulation including conduction ($N = 10$)

Equal values of H have been placed together for easier comparison. Lines 17 and 22 are simply reprints of lines 11 and 12 from table 3.2 and are included for completeness.

Clearly, as expected, all the final temperatures are higher with conduction included, even for the smallest values of H. The exception to this is, of course, the values of T_1 which are largely unaffected. Also, conduction seems to have almost totally obliterated the subtle effects of differences in directional behaviour and emissivity between lines 20-22. However, in lines 15-17 a small but significant difference can be detected, and a tiny difference is also visible in lines 25-27.

The most interesting effect to observe is that the effect of low emissivity seems to have been reversed for $H = 0.1\mathrm{WK}^{-1}$. Consider the first five cases (i.e. lines 13-17). Line 16 is derived from the optical constants of gold at 100μm and all the surfaces have $\epsilon_h = 0.00572$. In table 3.2 this gave rise to the lowest tube temperatures due to the fact of having the lowest emissivities of all the simulations. In table 3.4, however, it gives the highest tube temperatures.

The next lowest emissivities belong to line 17 consisting of surfaces at $\epsilon_h = 0.00766$, $\epsilon_h = 0.00741$ and $\epsilon_h = 0.00572$. This line also gives the next highest tube temperatures.

The lowest tube temperature is shown by line 13 which has the largest emissivity ($\epsilon_h = 0.03$). Clearly, the larger the emissivity, the more energy per time step the surface will be able to lose to empty space. However, the larger emissivity also implies a larger absorptivity and hence a greater amount of the radiation emitted by the other surfaces will be absorbed per time step. It seems from these results that, when $H > 0.01\text{WK}^{-1}$, the former effect is more important than the latter with the larger emissivity surfaces being more efficient at losing the conducted heat from the system before it reaches the telescope tube.

Notice, however, that line 14 also has an emissivity of $\epsilon_h = 0.03$ but shows a much higher tube temperature. Indeed, line 14 shows one of the highest tube temperatures of all, second only to line 16. Obviously, even though the conduction is destroying the subtle differences between the different directional behaviour of lines 15-17, it cannot remove the major differences between diffuse surfaces and directional ones.

The greater efficiency of higher emissivity surfaces at removing conducted heat to space before it can proceed through the system is still evident in line 14. Notice the fact that it has a higher T_2 than line 16 but that T_3 is still slightly less. Clearly the efficiency of removing the heat to space is being countered by the inefficiency of a diffuse surface to prevent heat being radiated to the inner sunshield.

In lines 18-22 with $H = 0.01\text{WK}^{-1}$, the efficiency of higher emissivity surfaces at ejecting unwanted heat to outer space before it has a chance to reach the telescope tube is no longer apparent. What *is* still apparent is the better performance of the directional surface compared with the diffuse surface (lines 18 and 19).

In lines 23-27 ($H = 0.0042\text{WK}^{-1}$) the lower emissivity surfaces still give rise to the lowest tube temperatures (as when there was no conduction). However, the high emissivity surfaces show a smaller rise in temperature from table 3.2 compared with the low emissivity surfaces. This again is due to the increased efficiency of the higher emissivity surfaces at removing conducted heat from the system. Thus, while it is still better to use low emissivity surfaces in passive cooling, the effects of conduction reduce the improvement slightly over high emissivity surfaces.

The very small differences between lines 25-27 imply that modelling of the directional properties measured at the correct wavelength is not very important, certainly for first-order approximations for this design of telescope. However, it should also be noted that the differences, while small, are significant (compare the differences in values of T_2) and the effect of the correct directionality is

likely to depend heavily on the design of the telescope.

3.10.2 Tilted sunshields

The results of simulations run with tilted sunshields are summarised in table 3.5. The angles β and γ refer to the angles in figure 3.13. In all cases, conduction was not modeled (i.e. $H = 0\text{WK}^{-1}$).

	β (degrees)	γ (degrees)	Radiative properties of gold	T_1, K	T_2, K	T_3, K
28	5	10	high emissivity, directional	212.6	80.4	13.4
29	5	10	high emissivity, diffuse	211.4	89.4	15.4
30	5	10	opt. con. at 5μm	212.9	59.6	6.1
31	5	10	opt. con. at 100μm	214.0	53.6	5.6
32	5	10	opt. con. at 10, 30, 100μm	213.6	58.1	5.9
33	10	20	high emissivity, directional	212.0	74.3	11.8
34	10	20	high emissivity, diffuse	212.1	83.4	13.8
35	10	20	opt. con. at 5μm	214.6	54.9	5.8
36	10	20	opt. con. at 100μm	213.4	49.9	5.5
37	10	20	opt. con. at 10, 30, 100μm	213.9	53.5	5.7

Table 3.5 Results from the Monte Carlo simulation including tilted sunshields (no conduction)

The advantages of opening out the sunshields to allow specularly reflected photons to escape are obvious. All simulations in lines 28-32 show a $\simeq 10 - 15\%$ drop in tube temperature over lines 1-5 in table 3.2.

A further drop in temperatures is evident when the shields are opened out even more in lines 33-37, as would be expected. The order of the five cases from hottest to coldest is the same as in table 3.2 but with all temperatures significantly lower.

Both the high emissivity cases (lines 28 & 29 and 33 & 34) show similar drops in temperature as the sunshields are opened out. It is interesting to note that lines 30 and 32 show a greater drop in temperature (0.7K and 0.6K respectively) than line 31 (only 0.2K). This could be as a result of the highly directional nature of line 31 (derived from optical constants at 100μm), with a peak emissivity at very high angles, not benefiting from the opening of the shields as much as the other cases.

Finally, simulations were run combining tilted sunshields with conduction. All simulations were performed with one of the two extreme cases, very high conductivity ($H = 0.1\text{WK}^{-1}$) or very low conductivity ($H = 0.0042\text{WK}^{-1}$). The results are summarised in table 3.6.

Once again (as in table 3.4) all temperatures are higher than with no conduction. Also, when $H = 0.1\text{WK}^{-1}$, the cases with the higher emissivities obtain a lower temperature than the low emissivity cases, including (this time) the diffuse case (lines 39 and 44).

	H WK^{-1}	β	γ	Radiative properties of gold	T_1, K	T_2, K	T_3, K
38	0.1	5	10	high emissivity, directional	212.5	88.8	34.0
39	0.1	5	10	high emissivity, diffuse	211.5	94.9	34.9
40	0.1	5	10	opt. con. at 5μm	212.8	93.4	35.2
41	0.1	5	10	opt. con. at 100μm	214.0	97.7	35.9
42	0.1	5	10	opt. con. at 10, 30, 100μm	213.9	94.9	35.5
43	0.1	10	20	high emissivity, directional	211.9	85.2	33.4
44	0.1	10	20	high emissivity, diffuse	212.3	90.7	34.2
45	0.1	10	20	opt. con. at 5μm	214.6	92.7	35.1
46	0.1	10	20	opt. con. at 100μm	213.3	97.4	35.9
47	0.1	10	20	opt. con. at 10, 30, 100μm	213.5	94.4	35.5
48	0.0042	5	10	high emissivity, directional	212.6	80.8	17.5
49	0.0042	5	10	high emissivity, diffuse	211.9	89.7	18.9
50	0.0042	5	10	opt. con. at 5μm	212.9	64.2	15.3
51	0.0042	5	10	opt. con. at 100μm	212.8	62.0	15.2
52	0.0042	5	10	opt. con. at 10, 30, 100μm	213.9	63.6	15.3
53	0.0042	10	20	high emissivity, directional	212.0	74.9	16.7
54	0.0042	10	20	high emissivity, diffuse	212.3	83.7	17.9
55	0.0042	10	20	opt. con. at 5μm	214.6	60.8	15.1
56	0.0042	10	20	opt. con. at 100μm	214.1	60.0	15.0
57	0.0042	10	20	opt. con. at 10, 30, 100μm	213.6	60.6	15.1

Table 3.6 Results from the Monte Carlo simulation including tilted sunshields and conduction

It seems opening the sunshields has improved the cooling efficiency of the high emissivity cases considerably more than the low emissivity ones. When conduction is high, the low emissivity cases (lines 40-42 and 45-47) show a very small difference in tube temperature from table 3.4. The lowest emissivity case (lines 41 and 46, $\epsilon_h = 0.00572$) shows a drop in temperature of only 0.1K when the sunshields are opened out. The next lowest emissivity, and most realistic, case (lines 42 and 47, $\epsilon_h = 0.00766, 0.00741$ and 0.00572) shows only a 0.2K drop. In both these cases the temperature drop is not magnified when the shields are opened out further.

The low conductivity cases show a much larger drop in temperature. The lowest emissivity case (lines 51 and 56) shows a 0.4K drop compared with table 3.4, whilst the next lowest, and most realistic case (lines 52 and 57), shows a drop of 0.5K. Both show a further drop of 0.2K when the shields are opened out further.

These temperature drops are insignificant compared to the dramatic effect on the high emissivity surfaces ($\epsilon_h = 0.03$). For the high conductivity cases both show a drop in tube temperature of $\simeq$ 1.0K when $\beta = 5°, \gamma = 10°$ (lines 38 and 39) and a drop of $\simeq$ 1.6K when $\beta = 10°, \gamma = 20°$ (lines 43 and 44). When conductivity is low, both high emissivity cases show a 1.5K temperature drop when $\beta = 5°, \gamma = 10°$ (lines 48 and 49) and a drop of $\simeq$ 2.4K when $\beta = 10°, \gamma = 20°$ (lines 53 and 54).

The dramatic increase in cooling efficiency has enabled the diffuse case to perform better than

the low emissivity directional cases when conductivity is high, although it still does not perform as well as the high emissivity directional case. When conductivity is sufficiently low, however, the diffuse case still performs worst, being over a degree hotter than the high emissivity directional case, and $\simeq$ 3K hotter than the low emissivity directional cases.

Low emissivity now plays a less dramatic rôle in reducing the tube temperature, but it still produces a significant effect reducing the tube temperature by $\simeq$ 2K (a 12% effect at 17K).

Chapter 4

Experimental Measurements of Emissive Properties

4.1 Methods of measurement

It was clear that to add weight to my modelling predictions, realistic values for the directional emissions should be used. Unfortunately, as already stated, there exists such a dearth of information on the properties of gold at anything other than normal incidence, that I embarked on a program of measurements myself.

As with the simulation model, the first decision to make was how to go about it. There exists a variety of ways of making such measurements. These will be presented here along with a discussion of the advantages and difficulties involved with each method.

4.1.1 Direct emissivity measurement

The most direct method for measuring emissivity is to directly measure the infra-red emissions from a sample surface. This has been done by Clarke et al. [45] and, notably, in previous work at this establishment by Jones and Pantinakis [46].

Although this method is commendable in that it directly measures the emissivity, it is notoriously difficult to obtain reliable results. The biggest problem is emissions from the surrounding equipment and environment.

Whilst the latter can be discriminated against by 'chopping' the radiation emitted from the sample, giving it a distinctive frequency, and using a phase sensitive detector to eliminate non-chopped radiation (see section 4.3), emissions from the equipment itself are much more difficult to overcome.

In both the references given, the effects of emissions from the equipment are reduced by cooling the surrounding equipment to liquid Nitrogen temperatures. The surroundings are also made black to reduce any stray reflections in the system.

The other obvious way of reducing the effect of the equipment is to raise the temperature of the sample, thereby raising the emissions so that they effectively 'drown-out' any environmental sources. This was done by Derek Price [47] and Brannon & Goldstein [48].

Clearly this method is best suited to measuring reasonably high emissivity materials at room temperature or above. However, given that the materials of most interest in passive cooling are, by nature, low emissivity, and we wish to know these properties at cryogenic temperatures, this method is not really applicable since the emissive powers at low temperatures are so very small.

4.1.2 Absorptivity measurement

Another way of measuring the emissivity is to measure the absorptivity, since by Kirchhoff's law (equation 2.13) these two properties are the same. If infra-red radiation is incident on a sample, that sample will absorb some of that radiation and hence heat up slightly. Thus, this method relies on an accurate procedure for detecting this heating.

Fulk and Reynolds [49] measured the heating indirectly by measuring the boil-off rate of liquid Nitrogen. Basically their equipment (see figure 4.1) consisted of a dewar containing liquid Nitrogen and coated on the outside with the sample of interest. Around this dewar was an outer can kept at a constant temperature by a water bath. This outer can then emitted infra-red radiation onto the sample surface, the sample surface absorbed some of this radiation, heated up and boiled off some of the liquid nitrogen in the dewar. The rate of production of gaseous Nitrogen was then measured.

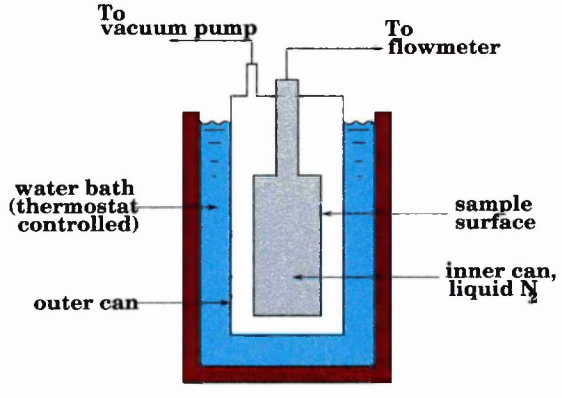

Figure 4.1 Equipment used by Fulk and Reynolds.

Clearly there are many problems involved with this method. Firstly, the sample of interest has to be specially prepared on the outside surface of a dewar. Secondly, the accuracy to which the absorptivity of the sample is known is limited by the accuracy to which the emissivity of the outer can is known. Also, the properties are being measured at liquid Nitrogen temperatures (since the sample is in good thermal contact with the inside of the dewar) and at a whole spectrum of wavelengths. Finally, there is no way to make directional measurements.

Although this method is doubtless good for low temperature measurements of hemispherical-total emissivity, it is not suitable for the type of measurements I wished to make.

Another, more versatile, method is proposed by E.V. Potapov [50]. Here, the sample (labelled 'S' in figure 4.2) is fixed in a copper holder at an angle to the incoming radiation. Presumably, with a careful design of holder, this angle could be changed as desired. Next to the sample is a helical cavity (labelled 'H_1') effectively acting as a blackbody. Above this arrangement are two more such blackbodies ('H_2' and 'H_3'), not in thermal contact with the structure holding the sample.

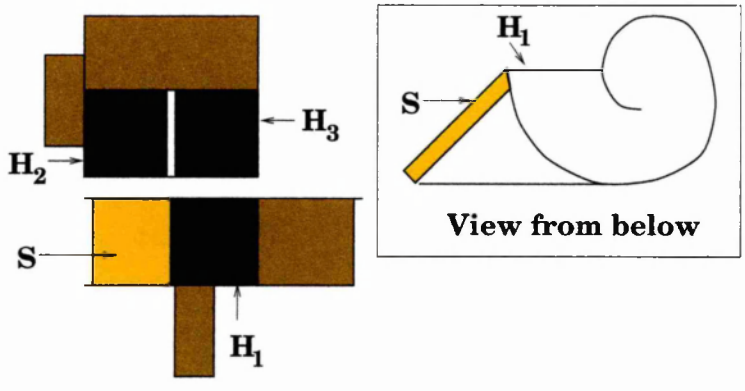

Figure 4.2 Equipment used by Potapov.

The idea behind this equipment is to shine a source of radiation simultaneously on the sample and the blackbody immediately above it. This radiation then heats both structures. Two thermometers measure the change in temperature of each structure. Given the blackbody has an absorptivity of 1, the ratio of the two changes in temperature can be used to give the absorptivity of the sample.

However, a correcting factor must be applied to allow for the difference in heat capacities of the two structures. This is found by shining the radiation on the two adjacent blackbodies.

Potapov notes that 'the sensitivity of the circuit was 10^{-8}W'. However, he also notes that 'the low sensitivity of the system made it possible to carry out measurements only on metals which had a sufficiently high absorption coefficient'.

Clearly, the major problem in 1965 was getting a source of infra-red radiation powerful enough to produce measurable heating when the absorptivity was low. Although these days there exist I-R lasers capable of emitting several watts of power, these would have to be passed through some system of beam-widening since a large source is needed, capable of illuminating two parts of the equipment at once, and lasers produce narrow beams.

However, powerful I-R sources bring other problems. If the sample has a particularly low absorptivity (as in candidate passive-cooling materials) then an intense source would be needed to produce a significant amount of heating. This intense source would no doubt heat up the blackbody appreciably, such that it may start radiating onto the sample holder structure causing additional heating.

I feel sure that it would be possible to account for this effect, but this method seems overly complicated for rapidly building up a picture of the sample's directional behaviour. For a longer-term project, however, the accuracy of this method may well be worth the time and money involved.

A similar method is proposed by Biondi [51]. The slight difference here is that the radiation is reflected from the sample surface onto a black surface. However, since this black surface is not a cavity, it may well not be perfectly black. Thus, as with Fulk and Reynolds, the accuracy of the results rely on the accuracy to which the absorptivity of the black surface is known.

Biondi claims that his procedure can produce 'data reproducible to within two percent'. However, when considering very low emissivity surfaces, especially at cryogenic temperatures, two percent can be considerably larger than the absorptivity being measured and would therefore produce no useful results.

4.1.3 Reflectivity measurement

A much more common way of finding a surface's emissivity is to measure the reflectivity and calculate it from that ($\epsilon' = 1 - \rho'$) as mentioned in chapter 2. Also it is worth noting that although it is possible to calculate the directional-hemispherical reflectivity (ρ') from measurements of emissivity, it is not possible to calculate the bi-directional reflectivity (ρ''). However, it is possible to calculate the directional-hemispherical reflectivity *and* the emissivity from measurements of the bi-directional reflectivity.

Much work has been done in this area in the past. However, in the infra red there has always been the problem of getting a strong enough source of radiation. At least, this was a problem until recently with the advent of infra red lasers.

Consider, for example, the apparatus of Smith [52], or Makino et al [53]. In both cases, the

apparatus appears quite daunting at first. However, on closer inspection it is clear that most of the apparatus is concerned with producing a strong, parallel beam of infra red radiation. The lack of infra red lasers is apparent in the choice of radiation source; a blackbody in the case of Smith and a SiC light source in the case of Makino et al.

Lasers are used by Drolen [54], but here the complications arise in a system for selecting one of many lasers and focusing it on the sample.

If we replace these complicated optics with a single laser source, then we are left with the much simpler arrangement of a laser, a sample, and a detector, as in previous work done in this department [55]. Indeed, it was on this equipment that my apparatus was based. The price of this increased simplicity is not being able to easily vary the wavelength of the incident radiation, but it is a relatively small price to pay.

Another common way of measuring surface properties using reflection techniques is ellipsometry [56, 57, 58]. In this method, a source of radiation is polarised at 45° to the plane of incidence and then reflected, at a high angle of incidence, off the sample. The reflected light is found to be elliptically polarised due to the difference in reflectivities for the two orthogonal polarisations (particularly at grazing incidence). This ellipticity is measured, as is the phase difference between the two polarisations.

This method is often used for measuring the optical constants of materials, but unfortunately cannot be used to directly measure the absolute reflectivity. Additionally, it is rather complicated and requires a lot of expensive specialist equipment. For these reasons I decided against this method.

A variation on the simple single-reflection apparatus is to use multiple reflection techniques. Essentially this involves reflecting the source of radiation off the sample many times. Clearly, each time the light is reflected, the reflected intensity will be ρ times the initial intensity. Thus, for n reflections, the experimenter is actually measuring ρ^n. This allows for much greater accuracy.

Bennett and Koehler [59] describe an apparatus which gives two reflections from the sample being investigated. Although the number of elements in the apparatus seems a little excessive, some of this may be due to constraints of space or some other complication. The basic method is sound and such measurements of ρ^2 give reflectivity measurements of high reflectivity samples with a reported accuracy of ± 0.001.

Toscano and Cravalho [31] describe an apparatus which gives 8 reflections, although this is done by means of having four separate surfaces. This could place constraints on the samples being used since it would be necessary to have four identical samples. It is possible that four matched samples could be calibrated, and the one sample replaced with some other sample of interest, but then there

would only be two reflections on the sample of interest.

The clear disadvantage with both sets of multiple reflection apparatus described above is the inability to investigate the behaviour of the optical properties in more than one direction. However, I decided to also use a multiple reflection apparatus in order to get high accuracy measurements of reflectivity, even if only at one angle.

4.2 Bi-directional reflectometer

As mentioned above, the measurement of bi-directional reflectivity was a continuation of previous work done in this department. However, whereas the previous work had been concerned with materials used as absorbers of solar energy, my own work was concerned with high-reflectivity metals. In this study, I was particularly interested in the bi-directional reflectivity at grazing incidence, since this is where the behaviour of metals differs from the diffuse model most dramatically.

The previous equipment was not well suited to this task, since the maximum sample diameter that could be accommodated was 30mm [60]. In order to accommodate wider samples, my supervisor, Barrie Jones, redesigned the sample holder. The new design is shown in figure 4.3.

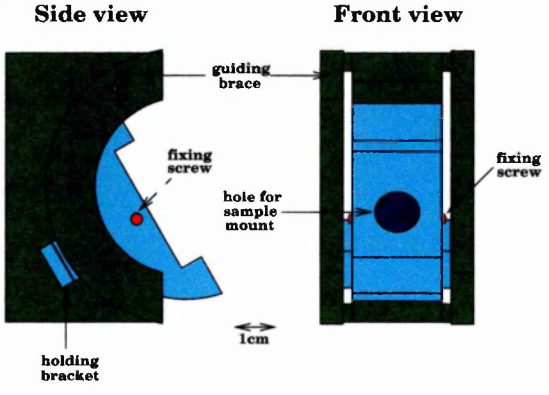

Figure 4.3 A diagram of the mk1 sample holder.

The 'mk1 sample holder' essentially consists of two parts; the sample holder itself (coloured in blue), and the base unit in which it sits (coloured in green). The sample holder is an almost semi-circular device which sits snugly in a matching recess in the base unit. It has a rough scale etched onto the side to allow a measurement of the angle at which the sample was tilted with respect to the vertical. It is held in place by two 'holding brackets' (one on each side) which allow it to slide freely in a circular motion caused by the restriction of the 'guiding braces' (again, one on each side).

The centres of the circles describing the back of the sample holder, the matching recess in the base unit, and both curved surfaces of the guiding braces lie on the same point some 5mm in front of the sample holder. This point is clearly on the axis of rotation of the sample holder. Thus, if a sample is placed in the holder such that the sample surface is 5mm in front of the sample holder, the sample surface will lie on its own axis of rotation and the laser spot will always be incident on the same point on the surface (provided the laser is carefully aligned).

The samples were mounted on specially constructed sample mounts which simply consisted of a flat plate for affixing the sample to, and a round protrusion on the back which fitted into the hole on the sample holder. Two fixing screws (shown in red) held the sample mount firmly in place.

Other screws on the holding brackets (not shown) were used to prevent the sample holder from slipping once the desired position had been attained.

This whole sample holder was then placed on top of two rotating stages. The lower rotating stage also supported the primary detector, which was either a photodiode or a bolometer depending on the wavelength being measured. Figure 4.4 shows this arrangement, but with the mk2 sample holder (described later) in place. The mk1 sample holder arrangement differed only in the mounting bracket used to fix the sample holder to the top rotating stage.

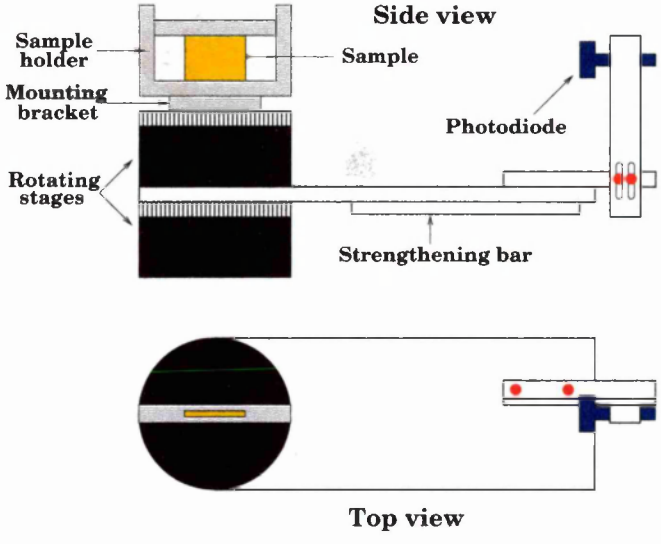

Figure 4.4 A diagram of the sample holder/primary detector setup.

The sample holder was carefully mounted on the rotating stages in such a way that the axis of rotation of the sample holder crossed the axis of rotation of the rotating stages at a point as close as possible to the centre of the sample surface. This was to ensure that, no matter how much the

sample was rotated in any plane, the laser spot would always be incident on the centre of the sample surface.

This combination of equipment was mounted on an optical bench in the path of a fixed laser (shown schematically in figure 4.5 [61]). Also shown in figure 4.5, on the top view, are the chopper blades and secondary detector, which will be discussed below. With this arrangement, the lower rotating stage could be adjusted to give a desired angle between the fixed laser and the primary detector. The upper rotating stage was then adjusted until the desired incident direction on the sample was achieved. This of course also defined the direction of reflection onto the detector.

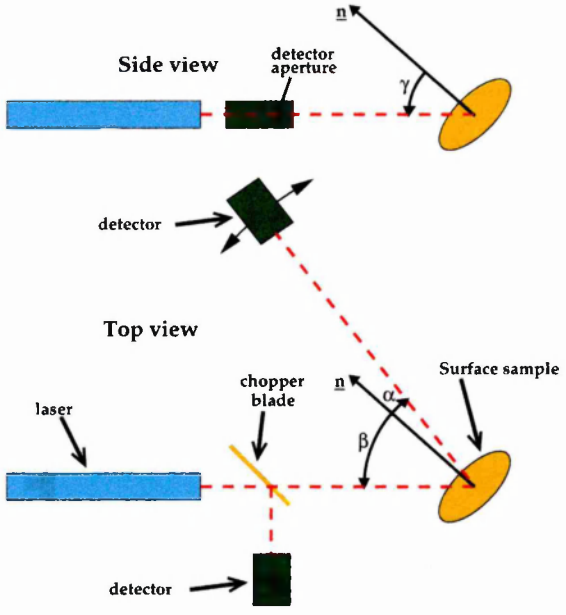

Figure 4.5 A diagram of the apparatus used in my experimentation.

Of course, the laser needed to be aligned carefully since it was not a permanent fixture. This was achieved by mounting a fluorescent wand, with a small cross drawn on it, in the path of the beam. For the infra-red lasers this wand was necessary to find the beam. For the visible laser, it was simply a tool for aligning the laser.

This wand was mounted in a holder which in turn was mounted on a standard optical bench fitting. This allowed the wand to be moved along the optical bench without changing its lateral or vertical position.

The laser was mounted on a vertically adjustable stage, which in turn was mounted on a horizontally adjustable stage. This gave complete mobility when adjusting the laser.

The alignment was performed by placing the wand as close as possible to the laser and adjusting

the movable stages at the front of the laser until the laser spot was centred on the cross. Then the wand was moved as far away as possible from the laser and the adjustable stages at the back of the laser were now adjusted to again line up the spot on the cross.

Of course, this second adjustment almost invariably necessitated the adjustable stages at the front of the laser to be realigned, and vice versa. This process was repeated many times, each time needing smaller and smaller adjustments as the laser neared alignment. With practice this alignment took less than five minutes until the required adjustments became too small to be detectable with the naked eye.

The apparatus, particularly the sample holder, was designed to allow complete manoeuvrability of the sample with respect to the incident radiation and the primary detector. I even deduced how to relate the readings of the two rotating stages and the scale on the sample holder to the radiometric angles of incidence (θ_i, ϕ_i) and reflection (θ_r, ϕ_r).

However, after some use of the equipment I soon realised (as mentioned in section 2.7) that it was only possible to measure a signal in the specular direction. This is primarily due to the samples being of very high reflectivity and quality and the long wavelengths involved in my work.

In the course of an experiment, therefore, the bottom rotating stage (and therefore the primary detector) was moved through a set number of angles whilst at each adjustment the top rotating stage (and hence the sample) was turned back exactly half the angle of the bottom rotating stage to ensure the specularly reflected laser beam was still incident on the detector*.

Typically the bottom rotating stage was moved around in steps of 10°, thus producing a change in the angle of incidence and reflection of 5°. This was done at every angle from the smallest possible (usually $5-10°$ before the primary detector got in the way of the laser beam) to the largest possible (usually $\simeq 80°$ before the laser spot became too wide for the sample).

A major problem with the mk1 sample holder was the fact that the samples had a tendency to tilt in the vertical plane, causing the laser spot to drift out of the primary detector's field of view. This was due to the hole for the sample mounts being very slightly too large.

To alleviate this problem, the mk2 sample holder was designed (primarily by Barrie, but with some of my own modifications) as shown in figure 4.6.

This sample holder eliminated the problem of the vertical tilt in samples at the expense of being able to adjust the sample's vertical inclination if required. In other words, the angle γ in figure 4.5 was now always zero. As already explained, only the specular direction was producing any results

*In fact the sample was turned back until the laser spot was once again central on the detector. The top rotating stage reading was then taken and, unsurprisingly, showed it had been moved through half the angle the bottom rotating stage had been moved through.

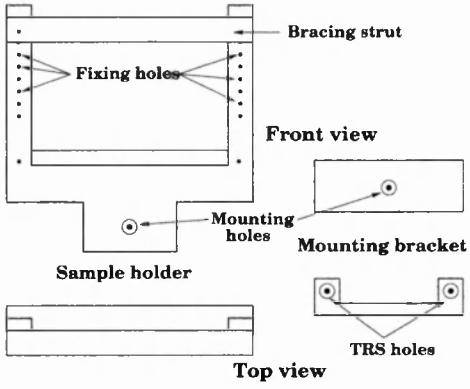

Figure 4.6 A diagram of the mk2 sample holder.

and this was always in the horizontal plane, so the inability to adjust the vertical inclination was not a problem.

The mk2 sample holder was carefully designed such that the surface of the sample being studied was level with the support struts at either side. Barrie's original design had the support struts slightly forward of the sample's surface with the result that the struts obscured the beam at high angles of incidence. Parts of the struts were cut away to try and avoid this problem, but this measure was not sufficient. Therefore I redesigned the sample holder (with a few amendments from Barrie to save on workshop time) to remove this problem. The sample holder itself then had to be mounted slightly further back on the rotating stage so that the axis of rotation still lay on the sample surface (as before with the mk1 sample holder). This was achieved by simply inserting a metal washer between the base of the sample holder and the mounting bracket.

The sample holder was fixed to the mounting bracket by means of a bolt passing through the 'mounting holes' (see figure 4.6). The mounting bracket was in turn fixed to the top rotating stage by means of screws passing through the holes labelled 'TRS holes'. Two metal bars (drawn in red) pressed against the sample from behind and kept it fixed flush with the front of the two vertical struts. The bracing strut (drawn in green), against which the top of the sample was pressed, was movable to accommodate any size of sample. It could be screwed into any one of the many 'fixing holes' depending on the height of the sample.

As well as the laser, the primary detector and the sample holder, the bi-directional reflectometer had two other components. The first of these was a set of gold plated chopper blades mounted between the laser and the sample (as shown in figure 4.5). This provided two useful functions. Firstly it chopped the radiation, allowing better discrimination against background noise (see below).

Secondly, it reflected the beam (for the half of the time that the blade was obstructing the beam) into the secondary detector. This detector was used to monitor and compensate for any drift in the laser power.

Measuring the absolute reflectivity with this equipment was very simple. The sample was rotated through a variety of angles (as explained above) and a reading taken at each position. After the reading at the highest incident angle, the sample holder was removed, and a direct reading of the laser power was taken by the primary detector. Usually I continued the experiment as described in section 4.5.

For every reading of the laser power reflected off the sample, a reading from the secondary detector was also taken. Dividing one reading by the other allows us to obtain the desired result.

To demonstrate, let us denote the emitted laser intensity I_0. The optical components between the laser and the secondary detector will attenuate this intensity by some fraction which we call H. The optical components between the laser and the primary detector (not including the sample) will be different if only in as much as the chopper blade is not included, so we shall denote the attenuation of the beam between the laser and the primary detector as G. Finally, when reflected off the sample, the intensity will be reduced by a factor $\rho''(\theta)$.

So, for an angle of interest, we shall denote the readings of the primary and secondary detectors respectively as $M_1(\theta)$ and $M_2(\theta)$. It is clear that:

$$M_1(\theta) = I_0(t_1)G\rho''(\theta) \tag{4.1}$$

$$M_2(\theta) = I_0(t_1)H \tag{4.2}$$

It is clear that M_2 does not in fact vary with θ. However, it *does* vary with time as I_0 varies due to laser drift, and since the measurements at different angles are taken at different times, $M_2(\theta)$ denotes the secondary detector reading taken at the time that the angle of incidence was θ. In this case, the time is denoted as t_1.

To find the absolute reflectivity, we also need the direct measurement of the laser power by the primary detector. We shall denote this $M_{1,direct}$ and the corresponding secondary detector reading $M_{2,direct}$. It is clear that:

$$M_{1,direct} = I_0(t_2)G \tag{4.3}$$

$$M_{2,direct} = I_0(t_2)H \tag{4.4}$$

Clearly, since these readings were taken at a different time from those mentioned above, I_0 may well be different. We can eliminate that by dividing equation 4.1 by equation 4.2 to give:

$$\frac{M_1(\theta)}{M_2(\theta)} = \frac{G\rho''(\theta)}{H} \tag{4.5}$$

To find the absolute reflectivity, we must now divide equation 4.3 by equation 4.4 and then divide equation 4.5 by the result, thus:

$$\frac{M_{1,direct}}{M_{2,direct}} = \frac{G}{H} \tag{4.6}$$

$$\Rightarrow \frac{\frac{M_1(\theta)}{M_2(\theta)}}{\frac{M_{1,direct}}{M_{2,direct}}} = \rho''(\theta) \tag{4.7}$$

4.3 Phase sensitive detection

Phase sensitive detection is a very powerful method for extracting a signal from a noisy environment. The technique relies on 'chopping' the signal to enable better discrimination against noise.

As an example I shall describe the method used in my experiments (detailed above). In this case, the source of the signal to be measured was the laser. Attempting to measure the power of the laser beam was hampered by other sources of light in the laboratory. To eliminate such interference I introduced the chopper blades into the equipment (as shown in figure 4.5).

These chopper blades were formed by a gold-plated metal disk with two 90° holes cut into it, as shown in figure 4.7. This disk was then rotated at high speeds (typically between 50 and 100Hz) whilst the laser was directed at some point mid-way between the centre and the circumference.

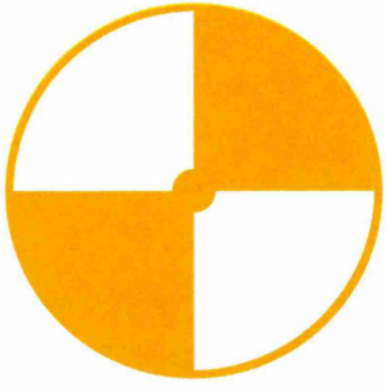

Figure 4.7 A typical chopper blade.

It is clear that this set-up would allow the laser beam to pass during 50% of the rotation of the blades (i.e. when the laser passed through the holes). Also, the resultant beam (essentially a dc signal) would be modulated by a square wave with a frequency double that of the metal disk as the beam is effectively turned off and on by the rotation of the disk.

Figure 4.8 shows such a square wave with random noise added onto the signal. The idea behind phase sensitive detection is that only the signal is chopped, whilst the noise is present throughout the period of the chopper blades. To achieve this, the chopper blades must be placed as close as possible to (in this case) the laser to avoid chopping any environmental sources.

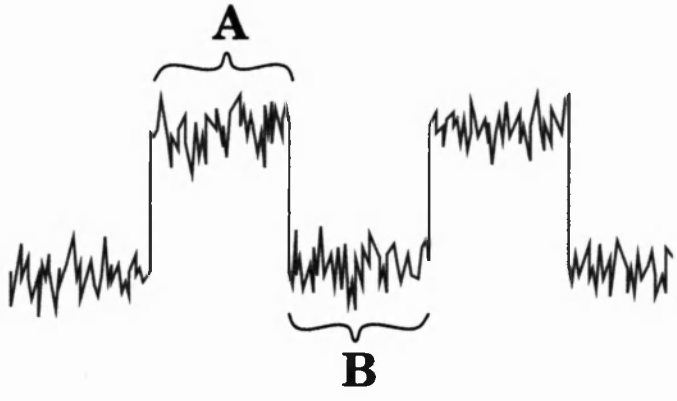

Figure 4.8 An example of a chopped signal.

The section of the signal marked 'A' in figure 4.8 consists of the signal we're interested in plus the environmental noise. The section marked 'B' consists only of noise. Thus, to extract the signal one needs to subtract the detector reading in section 'B' from the detector reading in section 'A'. This is done by means of a phase sensitive detector (PSD).

A PSD is a device designed to specifically perform such a task. To do this, it must be fed a reference signal of the same frequency as the modulation of the laser beam (i.e. double the rotation frequency of the chopper blades).

This reference signal must also be in phase with the laser beam. Clearly, if we move sections 'A' and 'B' in figure 4.8 one-quarter period to one side, they will each contain a quarter-wavelength of noise and a quarter-wavelength of signal+noise, as shown in figure 4.9. If we now subtract section 'A' from section 'B' they will cancel each other out and we will have a reading of zero.

In my apparatus, the PSD was fed a reference signal from the device driving the chopper blades. This was taken from a light sensitive detector mounted close to the circumference of the blades. An LED shone into the detector and was blocked as the blades passed between the two, thus producing

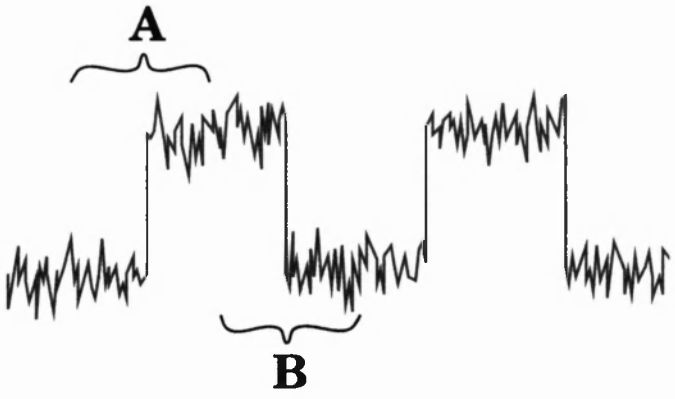

Figure 4.9 An out-of-phase chopped signal.

a square wave of the correct frequency.

This reference signal was not in phase with the signal from the laser beam, however, due to various phase differences between the two electronic lines. The 'phase' control of the PSD was then adjusted until the PSD was in phase with the laser signal. One way to tell if the PSD is correctly in phase is to adjust the phase control until the PSD output is a maximum. However, it is often easier to adjust until the PSD output is a minimum (i.e. zero) and then add 90° to the phase adjustment.

So far I have been considering one chop of the signal modulation at a time. However, if the noise is truly random, it is highly unlikely it will perfectly average to zero over the space of one rotation of the blades. For this to occur, we must average the signal over many rotations of the blades. Typically, in my experiments, I averaged over 1 or 3 seconds, being roughly 35 or 105 rotations of the blades and, therefore, 70 or 210 periods of the modulation of the signal.

Of course, the noise would average after only one period of the chopping frequency if the noise was in the form of a DC signal (e.g. ambient light in the laboratory). The important point to remember about phase sensitive detection is that *only* the chopped signal is measured. Any other signal that is present throughout the chopping period is discriminated against.

A problem occurs when the environmental light sources are also modulated somehow. This was the case in my laboratory where the main source of environmental light were fluorescent tubes. In early experiments, I found that the light produced by these fluorescent tubes was modulated at a frequency of 100Hz. Thus, for the PSD to work effectively, I had to make sure that the frequency of modulation of the signal was in no way a simple multiple of 100Hz. For this reason, I chose 70Hz as the frequency with which to modulate the signal.

4.4 Lasers and detectors

In order to measure the optical properties of the sample at a range of wavelengths, four lasers were used. Two were already owned by the Open University and were a 3mW 633nm Helium-Neon laser and a 1mW 1152nm Helium-Neon laser. Both were manufactured by Scientifica-Cook (London).

Although fairly low-powered, these lasers were adequate for the experiments performed, particularly since the detectors used for these lasers were sensitive photodiodes. Indeed, the laser power had to be attenuated to avoid overpowering the photodiodes.

The 1152nm laser was extremely sensitive to environmental temperature changes. The slightest variation in temperature caused the laser power to fluctuate wildly. This was partially countered by the secondary detector monitoring the laser power, and also by long integration times on the PSD. A water cooled jacket was constructed in an attempt to try to stabilise the laser temperature, but was not very effective due to the difficulty of sufficiently insulating the entire laser from the laboratory environment.

Two more lasers were bought specifically for these experiments. They were a 10.6μm CO_2 laser (model LM4) and a 5.4μm CO laser (model CO-10 WOVO). Both lasers were purchased from Edinburgh Instruments* although the 5.4μm laser was built by Laser Photonics†.

The 10.6μm laser was 6W continuous wave power with excellent stability (the extra power was needed for these longer wavelengths since the detectors for these two lasers were nothing like as sensitive as the photodiodes used previously). Unfortunately, the 5.4μm laser was not nearly as good.

The 5.4μm laser took approximately 18 months to be delivered, greatly hampering the experimental schedule. In that time, two lasers had been built by Laser Photonics since the first model had not performed to specifications. After failing to produce a laser with sufficient output power, a sub-standard laser was shipped to the UK. This was damaged in transit and so a further delay was necessary whilst it was returned to the manufacturers and repaired.

On arrival, the laser was very difficult to use. Much time needed to be spent each day finding the optimum temperature to run the cooling bath in order to get the maximum power out of the laser. The maximum power achievable was of the order of 800mW, nowhere near the 4W originally quoted for this laser. This caused major problems in subsequent experiments, particularly in the multiple reflection cell (see below).

*Heriot-Watt Research Park, Riccarton, Currie, Edinburgh

†12351 Research Parkway, Orlando, Florida 32826, USA

As mentioned above, the 633nm and the 1152nm laser powers were measured by a pair of photodiodes attached to two PSD's. The integration time and phase controls on both PSD's were set to the same values. Neutral density filters were used to attenuate the laser beam to prevent overloading of the photodiodes or, more accurately, the PSD's.

For the 5.4μm and 10.6μm lasers, bolometers were used instead. These were initially attached to a Coherent* Fieldmaster which simply gave a moment-by-moment reading of the bolometer's output. Later, a Coherent Labmaster was purchased. This was a two channel device which had a number of useful features. Primary among these was the ability to integrate the signal from one or both channels over a period of time.

Although the bolometers were not connected to a phase sensitive detector, the chopper blades were still used at these wavelengths to act as a beam splitter reflecting half the beam into the secondary detector to monitor laser drift. Since the response time of the bolometers was much less than the period of rotation of the blades, this did not affect the bolometer output (apart from attenuating it, of course). For these lasers, a PSD was not necessary since the laser power was so much greater than any environmental sources.

All the lasers were plane polarised, and experiments were performed at both polarisations. In the case of the two He-Ne lasers, the polarisations was rotated through 90° by means of a $\frac{\lambda}{2}$ plate placed in the path of the beam. The 5.4μm and 10.6μm lasers were simply turned on their sides to rotate the plane of polarisation. This necessitated re-alignment of the laser, but saved the large sums of money needed to buy $\frac{\lambda}{2}$ plates at these wavelengths.

4.5 Experimental method

The course of a typical experiment proceeded like this. First the laser was switched on and allowed to settle down. All the lasers mentioned above exhibited a cyclic variation of power when first switched on. This variation lasted for a certain length of time dependent on the laser. The 5.4μm laser had its own problems described above. Usually the laser would be switched on using a timer switch at 5am or so, so that it had stabilised by the start of the day.

If the PSD's were being used, they needed to settle down as well. Usually, once the PSD's were on, they weren't switched off until the laser was changed. Still, one PSD showed a very slow variation in its zero offset over the course of the day. This entailed the zero offset being set at the beginning of an experiment and checked at the end. Usually there was no detectable variation over

*Coherent Components Group, 2301 Lindbergh Street, Auburn, CA 95603, USA

the course of an experiment.

The sample was mounted in the sample holder. It was then moved through a variety of angles of incidence as described above. When the maximum angle of incidence was reached, the sample was removed and a direct measurement of the laser power was made to allow the measurement of absolute reflectivities.

After the direct measurement of laser power had been made, the sample was replaced and again moved through a variety of angles of incidence, this time from the largest to the smallest angle. When the smallest angle of incidence had again been reached, the sample was once more removed and another direct measurement of laser power was made.

A typical experiment of this sort took approximately one hour. If the laser was infra-red, it took slightly longer due to the increased difficulty of lining up the laser spot with the centre of the detector. This was made much easier for the 10.6μm and 5.4μm lasers when the Coherent Labmaster was purchased. One of the features of the Labmaster was a display which showed, to the nearest fraction of a millimetre, where the laser spot was on the detector head.

Moving the sample and primary detector around caused the laser spot to move out of the detector's field of view. When using the PSD's, this caused the PSD output to drop to zero. Once the laser spot was positioned back on the detector, the PSD output rose, but slowly due to the integration time of at least 1 second. Thus, when the sample and primary detector had been moved, they were then left for 60 seconds, to ensure the PSD output had settled, before a reading was taken. Previous experiments had shown that the reading failed to change significantly for any time after 60 seconds.

When using the bolometers in conjunction with the Labmaster, the signals of both detectors were integrated over a period of 40 seconds during which 400 readings were taken. The Labmaster then displayed an average reading and a standard deviation for that period. Experiments showed that the standard deviation did not reduce greatly for longer periods of integration.

Originally I entered the readings into my lab book and later worked out the reflectivities by hand. After a while I wrote a computer program which took the raw data, divided one detector reading by the other, worked out the direct laser power, and divided all the readings by this power reading (as described above) automatically. This greatly reduced the amount of time necessary to produce finished results from an experiment. During the experiment, I copied the readings into the computer as well as keeping a copy in my lab book for back-up purposes.

Each experiment provided two readings for the reflectivity of the sample at each angle. To obtain a better idea of the variability of the readings, two experiments were performed on each sample,

giving a total of four readings at each angle. The two experiments were generally done on different days. The four readings were averaged to give the mean and the 95% confidence intervals.

4.6 Multiple reflection cell

In an attempt to get more accurate readings, at the expense of angular movement, the Multiple Reflection Cell was constructed [61]. Figure 4.10 shows the basic design (designed by Barrie).

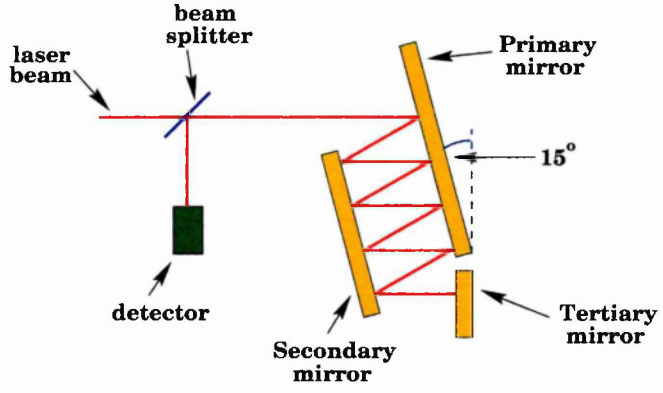

Figure 4.10 A schematic diagram of the multiple reflection cell

The idea behind this equipment was to increase the sensitivity of the detectors by bouncing the laser beam off the sample several times. As shown in figure 4.10 the incoming laser beam is reflected off the primary mirror, onto the secondary mirror, and back several times. On the ninth reflection the beam misses the primary mirror and is instead reflected onto the tertiary mirror. This then reflects the beam back along its path, bouncing between the primary and secondary mirrors, until it emerges from the multiple reflection cell. A beam splitter is used to reflect the beam into the detector. The grand total of reflections experienced by the beam from the gold mirrors is 17.

The beam reflects off the primary and secondary mirrors at an angle of 15° to the normal. Given that the surface properties of gold vary little up to 40° from the normal (see figure 2.5) this should give a reading of the near-normal reflectivity. The tertiary mirror reflects the beam back along the normal to the surface.

The multiple reflection cell was designed so that the separation between the primary and secondary mirrors was adjustable. I quickly found that by adjusting this separation, I could vary the number of reflections the beam experienced from 13 to 21 (as demonstrated in figure 4.11).

The three mirrors were carefully prepared such that they were as near as possible identical

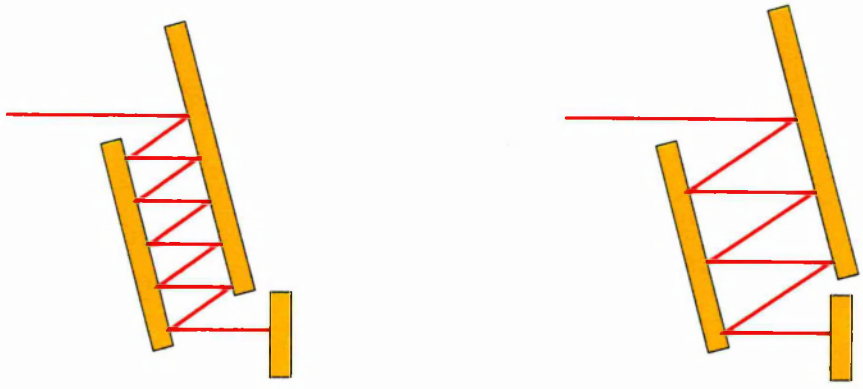

Figure 4.11 How to vary the number of reflections per surface by varying the separation between the mirrors in the multiple reflection cell

surfaces (see section 4.8.1). Thus, assuming they each had the same reflectivity, we have a method of measuring their absolute reflectivity. All we need to do is to take three measurements at each of 13, 17 and 21 reflections. Let us denote these measurements M_{13}, M_{17} and M_{21}. The only thing changing between these measurements is the alignment of the multiple reflection cell. Thus, if we divide one reading by the other, we can eliminate any effects of the apparatus.

For example, let us denote the emitted intensity of the laser as I_0. The optical components of the apparatus will, of course, reduce this intensity by some factor, G say. The only other attenuation of the beam will be caused by the reflectivity of the surfaces. Assuming they all have the same value, ρ, the beam intensity will be attenuated by a factor ρ at each reflection. Thus, for two reflections, the beam intensity is reduced by a factor ρ^2, and for 17 reflections it is attenuated by ρ^{17}.

Thus we see that:

$$M_{13} = I_0 G \rho^{13}$$

$$M_{17} = I_0 G \rho^{17}$$

$$M_{21} = I_0 G \rho^{21}$$

And clearly we have:

$$\frac{M_{17}}{M_{13}} = \frac{M_{21}}{M_{17}} = \rho^4 \tag{4.8}$$

$$\frac{M_{21}}{M_{13}} = \rho^8 \tag{4.9}$$

Of course, this is assuming that I_0 remains constant. Once again this is compensated for by having a second detector measuring the laser drift, as described at the end of section 4.2.

4.7 Multiple reflection experimental technique

The multiple reflection cell was always going to be difficult to use due to the precise alignments necessary. Initially, I practiced the experimental technique with the 633nm laser so that I could see where the laser beam was going. Only when I had a feel for the equipment could I move on to the infra-red lasers with the invisible beam.

Finding how many reflections there were on each surface was fairly easy. I soon realised that with the primary and secondary mirrors as far apart as possible, there were two reflections on each surface before the beam encountered the tertiary mirror.

To change the number of reflections per surface, I rotated the tertiary mirror so that it was no longer in the path of the beam. Then I placed a fluorescent wand in the path of the beam so that I could see the infra-red lasers. As the primary mirror was moved closer to the secondary mirror, the laser spot on the fluorescent wand moved sideways. Eventually it was hidden by the edge of the primary mirror (clearly visible by its effect on the laser spot) and another spot appeared to one side of where the laser spot had been. This was indicative of the number of reflections per surface increasing from two to three.

In general, when such an event was observed, it indicated that the number of reflections per surface had increased from n to n+1. Thus for any number of reflections per surface, one merely had to start with the primary and secondary mirrors as far apart as possible, and then move them closer together while counting the number of increases.

The tertiary mirror was then moved back into position and adjusted until the laser spot was incident on the detector.

The vertical alignment of the mirrors was vital as the slightest error would be amplified as the beam bounced back and forth. I found that the vertical alignment could be minutely adjusted by tightening or loosening the holding screws on the primary mirror holder. Once the multiple reflection cell had been set up, the vertical positioning of the laser spot on the detector was found with a fluorescent wand, and the holding screws on the primary mirror were adjusted until the spot was central on the detector.

Unfortunately, with the infra-red lasers, reflecting the laser beam back along its path proved highly complicated. The 10.6μm laser spot was too wide and tended to spill off the edge of the

tertiary mirror. Some attempt was made to focus the beam, but with a limited number of infra-red lenses in the department (due to cost), a solution could not be found that didn't involve focusing the laser to a point at some stage (something that was definitely to be avoided with a 6W laser).

The 5.4μm laser, as already mentioned, was much lower power than originally specified. This low power meant that, by the time the laser had been reflected back along its path, the laser power was too small to be detected by the bolometers.

For this reason, the tertiary mirror was removed when using the two longer wavelength lasers and the detector placed behind the multiple reflection cell. Unfortunately this also had the effect of reducing the number of reflections by roughly a factor of two.

A series of experiments were performed with each laser, measuring the properties of each sample. The sample denoted 'origgold' was measured first, since that was the basis of the multiple reflection cell. As described above, the absolute reflectivity was measured by varying the number of reflections from each mirror.

Once the reflectivity of the gold mirrors had been measured at that wavelength, the primary mirror was replaced with each of the other samples. Clearly the beam would now be attenuated by a factor consisting of some combination of the reflectivity of the gold mirrors and the reflectivity of the sample depending on how many reflections there were from each. Since the reflectivity of the gold mirrors was now known, the reflectivity of the sample could be measured.

For example, take the set-up in figure 4.10. If the primary mirror has been replaced with a different sample, there will be 8 reflections from the sample and 9 reflections from the remaining gold mirrors. Changing the configuration to each of the cases in figure 4.11 gives respectively 6 reflections from the sample and 7 from the gold mirrors, and 10 reflections from the sample and 11 from the gold mirrors.

Using the same reasoning that lead to equations 4.8 and 4.9 it is easy to see:

$$\frac{M_{17}}{M_{13}} = \frac{M_{21}}{M_{17}} = \rho^2 \rho_S^2$$

$$\frac{M_{21}}{M_{13}} = \rho^4 \rho_S^4$$

Where ρ is the reflectivity of the gold mirrors and ρ_S is the reflectivity of the sample. Thus, having already measured the value of ρ, ρ_S can be obtained.

Unfortunately, as mentioned above, the tertiary mirror was unable to be used with the longer wavelength lasers. This gave half the number of reflections per surface described above and so only values of ρ_S and ρ_S^2 could be measured.

Obviously the gold measurements were more accurate than those with any other sample due to the increased number of reflections. In the two equations above, values of ρ_S^4 are the maximum measured, whilst in equation 4.9 ρ^8 is being measured. The performance of the multiple reflection cell would be improved for other samples if they were produced in matched triplets in the same way the gold mirrors were produced, but this would make obtaining samples much harder.

4.8 Results of Experimental measurements

Above I have described the method of the experiments designed to measure the surface properties required by my Monte Carlo model. The results from these experiments, while very interesting, unfortunately were not useful for combining with the model, as will be explained below.

4.8.1 Sample surfaces

Over the course of my research, I took measurements on a variety of surfaces.

The very first readings were taken with an aluminium sample of unknown origin that was found in the laboratory. This was merely used to aid in initially setting up the apparatus. The sample did exhibit very peculiar properties which caused some initial concern about the equipment. The shape of the graphs of reflectivities against angle to the normal of the surface showed a typical $\rho_{||}$ curve when the light was polarised *perpendicular* to the plane of incidence, and a typical $\rho_{\perp}$ curve when polarised *parallel* to the plane of incidence.

Given the regular behaviour of all subsequent samples, however, one can only conclude that this was due to the sample, maybe because of some kind of surface layer. Since the surface had an unknown history, though, very little could be concluded.

The first sample acquired especially for the experiments was a 1 inch diameter circular gold sample purchased from Ealing Optics (denoted Gold1). Early results were obtained with this sample, but I was unhappy with the dimensions. The maximum width of 1 inch did not allow effective measurements to be made at grazing incidence.

Soon after, the second sample was bought from Ealing Optics (denoted Gold2). This was another gold mirror on a glass substrate, but this time a rectangular one measuring 1 inch $\times$ 2 inches. The longer side allowed better measurements at grazing incidence.

Once the apparatus was set up correctly and the experimental method established, we began asking for other samples from related projects. Four samples from the Gemini project were kindly loaned to us by Ruth Kneale. All the samples were sputtered onto a glass substrate and included

Sample	Quoted emissivity (at 4μm)
wht-4g	0.0262
421-53-3c	0.0111
dsi-1611-g	0.0128
dsi-1917-3	0.0100

Table 4.1 Quoted emissivity values of the Gemini samples at 4μm

bare Aluminium (denoted wht-4g), bare Silver (denoted dsi-1917-3), NiCrN/Ag/NiCrN (denoted 421-53-3c), and Ag/Hf/HfO_x/HfO_2 (denoted dsi-1611-g).

The naming system used by the Gemini project was used to denote the different samples. Sample wht-4g was sputtered in the WHT aluminising tank on La Palma in August 1994. It was then force tarnished in a high-humidity environment and cleaned with an excimer laser.

Sample dsi-1611-g and dsi-1917-3 were sputtered at the Deposition Sciences facility in California in December 1994 and March 1995 respectively. Sample 421-53-3c was sputtered in the Airco facility in California in June 1994. All three were exposed for two weeks next to the UKIRT primary mirror on Mauna Kea in April 1995.

The tarnishing of the Gemini samples was obvious to the naked eye. In some places, the metal sample had worn away entirely exposing the glass substrate. Sample wht-4g was circular with a diameter of 50mm, although the edges were so badly worn that only a 45mm diameter circle was useful. All other Gemini samples were square measuring 50mm × 50mm. The quoted emissivities of the Gemini samples are shown in table 4.1.

Around the same time a large gold mirror, measuring 68 × 68 × 6mm was kindly loaned to us by John Harris at the Royal Observatory, Edinburgh. The mirror had been previously used in research at that establishment and showed some signs of age (scratches, smears, etc). This provided a good indication of how an aged gold sample would perform against a brand new sample. Of unknown history, this again was a layer of gold on a glass substrate and was labeled roe1.

Whilst setting up the multiple reflectometer, three specially made gold mirrors were purchased from TecOptics*. These mirrors consisted of a gold film on a glass substrate. They had been made on one large piece of glass (to ensure almost identical surface properties) and then cut to size. The largest of these was also used in the bi-directional measurements (denoted 'origgold') and measured 25 × 50mm.

*2nd Avenue, Onchan, Isle of Man, IM3 4PA

Surface Sample	Identifying code	Measurements (mm)
Gold (pristine)	origgold	25 × 50
Silver (pristine)	khag	40 × 40
Aluminium (pristine)	khal	75 × 27
Gold (weathered)	roe-1	68 × 68
Silver (weathered)	dsi-1917-3	50 × 50
Aluminium (weathered)	wht-4g	50 mm diameter
NiCrN/Ag/NiCrN (weathered)	421-53-3c	50 × 50
Ag/Hf/HfO_x/HfO_2 (weathered)	dsi-1611-g	50 × 50

Table 4.2 A list of the samples, their codes, and sizes

Towards the end of my research, Clive Birch of Kendall-Hyde Ltd.† loaned me pristine samples of bare silver and bare aluminium. This allowed me to compare the pristine samples with the weathered Gemini samples. The aluminium sample was especially good having been evaporated on a glass slide and, therefore, being a good 75mm wide. The silver sample measured 40 × 40mm. These samples were labeled khag and khal (kh for Kendall Hyde and al and ag for Aluminium and Silver respectively).

Table 4.2 shows a summary of details for all the samples used in my experiments.

4.8.2 Bi-directional reflectometer

As described in section 4.5, each measured value of the reflectivity is the average of four readings. This average was also used to calculate the 95% confidence intervals to give an idea of the reliability of the measurements.

All the data collected are shown graphically in Appendix C. Certain features of the data are immediately obvious. The distinctive shape of the curves for the two polarisations are evident, particularly at shorter wavelengths.

Figure 4.12 (a reproduction of figure C.5) shows an especially good example of this feature. $\rho_\perp$ is a gently increasing slope approaching 1 as θ approaches 90°. In contrast, $\rho_{||}$ *decreases* as θ increases, reaching a minimum at around 80°. $\rho_{||}$ then sharply increases to 1 at $\theta = 90°$. Both polarisations should be the same at the normal to the surface since the direction of emission lies along the normal and the plane of incidence is undefined.

Another clear trend is the increase of reflectivity with wavelength. This makes it harder to see any structure in the curves, particularly $\rho_\perp$, since the amount of increase in the curve is comparable

†Kingsland Industrial Park, Stroudly Road, Basingstoke, Hants, RG24 8UG

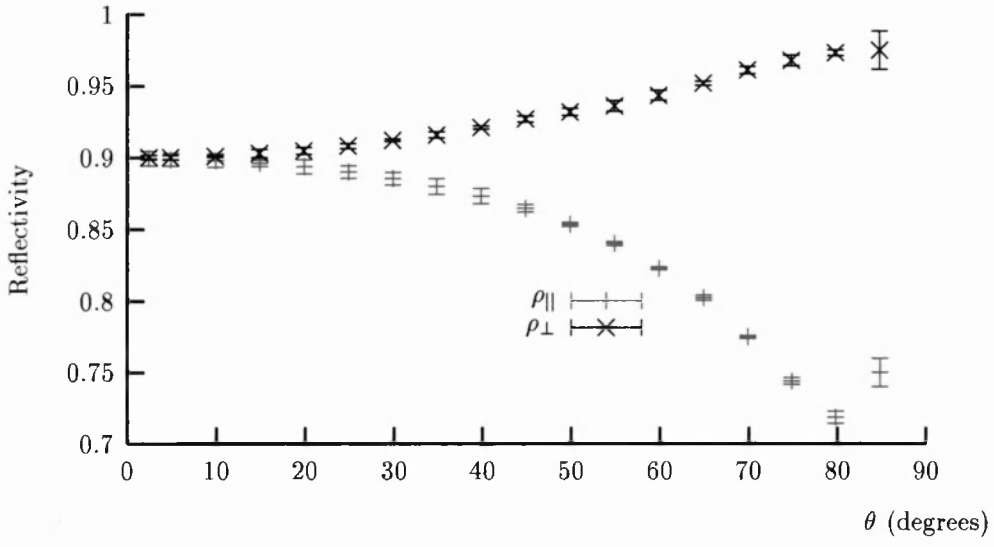

Figure 4.12 khal at 633nm (a reproduction of figure C.5)

to the errors in the readings. For instance, figure 4.13 (a reproduction of figure C.20) may well show a typical $\rho_\perp$ curve, increasing with θ, but it is very hard to tell due to the fact that $\rho_\perp$ starts with a value of 0.997 at 10° and the readings have typical errors of 0.001.

Two other features of figure 4.13 demand explanation since they appear in most graphs. The first, and most common feature, is the reduction in reflectivity of both polarisations at high values of θ. While $\rho_{||}$ is expected to reduce, $\rho_\perp$ is not. The cause of this reduction of reflectivity is the laser spot becoming too wide for the sample at such grazing incidence and effectively 'falling off' the edge of the sample.

This is not such a problem for sample khal due to its large width, but for all other samples a noticeable reduction in $\rho_\perp$ occurs around $\theta = 75°$. This casts doubt on the data above these values of θ.

The second unusual feature of figure 4.13 is the first reading ($\theta = 5°$) which is considerably lower than all other low-angle readings. This is almost certainly caused by the laser beam being partially obscured by the detector head. In a bid to get as close to the normal as possible, I positioned the detector head very close to the beam. Unfortunately, such obscuration is not obvious from the raw data and only comes out when the data is analysed. Thus, clearly unusual low-angle readings should not be considered as true representations of the reflectivity.

The typical curves for the two polarisations are not present in two cases. The first is sample

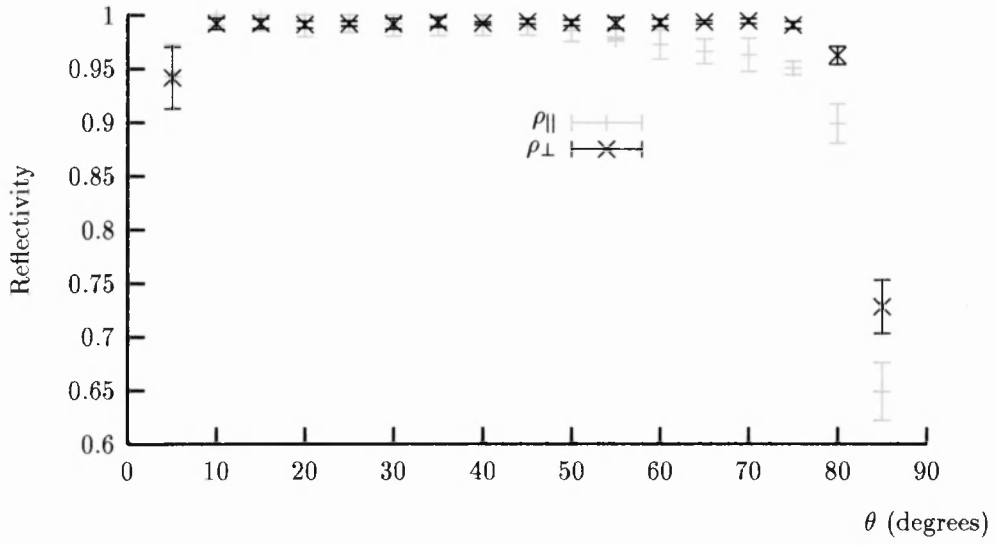

Figure 4.13 khag at 5.4μm (a reproduction of figure C.20)

dsi-1611-g (figures C.2, C.10, C.18, and C.26) which seems to have the behaviour reversed. The cause of this is unknown, and may be due to some property of the alloy. Since I was not told of anyone else performing independent measurements of the reflectivity at the two polarisations, I have no way of checking these results, but the fact they are consistent and this is the only sample to display such behaviour suggests that this is a real effect.

The typical behaviour is also reversed at 10.6μm it seems. The weathered samples (421-53-3c, dsi-1611-g, dsi-1917-3, roe1 and wht-4g) show a decrease in both polarisations, no doubt due to the surface contamination, which is inconclusive. However, the pristine samples (khag, khal and origgold) clearly show $\rho_\perp$ decreasing faster than $\rho_{||}$ in contradiction to the expected behaviour.

When I initially observed this, I could only conclude that this indicated the 10.6μm CO_2 laser was not vertically polarised as was indicated in the manual. I checked with Edinburgh Instruments, and they assured me that there was no way this could be the case. However, in order to check the polarisation, they also sent me a Brewster window for use at this wavelength. Unfortunately no instructions were sent with the window and tests of the laser with it proved inconclusive.

Having checked my lab books several times and repeated some experiments to make sure this was not caused by some simple oversight on my part, I can only produce three possible explanations for this behaviour.

- The laser is in fact *horizontally* polarised.

Sample code	Quoted emissivity (at 4μm)	Measured data (at 5.4μm)	
		measured at 10°	averaged from 0-20°
wht-4g	0.0262	0.0233	0.0239 ± 0.00313
421-53-3c	0.0111	0.0126	0.0126 ± 0.00089
dsi-1611-g	0.0128	0.0146	0.0145 ± 0.00298
dsi-1917-3	0.0100	0.0221	0.0213 ± 0.00534

Table 4.3 A comparison of quoted emissivity values of the Gemini samples with my own experimentally measured values

- The equipment that works perfectly well at all other wavelengths is consistently misbehaving at 10.6μm.
- The typical behaviour of the radiative properties of metals is reversed at 10.6μm.

Of the three, the first seems most likely to me. If so, the labels on the graphs of data at 10.6μm are incorrect and should be reversed.

In general, the experiments at 10.6μm seemed to produce the smallest error bars. I put this down to a combination of a stable laser and a very good detector (the bolometer/Labmaster combination). The experiments at 633nm and 5.4μm produce generally small error bars, but not as small as the 10.6μm experiments. In the case of the 633nm experiments, this is probably due to the stability of the laser. Whilst the 5.4μm laser was not at all stable, it seems to have been saved somewhat by combining it with the Labmaster.

By far the worst results were produced by the 1152nm laser. As described in section 4.4, this laser was very unstable and the PSD was not as effective in smoothing out the signal as the Labmaster. In later experiments I increased the integration time of the PSD in an attempt to eliminate this instability. While this had some beneficial effect, it still couldn't reduce it sufficiently.

Table 4.3 is a copy of table 4.1 with my own measured values of the emissivity (from $\epsilon' = 1 - \rho'$) added to see how well the equipment performed. Two measured values are shown. The first, measured at 10° is an average of both polarisations measured at $\theta = 10°$. The second is an average of all measurements from $\theta = 0°$ to $\theta = 20°$ for both polarisations (8 measurements in all). This was done since it can be seen in figure 3.15 (or indeed any graph of directional properties) that the emissivity of directional materials varies very little over the first 20 degrees. Thus, by averaging 8 readings it was hoped a more accurate result could be obtained. The quoted error is the standard deviation of those 8 measurements about this average.

My measured data shows excellent agreement with the reported emissivity values in three cases, at least within the standard deviation. The exception (dsi-1917-3) is the bare silver sample. It is

well known that silver tarnishes quicker than almost any other metal, and with at least 16 months between the two sets of readings, it is entirely conceivable that the sample simply tarnished between the experiments, thus accounting for an increase in emissivity.

To demonstrate the effects of tarnishing on silver, I measured the reflectivity of sample dsi-1917-3 again at the end of my PhD studies. These measurements are summarised in table C.28 and figure C.28 (reproduced as figure 4.15) and were taken some 13 months after the original readings in table C.27 and figure C.27 (reproduced as figure 4.14).

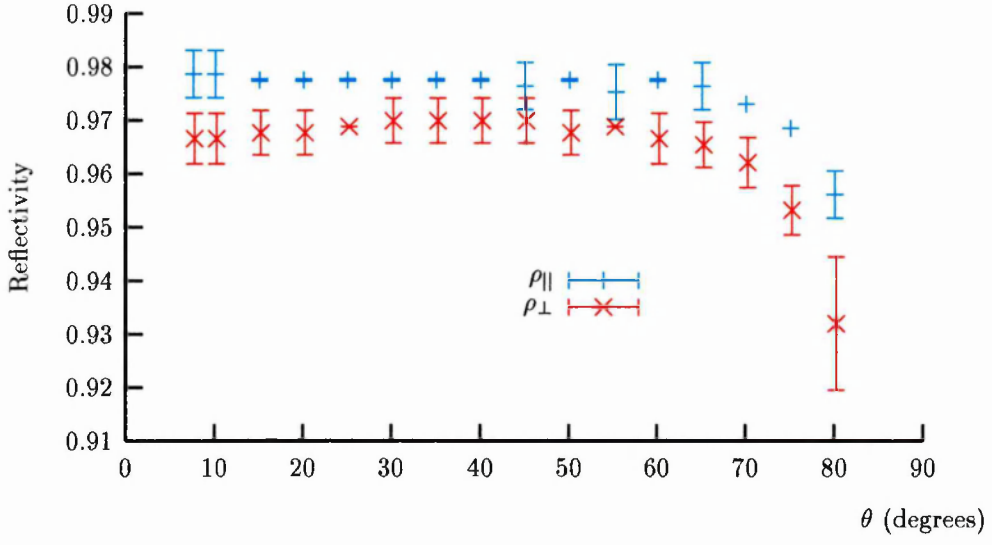

Figure 4.14 dsi-1917-3 at 10.6μm (original data, reproduced from figure C.27)

It is clear simply from comparing tables C.27 and C.28 that the reflectivity has reduced markedly over those 13 months. New readings of $\rho_\perp$ show a drop of around 0.010 in reflectivity, while readings of $\rho_{||}$ show a drop of at least 0.015. If this kind of tarnishing had taken place between the quoted readings in table 4.3 and my original readings, it would easily explain the discrepancy between the two.

Unfortunately my equipment was not sensitive enough to distinguish between the two samples 421-53-3c and dsi-1611-g, but could distinguish those two from the other two samples within the standard deviation.

An interesting feature to note is just how directional the weathered samples are, even at long wavelengths. It is well known that as a surface becomes pitted and scratched, the rough surface produces more diffuse behaviour. This seems to be the case at 10.6μm with both polarisations falling

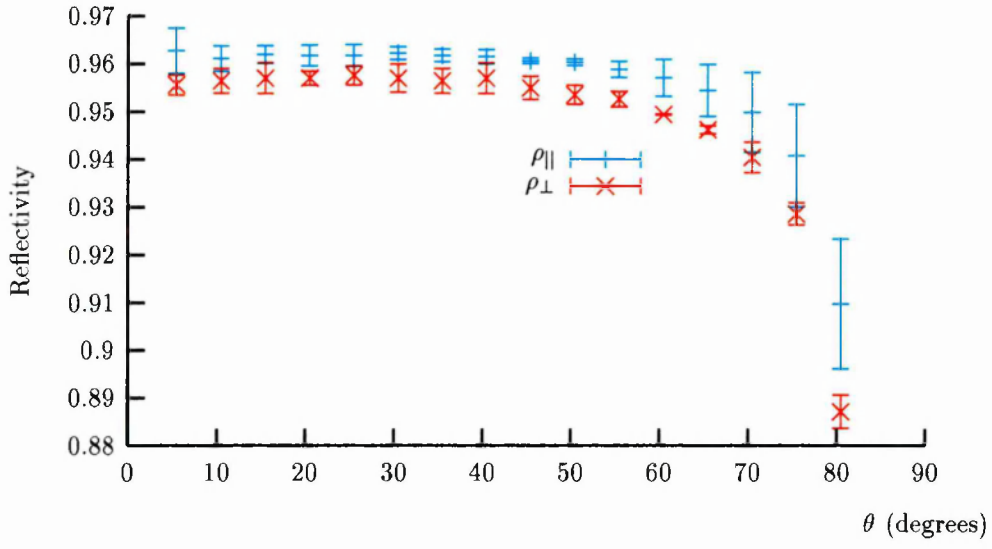

Figure 4.15 dsi-1917-3 at 10.6μm (more recent data, reproduced from figure C.28)

off as θ increases. However, at 5.4μm there is still a noticeable difference in the behaviour of the two polarisations, with $\rho_{\perp}$ rising as θ increases (at least up to the point where the laser spot becomes too large for the sample).

The pristine samples show a clear difference in the behaviour of the two polarisations at all wavelengths. In particular, sample khal shows an excellent example of this, no doubt due to the large width of the sample.

It is interesting to note that the aluminium samples show the greatest difference between the pristine sample and the weathered sample at 633nm, but at 10.6μm it is silver that shows the greatest signs of weathering, presumably due to different optical properties of the oxide layer in each case.

At all wavelengths, the pristine and weathered gold samples are indistinguishable (within the limit of the error bars) at small values of θ. At higher angles, the weathered gold (roe1) begins to show its true colours as it exhibits more diffuse behaviour while the pristine sample (origgold) shows the typical directionality of a metal.

4.8.3 Multiple Reflection Cell

The results from the multiple reflection cell are presented in table 4.4. Values of the reflectivity are given for each sample at each wavelength and for each polarisation. Quoted errors are 95% confidence intervals. Each sample was measured three times, once with three reflections off the sample, once

with four, and once with five. The reading from three reflections divided by the reading from five reflections gave a value for ρ^2 as described in section 4.7. Also shown in table 4.4 are readings from the bi-directional reflectometer measured at an angle of 15°, being the angle to the laser beam of the primary and secondary mirrors of the multiple reflection cell.

Sample	λ	$\rho_\perp$		$\rho_\parallel$	
		m.r.c data	b.d.r data	m.r.c data	b.d.r data
origgold	633nm	0.925 ± 0.007	0.923 ± 0.002	0.925 ± 0.002	0.918 ± 0.004
	1152nm	0.969 ± 0.004	0.959 ± 0.052	0.974 ± 0.004	0.973 ± 0.008
	5.4μm	0.978 ± 0.001	0.984 ± 0.015	0.977 ± 0.003	0.980 ± 0.006
	10.6μm	0.982 ± 0.005	0.986 ± 0.007	0.987 ± 0.005	0.990 ± 0.001
roel	633nm	0.936 ± 0.010	0.930 ± 0.006	0.940 ± 0.002	0.922 ± 0.002
	1152nm	0.993 ± 0.015	0.970 ± 0.015	0.984 ± 0.006	0.972 ± 0.011
	5.4μm	0.975 ± 0.001	0.984 ± 0.004	0.979 ± 0.006	0.985 ± 0.005
	10.6μm	0.982 ± 0.002	0.990 ± 0.004	0.988 ± 0.015	0.990 ± 0.004
421-53-3c	633nm	0.953 ± 0.009	0.936 ± 0.005	0.959 ± 0.005	0.930 ± 0.009
	1152nm	0.980 ± 0.010	0.964 ± 0.020	0.976 ± 0.011	0.962 ± 0.017
	5.4μm	0.971 ± 0.003	0.988 ± 0.012	0.978 ± 0.004	0.986 ± 0.004
	10.6μm	0.997 ± 0.000	0.991 ± 0.000	0.988 ± 0.000	0.986 ± 0.000
dsi-1611-g	633nm	0.890 ± 0.008	0.875 ± 0.006	0.891 ± 0.006	0.878 ± 0.004
	1152nm	0.971 ± 0.009	0.949 ± 0.012	0.963 ± 0.010	0.953 ± 0.011
	5.4μm	0.969 ± 0.008	0.989 ± 0.004	0.975 ± 0.003	0.982 ± 0.003
	10.6μm	0.989 ± 0.003	0.991 ± 0.000	0.992 ± 0.010	0.989 ± 0.005
dsi-1917-3	633nm	0.956 ± 0.009	0.932 ± 0.010	0.955 ± 0.030	0.925 ± 0.008
	1152nm	0.981 ± 0.022	0.962 ± 0.014	0.972 ± 0.012	0.964 ± 0.022
	5.4μm	0.962 ± 0.001	0.985 ± 0.008	0.977 ± 0.006	0.974 ± 0.004
	10.6μm	0.996 ± 0.001	0.968 ± 0.004	0.981 ± 0.007	0.978 ± 0.000

Table 4.4 Results from the Multiple Reflection Cell (m.r.c) compared with readings from the bi-directional reflectometer (b.d.r) at an angle of 15°

The reading from four reflections was divided by the reading from three, and the reading from five reflections was divided by the reading from four, each giving a value of ρ. These two values were used only to check that the value for ρ^2 was correct and weren't used in calculating ρ.

This procedure was repeated and the two values of ρ^2 averaged and the square-root taken to give a value for ρ with its associated error.

At 633nm and 1152nm the tertiary mirror was used to reflect the laser beam back along its path and so double the number of reflections, giving a value for ρ^4 instead of ρ^2. This was not possible at longer wavelengths as previously explained.

For the sample origgold, both the primary and secondary mirror (and, where applicable, the tertiary mirror) were coated in the sample substance thus doubling again the number of reflections on the sample.

The results are somewhat disappointing as the multiple reflection cell was designed to be an extremely sensitive measuring device. Unfortunately, as already mentioned, it was impossible to operate it as planned at the longer wavelengths. It is noticeable that, at these wavelengths, the results gathered with the bi-directional reflectometer were comparable, if not better, than those from the multiple reflection cell.

While the errors are generally low, they are often comparable with those associated with the bi-directional reflectometer data. Also, the error bars are occasionally very large; far too large to be of any use in measuring such very high reflectivity samples.

The readings from the two different pieces of apparatus show very good agreement, usually agreeing within the quoted 95% confidence intervals.

The problems with reflecting the longer wavelength lasers back along their path were reduced somewhat by focusing the beam slightly, but I was very wary against focusing the beam to a point for fear of damaging the samples.

Since the multiple reflection cell cannot make measurements at varying angles of incidence, its usefulness lies in the ability to make very accurate measurements. This may be achieved by taking more readings to provide better statistics, or redesigning it to allow more reflections per surface and hence higher powers of ρ to be measured. The errors of the readings of the sample origgold are consistently small. This is almost certainly due to the higher powers of ρ measured, owing to the fact that all the mirrors were made of the sample substance (as explained above).

If nothing else, however, the multiple reflection cell does provide a reference with which to check the low angle measurements of the bi-directional reflectometer readings. In this respect it performs well.

4.9 Problems combining experiments and simulations

When my research began, I hoped that measuring the radiative properties of candidate passive cooling materials would allow me to put realistic values into my Monte-Carlo model and more accurately estimate the effects of directional radiative properties on the equilibrium temperature of the telescope. Unfortunately, the experimental measurements proved to be of little use for combining with the model.

Although the readings were consistent (especially at longer wavelengths), they were only measured up to 10μm. This was the longest wavelength laser available to me. To measure the radiative transfer realistically, I would need the properties at 10μm, 30μm, and 100μm (as in line 5, table 3.2).

It would have been possible to put my readings in to the model to describe the properties of the inward-facing surface of the outer sunshield, but this seemed such a small part of the simulation as to hardly warrant the effort (particularly with time pressures mounting).

Another option would be to derive the optical constants of the metals from the experimental measurements and then extrapolate these values to longer wavelengths using the Drude free electron theory (which performs well at this task as described in section 2.9.1). There are several methods of deriving the optical constants of a material from experimental measurements of its radiative properties. They all ultimately fit into one of two categories, however; either calculating them from some equation, or fitting the results to a graph.

The idea of graph-fitting is very simple. One merely produces several graphs of radiative properties using different values of the optical constants and then find which curve most closely fits the experimental data. This method is described by Ivan Ŝimon [62] and more recently by Logofătu et al [63]. Unfortunately, for reasons explained below, this method was not applicable to my data.

The very first efforts of mine into this field were simply to take the equations relating the radiative properties to the optical constants (i.e. equations 2.15 and 2.16) and reverse their order giving the optical constants in terms of the radiative properties.

Equations 2.15 and 2.16 are rather complicated and not easy to reverse. I used the computer algebra package 'Mathematica' to perform this reversal, and the equations came out as approximately 10 pages worth of algebra. Coding this into a C program, I tried entering some measured data only to find the results extremely inconsistent.

A less 'brute-force' approach is given by Ditchburn [21]. This introduces two new variables; p and q defined as:

$$p^2 - q^2 = n^2 - \kappa^2 - \sin^2\theta \tag{4.10}$$

$$pq = n\kappa \tag{4.11}$$

These new variables are now expressed in terms of the ratio of reflectivities for the two orthogonal polarisations and the phase shift between the two polarisations after reflection from the sample surface. This method is intended for use with ellipsometry, but I reasoned it could be adapted to bi-directional reflectometry.

With some rearrangement, it is possible to express p and q solely in terms of the ratio of reflectivities at two different angles. Assuming that $|n^2 - \kappa^2| >> \sin^2\theta^*$ we can now find n and κ.

*Which is invariably true for metals at large λ.

Unfortunately, given the errors on my readings, the results produced by this method were also very unreliable.

The problems associated with deriving the optical constants of metals from experimental data are most succinctly summed up by Logofătu et al [64]. In this paper they plot graphs of various combinations of reflectivities and different angles. On these graphs are shown contour lines for values of n and κ.

One major problem with some methods is the regions of self-overlap. This occurs when the contours for values of n and κ overlap giving two, or even three, possible results.

The most serious problem, however, is shown in figures 3 and 7 of [64]. The contours of n and κ cluster together as the reflectivities approach 1. With very high reflectivity samples such as those required for passive cooling, the reflectivities are always going to be very close to 1. In this region of the graph, the tiniest error in the measurements can span a huge range of n and κ values making any reliable derivation of experimental measurements impossible.

This almost certainly explains the variation of n and κ values reported by Ordal et al [22]. Figure 4.16 shows five curves calculated using values of n and κ reported by Ordal et al. All values were measured at 5μm (unless labelled otherwise) and the curves are labelled with the names of the experimenters reporting the values of the optical constants.

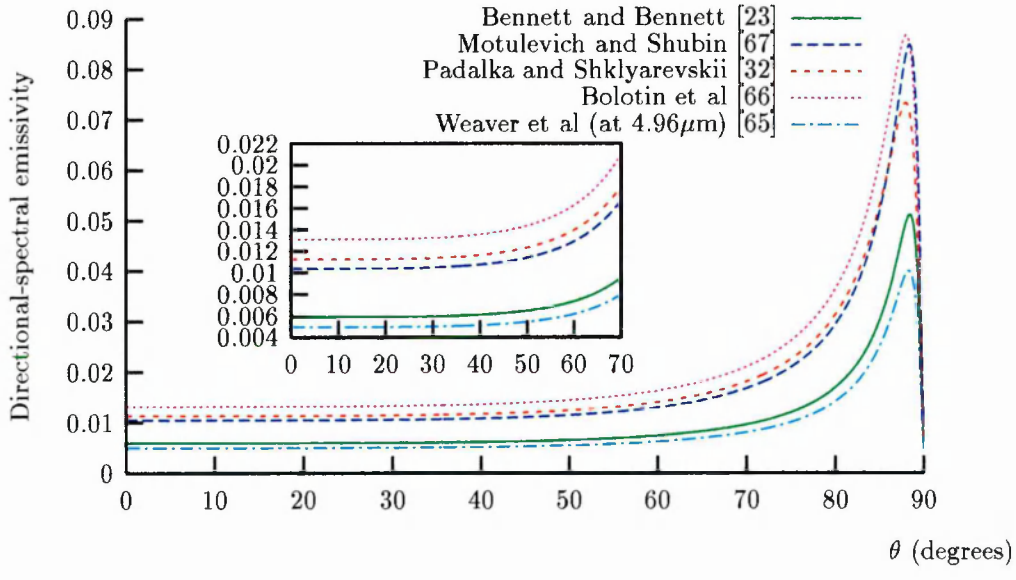

Figure 4.16 Graphs of the reflectivity of Gold at 5μm calculated from values of n and κ reported by different sources (inset shows an expanded view at low θ)

From this evidence it seems any attempt to measure reliable optical constants for the express

purpose of extrapolating radiative properties to other angles and wavelengths is likely to introduce possibly large errors into the values of those properties. Thus, in order to model such processes accurately, there seems little choice but to embark on an extended and comprehensive measurement program, at least at the three wavelengths characteristic of the equilibrium temperatures of an EDISON-like telescope.

Chapter 5

Conclusions

At the start of my PhD I set out to answer a relatively simple question: Is the equilibrium temperature of a passively cooled telescope affected by modelling the directional radiative properties correctly? I can now confidently say yes! However, the exact size and nature of the effect on the equilibrium temperature of the telescope is dependent on many other factors.

5.1 Experimental measurements

I have stressed that there is a major lack of reliable data concerning the directional radiative properties of candidate passive cooling materials and what data exist are invariably inconsistent from experimenter to experimenter. Clearly, if a passively cooled telescope is to become a reality, accurate data will be needed to effectively predict the thermal performance of the telescope. Thus, some experimental project will need to be set up to perform these measurements.

I have described the two pieces of apparatus developed over the course of my research; the bi-directional reflectometer (see section 4.2) and the multiple reflection cell (see section 4.6).

The multiple reflection cell was designed to provide high-accuracy measurements at the expense of easily varying the angle at which these measurements were taken. As explained in section 4.8.3 the multiple reflection cell did not perform as well as had been hoped. This was almost certainly due to problems with the lasers preventing the apparatus from being used as originally intended. The inability to achieve the maximum possible number of reflections on the sample surfaces greatly reduced the sensitivity of the apparatus.

The equipment may have given more accurate results if a long program of repeated measurements had been undertaken to provide a better understanding of the variance of the readings. Unfortunately there was not enough time for me to perform such a program of readings and so this will be left for

future investigation.

The bi-directional reflectometer was a great success. Consisting of only a few components, nearly all of which were very cheap, it produced consistent and accurate data when not hampered by unstable and/or weak laser sources. The data produced also showed excellent agreement with other measurements for those samples (i.e. the Gemini samples) which had been previously studied by other researchers (see table 4.3).

The only expensive components in the apparatus were the lasers themselves. However, it seems necessary to have a stable and suitably powerful laser to produce good results, and such a laser will no doubt be expensive. The measurements at 1152nm show how disappointing the performance is when the apparatus is let down by an unreliable laser.

A very important rôle in the apparatus is performed by the detectors and measurement device. In this area the Coherent Labmaster performed excellently and greatly improved the accuracy of the equipment. Thus, for accurate and reliable measurements it seems the most important factors are a reliable laser and an effective measurement device. All the other components were either standard optical-bench fittings or simple devices made by our on-site workshop.

The bi-directional reflectometer also allowed a picture of the directionality of the surface properties to be built up very quickly. Taking only an hour or so to take two measurements at each of approximately fifteen different angles, this apparatus was very effective in making the kinds of measurements required to gather data needed to model passive cooling.

The measurements taken (see appendix C) also show several interesting facts about the samples. As expected, it was shown that silver tarnishes very quickly. Measurements taken at the end of my research (see figure C.28 and table C.28) show a roughly 50% rise in emissivity ($\epsilon'_\lambda = 1 - \rho'_\lambda$) compared with measurements taken 13 months earlier (figure C.27 and table C.27). During those 13 months, the sample was kept covered but open to the air in the laboratory.

Also shown was how silver and aluminium were affected by weathering. Both samples showed a decrease in reflectivity when weathered, though the size of the decrease varied depending on the wavelength of light being measured.

The gold samples ('origgold' and 'roe1') showed exactly why this is such a useful surface for passive cooling. The difference in reflectivity between the fresh sample and the weathered sample was undetectable at all wavelengths, except at grazing incidence and long wavelength where the weathered sample appeared more diffuse. This integrity of surface properties even after weathering is one of the most useful properties of gold for passive cooling design and far outweighs the fact that fresh silver has a lower emissivity.

The most interesting finding was just how directional even the very weathered surfaces were. Conventional wisdom tells us that when a metal surface becomes weathered, it quickly exhibits diffuse behaviour in both emission and reflection. However, all my measurements show very directional behaviour, even from the Gemini samples which were so weathered the coating had worn off the substrate in places.

This should add weight to the argument for modelling directional surface properties correctly since the surfaces of a passively cooled telescope will continue to exhibit directional behaviour even after substantial weathering.

The experimental measurements taken during my research were unfortunately limited to the near and mid infra-red. Thus, while they will be of use to engineers working at room temperatures (possibly ground-based telescopes), they are of little relevance to cryogenic studies, such as space-based infra-red telescopes. For this reason, more measurements need to be taken.

Another conclusion from my experimental results is that it will be virtually impossible to derive any meaningful optical constants from experimental measurements of such low emissivity samples. As has already been discussed in chapter 4, the solution space of the equations for the optical constants is so dense at these low emissivities that the slightest error will produce a huge difference in result. This explains the variation of results quoted in the literature [22].

Thus, to effectively combine experimental measurements with computer simulations, one will need to either measure the surface properties at a huge number of different angles (requiring automation of the measuring process – see later) or to find the optical constants which best describe the shape of the measured curve of surface properties against θ. If this latter method is used, however, it should be warned that these optical constants may well not be the 'true' optical constants of the material and should not be used to extrapolate readings into other areas (i.e. to different wavelengths or temperatures) without extreme caution.

Clearly, the most reliable way to obtain data for computer simulations would be to measure it directly. This needs to be done at longer wavelengths than those I have investigated (e.g. at least up to 100μm) and, most importantly, at cryogenic temperatures. All the data used in my simulations were measured at room temperature. There currently exists a major dearth of reliable data measured at cryogenic temperatures, partly because of the great problems involved in such a study.

5.2 Monte-Carlo results

My Monte-Carlo model is not very accurate in terms of the structural aspects of a telescope such as EDISON. For instance, all the surfaces have infinite thermal conductivity. Also, the conductivity between different components of the telescope is modeled in a rather crude manner. However, the radiative heat transfer is modeled more realistically than any previous study, and for this reason I believe my results have much to tell us about possible future passively cooled space telescopes.

As mentioned at the start of this chapter, directional radiative properties definitely have an effect on the equilibrium temperature of a passively cooled observatory. This was clear right from the very start of my research.

Perhaps the most striking thing to come out of my research is the fact that the effects of modelling the directional properties correctly is smaller than the effect of modelling gold surfaces with a realistic value of the emissivity. The currently quoted value of '0.03 in the infra-red' has been shown to be a gross over-estimate. However, this can be an advantage or a disadvantage depending on the design of the telescope.

Initially, all the results looked very promising for passive cooling. As shown by table 3.2, introducing realistic directional properties to the model produces a $\simeq 10\%$ reduction in temperature (lines 1 and 2). This would have a profound effect on the amount of energy in the system since the total emitted power varies as T^4.

A much greater effect was caused by introducing directional surfaces with *realistic emissivities* (lines 3-5). Line 5, being the most realistic model, shows a drop in temperature of 63% from the high-emissivity diffuse case. This is a huge effect and much larger than I was expecting.

At this stage I was very encouraged by my results. They seemed to be suggesting that previous studies of passive cooling were simply very pessimistic and that passively cooled telescopes would be even more efficient than anyone had imagined.

5.2.1 Conduction

In an attempt to make the structural side of my model a little more realistic I added the effects of conduction, although as explained this was modeled rather crudely. Conduction has long been a problem in cryogenics, and it is no surprise that much time, effort and money has been put into developing materials with very low coefficients of conduction. However, even with these very low values, conduction had a significant effect on the results of my model.

Table 3.4 shows the results of simulations performed with conduction modeled (assuming a

10m×10m model as explained previously). As already mentioned, three values of the conduction coefficient (H) were used; 0.1WK^{-1} being a realistic estimate based on current high conductivity structures, 0.01WK^{-1} investigating the effects of a ten-fold decrease in conductivity, and 0.0042WK^{-1} being a value for low conductivity structures derived from previously published studies [3].

As noted in chapter 3 the higher levels of conduction produced a reversal in the effects of emissivity. Now the higher emissivity surfaces removed heat from the system more effectively. With little or no conduction, the most important thing was to prevent heat from being absorbed by the inner surfaces. For this, a low absorptivity (and hence emissivity) surface was ideal. With high levels of conduction, however, this is not enough since the heat can now conduct to the inner surfaces. Now we need to remove this heat from the system before it has a chance to conduct that far. To do this, higher emissivity surfaces seem more effective.

However, it is also noticeable that diffuse surfaces (as in line 14) are still less efficient at preventing the heat from radiating from the outer surfaces to the inner surfaces. This is evident by the fact that line 14 has a higher value for T_2 than, say, line 16 showing that more of the energy from the outer sunshield has been absorbed by radiative transfer*. However, line 14 has a lower T_3 than line 16 showing that the higher emissivity has removed this excess heat more effectively before it can conduct to the telescope tube. This seems to imply that the high emissivity surfaces remove excess energy more efficiently for the plane-cylinder geometry than for the plane-plane geometry.

For the cases where $H = 0.1\text{WK}^{-1}$, these two effects seem to balance out. The high emissivity, diffuse case (line 14) has a tube temperature only 0.2K higher than the realistic low emissivity, directional case (line 17).

From these results it seems that for a two-shield EDISON-type design, with both sunshields parallel to the axis of the telescope tube, the traditional diffuse approximation will give, apparently by chance, approximately the correct result for the tube temperature if and only if the conduction is high enough. For the low conductivity cases, there is a difference of nearly 5K between the diffuse case (line 24) and the most realistic case (line 27).

Notice that the results of simulations performed with $H = 0.01\text{WK}^{-1}$ show once again that the lower emissivity surfaces achieve lower tube temperatures. Although a difference of 3.3K (between lines 19 and 22) doesn't sound a great deal, at the low temperatures involved ($\simeq 23K$) this actually represents a 14% change in temperature. This represents a substantial effect.

For the very low conductivity structures already proposed, the low emissivity surfaces still pro-

*Since the outer sunshield is always roughly the same temperature, the conducted heat should be approximately the same

duce better results than high emissivity surfaces. The dramatic improvement observed in the absence of conduction is now somewhat muted, although still significant. Thus, at these values of low conductivity, the directionality of materials is still important, as is the correct value for the emissivity of the surfaces.

It should be noted that I pessimistically chose the highest conductivity value reported in [3]. Those conductivity values include contributions from the support straps in the telescope structure and the wires connecting the electrical systems. The calculation of the conduction along the support straps is reported in [3] to be 'very conservative as the straps are currently specified for a large safety factor.' Thus, if my conduction values are the most pessimistic of a conservative set of values, and *still* the directionality and emissivity are playing an important rôle in cooling the telescope tube, this effect can only be magnified if realistic state-of-the-art conduction values were used.

5.2.2 Tilted sunshields

More recent designs for passively cooled telescope include tilted sunshields. The idea behind this is to encourage reflected radiation to escape from the cavities between the telescope components. The problem with tilted sunshields is the fact that they would need to be deployable after launch. Deployable systems on satellites are prone to failure and are avoided unless absolutely necessary. I investigated the effects of tilting the sunshields to see if the effect was large enough to warrant the extra problems involved.

As expected, opening out the sunshields produced a reduction of temperature in all cases. Table 3.5 shows the results for all the different simulations performed with tilted sunshields. Note that for all these cases there was no conduction modeled.

The higher emissivity cases show the largest improvement in tube temperature. The best improvement (14.7% for $\beta = 5°, \gamma = 10°$ and 24.8% for $\beta = 10°, \gamma = 20°$) is shown by the high emissivity directional surface (lines 28 and 33). This performs significantly better than the diffuse surface with reductions of 12.5% and 21.6%.

The low emissivity directional surfaces show smaller reductions, but the most realistic case (lines 32 and 37) still show a 9.2% and 12.3% reduction in temperature as the sunshields are opened out. Thus, if conduction can be eliminated, opening out the sunshields is a very effective way of reducing the equilibrium tube temperature.

Quite different results arise when conduction is modeled. Table 3.6 shows the results of simulations performed with tilted sunshields and conduction coefficients of $H = 0.1$ and 0.0042WK^{-1}. Once again, there is a reduction in temperature for all cases compared to table 3.4. Also the high

emissivity surfaces show the largest reductions.

It seems from comparing the two halves of table 3.6 with different values of conduction that the higher conductivity greatly reduces the temperature drop from table 3.4. When conductivity is high, the largest temperature drops are 1.0K for $\beta = 5°, \gamma = 10°$ and 1.7K for $\beta = 10°, \gamma = 20°$. With lower conductivity we see reductions of 1.5K for $\beta = 5°, \gamma = 10°$ and 2.5K for $\beta = 10°, \gamma = 20°$. As already mentioned, 0.0042WK^{-1} is a very pessimistic estimate of the values of conductivity currently achievable. It seems with even lower conductivity present, the temperature reductions caused by opening the sunshields will be even greater.

Another important point is raised by this study, however. The high emissivity diffuse case (lines 49 and 54) shows an improvement of 7.4% when the shields are opened out by 5° and 10°, and an improvement of 12.3% when the shields are opened out further. However, the most realistic low emissivity directional case (lines 52 and 57) show only an improvement of 3.2% and 4.4% as the shields are opened out.

It seems when $\beta = 5°, \gamma = 10°$, the incorrect high emissivity diffuse case produces an effect more than twice as large as the most realistic case, and when $\beta = 10°, \gamma = 20°$, the effect is nearly three times as large. This shows a major weakness of the traditional cooling model. Although choosing a high emissivity and diffuse emission can be seen as simply finding a pessimistic estimate of the radiative transfer involved, in some cases it produces an artificially large effect.

As already mentioned, deployable systems on a satellite are notoriously problematic. Designers of a passively cooled telescope might agree that such problems are worth overcoming if they result in a 12.3% improvement in the telescope temperature. However, if they realised it would produce only a 4.4% effect, the effort might not be considered worth the reward. Thus, it is vital that the radiative exchange between elements in a passively cooled telescope is modeled correctly. To provide pessimistic estimates, the researchers could then simply aim for lower temperatures, but it is vital that the effects of each part of the structure is known accurately to prevent a pessimistic estimate giving rise to an over optimistic result as seen here.

5.3 Summing up

I have shown that there are several factors defining the equilibrium telescope tube temperature. The biggest question my research has raised is whether gold is the best surface covering for a passively cooled telescope.

If the conduction between telescope elements can be reduced to $H = 0.0042\text{WK}^{-1}$, then gold

is an excellent choice. The combination of low emissivity and directionality produces a very low telescope temperature. At these levels of conduction the directional properties play an important rôle in reducing the telescope temperature and need to be modeled correctly. Current models of 'diffuse gold' surfaces are a little pessimistic and as such will not jeopardise the mission by recommending less cooling than is really required, but could erroneously recommend unnecessary procedures (such as tilted sunshields, discussed above).

Tilting the sunshields seems effective if conduction is very low. For higher conductivity materials, however, tilting the sunshields seems to have a small effect, even for higher emissivity surfaces. Ultimately, of course, the decision to tilt the sunshields will only be taken if the corresponding improvement in performance of the passive cooling is deemed worth the extra problems involved in such a design. As shown, the true effect of tilting the sunshields will only be shown by modelling the radiative exchanges correctly.

In all cases, directional surfaces performed significantly better than diffuse surfaces of the same hemispherical emissivity. This shows the necessity of modelling these effects properly. As I have said, many aspects of my model are quite crude and it would require a huge amount of work to convert my model into a complete modelling package. Much better, therefore, to adapt already existing modelling packages to model radiative transfer correctly. This needs to be done sometime in the next 10 years if a passively cooled space telescope is to be launched in that time.

5.4 Further study

As always with a limited period of study such as a PhD I did not have enough time or money to investigate everything I would have liked to. Although my research has drawn firm conclusions about the aspects of radiative heat transfer that it investigated, it is also part of a much wider field of ongoing study. Thus, I now present my ideas of what should be done next to build upon the work I have already done.

As shown above, there are two methods of reducing the temperature of the telescope tube in a passively cooled observatory. If conduction is present (as it surely must be) a high emissivity surface is more efficient at ejecting unwanted heat from the system before it has a chance to conduct to the inner surfaces. However, a low emissivity surface is more effective at preventing the heat from radiating onto the inner surfaces.

Perhaps the best results would be to combine these two effects. If inward facing surfaces (i.e. those facing towards the centre of the telescope tube) could be made very high emissivity (i.e. black)

they would be able to radiate heat away into space. To prevent this radiation being absorbed by the outward facing surfaces, however, these should be coated in a very low emissivity (and, hence, absorptivity) substance (e.g. gold). Due to the major restructuring of my monte-carlo code this would require, I was unable to investigate this, but it seems a logical next step.

As mentioned regularly in this thesis, there is still a major lack of reliable data concerning the radiative properties of candidate materials for passive cooling. Obviously a major experimental investigation needs to be undertaken.

The bi-directional reflectometer developed during my research and described in chapter 4 seems well suited to such an investigation, and would be greatly improved if it were automated, thus requiring less human effort and speeding up the data collection process. To do this, stepper-motor driven rotating stages would be needed, integrated with some controlling and recording device (probably a PC). I had hoped to make this improvement myself, but the cost of such motor driven rotating stages was larger than our group's already strained budget and so I was forced to abandon this avenue of exploration.

A system for quickly selecting one of many possible wavelengths as used by Drolen [54] would improve matters slightly but, given that a new laser only took approximately 10 minutes to set up, it hardly seems worth the effort.

The most important improvement would be a wider range of lasers allowing measurements to be taken at many wavelengths up to at least 100μm. This would provide useful data for inclusion in the Monte-Carlo model, providing a realistic estimate of the performance of passive cooling designs, as well as being useful to the wider community of physicists involved in modelling infra-red heat exchange.

If gold is to be the surface of choice for a passively cooled space telescope, some measurements need to be done on samples weathered in space. My research took measurements on a gold sample weathered on Earth, but to be sure how resistant gold will be to space conditions, and whether the directional properties will be as persistent as on Earth, actual measurements need to be taken. During my research, Barrie and I tried to arrange to borrow some samples from the ELDEF mission, but this could not be organised before my studies finished.

Another area of research which I had hoped to investigate, and which *needs* investigating, is the measurement of surface properties at cryogenic temperatures. During my research, Barrie had designed a low temperature enclosure into which the multiple reflection cell was designed to fit. Unfortunately, lack of technician time in the workshop meant that the equipment was never finished.

Obviously it would be very difficult to have something like the bi-directional reflectometer en-

closed in a cryogenic enclosure (although it may be possible if some kind of movable window could be constructed to allow reflected radiation to escape the enclosure). However, measurements could easily be taken at near normal incidence and at grazing incidence. The difference between these measurements would give an indication of the directionality of the surface.

In order to obtain reliable data for simulations, though, measurements must be made at many angles, both at room temperature and cryogenic temperatures. It has already been explained that derived optical constants for high reflectivity samples such as gold can be unreliable and so the surface properties needed for simulations must be measured directly.

Thus, for computer models to reliably predict the performance of a passively cooled telescope, surface properties of candidate materials must be measured at many different angles, many different wavelengths, and many different temperatures. This is a major undertaking, but should be achievable before such missions are due to be launched. Such data would also be very useful to the wider infrared community and to designers of cryogenic systems.

Clearly, however, there will always be a certain amount of doubt about any computer model. The most useful types of experiment for planning such a mission will of course be precursor missions in space. Whether these consist of actual passively cooled designs (maybe scaled down versions) or conventional designs utilising some passive cooling technology, they will be vitally important in improving our understanding of the processes involved. Obviously this kind of experiment will cost large sums of money and will probably occur much closer to the launch date of a passively cooled mission.

Appendix A

An EDISON test problem

What are the equilibrium temperatures, T_1 and T_2, of two parallel plates of equal size given:

- The Sun as a distant source with a blackbody spectrum at 5780K radiating normal to plate 1 (i.e. no solar radiation reaches plate 2).
- Square plates (i.e. a = b, see figure A.1) with some fixed separation (c).
- All surfaces are grey and diffuse with same emissivity, absorptivity and reflectivity.
- The surroundings are at 0K.

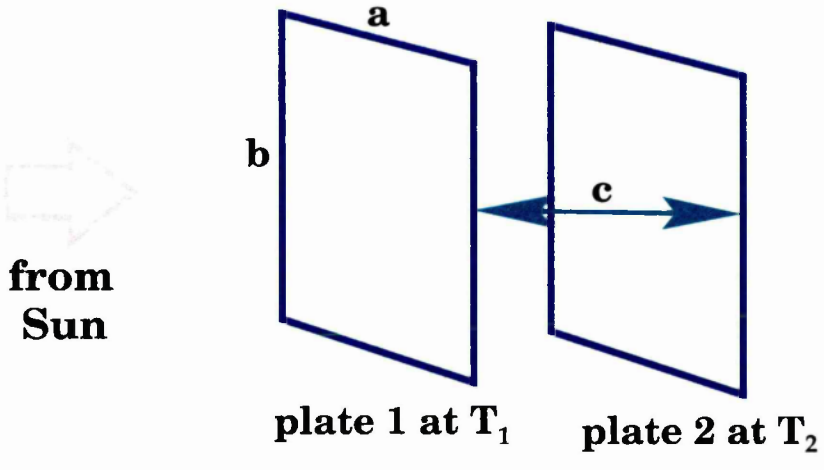

Figure A.1 Diagram of plate geometry.

A.1 Solution

If we assume the following:

- The temperatures T_1 and T_2 are uniform across each plate
- The surfaces are diffuse-grey (i.e $\alpha = \alpha'$, $\epsilon = \epsilon'$, $\alpha = \epsilon$, $\rho = 1 - \alpha = 1 - \epsilon$)
- The incident and reflected energy flux is uniform across each plate

then the radiative balance in equilibrium can be calculated using enclosure theory (as described in [17] §7-4. Unfortunately, the last assumption is a simplification and doesn't correctly describe the radiative exchange (particularly reflection) near the edges of the plates. For this reason, this treatment will only be accurate when one of the following criteria is satisfied

- α is high (little reflection)
- $\frac{c}{a}$ (or $\frac{c}{b}$) is large (approximately uniform irradiation)
- $\frac{c}{a}$ (or $\frac{c}{b}$) is small (edge effects insignificant)

Using enclosure theory, we simply define the energy incident on and output from both of the inner surfaces. Notice that the energy output from each surface consists of energy emitted by that surface plus any of the incident energy that is reflected.

Some energy also enters (or leaves) the system via the outer surfaces of the plates. When the plates are in equilibrium, the total energy absorbed by both surfaces of each plate must equal zero (by Kirchhoff's law). The energy balances are depicted graphically in figure A.2.

The outer surface of each plate will emit some fraction of a blackbody's emissive power defined by the plate's emissivity. The outer surface of plate 1 will also absorb some fraction of the incident solar radiation (defined by its absorptivity to solar radiation). Thus, we can say:

$$q_1 = \alpha'_{\odot} Q_{\odot} - \epsilon_1 \sigma T_1^4 \tag{A.1}$$

$$q_2 = -\epsilon_2 \sigma T_2^4 \tag{A.2}$$

where $\alpha'_{\odot}$ is the absorptivity of the outer surface of plate 1 for solar radiation normal to the surface, and $Q_{\odot}$ is the amount of solar radiation incident on the surface.

Clearly, Kirchhoff's law gives us the general relation:

$$q_n = q_{o,n} - q_{i,n} \tag{A.3}$$

For $n = 1$ or 2. This is simply stating that each plate is emitting as much energy as it is absorbing (i.e. it is in thermal equilibrium). Also, remember that $q_{o,n}$ consists of *reflected* as well as emitted radiation. This implies:

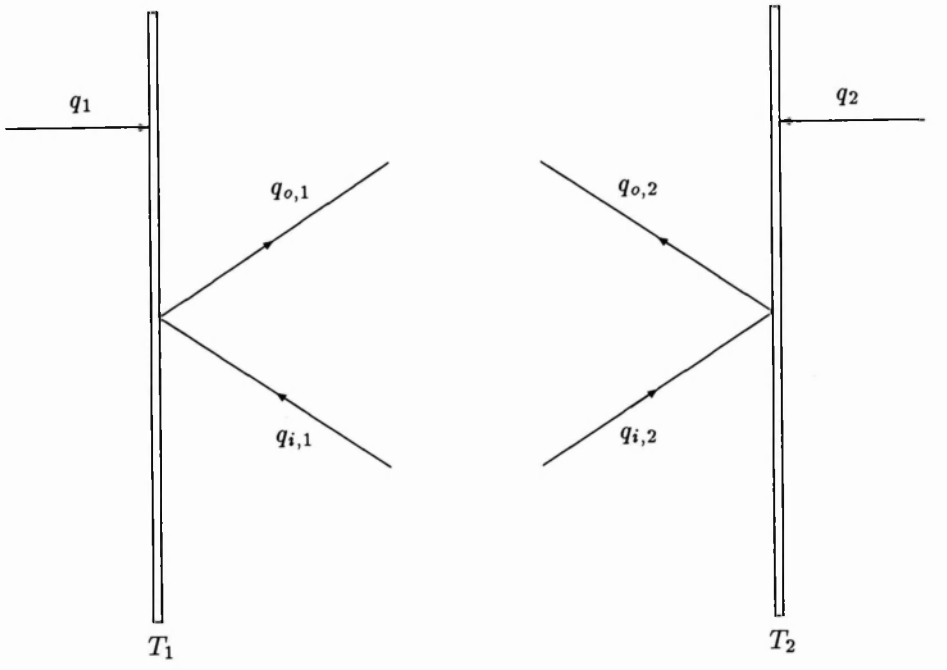

Figure A.2 The balance of energies for the two plate system

$$q_{o,n} = \epsilon_n \sigma T_n^4 + \rho_n q_{i,n} = \epsilon_n \sigma T_n^4 + (1 - \epsilon_n) q_{i,n} \tag{A.4}$$

The configuration factor (F) defines how much of the energy leaving one surface will arrive at the other surface. This allows us to say:

$$q_{i,1} = q_{o,2} F \tag{A.5}$$

Since this configuration of surfaces is symmetric, the configuration factor from plate 1 to plate 2 is the same as the configuration factor from plate 2 to plate 1. Thus, the above equation will hold if we swap the '1' and '2' suffixes.

Substituting the value of $q_{i,1}$ from equation A.4 into equation A.3 gives:

$$\begin{aligned} q_1 &= q_{o,1} - \frac{1}{1-\epsilon_1}(q_{o,1} - \epsilon_1 \sigma T_1^4) \\ &= \left(\frac{\epsilon_1}{1-\epsilon_1}\right)(\sigma T_1^4 - q_{o,1}) \end{aligned} \tag{A.6}$$

Also, substituting the value for $q_{i,1}$ from equation A.5 into equation A.3 gives an alternative expression for q_1:

$$q_1 = q_{o,1} - F q_{o,2} \tag{A.7}$$

Following the same logic yields the following equations for q_2:

$$q_2 = \left(\frac{\epsilon_2}{1-\epsilon_2}\right)(\sigma T_2^4 - q_{o,2}) \tag{A.8}$$

$$q_2 = q_{o,2} - F q_{o,1} \tag{A.9}$$

Solving for $q_{o,1}$ and $q_{o,2}$ from equations A.6 and A.8 gives:

$$q_{o,1} = \sigma T_1^4 - \frac{1-\epsilon_1}{\epsilon_1} q_1 \tag{A.10}$$

$$q_{o,2} = \sigma T_2^4 - \frac{1-\epsilon_2}{\epsilon_2} q_2 \tag{A.11}$$

Using this we can now substitute for $q_{o,1}$ and $q_{o,2}$ in equations A.7 and A.9:

$$q_1 = \sigma T_1^4 - \frac{1-\epsilon_1}{\epsilon_1} q_1 - F\left(\sigma T_2^4 - \frac{1-\epsilon_2}{\epsilon_2} q_2\right) \tag{A.12}$$

$$q_2 = \sigma T_2^4 - \frac{1-\epsilon_2}{\epsilon_2} q_2 - F\left(\sigma T_1^4 - \frac{1-\epsilon 1}{\epsilon 1} q_1\right) \tag{A.13}$$

Values for q_1 and q_2 have already been given in equations A.1 and A.2. Substituting these expressions into equations A.12 and A.13 yields:

$$(\alpha'_\odot Q_\odot - \epsilon_1 \sigma T_1^4) = \sigma T_1^4 - \frac{1-\epsilon_1}{\epsilon_1}(\alpha'_\odot Q_\odot - \epsilon_1 \sigma T_1^4) - F\left(\sigma T_2^4 + \frac{1-\epsilon_2}{\epsilon_2}\epsilon_2 \sigma T_2^4\right) \tag{A.14}$$

$$-\epsilon_2 \sigma T_2^4 = \sigma T_2^4 + \frac{1-\epsilon_2}{\epsilon_2}\epsilon_2 \sigma T_2^4 - F\left(\sigma T_1^4 - \frac{1-\epsilon_1}{\epsilon_1}(\alpha'_\odot Q_\odot - \epsilon_1 \sigma T_1^4)\right) \tag{A.15}$$

Now, if we solve equation A.14 for σT_1^4 we get:

$$\epsilon_1 \sigma T_1^4 + \sigma T_1^4 + \frac{1-\epsilon_1}{\epsilon_1}\epsilon_1 \sigma T_1^4 = \frac{1-\epsilon_1}{\epsilon_1}\alpha'_\odot Q_\odot + \alpha'_\odot Q_\odot + F\sigma T_2^4 + F\frac{1-\epsilon_2}{\epsilon_2}\epsilon_2 \sigma T_2^4 \tag{A.16}$$

$$\Rightarrow \sigma T_1^4 [1 + \epsilon_1 + (1 - \epsilon_1)] = \sigma'_\odot Q_\odot \left[1 + \frac{1 - \epsilon_1}{\epsilon_1}\right] + \sigma T_2^4 [F + F(1 - \epsilon_2)] \tag{A.17}$$

$$\Rightarrow \sigma T_1^4 = \frac{\sigma'_\odot Q_\odot}{2\epsilon_1} + \frac{\sigma T_2^4 F}{2} [2 - \epsilon_2] \tag{A.18}$$

Similarly, solving equation A.15 for σT_2^4 gives us:

$$\epsilon_2 \sigma T_2^4 + \sigma T_2^4 + \frac{1 - \epsilon_2}{\epsilon_2} \epsilon_2 \sigma T_2^4 = F \sigma T_1^4 - \frac{1 - \epsilon_1}{\epsilon_1} F \alpha'_\odot Q_\odot + \frac{1 - \epsilon_1}{\epsilon_1} F \epsilon_1 \sigma T_1^4 \tag{A.19}$$

$$\Rightarrow \sigma T_2^4 [1 + \epsilon_2 + (1 - \epsilon_2)] = -\sigma'_\odot Q_\odot \left[F \frac{1 - \epsilon_1}{\epsilon_1}\right] + \sigma T_1^4 [F + F(1 - \epsilon_1)] \tag{A.20}$$

$$\Rightarrow \sigma T_2^4 = \frac{\sigma'_\odot Q_\odot}{2} \left[F \frac{1 - \epsilon_1}{\epsilon_1}\right] + \frac{\sigma T_1^4 F}{2} [2 - \epsilon_1] \tag{A.21}$$

Now we substitute for σT_2^4 (from equation A.21) in equation A.18:

$$\sigma T_1^4 = \frac{\sigma'_\odot Q_\odot}{2\epsilon_1} + \left\{ \frac{\sigma'_\odot Q_\odot}{4} \left[F \frac{1 - \epsilon_1}{\epsilon_1}\right] + \frac{\sigma T_1^4 F}{4} [2 - \epsilon_1] \right\} [2 - \epsilon_2] F \tag{A.22}$$

$$\Rightarrow \sigma T_1^4 \left[1 - \frac{(2 - \epsilon_1)(2 - \epsilon_2) F^2}{4}\right] = \frac{\sigma'_\odot Q_\odot}{2\epsilon_1} \left[1 - \frac{(1 - \epsilon_1)(2 - \epsilon_2) F^2}{2}\right] \tag{A.23}$$

Thus, we can obtain a value for T_1 from equation A.23, and from there find T_2 from equation A.21. The only further piece of information required is the value of F, the configuration factor.

The configuration factor for two parallel finite planes [37] is given by the formula:

$$\begin{aligned} \mathrm{F} \;=\; & \frac{2}{\pi XY} \left\{ \ln \left[\frac{(1 + X^2)(1 + Y^2)}{1 + X^2 + Y^2}\right]^{\frac{1}{2}} + X\sqrt{1 + Y^2} \tan^{-1} \frac{X}{\sqrt{1 + Y^2}} + \right. \\ & \left. Y\sqrt{1 + X^2} \tan^{-1} \frac{Y}{\sqrt{1 + X^2}} - X \tan^{-1} X - Y \tan^{-1} Y \right\} \end{aligned} \tag{A.24}$$

Where $X = \frac{a}{c}$ and $Y = \frac{b}{c}$ (see figure A.1).

A.2 Comparing with the model

To test the model, the equilibrium temperatures of the plates were calculated for many values of the absorptivity (which in turn defined the emissivity and reflectivity by Kirchhoff's law) and the aspect ratio (N), defined as $\frac{a}{c}$ ($= \frac{b}{c}$ since the plates are square).

The model shows excellent agreement for $N < 10$ and $N > 100$. As mentioned above, unless N is either large or small enough, the enclosure theory arguments above do not hold. To check that this was the cause behind the disagreement between the analytical results and the Monte-Carlo results,

N	F (calculated)	α	T_1 (K) analytical result	T_1 (K) model result	T_1 (K) %error	T_2 (K) analytical result	T_2 (K) model result	T_2 (K) %error
0.1	3.16×10^{-3}	0.20	329.6	329.2	-0.12	44.0	44.3	0.68
1.0	0.19982	0.20	330.0	330.0	0.00	125.0	125.1	0.08
		0.50	330.3	330.2	-0.03	156.7	156.9	0.13
$3\frac{1}{3}$	0.579531	0.20	333.0	333.5	0.15	175.1	176.9	1.03
10	0.82700	0.20	340.5	342.2	0.50	216.3	222.8	3.01
		0.50	345.6	346.6	0.29	251.0	253.3	0.92
10^2	0.98042	0.20	358.0	359.5	0.42	268.9	272.6	1.38
10^3	0.99801	0.20	362.6	362.8	0.06	279.5	279.7	0.07
		0.50	360.1	360.1	0.00	286.1	286.2	0.03

Table A.1 A comparison of results from the Monte-Carlo model with those calculated analytically using enclosure theory

Barrie also produced a Monte-Carlo model. His model was much shorter, using a machine-supplied random number generator. Although it was based on the same basic ideas as my model, it was coded in a different language (PASCAL) and was designed solely for the solution of the two plate problem. The output from this second model agreed with my own results perfectly, implying it is the analysis that is at fault in the range $10 \leq N \leq 100$ rather than the model.

A complete list of parameters (N and α) and the corresponding temperatures (calculated and modeled) are shown in table A.1. Values of the configuration factor (F) are included for completeness.

Appendix B

Code for a Monte-Carlo model of a simplified EDISON geometry

```
#include <stdio.h>
#include <math.h>

/* Definitions for random number generator */
#define IM1 2147483563
#define IM2 2147483399
#define AM (1.0/IM1)
#define IMM1 (IM1-1)
#define IA1 40014
#define IA2 40692
#define IQ1 53668
#define IQ2 52774
#define IR1 12211
#define IR2 3791
#define NTAB 32
#define NDIV (1+IMM1/NTAB)
#define EPS 1.2e-7
#define RNMX (1.0-EPS)

float cdfd[101], ad[101], cdfg[101], ag[101], cdfb[101], ab[101];
long R, S, box[NTAB], iy;
```

```
float twopi = M_PI * 2;

/* Function to handle photon bundles bouncing between sunshields */
float bounce(int alpha, int N, char epsilon[], float a[], char rho[],
             float *reabsorb, float tandiff, float d, float angleone,
             float angletwo, float b, float l, float r);

/* Function to handle radiative transfer from Plane To Cylinder */
void ptc(int surfe, char epsilon[], char rho[], float a[], float *x, float *y,
         float *z, float i, float j, float k, float r, float h, float b,
         float d, float angletwo, float l);

/* Function to handle radiative transfer from Cylinder To Plane */
void ctp(int surfe, char epsilon[], char rho[], float a[], float *x, float *y,
         float *z, float i, float j, float k, float r, float h, float b,
         float d, float angletwo, float l);

/* Function to calculate amount of solar energy absorbed per time step */
float sun(float solarflux, float su1, int N);

/* Funstion to calculate whether a surface will absorb a photon bundle */
float absorb(float theta, char e);

/* Function to initialise the Cumulative Distribution Functions required */
void initcdf();

/* Function to calculate the angle of emission/reflection of a photon bundle */
float angle(char e);

/* Function to initialise random number generator */
void initran();

/* Random number generator */
```

```
float myrandom();

main()
{
  char epsilon[5], rho[5];
  float T[3], e[5], a[5], C[3];
  float theta, phi, angleone, angletwo, tandiff;
  float x, y, z, i, j, k, r, h, b, l, d;
  float dE, dt, reabsorb, alpha;
  double sigma = 5.729e-8;                    /* Stefan-Boltzmann constant */
  double sigmaone;
  float solarflux = 1353;                  /* Watts per square metre at 1 A.U. */
  float hits = 0.0;
  float power, eb[3];
  int p, ts, n, N;

  initcdf();              /* Generate the cumulative distribution function */
  initran();              /*        Initialise the random number generator */

  fprintf(stderr, "\nPlease input the height, width, and temperature of the
                  outer shield (m & K)\n");
  scanf("%f %f %f", &l, &b, &T[0]);

  fprintf(stderr, "\nPlease input the emissivity and absorptivity of surface
                  1\n");              /* Sun facing surface of outer shield */
  scanf("%f %f", &e[0], &a[0]);

  fprintf(stderr, "\nPlease input the emissivity and absorptivity of surface
                  2\n");                    /* Inner surface of outer shield */
  scanf("%f %f", &e[1], &a[1]);

  fprintf(stderr, "\nPlease input the emission characteristics of surface 2
                  (d/g/b)\n");
```

```
scanf("%s", &epsilon[0]);

fprintf(stderr, "\nPlease input the reflection characteristics of surface 2
                (d/s)\n");
scanf("%s", &rho[0]);

fprintf(stderr, "\nPlease input the heat capacity of the outer shield
                (J/K)\n");
scanf("%f", &C[0]);

fprintf(stderr, "\nPlease input the temperature of the inner shield (K)\n");
                  /* Height and width assumed to be same as outer shield */
scanf("%f", &T[1]);

fprintf(stderr, "\nPlease input the emissivity and absorptivity of surface
                3\n");                  /* Outer surface of inner shield */
scanf("%f %f", &e[2], &a[2]);

fprintf(stderr, "\nPlease input the emission characteristics of surface 3
                (d/g/b)\n");
scanf("%s", &epsilon[1]);

fprintf(stderr, "\nPlease input the reflection characteristics of surface 3
                (d/s)\n");
scanf("%s", &rho[1]);

fprintf(stderr, "\nPlease input the emissivity and absorptivity of surface
                4\n");                  /* Inner surface of inner shield */
scanf("%f %f", &e[3], &a[3]);

fprintf(stderr, "\nPlease input the emission characteristics of surface 4
                (d/g/b)\n");
scanf("%s", &epsilon[2]);
```

```
fprintf(stderr, "\nPlease input the reflection characteristics of surface 4
                (d/s)\n");
scanf("%s", &rho[2]);

fprintf(stderr, "\nPlease input the heat capacity of the inner shield
                (J/K)\n");
scanf("%f", &C[1]);

fprintf(stderr, "\nPlease input the radius, height and temperature of the
                cylinder (m & K)\n");
scanf("%f %f %f", &r, &h, &T[2]);

fprintf(stderr, "\nPlease input the emissivity and absorptivity of the
                cylinder\n");
                    /* Outer surface (excluding the open end, of course) */
scanf("%f %f", &e[4], &a[4]);

fprintf(stderr, "\nPlease input the emission characteristics of the cylinder
                (d/g/b)\n");
scanf("%s", &epsilon[3]);

fprintf(stderr, "\nPlease input the reflection characteristics of the
                cylinder (d/s)\n");
scanf("%s", &rho[3]);

fprintf(stderr, "\nPlease input the heat capacity of the cylinder (J/K)\n");
scanf("%f", &C[2]);

fprintf(stderr, "\nPlease input the minimum separation between the cylinder
                and inner shield\n");
scanf("%f", &d);
```

```
  fprintf(stderr, "\nPlease input the angle to the vertical of the inner shield
                   (degrees)\n");
  scanf("%f", &angletwo);
  angletwo *= M_PI / 180.0;

  fprintf(stderr, "\nPlease input the angle to the vertical of the outer shield
                   (degrees)\n");
  scanf("%f", &angleone);
  angleone *= M_PI / 180.0;

  tandiff = tan(angletwo) - tan(angleone);                  /* Useful later */

  fprintf(stderr, "\nPlease input the length of time step (s)\n");
  scanf("%f", &dt);

  fprintf(stderr, "\nPlease input the number of time steps\n");
  scanf("%d", &ts);                        /* dt x ts = length of simulation */

  fprintf(stderr, "\nPlease input the number of bundles per step\n");
  scanf("%d", &N);

/* Let's cut down on the number of multiplications */

  sigmaone = sigma * dt * e[4] * M_PI * r;        /* Used with the cylinder */
  sigma *= dt * l * b;                  /* Used when considering the shields */
  solarflux *= l * b * dt;      /* Solar energy absorbed by outer shield in */
                                /* one time step.                           */

/* Right, let's start some work!!  */

  for(p = 0 ; p < ts ; p++)                     /* Run for "ts" time steps */
    {
/* Consider surface 1 (outer surface of outer sunshield) */
```

```
      power = pow(T[0], 4) * sigma * e[0];    /* Emitted power from the     */
                                              /* surface for this time step */
      eb[0] = sun(solarflux, a[0], N) - power;   /* Add absorbed solar flux */
                                          /* to energy balance       */
/* Consider surface 2 (inner surface of outer sunshield) */

      power *= e[1] / e[0];
      dE = power / N;        /* Energy per photon bundle for this time step */

      hits = bounce(0, N, epsilon, a, rho, &reabsorb, tandiff, d, angleone,
             angletwo, b, 1, r);          /* Find number of photon bundles */
                                          /* hitting other surface         */

      eb[0] += reabsorb * dE - power; /* Bundles reabsorbed by this surface */
      eb[1] = hits * dE;              /* Bundles absorbed by other surface */

/* Consider surface 3 (outer surface of inner sunshield) */

      power = pow(T[1], 4) * sigma * e[2];      /* Energy per photon bundle */
      dE = power / N;             /* recalculated to account for different */
                                          /* emissivity of this surface */

      hits = bounce(1, N, epsilon, a, rho, &reabsorb, tandiff, d, angleone,
                    angletwo, b, 1, r);       /* Intra sunshield exchanges */

      eb[1] += reabsorb * dE - power;
      eb[0] += hits * dE;     /* Bundles absorbed by each surface as before */

/* Consider surface 4 (inner surface of inner sunshield) */

      power *= e[3] / e[2];
      dE = power / N;           /* Photon bundle energy again recalculated */
```

```
      reabsorb = 0;          /* Variables have to be reset outside the ptc() */
      hits = 0;             /* function as it is recursively called by ctp() */

      for(n = 0 ; n < N ; n++)
{
  y = myrandom() * b - b/2;     /*In range -b/2 to +b/2*/
  z = myrandom() * l;
  x = r + d + z * tan(angletwo);   /* Random point on the sunshield */

  theta = angle(epsilon[2]);            /* Random angle of emission */
  phi = myrandom() * twopi;

  i = sin(theta)*sin(phi)*sin(angletwo) - cos(theta)*cos(angletwo);
  j = sin(theta)*cos(phi);
  k = sin(theta)*sin(phi)*cos(angletwo) + cos(theta)*sin(angletwo);
                    /* Find component vectors of the direction of emission */

  ptc(2, epsilon, rho, a, &x, &y, &z, i, j, k, r, h, b, d, angletwo, l);
              /* Send photon bundles from Plane To Cylinder, bounce as much */
              /* as necessary and return descriptive x,y,z values           */

  if(x == -1 && y == -1 && z == -2)
    hits += dE;                              /* Absorbed by cylinder */
  else
    if(x == -1 && y == -1 && z == -3)
      reabsorb += dE;                     /* Reabsorbed by sunshield */
  else
    if(!(x == -1 && y == -1 && z == -1))        /* Shouldn't happen */
      printf("\nDanger Will Robinson!!!! (plane)\n\n");
}

      eb[1] += reabsorb - power;
```

```
      eb[2] = hits;                                /* Update energy balances */

/* Consider curved cylinder surface */

      power = pow(T[2], 4) * sigmaone * 2 * h;
      dE = power / N;                 /* Photon energy recalculated as usual */

      reabsorb = 0;                               /* Variables reset as before */
      hits = 0;

      for(n = 0 ; n < N ; n++)
{
  alpha = myrandom() * twopi;    /* Random angle defines random       */
  y = r * cos(alpha);            /* point on curved cylinder surface */
  x = r * sin(alpha);

  if(x >= 0)
    {
      z = myrandom() * h;               /* Random height on cylinder */

      theta = angle(epsilon[3]);         /* Random angle of emission */
      phi = myrandom() * twopi;

      i = sin(theta)*cos(phi)*cos(alpha) + cos(theta)*sin(alpha);
      j = cos(theta)*cos(alpha) - sin(theta)*cos(phi)*sin(alpha);
      k = sin(theta) * sin(phi);
            /* Component vectors of emission direction calculated once more */

         ctp(3, epsilon, rho, a, &x, &y, &z, i, j, k, r, h, b, d, angletwo, 1);
              /* Send photon bundle from Cylinder To Plane, bounce as much */
              /* as necessary and return descriptive x,y,z values          */

      if(x == -1 && y == -1 && z == -3)
```

```
        hits += dE;                    /* Absorbed by the sunshield */
      else
        if(x == -1 && y == -1 && z == -2)
          reabsorb += dE;              /* Reabsorbed by the cylinder */
      else
        if(!(x == -1 && y == -1 && z == -1))    /* Shouldn't happen */
          printf("\nDanger Will Robinson!!! (cylinder)\n\n");
    }
        }

      eb[1] += hits;                              /* Update energy balances */
      eb[2] += reabsorb - power;

/* Consider cylinder ends */

      power *= r / (2 * h);              /* (pi r^2) instead of (2 pi r h) */

      power += power * 0.8 / e[4];               /* One end at e[4] and one */
                                                 /* nearly black surface    */
      eb[2] -= power;                            /* emit into empty space   */

/* Now balance up the energies */

      eb[0] -= conduction * (T[0] - T[1]);             /* Simple treatment */
      eb[1] += conduction * (T[0] - T[1]);             /* of conduction    */
      eb[1] -= conduction * (T[1] - T[2]);
      eb[2] += conduction * (T[1] - T[2]);

      T[0] += eb[0] / C[0];          /* Calculate temperatures for next time */
      T[1] += eb[1] / C[1];          /* step using heat capacitancies        */
      T[2] += eb[2] / C[2];

      printf("%13.12f\t%13.12f\t%13.12f\n", T[0], T[1], T[2]);
```

```
                        /* Print out the results for latest time step */
    }

}

float bounce(int alpha, int N, char epsilon[], float a[], char rho[],
             float *reabsorb, float tandiff, float d, float angleone,
             float angletwo, float b, float l, float r)
                   /* Follow photon bundles bouncing between the sunshields */
{
  float theta, phi, topangle, bottomangle, tmpangle;
  float i, j, k, iprime, kprime;
  float x, y, z, q;
  int surfe, n, multiple;
  float hits = 0.0;
  *reabsorb = 0;

  for(n = 0 ; n < N ; n++)
    {
      surfe = alpha;              /* Emitting surface (passed from main() ) */
      y = myrandom() * b - b/2;
      z = myrandom() * l;                       /* Random point of emission */

      x = r + d*(2 - surfe) + z*tan(surfe ? angletwo : angleone);
          /* x co-ordinate defined by z co-ord + angle of tilt of sunshield */

      if(surfe)         /* Which shield are we considering this time round? */
{
  multiple = 1;
  topangle = angletwo;
  bottomangle = angleone;
}
      else          /* Key variables are defined by shield being considered */
```

```
{
  multiple = -1;
  topangle = angleone;
  bottomangle = angletwo;
}

      theta = angle(epsilon[alpha]);          /* Random emission direction */
      phi = myrandom() * twopi;

      iprime = multiple * cos(theta);
      j = sin(theta) * cos(phi);              /* Since j' = j */
      kprime = sin(theta) * sin(phi);

      i = iprime*cos(topangle) + kprime*sin(topangle); /* Component vectors */
      k = kprime*cos(topangle) - iprime*sin(topangle); /* of emission dirn. */
                  /* Component vectors of emission direction are calculated */

      while(1)     /* Infinite loop 'till photon bundle is absorbed or lost */
        {
  q = multiple * (d - z*tandiff) / (i - k*tan(bottomangle));
  /* No. of multiples of unit direction vector needed to reach other shield */

  x += q*i;
  z += q*k;                    /* Scale component vectors accordingly */

  if(z < 0 || z > 1)
    break;
  y += q*j;
  if(y < -b/2 || y > b/2)          /* Does it miss the other shield? */
    break;                           /* If so, break out of the loop */

  theta = acos(multiple * (i*cos(bottomangle) - k*sin(bottomangle)));
                  /* Angle to normal of incident direction on other shield */
```

```
  if(myrandom() <= (absorb(theta, epsilon[alpha]) * a[alpha+1]))
                                                    /* Is it absorbed? */
    {
      if(surfe == alpha)
++hits;        /* If so, is it absorbed by the other shield */
      else
++*reabsorb;       /* or reabsorbed by the emitting surface */
      break;
    }

  multiple *= -1;
  tmpangle = topangle;              /* Set up any changing variables */
  topangle = bottomangle;           /* for the next loop             */
  bottomangle = tmpangle;
    surfe = (surfe ? 0 : 1);

  if (rho[surfe] == 's')                    /* Specular reflection */
    {                   /* (direction defined by incoming direction */
      iprime = i;
      i = k*sin(2 * topangle) - iprime*cos(2 * topangle);
      k = iprime*sin(2 * topangle) + k*cos(2 * topangle);
    }
  else                      /* Diffuse reflection (as if re-emitted) */
    {
      theta = angle(epsilon[alpha]);    /* Random angle of emission */
         phi = myrandom() * twopi;  /* unrelated to incoming direction */

            iprime = multiple * cos(theta);
             j = sin(theta) * cos(phi); /* Since j' = j */
         kprime = sin(theta) * sin(phi);

      i = iprime*cos(topangle) + kprime*sin(topangle);
```

```
      k = kprime*cos(topangle) - iprime*sin(topangle);
                /* Component vectors of emission direction calculated again */
       }
        }
    }
 return hits;
}

void ptc(int surfe, char epsilon[], char rho[], float a[], float *x, float *y,
         float *z, float i, float j, float k, float r, float h, float b,
         float d, float angletwo, float l)
                          /* Follow photon bundles from Plane To Cylinder */
{
  float n, oldi, theta, phi;
  float temp, beta;

  n = (r * r *( i * i + j * j)) - ((i * *y - j * *x)*(i * *y - j * *x));
  if(n < 0)                       /* Does equation 3.8 have a real solution? */
    {
      *x = *y = *z = -1;
      return;                     /* If not, set x,y,z and break out of loop */
    }


  temp = (i * *x + j * *y);

  n = (temp < 0 ? temp + sqrt(n) : temp - sqrt(n));  /* + or - in equ. 3.8? */

  n *= (-1) / (i * i + j * j);
                         /* Multiple of unit vector which reaches cylinder */

  *x += n * i;
  *y += n * j;           /* Scale vectors to point of incidence on cylinder */
```

```
*z += n * k;

if(*z > h || *z < 0)                          /* Does it miss the cylinder? */
  {
    *x = *y = *z = -1;
    return;                        /* If so, set x,y,z and break out of loop */
  }

n = (i * *x + j * *y) / r;          /* Dot product with normal to cylinder */

n *= (-1);                        /* To make sure theta is 0-pb2, NOT pb2-pi! */
theta = acos(n);      /* Angle of incident direction to normal to cylinder */


if(myrandom() <= (absorb(theta, epsilon[surfe]) * a[surfe + 1]) )
  {                                      /* Is it absorbed by the cylinder? */
    *x = *y = -1;
    *z = -2;
    return;                        /* If so, set x,y,z and break out of loop */
  }

if(rho[3] == 's')                                    /* Specular reflection */
  {
    oldi = i;                               /* Since we're about to modify i */

    beta = 2 * atan(*x / *y);         /* in fact this is 2*alpha-in-thesis, */
                                      /* since that's what we need here     */
    i = oldi*cos(beta) - j*sin(beta);
    j = -oldi*sin(beta) - j*cos(beta);
  }
else                                /* Diffuse reflection (as if re-emitted) */
  {
    theta = angle('d');
```

```
      phi = myrandom() * twopi;
      beta = atan(*x / *y);

      i = sin(theta)*cos(phi)*cos(beta) + cos(theta)*sin(beta);
      j = cos(theta)*cos(beta) - sin(theta)*cos(phi)*sin(beta);
      k = sin(theta) * sin(phi);
    }

  ctp(surfe, epsilon, rho, a, x, y, z, i, j, k, r, h, b, d, angletwo, l);
                                    /* Bounce back from Cylinder To Plane */
}

void ctp(int surfe, char epsilon[], char rho[], float a[], float *x, float *y,
         float *z, float i, float j, float k, float r, float h, float b,
         float d, float angletwo, float l)
                          /* Follow photon bundles from Cylinder To Plane */
{
  float n, theta, phi, oldi;

  if( i <= 0 )                  /* Instant check if it'll hit the sunshield */
    {
      *x = *y = *z = -1;
      return;                    /* If not, set x,y,z and break out of loop */
    }

  n = (r + d - *x + *z * tan(angletwo)) / ( i - k * tan(angletwo));
                          /* ^^^^How far to sunshield? */
  *y += n * j;
  *z += n * k;                        /* Scale vectors to point of incidence */

  if(*y > b/2 || *y < -b/2 || *z > l || *z < 0)
    {                                       /* Does it miss the sunshield? */
      *x = *y = *z = -1;
```

```
    return;                          /* If so, set x,y,z and break out of loop */
  }

*x += n * i;                                /* Don't scale x unless you need to */

n = i * cos(angletwo) - k * sin(angletwo);      /* Dot product with normal */
theta = acos(n);                                    /* Angle of incidence */

if(myrandom() <= (absorb(theta, epsilon[surfe]) * a[surfe + 1]) )
  {                                        /* Is it absorbed by the sunshield? */
    *x = *y = -1;
    *z = -3;
    return;                          /* If so, set x,y,z and break out of loop */
  }

if(rho[2] == 's')                                    /* Specular reflection */
  {
    oldi = i;                                 /* Since we're about to modify i */

    i = k*sin(2*angletwo) - oldi*cos(2*angletwo);
    k = oldi*sin(2*angletwo) + k*cos(2*angletwo);
  }
else                                  /* Diffuse reflection (as if re-emitted) */
  {
    theta = angle('d');
    phi = myrandom() * twopi;

    i = sin(theta)*sin(phi)*sin(angletwo) - cos(theta)*cos(angletwo);
    j = sin(theta) * cos(phi);
    k = sin(theta)*sin(phi)*cos(angletwo) + cos(theta)*sin(angletwo);
  }

ptc(surfe, epsilon, rho, a, x, y, z ,i, j, k, r, h, b, d, angletwo, l);
```

```
                                /* Bounce it back from Plane To Cylinder */
}

float sun(float solarflux, float su1, int N)
{                       /* Calculate solar flux absorbed by outer sunshield */
  float z = solarflux / N;
  float balance = 0;
  int q;

  for(q = 0 ; q < N ; q++)           /* For each photon bundle from the Sun */
    {
      if(myrandom() <= su1)  /* See if it will be absorbed by the sunshield */
 balance += z;            /* and add to the energy balance if it is */
    }

  return balance;                       /* Amount of solar energy absorbed */
}

float absorb(float theta, char e)   /* Check whether photon bundles are     */
{                                   /* absorbed given emissivity properties */
  float y;                          /* and angle of incidence               */
  int c, b;

  theta *= 200 / M_PI;         /* Relate theta to the array of 100 elements */
  c = theta;
  b = c + 1;
  theta -= c;        /* Extrapolate from c to c+1 by the fraction remaining */

  switch (e)
    {
    case 'd':                                          /* Diffuse properties */
      y = ((ad[b] - ad[c]) * theta) + ad[c];
      break;
```

```
    case 'g':                                          /* Properties of Gold */
      y = ((ag[b] - ag[c]) * theta) + ag[c];
      break;

    case 'b':                                          /* Bizarre properties */
      y = ((ab[b] - ab[c]) * theta) + ab[c];
      break;
    }
  return y;                  /* Absorptivity for that surface at that angle */
}

void initcdf()                 /* Generate cumulative distribution function */
{
  double I = 0;
  double parallel, perpend, e, th, ct, sub;
  float n, k, step, b;
  float pb2 = M_PI/2;
  int z = 0;
  n = 7.62;
  k = 71.5;
  step = M_PI / 20000;               /* Integrate funstion over 1000 steps */

  for(th = 0 ; th <= pb2 ; th += step)
    {
      ct = cos(th);
      parallel = 4*n*ct/((n*n+k*k)*(ct*ct)+2*n*ct+1);
      perpend = 4*n*ct/(ct*ct+2*n*ct+n*n+k*k);
      e = (parallel + perpend)/2;              /* Emissivity at this angle */
      if(th/pb2 >= z/100.0)              /* 100 steps from 0 -> 90 degrees */
{                                    /* (one for each array element) */
  ag[z] = e;            /* Generate lookup tables of absorptivities */
  z++;
```

```
}

      e *= step*sin(th)*ct*2;                    /* 2 comes from S&H equ. 3-5 */
      I += e;                                        /* Numerical integration */
    }
  ag[z] = sub = cdfg[0] = th = 0;                          /* Tie up loose ends */
  z = 1;
  b = 0.01;                                                  /* Reset variables */

  do
    {
      ct = cos(th);
      parallel = 4*n*ct/((n*n+k*k)*(ct*ct)+2*n*ct+1);
      perpend = 4*n*ct/(ct*ct+2*n*ct+n*n+k*k);
      e = (parallel + perpend)/2;                /* Emissivity at this angle */
      e *= step*sin(th)*ct*2;
      sub += e;                                      /* Numerical integration */
      if(sub/I > b)                    /* Integral from 0 -> theta divided by */
{                              /* integral from 0 -> 90 = CDF          */
  cdfg[z] = th;
  z++;
  b += 0.01;                                               /* 100 steps */
}
      th += step;
    }
  while(b <= 1.0);

  z = I = 0;                                                 /* Reset variables */
  n = 56.6;          /* And repeat above steps for different n and k values */
  k = 192;

  for(th = 0 ; th <= pb2 ; th += step)
    {
```

```
      ct = cos(th);
      parallel = 4*n*ct/((n*n+k*k)*(ct*ct)+2*n*ct+1);
      perpend = 4*n*ct/(ct*ct+2*n*ct+n*n+k*k);
      e = (parallel + perpend)/2;
      if(th/pb2 >= z/100.0)
{
  ad[z] = e;
  z++;
}

      e *= step*sin(th)*ct*2;         /* 2 comes from S&H equ. 3-5 */
      I += e;
    }
  ad[z] = sub = cdfd[0] = th = 0;
  z = 1;
  b = 0.01;

  do
    {
      ct = cos(th);
      parallel = 4*n*ct/((n*n+k*k)*(ct*ct)+2*n*ct+1);
      perpend = 4*n*ct/(ct*ct+2*n*ct+n*n+k*k);
      e = (parallel + perpend)/2;
      e *= step*sin(th)*ct*2;
      sub += e;
      if(sub/I > b)
{
  cdfd[z] = th;
  z++;
  b += 0.01;
}
      th += step;
    }
```

```
  while(b <= 1.0);

  z = I = 0;
  n = 239;
  k = 404;

  for(th = 0 ; th <= pb2 ; th += step)
    {
      ct = cos(th);
      parallel = 4*n*ct/((n*n+k*k)*(ct*ct)+2*n*ct+1);
      perpend = 4*n*ct/(ct*ct+2*n*ct+n*n+k*k);
      e = (parallel + perpend)/2;
      if(th/pb2 >= z/100.0)
{
  ab[z] = e;
  z++;
}

      e *= step*sin(th)*ct*2;          /* 2 comes from S&H equ. 3-5 */
      I += e;
    }
  ab[z] = sub = cdfb[0] = th = 0;
  z = 1;
  b = 0.01;

  do
    {
      ct = cos(th);
      parallel = 4*n*ct/((n*n+k*k)*(ct*ct)+2*n*ct+1);
      perpend = 4*n*ct/(ct*ct+2*n*ct+n*n+k*k);
      e = (parallel + perpend)/2;
      e *= step*sin(th)*ct*2;
      sub += e;
```

```
      if(sub/I > b)
{
  cdfb[z] = th;
  z++;
  b += 0.01;
}
      th += step;
    }
  while(b <= 1.0);
}

float angle(char e)              /* Generate a random angle weighted by the */
{                                /* appropriate emissive properties         */
  float r, y;
  int b, c;

  r = myrandom();
  r *= 100;                                    /* Random number from 0-100 */
  c = r;
  b = c + 1;
  r -= c;            /* Extrapolate between c and c+1 by fraction remaining */

  switch (e)
    {
    case 'd':                                          /* Diffuse properties */
      y = ((cdfd[b] - cdfd[c]) * r) + cdfd[c];
      break;

    case 'g':                                          /* Properties of Gold */
      y = ((cdfg[b] - cdfg[c]) * r) + cdfg[c];
      break;

    case 'b':                                          /* Bizarre properties */
```

```
      y = ((cdfb[b] - cdfb[c]) * r) + cdfb[c];
      break;
    }
  return y;                              /* Correctly weighted random angle */
}

void initran()                         /* Initialise the random number generator */
{                                      /* (from numerical recipes in C)          */
  int j;
  long k;

  fprintf(stderr, "\nPlease input seed for random number generator\n");
  scanf("%ld", &R);
  if(R < 1)
    R = 1;

  S = R;

  for(j = NTAB+50 ; j >= 0 ; j--)
    {
      k = R / IQ1;
      R = IA1 * (R - k * IQ1) - k * IR1;

      if(R < 0)
R += IM1;

      if(j < NTAB)
box[j] = R;
    }
  iy = box[0];
}

float myrandom()                       /* Generate univariate random numbers */
```

```
{                                       /* (from numerical recipes in C)      */
  int j;
  long k;
  float temp;

  k = R / IQ1;
  R = IA1 * (R - k * IQ1) - k * IR1;
  if(R < 0)
    R += IM1;

  k = S / IQ2;
  S = IA2 * (S - k * IQ2) - k * IR2;
  if (S < 0)
    S += IM2;

  j = iy / NDIV;
  iy = box[j] - S;
  box[j] = R;
  if(iy < 1)
    iy += IMM1;

  if((temp=AM*iy) > RNMX)
    return RNMX;
  else
    return temp;
}
```

Appendix C

Experimental data

Presented here is a summary of all the experimental data collected during my study and discussed in chapters 5 and 6.

C.1 Graphs

Below is a collection of figures graphically showing the averaged data for each sample at each wavelength.

C.1.1 633nm

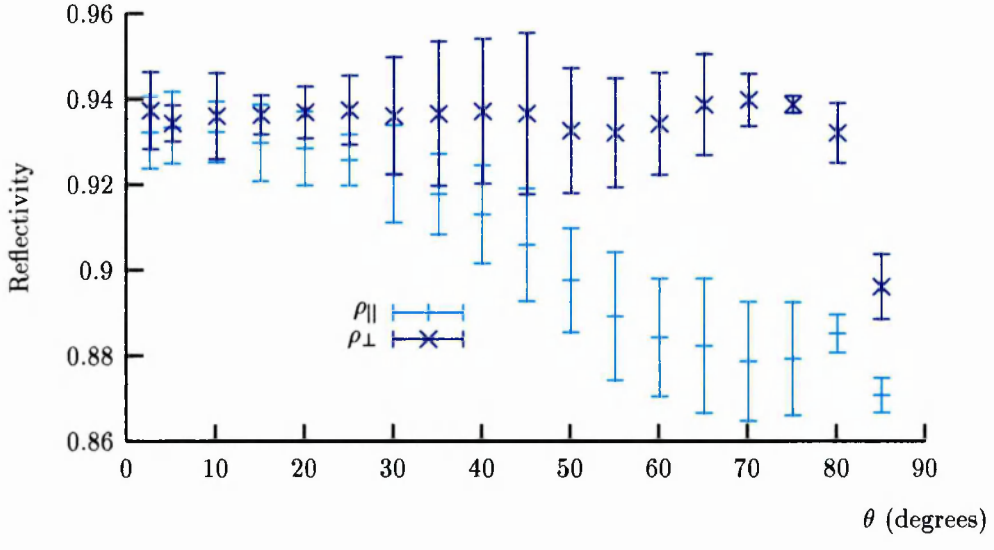

Figure C.1 421-53-3c at 633nm

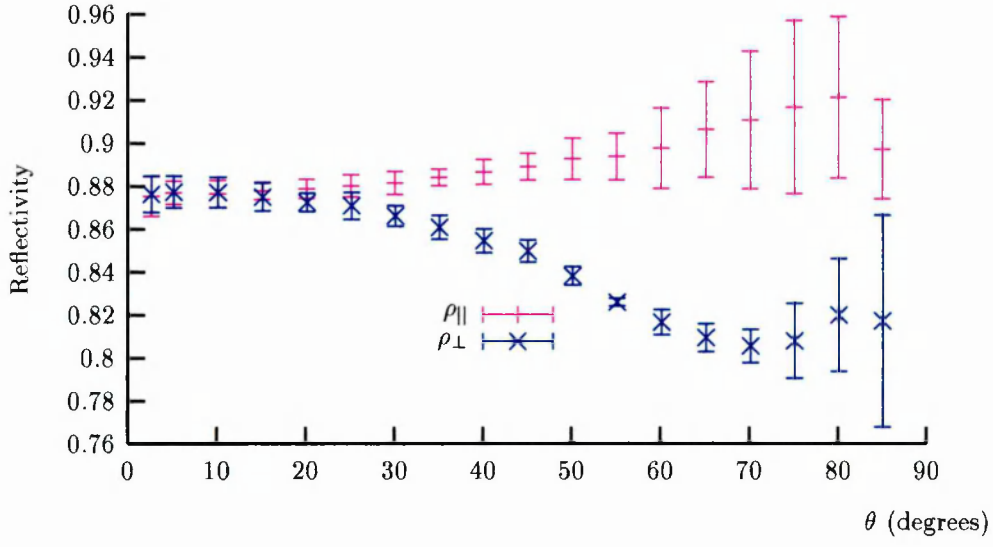

Figure C.2 dsi-1611-g at 633nm

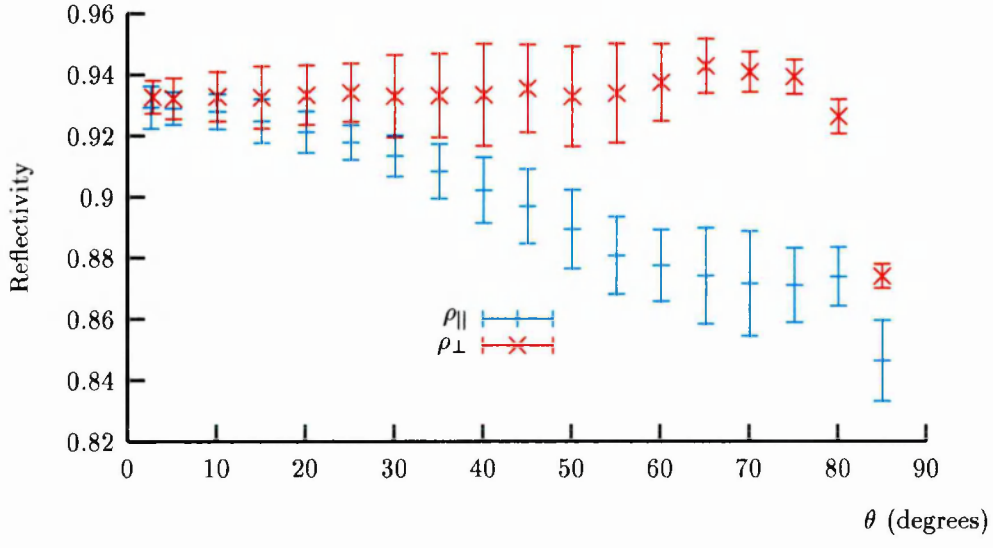

Figure C.3 dsi-1917-3 at 633nm

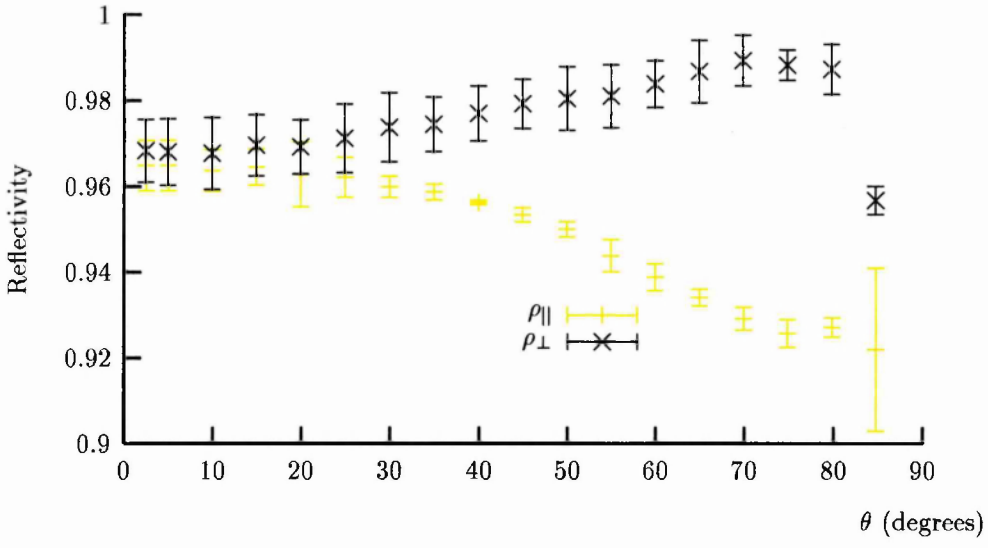

Figure C.4 khag at 633nm

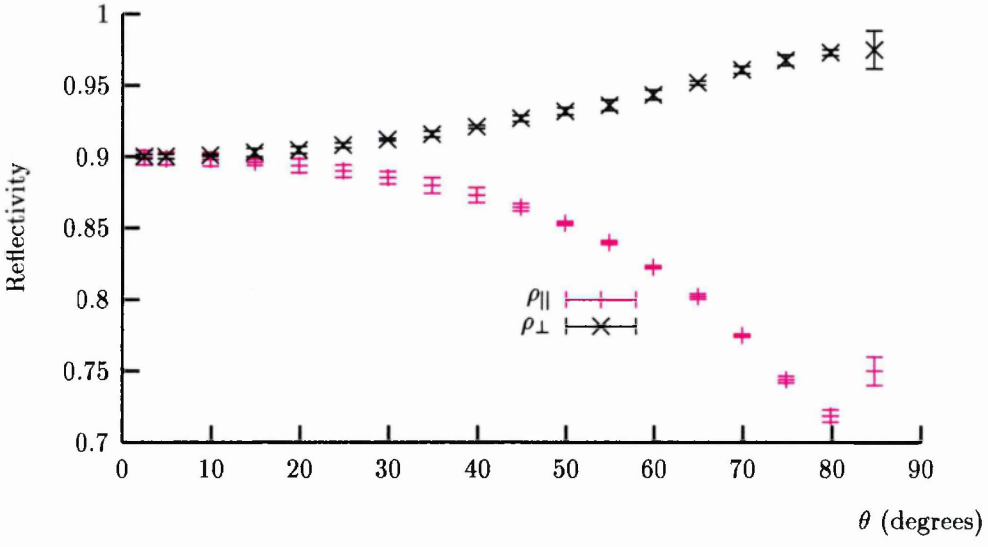

Figure C.5 khal at 633nm

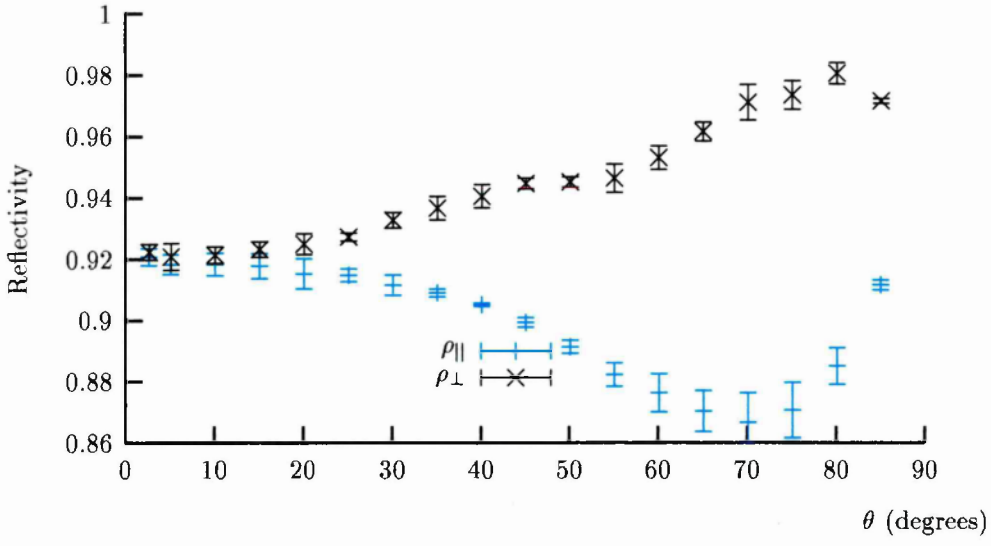

Figure C.6 origgold at 633nm

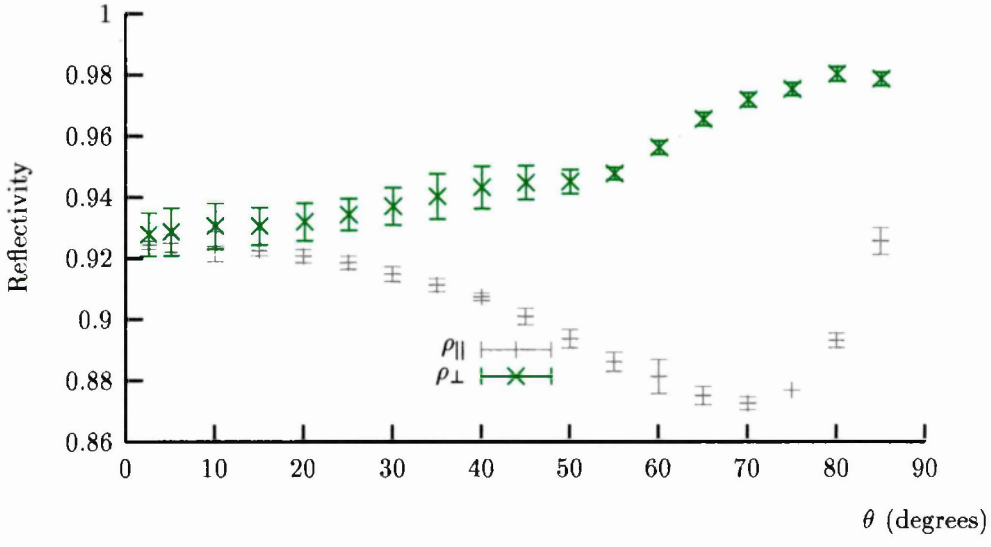

Figure C.7 roe1 at 633nm

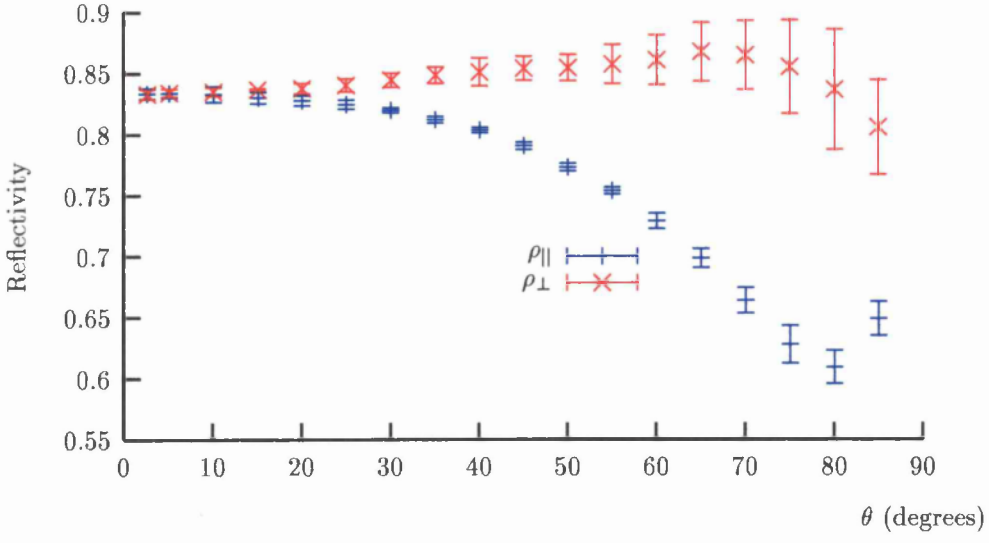

Figure C.8 wht-4g at 633nm

C.1.2 1152nm

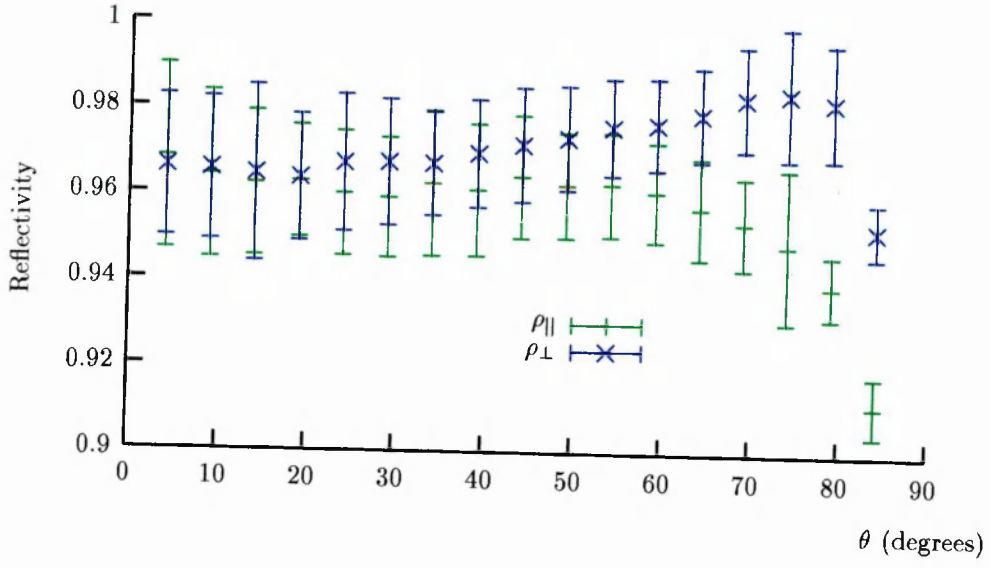

Figure C.9 421-53-3c at 1152nm

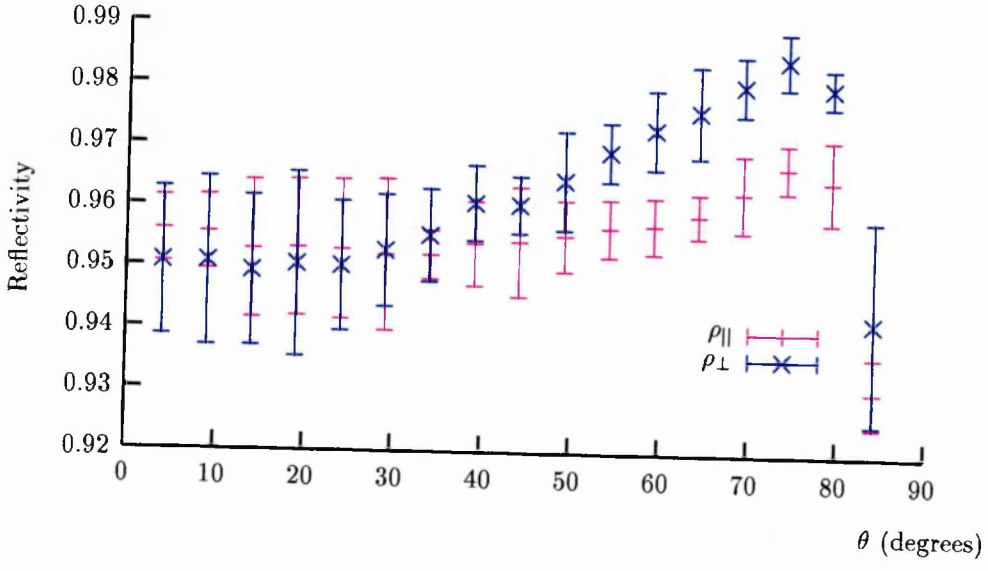

Figure C.10 dsi-1611-g at 1152nm

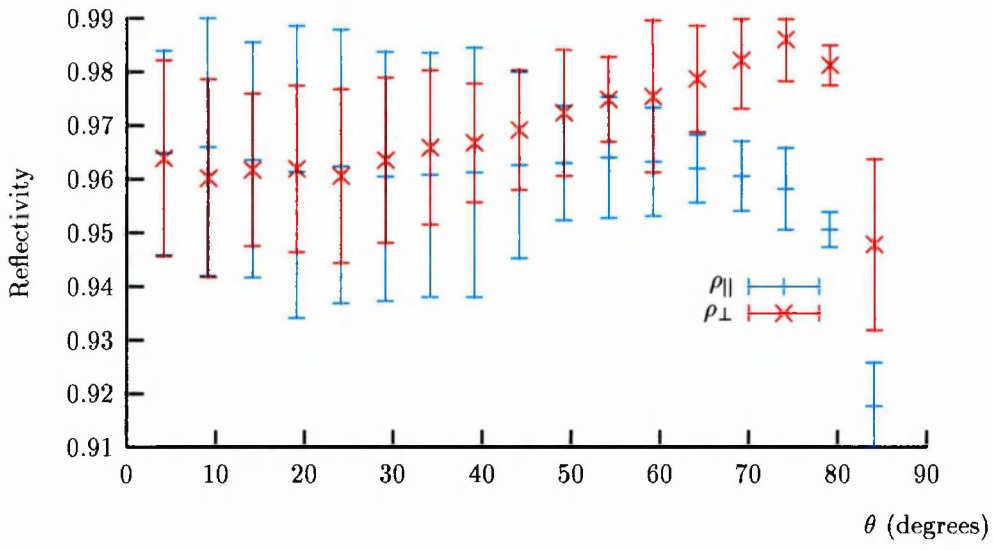

Figure C.11 dsi-1917-3 at 1152nm

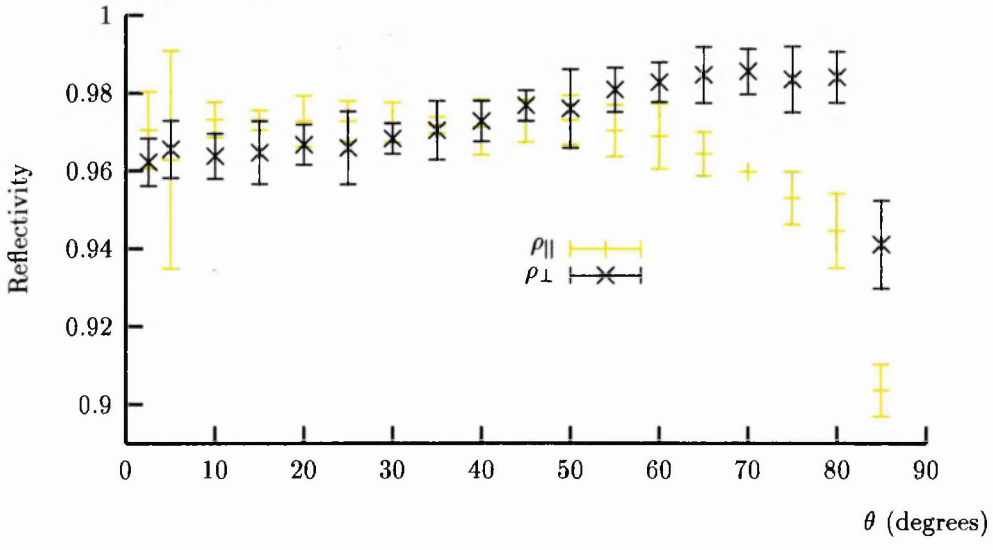

Figure C.12 khag at 1152nm

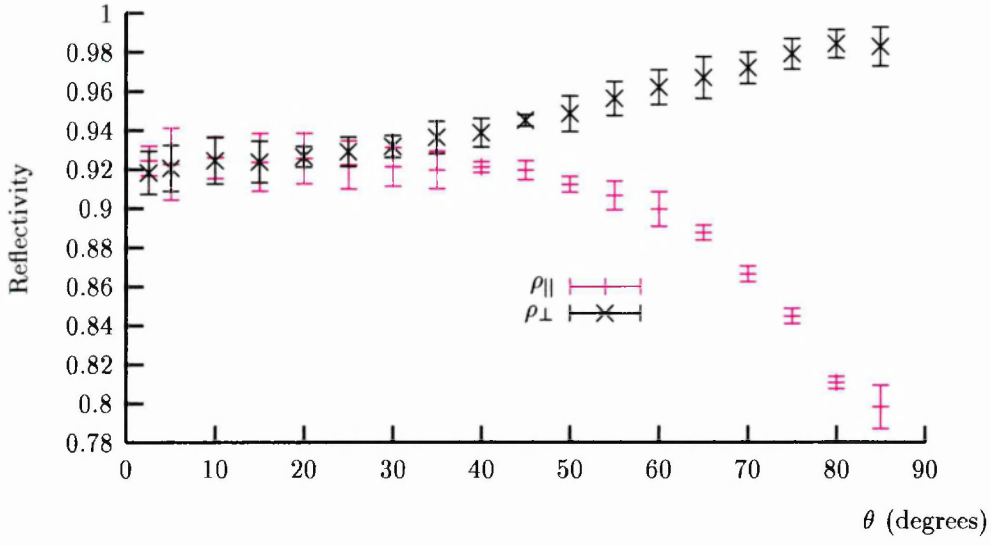

Figure C.13 khal at 1152nm

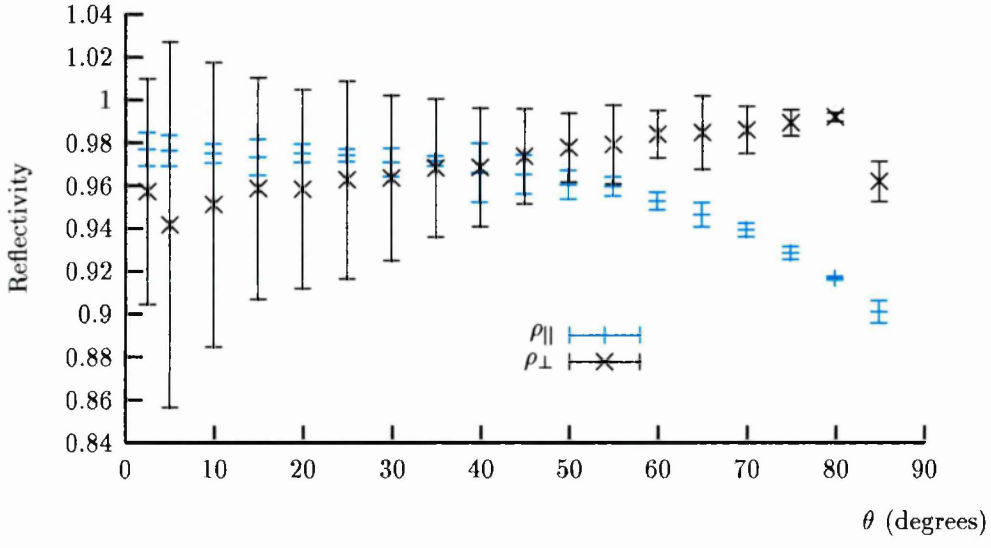

Figure C.14 origgold at 1152nm

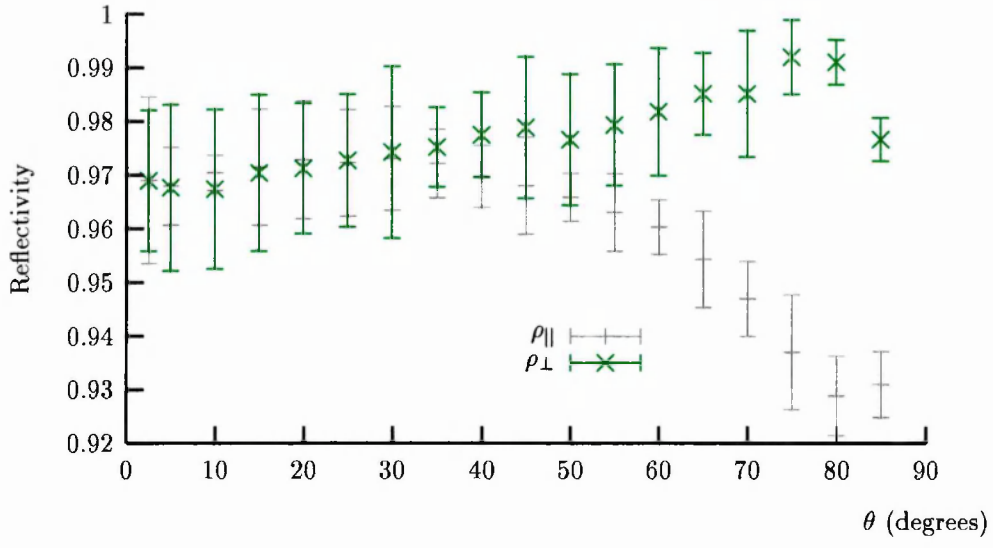

Figure C.15 roel at 1152nm

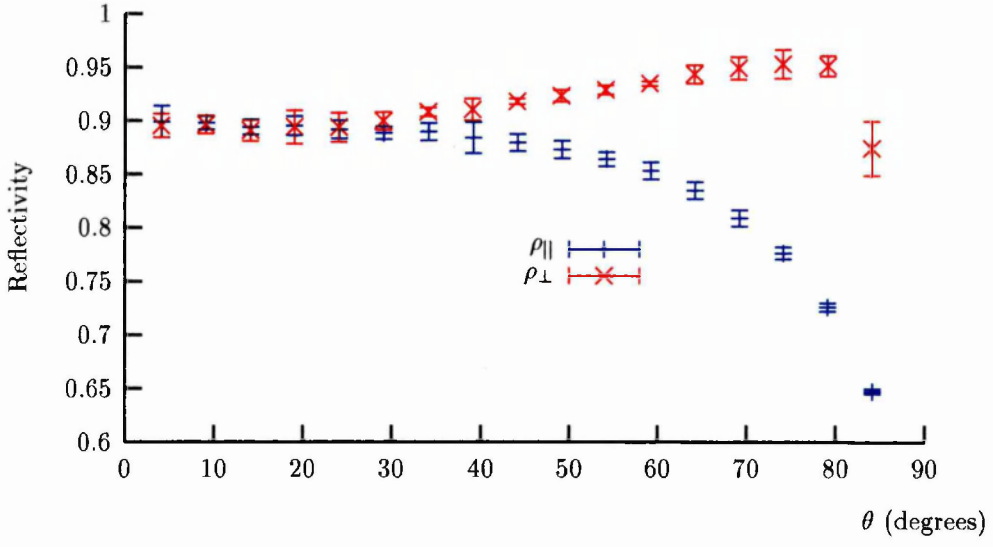

Figure C.16 wht-4g at 1152nm

C.1.3 5.4μm

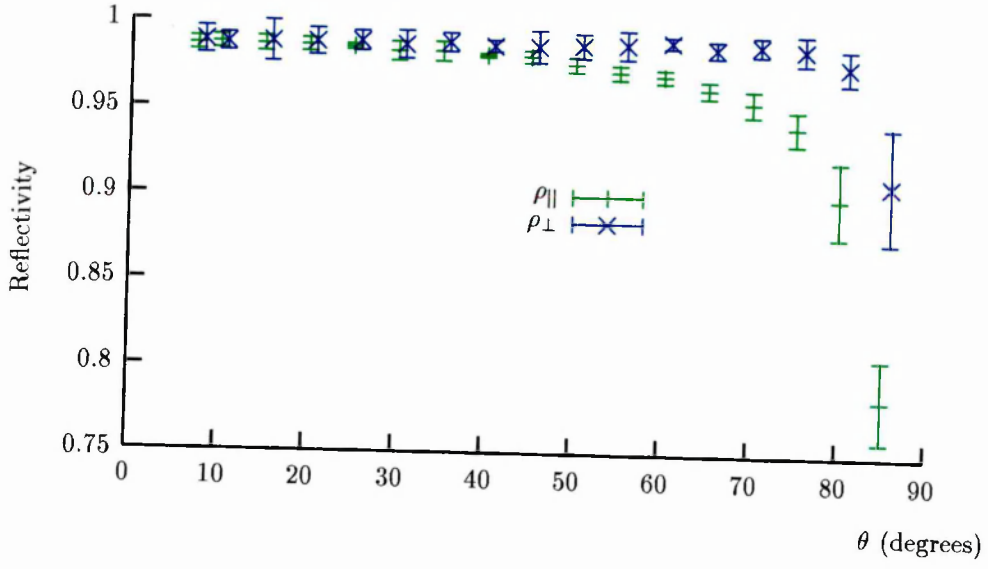

Figure C.17 421-53-3c at 5.4μm

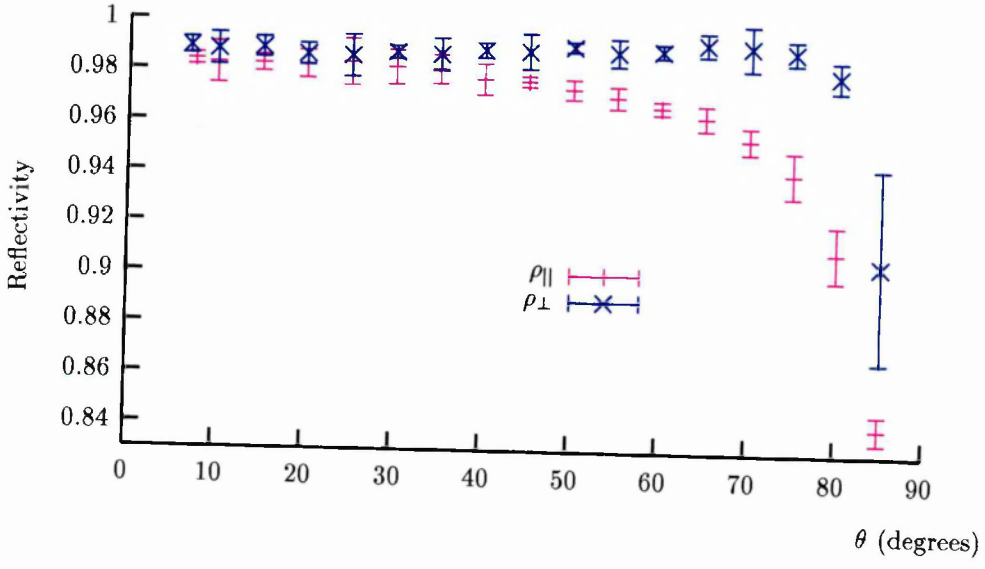

Figure C.18 dsi-1611-g at 5.4μm

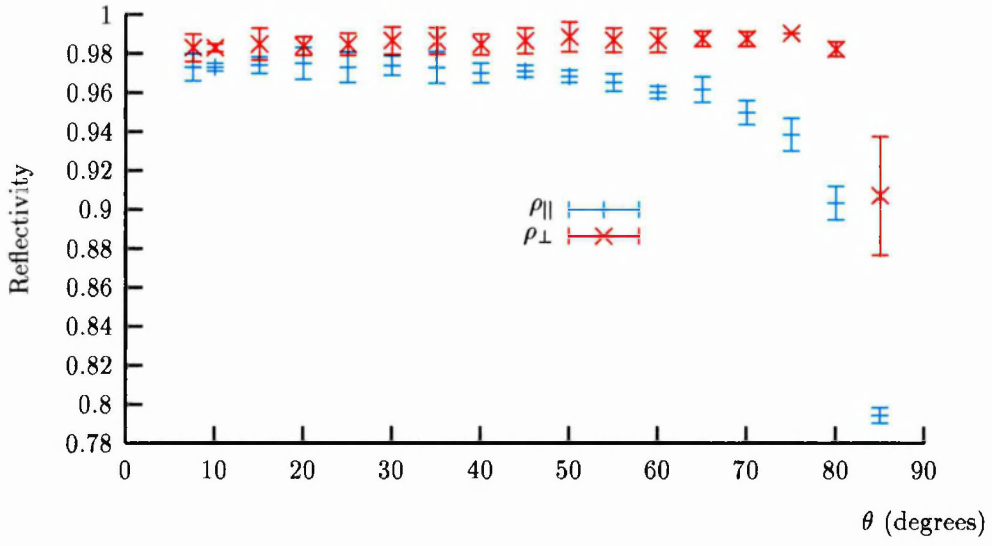

Figure C.19 dsi-1917-3 at 5.4μm

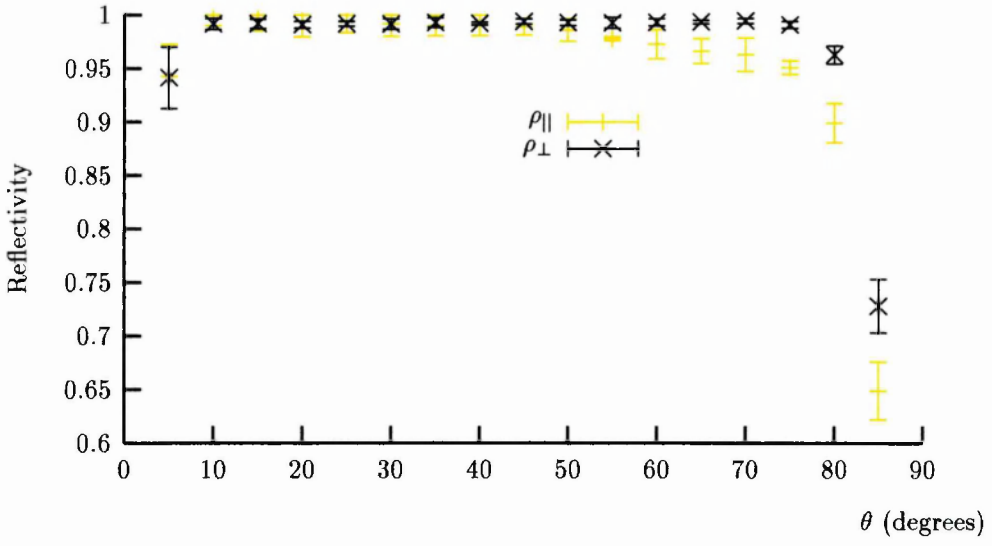

Figure C.20 khag at 5.4μm

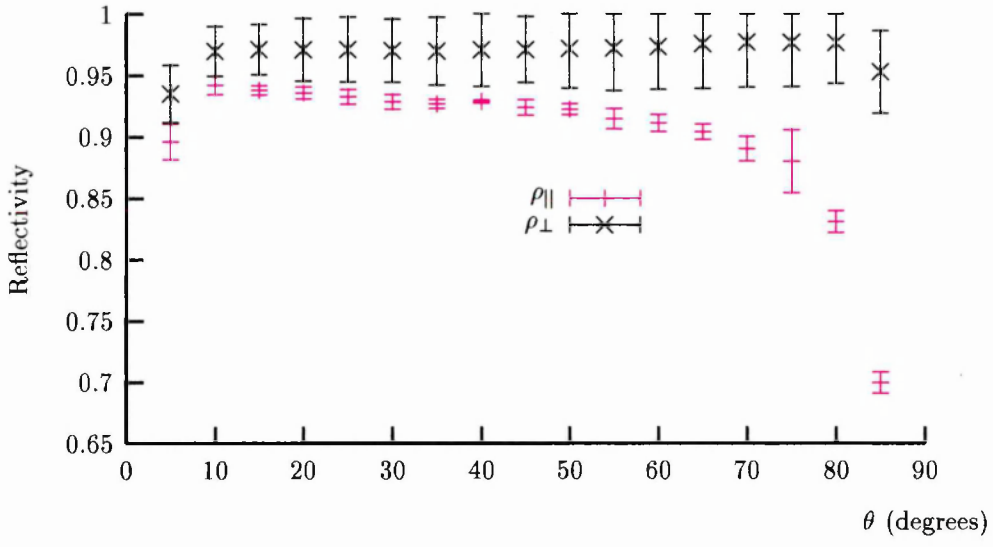

Figure C.21 khal at 5.4μm

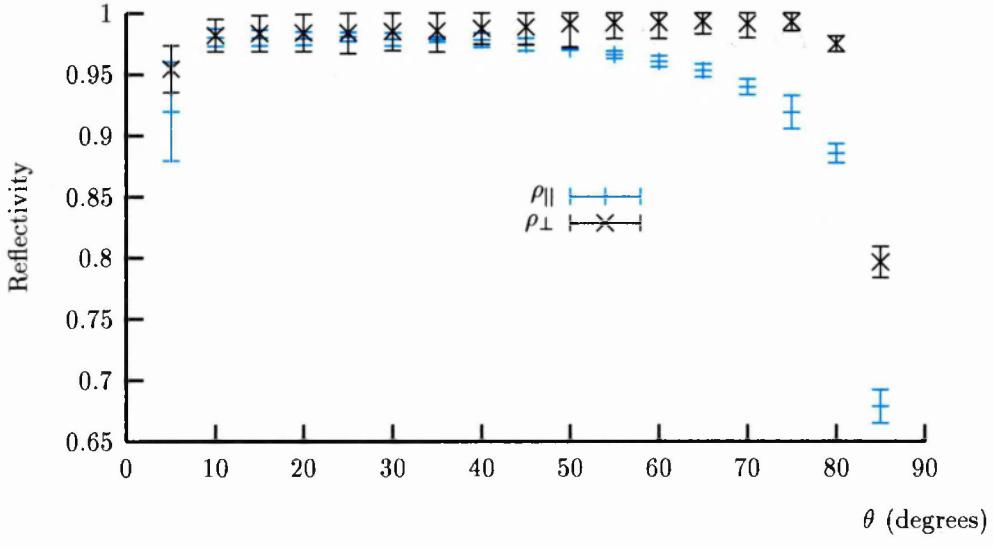

Figure C.22 origgold at 5.4μm

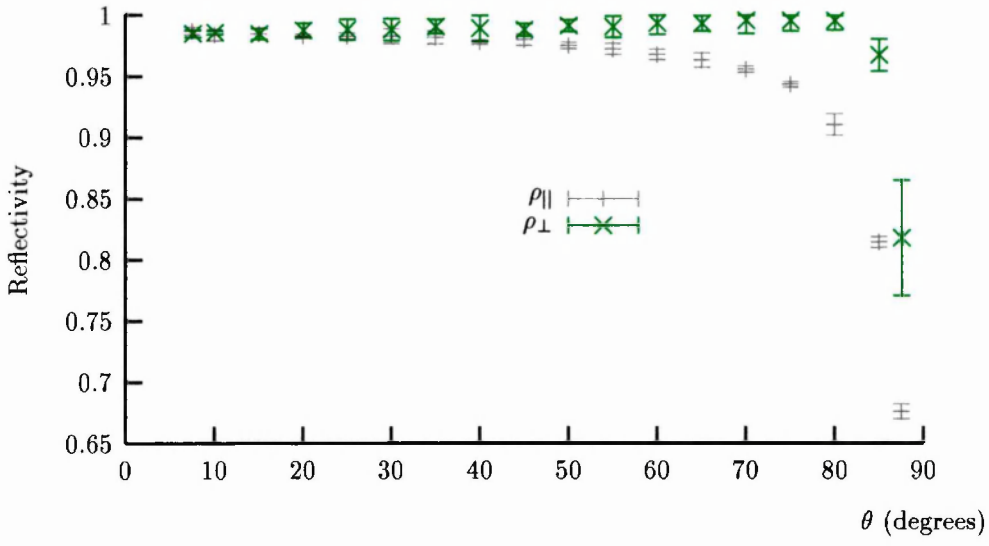

Figure C.23 roe1 at 5.4μm

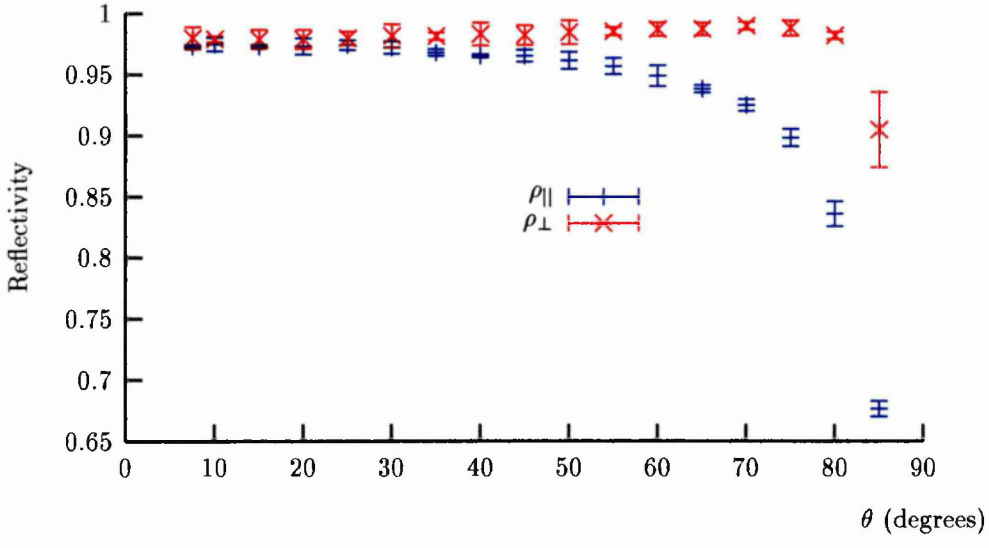

Figure C.24 wht-4g at 5.4μm

C.1.4 10.6μm

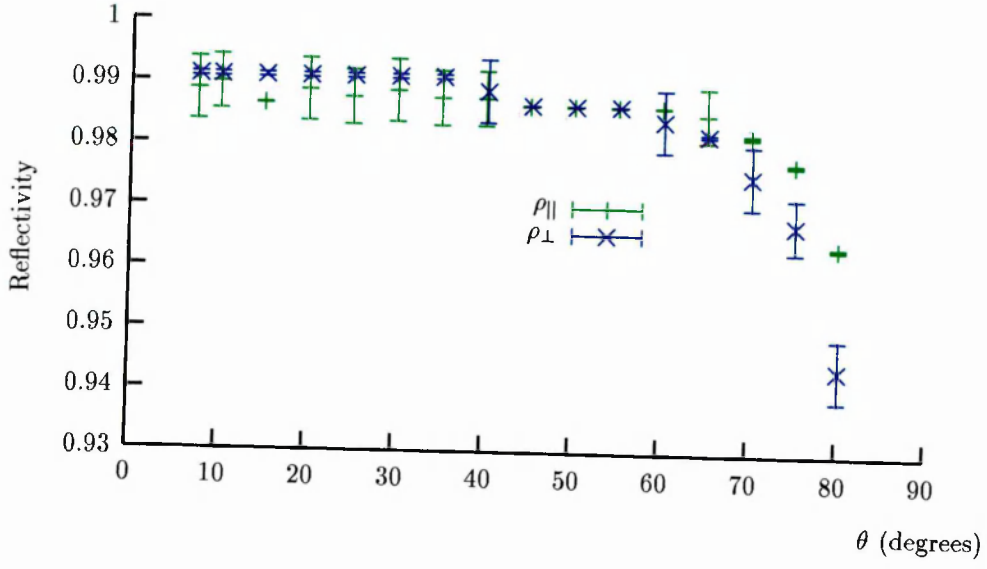

Figure C.25 421-53-3c at 10.6μm

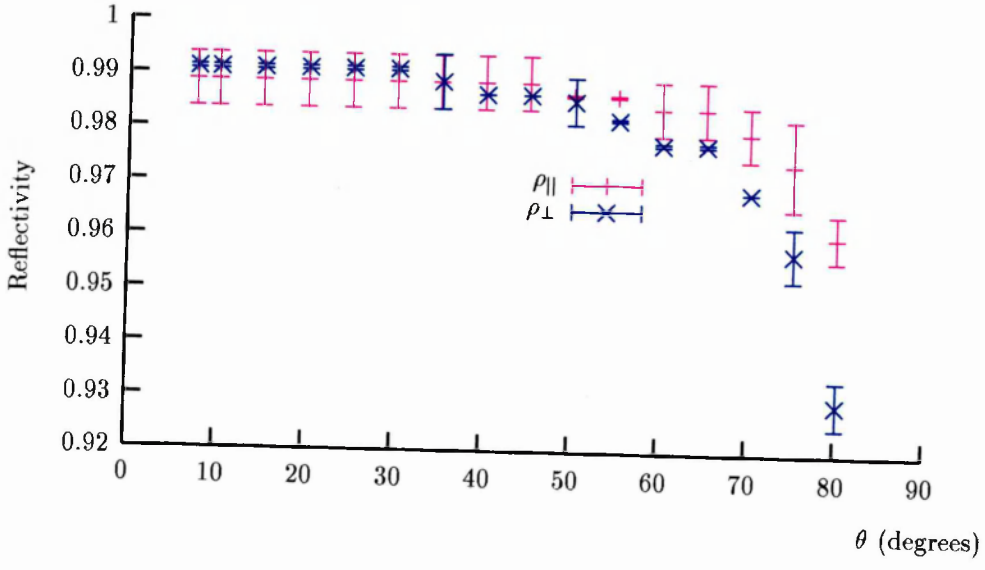

Figure C.26 dsi-1611-g at 10.6μm

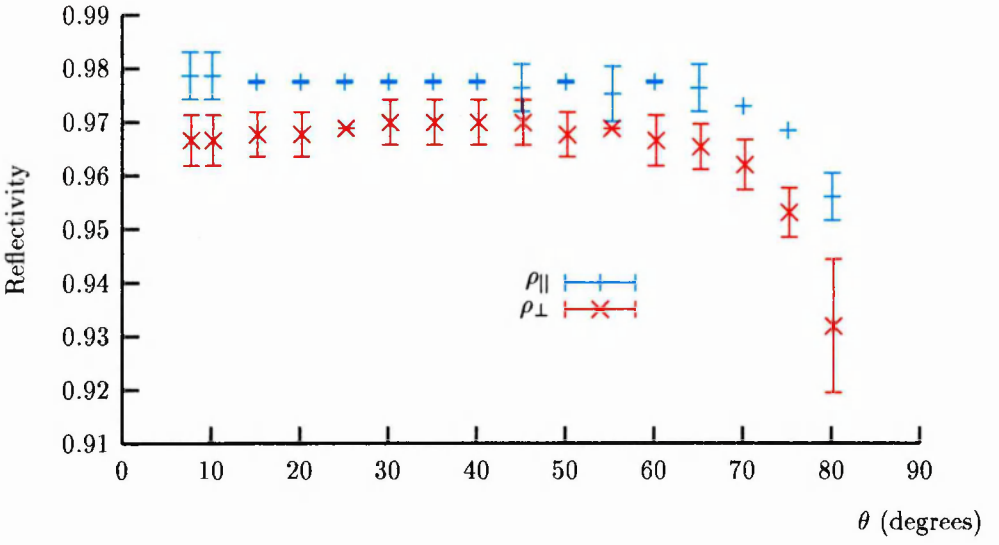

Figure C.27 dsi-1917-3 at 10.6μm (original data)

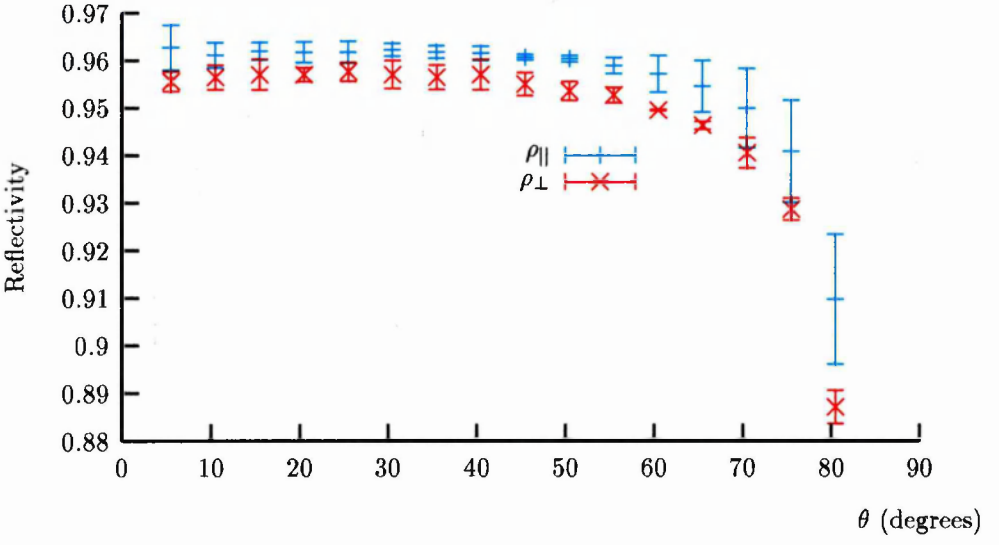

Figure C.28 dsi-1917-3 at 10.6μm (more recent data)

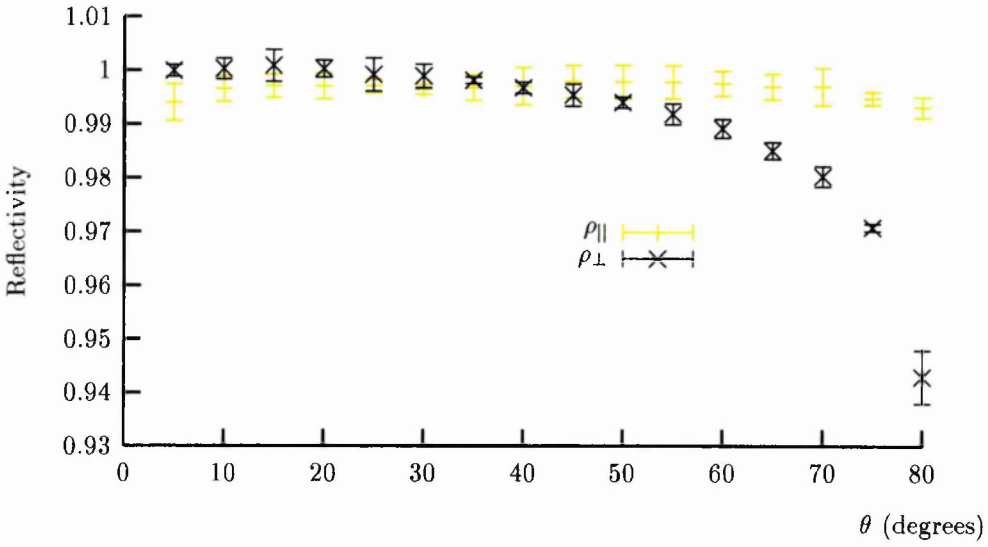

Figure C.29 khag at 10.6μm

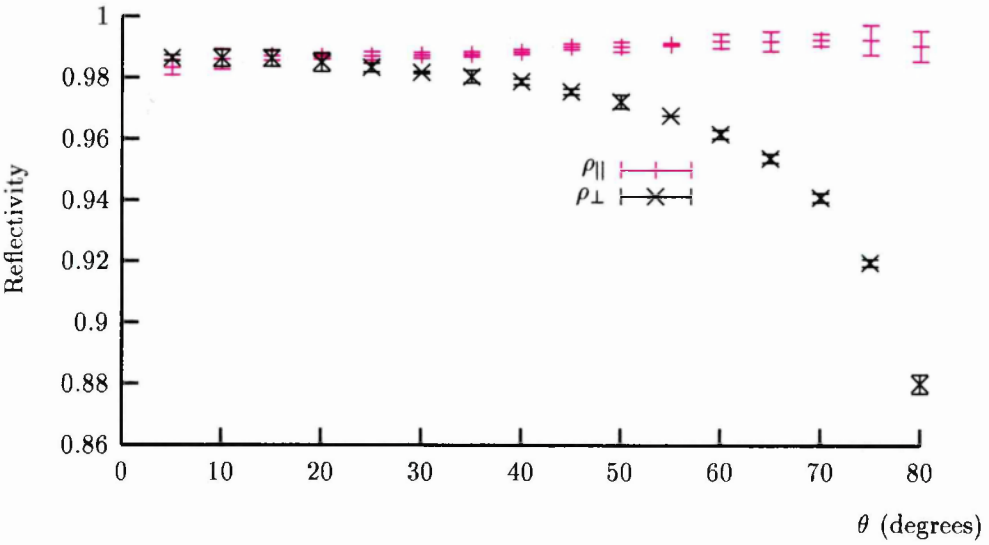

Figure C.30 khal at 10.6μm

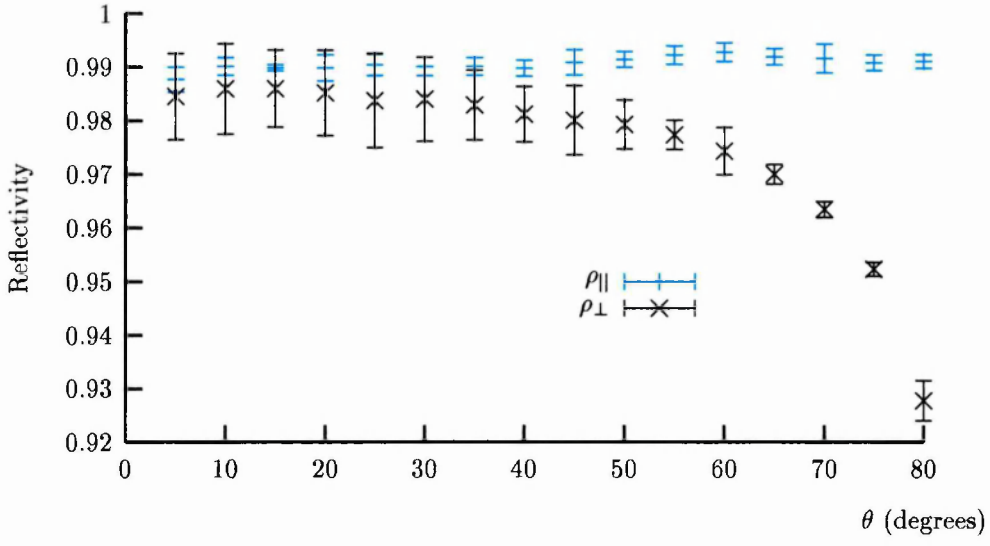

Figure C.31 origgold at 10.6μm

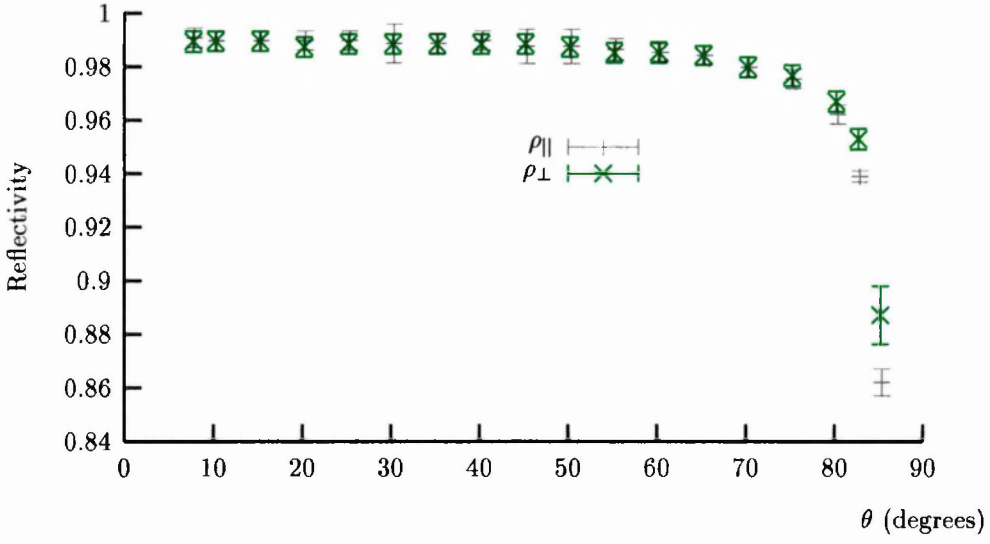

Figure C.32 roel at 10.6μm

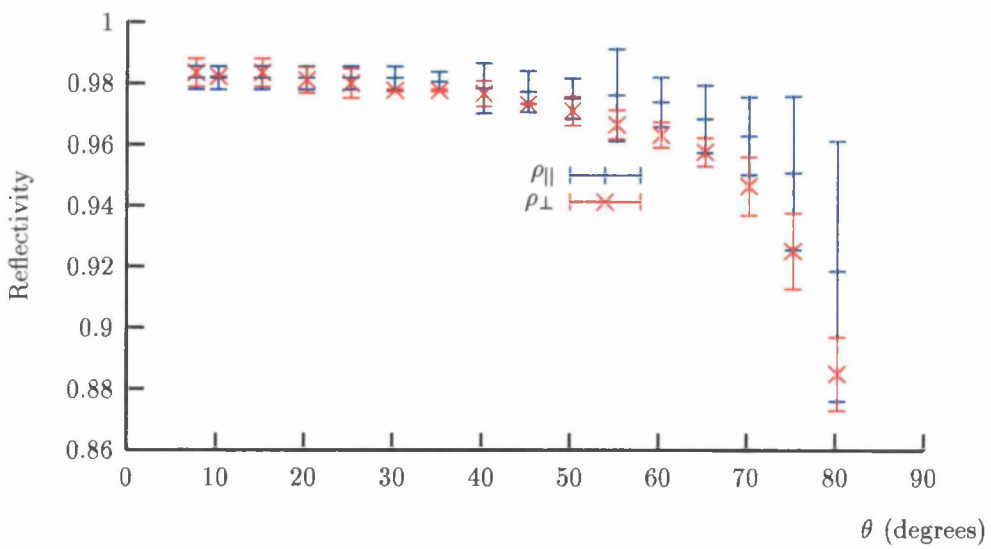

Figure C.33 wht-4g at 10.6μm

C.2 Tables

Below is the complete data set shown graphically in the previous section, here presented in table form. All errors are 95% confidence intervals.

C.2.1 633nm

θ (degrees)	$\rho_{\|}$	$\rho_{\perp}$
2.6	0.932 ± 0.008	0.937 ± 0.009
5.2	0.933 ± 0.008	0.934 ± 0.004
10.2	0.932 ± 0.007	0.93 ± 0.01
15.1	0.930 ± 0.009	0.936 ± 0.005
20.1	0.928 ± 0.009	0.937 ± 0.006
25.1	0.926 ± 0.006	0.937 ± 0.008
30.1	0.92 ± 0.01	0.93 ± 0.01
35.1	0.918 ± 0.009	0.94 ± 0.02
40.1	0.91 ± 0.01	0.94 ± 0.02
45.1	0.90 ± 0.01	0.94 ± 0.02
50.1	0.90 ± 0.01	0.93 ± 0.01
55.1	0.89 ± 0.01	0.93 ± 0.01
60.1	0.88 ± 0.01	0.93 ± 0.01
65.1	0.88 ± 0.02	0.94 ± 0.01
70.1	0.88 ± 0.01	0.940 ± 0.006
75.1	0.88 ± 0.01	0.939 ± 0.002
80.1	0.885 ± 0.004	0.932 ± 0.007
85.1	0.871 ± 0.004	0.896 ± 0.008

Table C.1 Averaged data from 4 experiments on sample 421-53-3c at 633nm

θ (degrees)	$\rho_{\|\|}$	$\rho_{\perp}$
2.6	0.875 ± 0.009	0.876 ± 0.008
5.1	0.877 ± 0.005	0.877 ± 0.007
10.1	0.876 ± 0.006	0.877 ± 0.007
15.1	0.878 ± 0.004	0.875 ± 0.007
20.1	0.879 ± 0.004	0.872 ± 0.004
25.1	0.880 ± 0.005	0.871 ± 0.006
30.1	0.881 ± 0.005	0.866 ± 0.005
35.1	0.884 ± 0.004	0.861 ± 0.006
40.1	0.886 ± 0.006	0.854 ± 0.006
45.1	0.889 ± 0.006	0.850 ± 0.005
50.1	0.89 ± 0.01	0.838 ± 0.004
55.1	0.89 ± 0.01	0.826 ± 0.002
60.1	0.90 ± 0.02	0.816 ± 0.006
65.1	0.91 ± 0.02	0.809 ± 0.007
70.1	0.91 ± 0.03	0.805 ± 0.008
75.1	0.92 ± 0.04	0.81 ± 0.02
80.1	0.92 ± 0.04	0.82 ± 0.03
85.1	0.90 ± 0.02	0.82 ± 0.05

Table C.2 Averaged data from 4 experiments on sample dsi-1611-g at 633nm

θ (degrees)	$\rho_{\|\|}$	$\rho_{\perp}$
2.7	0.929 ± 0.007	0.933 ± 0.005
5.1	0.929 ± 0.005	0.932 ± 0.007
10.1	0.928 ± 0.006	0.933 ± 0.008
15.1	0.925 ± 0.007	0.93 ± 0.01
20.1	0.921 ± 0.007	0.93 ± 0.01
25.1	0.918 ± 0.006	0.93 ± 0.01
30.1	0.913 ± 0.007	0.93 ± 0.01
35.1	0.908 ± 0.009	0.93 ± 0.01
40.1	0.90 ± 0.01	0.93 ± 0.02
45.1	0.90 ± 0.01	0.93 ± 0.01
50.1	0.89 ± 0.01	0.93 ± 0.02
55.1	0.88 ± 0.01	0.93 ± 0.02
60.1	0.88 ± 0.01	0.94 ± 0.01
65.1	0.87 ± 0.02	0.943 ± 0.009
70.1	0.87 ± 0.02	0.941 ± 0.007
75.1	0.87 ± 0.01	0.939 ± 0.006
80.1	0.87 ± 0.01	0.926 ± 0.006
85.1	0.85 ± 0.01	0.874 ± 0.004

Table C.3 Averaged data from 4 experiments on sample dsi-1917-3 at 633nm

θ (degrees)	$\rho_{\|\|}$	$\rho_{\perp}$
2.4	0.965 ± 0.006	0.968 ± 0.007
4.9	0.965 ± 0.006	0.968 ± 0.008
9.9	0.964 ± 0.005	0.968 ± 0.008
14.9	0.964 ± 0.004	0.969 ± 0.007
19.9	0.963 ± 0.007	0.969 ± 0.006
24.9	0.962 ± 0.005	0.971 ± 0.008
29.9	0.960 ± 0.002	0.974 ± 0.008
34.9	0.959 ± 0.002	0.974 ± 0.006
39.9	0.9562 ± 0.0005	0.977 ± 0.006
44.9	0.953 ± 0.002	0.979 ± 0.006
49.9	0.950 ± 0.002	0.980 ± 0.007
54.9	0.944 ± 0.004	0.981 ± 0.007
59.9	0.939 ± 0.003	0.984 ± 0.005
64.9	0.934 ± 0.002	0.987 ± 0.007
69.9	0.929 ± 0.003	0.989 ± 0.006
74.8	0.926 ± 0.003	0.988 ± 0.004
79.8	0.927 ± 0.002	0.987 ± 0.006
84.8	0.92 ± 0.02	0.957 ± 0.003

Table C.4 Averaged data from 4 experiments on sample khag at 633nm

θ (degrees)	$\rho_{\|\|}$	$\rho_{\perp}$
2.4	0.899 ± 0.005	0.900 ± 0.002
4.9	0.899 ± 0.004	0.900 ± 0.002
9.9	0.898 ± 0.005	0.9010 ± 0.0005
14.9	0.896 ± 0.002	0.903 ± 0.003
19.9	0.894 ± 0.005	0.905 ± 0.002
24.9	0.890 ± 0.004	0.908 ± 0.002
29.9	0.885 ± 0.004	0.9121 ± 0.0009
34.9	0.880 ± 0.005	0.916 ± 0.002
39.9	0.873 ± 0.005	0.921 ± 0.001
44.9	0.865 ± 0.003	0.927 ± 0.002
49.9	0.853 ± 0.001	0.932 ± 0.002
54.9	0.840 ± 0.001	0.936 ± 0.004
59.9	0.822 ± 0.001	0.943 ± 0.003
64.9	0.802 ± 0.002	0.952 ± 0.001
69.9	0.774 ± 0.001	0.961 ± 0.002
74.8	0.744 ± 0.002	0.968 ± 0.004
79.8	0.719 ± 0.004	0.973 ± 0.002
84.8	0.75 ± 0.01	0.97 ± 0.01

Table C.5 Averaged data from 4 experiments on sample khal at 633nm

θ (degrees)	$\rho_{\|\|}$	$\rho_{\perp}$
2.6	0.921 ± 0.003	0.922 ± 0.003
5.1	0.918 ± 0.003	0.921 ± 0.004
10.1	0.918 ± 0.004	0.921 ± 0.003
15.1	0.918 ± 0.004	0.923 ± 0.003
20.1	0.915 ± 0.005	0.925 ± 0.003
25.1	0.915 ± 0.002	0.927 ± 0.001
30.1	0.911 ± 0.003	0.933 ± 0.003
35.1	0.909 ± 0.001	0.937 ± 0.004
40.1	0.9051 ± 0.0005	0.940 ± 0.004
45.1	0.899 ± 0.002	0.945 ± 0.002
50.1	0.891 ± 0.002	0.945 ± 0.002
55.1	0.882 ± 0.004	0.946 ± 0.005
60.1	0.876 ± 0.006	0.953 ± 0.004
65.1	0.870 ± 0.007	0.961 ± 0.003
70.1	0.86 ± 0.01	0.971 ± 0.006
75.1	0.871 ± 0.009	0.973 ± 0.005
80.1	0.885 ± 0.006	0.981 ± 0.003
85.1	0.912 ± 0.002	0.9715 ± 0.0008

Table C.6 Averaged data from 4 experiments on sample origgold at 633nm

θ (degrees)	$\rho_{\|\|}$	$\rho_{\perp}$
2.6	0.924 ± 0.001	0.928 ± 0.007
5.1	0.925 ± 0.003	0.929 ± 0.008
10.1	0.924 ± 0.005	0.930 ± 0.008
15.1	0.922 ± 0.002	0.930 ± 0.006
20.1	0.921 ± 0.002	0.932 ± 0.006
25.1	0.918 ± 0.002	0.934 ± 0.005
30.1	0.915 ± 0.002	0.937 ± 0.006
35.1	0.911 ± 0.002	0.940 ± 0.007
40.1	0.907 ± 0.001	0.943 ± 0.007
45.1	0.901 ± 0.003	0.945 ± 0.006
50.1	0.894 ± 0.003	0.945 ± 0.004
55.1	0.886 ± 0.003	0.947 ± 0.002
60.1	0.881 ± 0.006	0.956 ± 0.002
65.1	0.875 ± 0.003	0.965 ± 0.002
70.1	0.872 ± 0.002	0.972 ± 0.002
75.1	0.877 ± 0.000	0.975 ± 0.002
80.1	0.893 ± 0.002	0.980 ± 0.002
85.1	0.925 ± 0.004	0.978 ± 0.002

Table C.7 Averaged data from 4 experiments on sample roe1 at 633nm

θ (degrees)	$\rho_{\|\|}$	$\rho_{\perp}$
2.6	0.833 ± 0.004	0.833 ± 0.004
5.1	0.833 ± 0.004	0.834 ± 0.003
10.1	0.833 ± 0.006	0.835 ± 0.003
15.1	0.830 ± 0.005	0.8364 ± 0.0009
20.1	0.828 ± 0.004	0.837 ± 0.004
25.1	0.824 ± 0.004	0.840 ± 0.005
30.1	0.820 ± 0.002	0.844 ± 0.006
35.1	0.812 ± 0.003	0.848 ± 0.007
40.1	0.803 ± 0.002	0.85 ± 0.01
45.1	0.790 ± 0.003	0.85 ± 0.01
50.1	0.773 ± 0.003	0.85 ± 0.01
55.1	0.754 ± 0.003	0.86 ± 0.02
60.1	0.729 ± 0.006	0.86 ± 0.02
65.1	0.698 ± 0.008	0.87 ± 0.02
70.1	0.66 ± 0.01	0.86 ± 0.03
75.1	0.63 ± 0.02	0.85 ± 0.04
80.1	0.61 ± 0.01	0.84 ± 0.05
85.1	0.65 ± 0.01	0.80 ± 0.04

Table C.8 Averaged data from 4 experiments on sample wht-4g at 633nm

C.2.2 1152nm

θ (degrees)	$\rho_{\|}$	$\rho_{\perp}$
4.1	0.97 ± 0.02	0.97 ± 0.02
9.1	0.96 ± 0.02	0.96 ± 0.02
14.1	0.96 ± 0.02	0.96 ± 0.02
19.2	0.96 ± 0.01	0.96 ± 0.01
24.1	0.96 ± 0.01	0.97 ± 0.02
29.2	0.96 ± 0.01	0.97 ± 0.01
34.2	0.96 ± 0.02	0.97 ± 0.01
39.2	0.96 ± 0.02	0.97 ± 0.01
44.2	0.96 ± 0.01	0.97 ± 0.01
49.2	0.96 ± 0.01	0.97 ± 0.01
54.2	0.96 ± 0.01	0.97 ± 0.01
59.2	0.96 ± 0.01	0.98 ± 0.01
64.2	0.96 ± 0.01	0.98 ± 0.01
69.2	0.95 ± 0.01	0.98 ± 0.01
74.1	0.95 ± 0.02	0.98 ± 0.02
79.2	0.939 ± 0.007	0.98 ± 0.01
84.2	0.911 ± 0.007	0.952 ± 0.006

Table C.9 Averaged data from 4 experiments on sample 421-53-3c at 1152nm

θ (degrees)	$\rho_{\|}$	$\rho_{\perp}$
4.0	0.956 ± 0.005	0.95 ± 0.01
9.1	0.955 ± 0.006	0.95 ± 0.01
14.1	0.95 ± 0.01	0.95 ± 0.01
19.1	0.95 ± 0.01	0.95 ± 0.01
24.1	0.95 ± 0.01	0.95 ± 0.01
29.1	0.95 ± 0.01	0.953 ± 0.009
34.1	0.952 ± 0.004	0.955 ± 0.008
39.1	0.954 ± 0.007	0.961 ± 0.006
44.1	0.954 ± 0.009	0.960 ± 0.005
49.2	0.955 ± 0.006	0.964 ± 0.008
54.2	0.957 ± 0.005	0.969 ± 0.005
59.2	0.957 ± 0.005	0.973 ± 0.006
64.2	0.959 ± 0.004	0.976 ± 0.007
69.2	0.963 ± 0.006	0.980 ± 0.005
74.1	0.967 ± 0.004	0.984 ± 0.005
79.2	0.965 ± 0.007	0.980 ± 0.003
84.2	0.930 ± 0.006	0.94 ± 0.02

Table C.10 Averaged data from 4 experiments on sample dsi-1611-g at 1152nm

θ (degrees)	$\rho_{\|\|}$	$\rho_{\perp}$
4.1	0.96 ± 0.02	0.96 ± 0.02
9.1	0.96 ± 0.02	0.96 ± 0.02
14.1	0.96 ± 0.02	0.96 ± 0.01
19.1	0.96 ± 0.03	0.96 ± 0.02
24.1	0.96 ± 0.03	0.96 ± 0.02
29.1	0.96 ± 0.02	0.96 ± 0.02
34.2	0.96 ± 0.02	0.96 ± 0.01
39.1	0.96 ± 0.02	0.97 ± 0.01
44.2	0.96 ± 0.02	0.97 ± 0.01
49.2	0.96 ± 0.01	0.97 ± 0.01
54.2	0.96 ± 0.01	0.975 ± 0.008
59.2	0.96 ± 0.01	0.97 ± 0.01
64.2	0.962 ± 0.006	0.97 ± 0.01
69.2	0.961 ± 0.006	0.982 ± 0.009
74.2	0.958 ± 0.008	0.986 ± 0.008
79.1	0.951 ± 0.003	0.981 ± 0.004
84.1	0.918 ± 0.008	0.95 ± 0.02

Table C.11 Averaged data from 4 experiments on sample dsi-1917-3 at 1152nm

θ (degrees)	$\rho_{\|\|}$	$\rho_{\perp}$
2.5	0.97 ± 0.01	0.962 ± 0.006
5.0	0.96 ± 0.03	0.965 ± 0.007
10.0	0.973 ± 0.004	0.964 ± 0.006
15.0	0.973 ± 0.003	0.965 ± 0.008
20.0	0.973 ± 0.007	0.967 ± 0.005
25.0	0.973 ± 0.005	0.966 ± 0.009
30.0	0.972 ± 0.005	0.968 ± 0.004
35.0	0.972 ± 0.002	0.970 ± 0.008
40.0	0.971 ± 0.007	0.973 ± 0.005
45.0	0.973 ± 0.005	0.977 ± 0.004
50.0	0.973 ± 0.006	0.98 ± 0.01
55.0	0.970 ± 0.007	0.981 ± 0.006
60.0	0.969 ± 0.008	0.983 ± 0.005
65.0	0.964 ± 0.006	0.985 ± 0.007
70.0	0.9598 ± 0.0000	0.985 ± 0.006
75.0	0.953 ± 0.007	0.983 ± 0.008
80.0	0.94 ± 0.01	0.984 ± 0.007
85.0	0.904 ± 0.007	0.94 ± 0.01

Table C.12 Averaged data from 4 experiments on sample khag at 1152nm

θ (degrees)	$\rho_{\|}$	$\rho_{\perp}$
2.5	0.924 ± 0.008	0.92 ± 0.01
5.0	0.92 ± 0.02	0.92 ± 0.01
10.0	0.93 ± 0.01	0.92 ± 0.01
15.0	0.92 ± 0.01	0.92 ± 0.01
20.0	0.92 ± 0.01	0.926 ± 0.005
25.0	0.92 ± 0.01	0.929 ± 0.007
30.0	0.92 ± 0.01	0.932 ± 0.006
35.0	0.92 ± 0.01	0.936 ± 0.008
40.0	0.921 ± 0.003	0.939 ± 0.007
45.0	0.920 ± 0.005	0.945 ± 0.003
50.0	0.912 ± 0.004	0.948 ± 0.009
55.0	0.907 ± 0.007	0.956 ± 0.009
60.0	0.900 ± 0.009	0.962 ± 0.009
65.0	0.888 ± 0.004	0.97 ± 0.01
70.0	0.866 ± 0.004	0.972 ± 0.008
75.0	0.845 ± 0.004	0.979 ± 0.008
80.0	0.811 ± 0.003	0.984 ± 0.007
85.0	0.80 ± 0.01	0.98 ± 0.01

Table C.13 Averaged data from 4 experiments on sample khal at 1152nm

θ (degrees)	$\rho_{\|}$	$\rho_{\perp}$
2.4	0.977 ± 0.008	0.96 ± 0.05
4.9	0.976 ± 0.007	0.94 ± 0.09
9.9	0.975 ± 0.004	0.95 ± 0.07
14.9	0.973 ± 0.008	0.96 ± 0.05
19.9	0.975 ± 0.004	0.96 ± 0.05
24.9	0.974 ± 0.003	0.96 ± 0.05
29.9	0.971 ± 0.007	0.96 ± 0.04
34.9	0.971 ± 0.002	0.97 ± 0.03
39.9	0.96 ± 0.01	0.97 ± 0.03
44.9	0.965 ± 0.009	0.97 ± 0.02
49.9	0.960 ± 0.007	0.98 ± 0.02
54.9	0.959 ± 0.004	0.98 ± 0.02
59.9	0.952 ± 0.004	0.98 ± 0.01
64.9	0.946 ± 0.006	0.98 ± 0.02
69.9	0.939 ± 0.003	0.98 ± 0.01
74.9	0.928 ± 0.003	0.989 ± 0.006
79.9	0.9165 ± 0.0009	0.992 ± 0.002
84.9	0.901 ± 0.005	0.962 ± 0.009

Table C.14 Averaged data from 4 experiments on sample origgold at 1152nm

θ (degrees)	$\rho_{\|}$	$\rho_{\perp}$
2.4	0.97 ± 0.02	0.97 ± 0.01
4.9	0.968 ± 0.007	0.97 ± 0.02
9.9	0.970 ± 0.003	0.97 ± 0.01
14.9	0.97 ± 0.01	0.97 ± 0.01
19.9	0.97 ± 0.01	0.97 ± 0.01
24.9	0.97 ± 0.01	0.97 ± 0.01
29.9	0.97 ± 0.01	0.97 ± 0.02
34.9	0.972 ± 0.006	0.975 ± 0.007
39.9	0.970 ± 0.006	0.977 ± 0.008
44.9	0.968 ± 0.009	0.98 ± 0.01
49.9	0.966 ± 0.004	0.98 ± 0.01
54.9	0.963 ± 0.007	0.98 ± 0.01
59.9	0.960 ± 0.005	0.98 ± 0.01
64.9	0.954 ± 0.009	0.985 ± 0.008
69.9	0.947 ± 0.007	0.98 ± 0.01
74.9	0.94 ± 0.01	0.992 ± 0.007
79.9	0.929 ± 0.007	0.991 ± 0.004
84.9	0.931 ± 0.006	0.977 ± 0.004

Table C.15 Averaged data from 4 experiments on sample roe1 at 1152nm

θ (degrees)	$\rho_{\|}$	$\rho_{\perp}$
4.0	0.90 ± 0.01	0.89 ± 0.01
9.1	0.898 ± 0.006	0.896 ± 0.008
14.1	0.894 ± 0.007	0.89 ± 0.01
19.1	0.895 ± 0.009	0.89 ± 0.02
24.1	0.892 ± 0.008	0.89 ± 0.01
29.1	0.889 ± 0.006	0.900 ± 0.008
34.1	0.890 ± 0.008	0.908 ± 0.004
39.1	0.88 ± 0.01	0.91 ± 0.01
44.1	0.880 ± 0.008	0.918 ± 0.003
49.2	0.873 ± 0.008	0.923 ± 0.005
54.2	0.864 ± 0.007	0.929 ± 0.004
59.2	0.853 ± 0.008	0.935 ± 0.002
64.2	0.835 ± 0.008	0.943 ± 0.009
69.1	0.809 ± 0.008	0.95 ± 0.01
74.1	0.776 ± 0.006	0.95 ± 0.01
79.1	0.726 ± 0.004	0.951 ± 0.009
84.1	0.647 ± 0.002	0.87 ± 0.03

Table C.16 Averaged data from 4 experiments on sample wht-4g at 1152nm

C.2.3 5.4μm

θ (degrees)	$\rho_{\|}$	$\rho_{\perp}$
7.9	0.986 ± 0.004	0.988 ± 0.008
10.4	0.987 ± 0.004	0.987 ± 0.005
15.4	0.986 ± 0.004	0.99 ± 0.01
20.4	0.986 ± 0.004	0.988 ± 0.008
25.4	0.985 ± 0.002	0.989 ± 0.006
30.4	0.983 ± 0.006	0.987 ± 0.008
35.4	0.983 ± 0.006	0.989 ± 0.005
40.4	0.981 ± 0.001	0.987 ± 0.003
45.4	0.981 ± 0.003	0.987 ± 0.009
50.4	0.976 ± 0.004	0.987 ± 0.007
55.4	0.972 ± 0.004	0.988 ± 0.008
60.4	0.970 ± 0.004	0.990 ± 0.003
65.4	0.963 ± 0.005	0.987 ± 0.005
70.4	0.955 ± 0.007	0.989 ± 0.005
75.4	0.94 ± 0.01	0.987 ± 0.008
80.4	0.90 ± 0.02	0.97 ± 0.01
85.4	0.78 ± 0.02	0.91 ± 0.03

Table C.17 Averaged data from 4 experiments on sample 421-53-3c at 5.4μm

θ (degrees)	$\rho_{\|}$	$\rho_{\perp}$
7.2	0.984 ± 0.002	0.989 ± 0.003
10.1	0.983 ± 0.008	0.988 ± 0.006
15.1	0.982 ± 0.003	0.989 ± 0.004
20.1	0.982 ± 0.005	0.986 ± 0.004
25.1	0.983 ± 0.009	0.986 ± 0.008
30.1	0.982 ± 0.007	0.988 ± 0.003
35.1	0.981 ± 0.006	0.987 ± 0.006
40.1	0.977 ± 0.006	0.989 ± 0.003
45.1	0.977 ± 0.002	0.989 ± 0.007
50.1	0.974 ± 0.004	0.991 ± 0.002
55.1	0.971 ± 0.004	0.989 ± 0.005
60.1	0.967 ± 0.003	0.989 ± 0.003
65.1	0.963 ± 0.005	0.992 ± 0.005
70.1	0.954 ± 0.005	0.991 ± 0.009
75.1	0.941 ± 0.009	0.990 ± 0.005
80.1	0.91 ± 0.01	0.980 ± 0.006
85.1	0.840 ± 0.006	0.90 ± 0.04

Table C.18 Averaged data from 4 experiments on sample dsi-1611-g at 5.4μm

θ (degrees)	$\rho_{\|}$	$\rho_{\perp}$
7.6	0.973 ± 0.007	0.983 ± 0.007
10.1	0.973 ± 0.002	0.983 ± 0.002
15.1	0.974 ± 0.004	0.985 ± 0.008
20.1	0.975 ± 0.008	0.984 ± 0.005
25.1	0.973 ± 0.008	0.985 ± 0.006
30.1	0.974 ± 0.005	0.987 ± 0.007
35.1	0.973 ± 0.008	0.987 ± 0.007
40.1	0.970 ± 0.005	0.985 ± 0.005
45.1	0.971 ± 0.003	0.987 ± 0.007
50.1	0.968 ± 0.003	0.989 ± 0.008
55.1	0.965 ± 0.004	0.987 ± 0.006
60.1	0.960 ± 0.003	0.987 ± 0.006
65.1	0.962 ± 0.007	0.988 ± 0.004
70.1	0.950 ± 0.006	0.988 ± 0.004
75.1	0.939 ± 0.008	0.991 ± 0.000
80.1	0.903 ± 0.009	0.983 ± 0.004
85.1	0.794 ± 0.004	0.91 ± 0.03

Table C.19 Averaged data from 4 experiments on sample dsi-1917-3 at 5.4μm

θ (degrees)	$\rho_{\|}$	$\rho_{\perp}$
5.0	0.94 ± 0.03	0.94 ± 0.03
10.0	0.997 ± 0.007	0.992 ± 0.005
15.0	1.00 ± 0.01	0.992 ± 0.004
20.0	0.99 ± 0.01	0.991 ± 0.003
25.0	0.99 ± 0.01	0.992 ± 0.002
30.0	0.99 ± 0.01	0.992 ± 0.005
35.0	0.990 ± 0.009	0.993 ± 0.005
40.0	0.99 ± 0.01	0.992 ± 0.001
45.0	0.989 ± 0.008	0.994 ± 0.002
50.0	0.98 ± 0.01	0.993 ± 0.003
55.0	0.978 ± 0.002	0.993 ± 0.005
60.0	0.97 ± 0.01	0.993 ± 0.003
65.0	0.97 ± 0.01	0.994 ± 0.002
70.0	0.96 ± 0.02	0.995 ± 0.002
75.0	0.951 ± 0.006	0.991 ± 0.003
80.0	0.90 ± 0.02	0.963 ± 0.008
85.0	0.65 ± 0.03	0.73 ± 0.02

Table C.20 Averaged data from 4 experiments on sample khag at 5.4μm

θ (degrees)	$\rho_{\|}$	$\rho_{\perp}$
5.0	0.90 ± 0.01	0.93 ± 0.02
10.0	0.942 ± 0.007	0.97 ± 0.02
15.0	0.938 ± 0.004	0.97 ± 0.02
20.0	0.936 ± 0.005	0.97 ± 0.03
25.0	0.932 ± 0.006	0.97 ± 0.03
30.0	0.928 ± 0.006	0.97 ± 0.03
35.0	0.927 ± 0.004	0.97 ± 0.03
40.0	0.929 ± 0.001	0.97 ± 0.03
45.0	0.924 ± 0.006	0.97 ± 0.03
50.0	0.922 ± 0.004	0.97 ± 0.03
55.0	0.915 ± 0.008	0.97 ± 0.03
60.0	0.911 ± 0.007	0.97 ± 0.03
65.0	0.904 ± 0.006	0.97 ± 0.04
70.0	0.89 ± 0.01	0.98 ± 0.04
75.0	0.88 ± 0.03	0.98 ± 0.04
80.0	0.831 ± 0.009	0.98 ± 0.03
85.0	0.700 ± 0.009	0.95 ± 0.03

Table C.21 Averaged data from 4 experiments on sample khal at 5.4μm

θ (degrees)	$\rho_{\|}$	$\rho_{\perp}$
5.0	0.92 ± 0.04	0.95 ± 0.02
10.0	0.980 ± 0.007	0.98 ± 0.01
15.0	0.980 ± 0.006	0.98 ± 0.01
20.0	0.979 ± 0.005	0.98 ± 0.02
25.0	0.981 ± 0.004	0.98 ± 0.02
30.0	0.978 ± 0.005	0.98 ± 0.02
35.0	0.978 ± 0.002	0.98 ± 0.02
40.0	0.978 ± 0.006	0.99 ± 0.01
45.0	0.974 ± 0.005	0.99 ± 0.01
50.0	0.970 ± 0.001	0.99 ± 0.02
55.0	0.966 ± 0.003	0.99 ± 0.01
60.0	0.960 ± 0.005	0.99 ± 0.01
65.0	0.953 ± 0.005	0.99 ± 0.01
70.0	0.940 ± 0.006	0.99 ± 0.01
75.0	0.92 ± 0.01	0.993 ± 0.007
80.0	0.885 ± 0.008	0.975 ± 0.006
85.0	0.68 ± 0.01	0.80 ± 0.01

Table C.22 Averaged data from 4 experiments on sample origgold at 5.4μm

θ (degrees)	$\rho_{\|\|}$	$\rho_{\perp}$
7.6	0.987 ± 0.003	0.985 ± 0.003
10.1	0.984 ± 0.005	0.985 ± 0.001
15.1	0.985 ± 0.005	0.984 ± 0.004
20.1	0.983 ± 0.002	0.987 ± 0.006
25.1	0.983 ± 0.003	0.988 ± 0.008
30.1	0.983 ± 0.006	0.988 ± 0.009
35.1	0.982 ± 0.005	0.991 ± 0.006
40.1	0.978 ± 0.002	0.99 ± 0.01
45.1	0.980 ± 0.005	0.988 ± 0.005
50.1	0.975 ± 0.003	0.991 ± 0.005
55.1	0.973 ± 0.004	0.991 ± 0.009
60.1	0.968 ± 0.004	0.993 ± 0.009
65.1	0.963 ± 0.006	0.993 ± 0.006
70.1	0.956 ± 0.003	0.99 ± 0.01
75.1	0.944 ± 0.002	0.996 ± 0.008
80.1	0.911 ± 0.009	0.996 ± 0.008
85.1	0.814 ± 0.004	0.97 ± 0.01
87.6	0.676 ± 0.006	0.82 ± 0.05

Table C.23 Averaged data from 4 experiments on sample roe1 at 5.4μm

θ (degrees)	$\rho_{\|\|}$	$\rho_{\perp}$
7.6	0.973 ± 0.001	0.980 ± 0.009
10.1	0.975 ± 0.006	0.979 ± 0.002
15.1	0.973 ± 0.001	0.979 ± 0.008
20.1	0.973 ± 0.007	0.979 ± 0.008
25.1	0.974 ± 0.004	0.979 ± 0.006
30.1	0.972 ± 0.005	0.981 ± 0.009
35.1	0.968 ± 0.003	0.981 ± 0.003
40.1	0.965 ± 0.001	0.983 ± 0.009
45.1	0.965 ± 0.005	0.982 ± 0.008
50.1	0.961 ± 0.007	0.98 ± 0.01
55.1	0.957 ± 0.007	0.985 ± 0.003
60.1	0.949 ± 0.008	0.987 ± 0.006
65.1	0.938 ± 0.003	0.987 ± 0.005
70.1	0.925 ± 0.005	0.990 ± 0.003
75.1	0.898 ± 0.007	0.988 ± 0.006
80.1	0.84 ± 0.01	0.982 ± 0.003
85.1	0.676 ± 0.006	0.90 ± 0.03

Table C.24 Averaged data from 4 experiments on sample wht-4g at 5.4μm

C.2.4 10.6μm

θ (degrees)	$\rho_{\|}$	$\rho_{\perp}$
7.7	0.989 ± 0.005	0.9910 ± 0.0003
10.2	0.990 ± 0.004	0.9910 ± 0.0003
15.2	0.9865 ± 0.0001	0.9910 ± 0.0003
20.2	0.989 ± 0.005	0.9910 ± 0.0003
25.2	0.988 ± 0.004	0.9910 ± 0.0003
30.2	0.989 ± 0.005	0.9910 ± 0.0003
35.2	0.988 ± 0.004	0.9910 ± 0.0003
40.2	0.988 ± 0.004	0.989 ± 0.005
45.2	0.9865 ± 0.0001	0.9865 ± 0.0000
50.2	0.9865 ± 0.0001	0.9865 ± 0.0000
55.2	0.9865 ± 0.0001	0.9865 ± 0.0000
60.2	0.9865 ± 0.0001	0.984 ± 0.005
65.2	0.985 ± 0.004	0.9821 ± 0.0002
70.2	0.9820 ± 0.0003	0.975 ± 0.005
75.2	0.9775 ± 0.0002	0.967 ± 0.004
80.2	0.9640 ± 0.0002	0.944 ± 0.005

Table C.25 Averaged data from 4 experiments on sample 421-53-3c at 10.6μm

θ (degrees)	$\rho_{\|}$	$\rho_{\perp}$
7.7	0.989 ± 0.005	0.9910 ± 0.0003
10.2	0.989 ± 0.005	0.9910 ± 0.0003
15.2	0.989 ± 0.005	0.9910 ± 0.0003
20.2	0.989 ± 0.005	0.9910 ± 0.0003
25.2	0.989 ± 0.005	0.9910 ± 0.0003
30.2	0.989 ± 0.005	0.9910 ± 0.0003
35.2	0.989 ± 0.005	0.989 ± 0.005
40.2	0.989 ± 0.005	0.9865 ± 0.0000
45.2	0.989 ± 0.005	0.9865 ± 0.0000
50.2	0.9864 ± 0.0002	0.985 ± 0.004
55.2	0.9864 ± 0.0002	0.9821 ± 0.0002
60.2	0.984 ± 0.005	0.9776 ± 0.0003
65.2	0.984 ± 0.005	0.9776 ± 0.0003
70.2	0.980 ± 0.005	0.9686 ± 0.0000
75.2	0.974 ± 0.008	0.957 ± 0.005
80.2	0.960 ± 0.004	0.929 ± 0.004

Table C.26 Averaged data from 4 experiments on sample dsi-1611-g at 10.6μm

θ (degrees)	$\rho_{\|}$	$\rho_{\perp}$
7.7	0.979 ± 0.004	0.966 ± 0.005
10.2	0.979 ± 0.004	0.966 ± 0.005
15.2	0.9775 ± 0.0002	0.968 ± 0.004
20.2	0.9775 ± 0.0002	0.968 ± 0.004
25.2	0.9775 ± 0.0002	0.969 ± 0.000
30.2	0.9775 ± 0.0002	0.970 ± 0.004
35.2	0.9775 ± 0.0002	0.970 ± 0.004
40.2	0.9775 ± 0.0002	0.970 ± 0.004
45.2	0.976 ± 0.004	0.970 ± 0.004
50.2	0.9775 ± 0.0002	0.968 ± 0.004
55.3	0.975 ± 0.005	0.969 ± 0.000
60.2	0.9775 ± 0.0002	0.966 ± 0.005
65.2	0.976 ± 0.004	0.965 ± 0.004
70.2	0.973 ± 0.000	0.962 ± 0.005
75.2	0.968 ± 0.000	0.953 ± 0.005
80.2	0.956 ± 0.004	0.93 ± 0.01

Table C.27 Averaged data from 4 experiments on sample dsi-1917-3 at 10.6μm

θ (degrees)	$\rho_{\|}$	$\rho_{\perp}$
5.5	0.963 ± 0.005	0.955 ± 0.002
10.5	0.961 ± 0.003	0.956 ± 0.003
15.5	0.962 ± 0.002	0.957 ± 0.003
20.5	0.962 ± 0.002	0.957 ± 0.001
25.5	0.962 ± 0.002	0.957 ± 0.002
30.5	0.962 ± 0.001	0.957 ± 0.003
35.5	0.962 ± 0.001	0.956 ± 0.003
40.5	0.961 ± 0.001	0.957 ± 0.003
45.5	0.9606 ± 0.0006	0.955 ± 0.002
50.5	0.9603 ± 0.0007	0.953 ± 0.002
55.5	0.959 ± 0.002	0.953 ± 0.002
60.5	0.957 ± 0.004	0.9495 ± 0.0001
65.5	0.954 ± 0.005	0.9463 ± 0.0009
70.5	0.950 ± 0.008	0.940 ± 0.003
75.5	0.94 ± 0.01	0.929 ± 0.002
80.5	0.91 ± 0.01	0.887 ± 0.003

Table C.28 Averaged data from 4 experiments on sample dsi-1917-3 at 10.6μm (performed 13 months after the experiments summarised in table C.27)

θ (degrees)	$\rho_{\|\|}$	$\rho_{\perp}$
5.0	0.994 ± 0.003	1.000 ± 0.001
10.0	0.996 ± 0.002	1.000 ± 0.002
15.0	0.997 ± 0.002	1.001 ± 0.003
20.0	0.997 ± 0.002	1.000 ± 0.002
25.0	0.997 ± 0.001	0.999 ± 0.003
30.0	0.9965 ± 0.0009	0.999 ± 0.002
35.0	0.997 ± 0.002	0.9982 ± 0.0006
40.0	0.997 ± 0.003	0.997 ± 0.001
45.0	0.998 ± 0.003	0.995 ± 0.002
50.0	0.998 ± 0.003	0.994 ± 0.001
55.0	0.998 ± 0.003	0.992 ± 0.002
60.0	0.998 ± 0.002	0.989 ± 0.002
65.0	0.997 ± 0.002	0.985 ± 0.002
70.0	0.997 ± 0.003	0.980 ± 0.002
75.0	0.995 ± 0.001	0.9709 ± 0.0007
80.0	0.993 ± 0.002	0.943 ± 0.005

Table C.29 Averaged data from 4 experiments on sample khag at 10.6μm

θ (degrees)	$\rho_{\|\|}$	$\rho_{\perp}$
5.0	0.983 ± 0.002	0.9864 ± 0.0009
10.0	0.986 ± 0.003	0.986 ± 0.003
15.0	0.987 ± 0.002	0.986 ± 0.003
20.0	0.9868 ± 0.0007	0.985 ± 0.003
25.0	0.987 ± 0.001	0.983 ± 0.001
30.0	0.9874 ± 0.0009	0.9817 ± 0.0004
35.0	0.9877 ± 0.0008	0.980 ± 0.002
40.0	0.9884 ± 0.0008	0.979 ± 0.001
45.0	0.9901 ± 0.0009	0.975 ± 0.001
50.0	0.990 ± 0.002	0.972 ± 0.002
55.0	0.9909 ± 0.0004	0.9676 ± 0.0000
60.0	0.992 ± 0.002	0.962 ± 0.001
65.0	0.992 ± 0.003	0.954 ± 0.001
70.0	0.993 ± 0.002	0.941 ± 0.002
75.0	0.992 ± 0.005	0.920 ± 0.001
80.0	0.991 ± 0.005	0.880 ± 0.003

Table C.30 Averaged data from 4 experiments on sample khal at 10.6μm

θ (degrees)	$\rho_{\|}$	$\rho_{\perp}$
5.0	0.988 ± 0.002	0.984 ± 0.008
10.0	0.990 ± 0.002	0.986 ± 0.008
15.0	0.9899 ± 0.0006	0.986 ± 0.007
20.0	0.990 ± 0.002	0.985 ± 0.008
25.0	0.990 ± 0.002	0.984 ± 0.009
30.0	0.990 ± 0.002	0.984 ± 0.008
35.0	0.990 ± 0.002	0.983 ± 0.007
40.0	0.990 ± 0.001	0.981 ± 0.005
45.0	0.991 ± 0.002	0.980 ± 0.006
50.0	0.991 ± 0.001	0.979 ± 0.005
55.0	0.992 ± 0.002	0.977 ± 0.003
60.0	0.993 ± 0.002	0.974 ± 0.004
65.0	0.992 ± 0.002	0.970 ± 0.002
70.0	0.992 ± 0.003	0.963 ± 0.001
75.0	0.991 ± 0.001	0.952 ± 0.001
80.0	0.991 ± 0.001	0.928 ± 0.004

Table C.31 Averaged data from 4 experiments on sample origgold at 10.6μm

θ (degrees)	$\rho_{\|}$	$\rho_{\perp}$
7.8	0.991 ± 0.004	0.989 ± 0.004
10.3	0.990 ± 0.004	0.989 ± 0.004
15.3	0.990 ± 0.004	0.989 ± 0.004
20.3	0.990 ± 0.004	0.987 ± 0.004
25.3	0.990 ± 0.004	0.988 ± 0.004
30.3	0.989 ± 0.007	0.988 ± 0.004
35.3	0.989 ± 0.004	0.988 ± 0.004
40.3	0.990 ± 0.004	0.988 ± 0.004
45.3	0.988 ± 0.006	0.988 ± 0.004
50.3	0.988 ± 0.006	0.987 ± 0.004
55.3	0.986 ± 0.004	0.985 ± 0.004
60.3	0.985 ± 0.003	0.985 ± 0.004
65.3	0.984 ± 0.003	0.984 ± 0.004
70.3	0.980 ± 0.004	0.980 ± 0.004
75.3	0.975 ± 0.004	0.977 ± 0.004
80.3	0.962 ± 0.004	0.967 ± 0.004
82.8	0.939 ± 0.002	0.953 ± 0.004
85.3	0.862 ± 0.005	0.89 ± 0.01

Table C.32 Averaged data from 4 experiments on sample roe1 at 10.6μm

θ (degrees)	$\rho_{\parallel}$	$\rho_{\perp}$
7.7	0.982 ± 0.004	0.983 ± 0.005
10.2	0.982 ± 0.004	0.9821 ± 0.0000
15.2	0.982 ± 0.004	0.983 ± 0.005
20.2	0.982 ± 0.004	0.981 ± 0.004
25.2	0.982 ± 0.004	0.980 ± 0.005
30.2	0.982 ± 0.004	0.9777 ± 0.0003
35.2	0.980 ± 0.003	0.9777 ± 0.0003
40.2	0.978 ± 0.008	0.976 ± 0.004
45.2	0.977 ± 0.007	0.9732 ± 0.0001
50.2	0.975 ± 0.007	0.971 ± 0.005
55.2	0.98 ± 0.01	0.966 ± 0.005
60.2	0.974 ± 0.008	0.963 ± 0.004
65.2	0.97 ± 0.01	0.957 ± 0.005
70.2	0.96 ± 0.01	0.94 ± 0.01
75.2	0.95 ± 0.03	0.92 ± 0.01
80.2	0.92 ± 0.04	0.88 ± 0.01

Table C.33 Averaged data from 4 experiments on sample wht-4g at 10.6μm

Bibliography

[1] Anthony J. LaRocca. Artificial Sources. In William L. Wolfe and George J. Zissis, editors, *Infrared Handbook*, chapter 2, pages 2–4. US Government Printing Office, Washington, DC, 4th edition, 1993.

[2] J.K. Davies. Infrared astronomy from the UK Infrared Telescope. *Contemporary Physics*, **33**(6):357–368, 1992.

[3] H.A. Thronson, T.G. Hawarden, A.J. Penny, and J.K. Davies. Edison : The International Infrared Space Observatory. Technical report, Rutherford Appleton Laboratory, United Kingdom, May 1993. Submitted in response to the European Space Agency Call for Mission Ideas for the Third Medium Mission Opportunity (M3).

[4] J.K. Davies, T.G. Hawarden, and C.M. Mountain. Radiatively cooled telescopes: a new direction for infrared space astronomy. *Acta Astronautica*, **25**(4):223–228, 1991.

[5] P.V. Mason. Long term performance of the passive thermal control systems of the IRAS spacecraft. *Cryogenics*, **28**:137–141, 1988.

[6] S.M. Volz, M.J. DiPirro, S.H. Castles, M.G. Ryschkewitsch, and R. Hopkins. Anomalous on-orbit behaviour of the NASA Cosmic Background Explorer (COBE) dewar. *Cryogenics*, **32**(2):77–84, 1992.

[7] T.G. Hawarden, R. Crane, H.A. Thronson, A.J. Penny, A.H. Orlowska, and T.W. Bradshaw. Radiative and hybrid cooling of infrared space telescopes. *Space Science Reviews*, **74**:45–56, 1995.

[8] A. Léger, J.M. Mariotti, B. Mennesson, M. Ollivier, J.L. Puget, D. Rouan, and J. Schneider. The DARWIN project. *Astrophysics and Space Science*, **241**:135–146, 1996.

[9] J. Mather. The next generation space telescope (NGST). In C. Eiroa, A. Alberdi, H. Thronson, T. De Graauw, and C.J. Schalinski, editors, *Infrared Space Interferometry: Astrophysics and*

the Study of Earth-like Planets, pages 227–232, Dordrecht, 1997. Kluwer Academic Publishers.

[10] Richard Hills. Optics of the far infra-red and submillimetre space telescope. *Space Science Reviews*, **74**:119–123, 1995.

[11] H. Shibai. The infrared imaging surveyor (IRIS) project. In C. Eiroa, A. Alberdi, H. Thronson, T. De Graauw, and C.J. Schalinski, editors, *Infrared Space Interferometry: Astrophysics and the Study of Earth-like Planets*, pages 279–281, Dordrecht, 1997. Kluwer Academic Publishers.

[12] M.W. Werner and L.L. Simmons. SIRTF - the moderate mission. *Space Science Reviews*, **74**:125–138, 1995.

[13] T.G. Hawarden, R.O. Cummings, C.M. Telesco, and H.A. Thronson. Optimised radiative cooling of infrared space telescopes and applications to possible missions. *Space Science Reviews*, **61**:113–144, 1992.

[14] A. Léger, J.-L. Puget, J.M. Mariotti, D. Rouan, and J. Schneider. How to evidence primitive life on an exo-planet? - the DARWIN project. *Space Science Reviews*, **74**:163–169, 1995.

[15] Roger Angel. *in The next generation space telescope*, page 81. Space Telescope Science Institute, Baltimore, 1989. P. Bély, C. Burrows, and G. Illingworth (eds.).

[16] F.E. Nicodemus et al. Geometrical Considerations and Nomenclature for Reflectance. Technical report, National Bureau of Standards, United States Department of Commerce, 1977. NBS monograph 160.

[17] R. Siegel and J.R. Howell. *Thermal radiation heat transfer.* Hemisphere Publishing Corporation, London, 3rd edition, 1992.

[18] Marcel J.E. Golay. A pneumatic infra-red detector. *Review of Scientific Instruments*, **18**(5):357–362, 1947.

[19] R.C. Weast, editor. *Handbook of Chemistry and Physics.* Chemical Rubber Company, Cleveland, 44th edition, 1962.

[20] R.W. Ditchburn. *Light.* Blackie and Son Limited, London, 2nd edition, 1963.

[21] R.W. Ditchburn. Some new formulas for determining the optical constants from measurements on reflected light. *Journal of the Optical Society of America*, **45**(9):743–748, 1955.

[22] M.A. Ordal, L.L. Long, R.J. Bell, S.E. Bell, R.R. Bell, R.W. Alexander, Jr., and C.A. Ward. Optical properties of the metals Al, Co, Cu, Au, Fe, Pb, Ni, Pd, Pt, Ag, Ti, and W in the infrared and far infrared. *Applied Optics*, **22**(7):1099–1119, 1983.

[23] H.E. Bennett and J.M. Bennett. Validity of the drude theory for silver, gold and aluminium in the infrared. In F. Abeles, editor, *Optical properties and electronic structure of metals and alloys*, pages 175–188. Wiley, New York, 1966.

[24] W.M. Toscano and E.G. Cravalho. Thermal radiative properties of the noble metals at cryogenic temperatures. *Journal of Heat Transfer - Transactions of the ASME, series C*, **98**:438–445, 1976.

[25] P. Drude. *Theory of Optics.* Longmans, New York, 1922.

[26] A.V. Sokolov. *Optical properties of metals.* American Elsavier Publishing Co., New York, 1967. p. 76.

[27] G.E.H. Reuter and E.H. Sondheimer. The anomalous skin effect in metals. *Proceedings of the Royal Society of London, Series A*, **195**:336–364, 1948.

[28] R.B. Dingle. The anomalous skin effect and the reflectivity of metals. I. *Physica*, **19**:311–347, 1953.

[29] P.W. Gilberd. The anomalous skin effect and the optical properties of metals. *Journal of Physics, F: Metal Physics*, **12**(8):1845–1860, 1982.

[30] T. Holstein. Optical and infrared volume absorptivity of metals. *Physical Review*, **96**:535–536, 1954.

[31] W.M. Toscano and E.G. Cravalho. Experimental measurements of the monochromatic near normal reflectance of gold at cryogenic temperatures. In *Proceeding of the Fifth International Heat Transfer Conference*, volume 1, pages 16–20, 1974.

[32] V.G. Padalka and I.N. Shklyarevskii. Determination of the micro-characteristics of Silver and Gold from the infrared optical constants and the conductivity at 82 and 295°K. *Optics and Spectroscopy*, **11**:285–288, 1961.

[33] R.P. Caren. Low-Temperature Emittance Determinations. In *Thermophysics and Temperature Control of Spacecraft and Entry Vehicles*, volume 18, pages 61–73. Academic Press, New York, 1966.

[34] J.F. Baumeister. Private communication, December 1993.

[35] H.A. Thronson. Private communication, October 1993.

[36] J.F. Baumeister. Relationship of optical coating on thermal radiation characteristics of non-isothermal cylindrical enclosures. Technical Report NASA Technical Memorandum 104408, NASA, 1991. Appendix A.

[37] H.Y. Wong. *Heat transfer for engineers.* Longman Group Limited, London, 1977. pp. 98-120.

[38] J.F. Baumeister. Application of ray tracing in radiation heat transfer. Technical Report NASA Technical Memorandum 106206, NASA, 1993.

[39] W.H. Press et al. *Numerical recipes in C : the art of scientific computing.* Cambridge University Press, Cambridge, 1992. Ch. 7, p. 282.

[40] R. P. Blake and B. W. Jones. The effect of realistic surface properties on low temperature space observatories. *Space Science Reviews*, **74**:175–179, 1995.

[41] M. Perlmutter and J.R. Howell. A strongly directional emitting and absorbing surface. *Journal of Heat Transfer*, **85**(3):282–283, 1963.

[42] J.M. Bennett and E.J. Ashley. Infrared reflectance and emittance of silver and gold evaporated in ultrahigh vacuum. *Applied Optics*, **4**(2):221–224, February 1965.

[43] R. P. Blake and B. W. Jones. Low temperature space observatories: the effect of realistic surface properties. *Journal of Geophysical Research - Planets*, **101**(E4):9303–9308, 1996.

[44] G. Brandli and A.J. Sievers. *Physics Reviews*, **B 5**:3550, 1972.

[45] F.J.J. Clarke, N.A. Boyd, and J.K. Leonard. Design of a sample chamber for spatial emissivity measurements using thermal imaging. In *Infrared Systems - design and testing*, pages 76–82, 6-10 June 1988.

[46] B.W. Jones and A. Pantinakis. A radiometric method for measuring directional total emittance at ambient temperatures. *Measurement Science and Technology*, **3**(5):515–522, 1992.

[47] D.J. Price. The emissivity of hot metals in the infra-red. *Proceedings of the Royal Society (London)*, **59**:118–131, 1947.

[48] R.R. Brannon and R.J. Goldstein. Emittance of oxide layers on a metal substrate. *Journal of Heat Transfer*, **92**:257–263, May 1970.

[49] M.M. Fulk and M.M. Reynolds. Emissivities of metallic surfaces at 76K. *Journal of Applied Physics*, **28**(12):1464–1467, December 1957.

[50] Potapov E.V. Optical properties of bismuth and antimony in the infrared region of the spectrum at low temperatures. *Soviet Physics JETP*, **20**(2):307–312, February 1965.

[51] Biondi M.A. Optical absorption of copper and silver at 4.2K. *Physical review*, **102**(4):964–967, May 1956.

[52] S.M. Smith. Specular reflectance of optical-black coatings in the far infrared. *Applied Optics*, **23**(14):2311–2326, July 1984.

[53] T. Makino, O. Sotokawa, and Y. Iwata. Transient behaviours in thermal radiation characteristics of heat-resisting metals and alloys in oxidation processes. *International Journal of Thermophysics*, **9**(6):1121–1130, 1988.

[54] B.L. Drolen. Bidirectional reflectance and surface specularity results for a variety of spacecraft thermal control materials. Technical report, American Institute of Aeronautics and Astronautics, Inc., 1991.

[55] A.A. De Silva and B.W. Jones. Bidirectional spectral reflectance and directional-hemispherical spectral reflectance of six materials used as absorbers of solar energy. *Solar Energy Materials*, **15**:391–401, 1987.

[56] M. Brückner, J.H. Schäfer, C. Schiffer, and J. Uhlenbusch. Measurements of the optical constants of solid and molten gold and tin at $\lambda = 10.6\mu$m. *Journal of Applied Physics*, **70**(3):1642–1647, August 1991.

[57] F.L. McCrackin, E. Passaglia, R.R. Stromberg, and H.L. Steinberg. Measurement of the thickness and refractive index of very thin films and the optical properties of surfaces by ellipsometry. *Journal of Research of the National Bureau of Standards - A. Physics and Chemistry*, **67A**(4):363–377, July-August 1963.

[58] R.J. Archer. Determination of the properties of films on silicon by the method of ellipsometry. *Journal of the Optical Society of America*, **52**(9):970–977, September 1962.

[59] H.E. Bennett and W.F. Koehler. Precision measurement of absolute specular reflectance with minimized systematic errors. *Journal of the Optical Society of America*, **50**(1):1–6, January 1960.

[60] A.A. De Silva. *Measurement of some radiative properties of solar absorber materials.* PhD thesis, The Open University, October 1986.

[61] R.P. Blake and B.W. Jones. The measurement of directional radiative properties with applications to passively cooled space telescopes. In C. Eiroa, A. Alberdi, H. Thronson, T. De Graauw, and C.J. Schalinski, editors, *Infrared Space Interferometry: Astrophysics and the Study of Earth-like Planets*, pages 157–161, Dordrecht, 1997. Kluwer Academic Publishers.

[62] I. Šimon. Spectroscopy in infrared by reflection and its use for highly absorbing substances. *Journal of the Optical Society of America*, **41**(5):336–345, 1951.

[63] P.C. Logofătu, D. Apostol, V. Damian, and R. Tumbar. Ambiguities in determining the optical constants for two reflection methods. *Applied Optics*, **35**(1):117–119, 1996.

[64] P.C. Logofătu, D. Apostol, V. Damian, and R. Tumbar. Optimum angles for determining the optical constants from reflectivity measurements. *Measurement Science Technology*, **7**:52–57, 1996.

[65] J.H. Weaver, C. Krafka, D.W. Lynch, and E.E. Koch. *Part 1: The Transition Metals.* Fachinformationszentrum, Karlsruhe, FDR, 1981.

[66] G.A. Bolotin, A.N. Voloshinskii, M.M. Kirilbra, M.M. Neskov, A.V. Sokolov, and B.A. Charikov. *Fiz. Met. Metalloved.*, **13**:823, 1962.

[67] G.P. Motulevich and A.A. Shubin. *Soviet Physics JETP*, **20**:560, 1965.